

# UC Davis

## UC Davis Electronic Theses and Dissertations

### Title

Exploring animal models of two 21st century pandemics: Zika virus and SARS-CoV-2

### Permalink

<https://escholarship.org/uc/item/3kd5j6vs>

### Author

Ball, Erin

### Publication Date

2022

Peer reviewed|Thesis/dissertation

Exploring animal models of two 21st century pandemics:  
Zika virus and SARS-CoV-2

By

ERIN BALL  
DISSERTATION

Submitted in partial satisfaction of the requirements for the degree of

DOCTOR OF PHILOSOPHY

in

Integrative Pathobiology

in the

OFFICE OF GRADUATE STUDIES

of the

UNIVERSITY OF CALIFORNIA

DAVIS

Approved:

 May 18, 2022

---

Lark L. Coffey, Chair

  
5/16/22  
Koen K.A. Van Rompay

 17 May 2022

---

Patricia A. Pesavento

Committee in Charge

2022

# TABLE OF CONTENTS

<b>ACKNOWLEDGEMENTS.....</b>	<b>v</b>
<b>ABSTRACT.....</b>	<b>vi</b>
<b>CHAPTER 1.....</b>	<b>1</b>
<b>Literature review and background- Zika virus and SARS-CoV-2</b>	
<b>1 Flavivirus and coronavirus overview.....</b>	<b>2</b>
1.1. What is a pandemic?.....	2
1.2. Introduction to arboviruses.....	4
1.3. Mosquito-borne flaviviruses of public health concern.....	9
1.4. Flavivirus structure and replication.....	19
1.5. Coronaviruses of public health concern.....	22
1.6. Coronavirus structure and replication.....	23
<b>2 Zika Virus.....</b>	<b>27</b>
2.1 Natural history and emergence.....	27
2.2 Virus structure and replication.....	30
2.3 Life cycle, mosquito vector, and transmission.....	30
2.4 Clinical human disease, treatment, and prevention.....	35
2.5 Animal models.....	38
2.6 Pathogenesis.....	49
<b>3 SARS-CoV-2.....</b>	<b>55</b>
3.1 Natural history and emergence .....	55
3.2 Virus structure and replication.....	57
3.3 Transmission.....	59
3.4 Clinical human disease, treatment, and prevention.....	64
3.5 Animal models.....	70
3.6 Pathogenesis.....	73
<b>4 Conclusion and hypotheses.....</b>	<b>76</b>
<b>CHAPTER 2.....</b>	<b>79</b>
<b>Zika virus persists in the male macaque reproductive tract.</b>	
Abstract and author summary.....	80
Introduction.....	82
Results.....	85

Discussion.....	103
Methods.....	112
Supplemental material.....	117
Acknowledgements.....	119
<b>CHAPTER 3.....</b>	<b>120</b>
<b>Early prenatal Zika virus exposure is associated with abnormalities of the lateral geniculate nucleus in juvenile rhesus macaques</b>	
Abstract.....	121
Introduction.....	122
Results.....	124
Discussion.....	129
Methods.....	131
Acknowledgements.....	135
<b>CHAPTER 4.....</b>	<b>136</b>
<b>SARS-CoV-2 vasculopathy in a Syrian golden hamster model</b>	
Abstract.....	137
Introduction.....	137
Results.....	138
Discussion.....	147
Methods.....	151
Supplemental material.....	157
Acknowledgements.....	159
<b>Epilogue.....</b>	<b>160</b>
<b>References.....</b>	<b>163</b>

## **ACKNOWLEDGEMENTS**

Firstly, thank you to the US Army Veterinary Corps, Long Term Health Education and Training program for funding this PhD.

To my current and previous coworkers, Jackson, Danilo, Anil, Chris, Hongwei, Will, Ana, Adam, and Okuny, thank you for the ceaseless technical and scientific support, for your sense of humor, and for creating a fun and entertaining lab, particularly during these unprecedented times. I will miss working with you all, especially our brainstorming and food tasting sessions.

To the pathology staff at the UC Davis Vet School and CNPRC, thank you for your assistance with my dissertation work, as well as my collaborative projects. To my qualifying exam and dissertation committee members, Drs. Pesavento, Van Rompay, Reader, Woolard, and Shah, thank you for your support and guidance. To Lark, Patty and Koen in particular, thank you also for your guidance, mentorship, for treating me as a colleague, for your understanding of my “unique” situation as an Army officer and the world’s oldest living PhD student ☺, and, of course, for fostering a fun, productive, resilient, and supportive lab environment.

To my family, Mom, Dad, Amanda, Patrick, Cathy, thank you for your unconditional love and support. Our family zooms were a welcome distraction from the combined stress of the PhD program and quarantine. You always help to keep things in perspective. Finally, to Jared- I could never have done this without your understanding and support. Thank you for knowing when to drag me away from my computer to do something fun, and when to vacate the house and leave me to it ☺ Thank you for being you. I’m so excited for our Thailand adventure! I love you more!

## **ABSTRACT**

Zika virus (ZIKV) and severe acute respiratory syndrome coronavirus 2 (SARS-CoV-2) are the etiologic agents responsible for the two major pandemics of the 21<sup>st</sup> century (so far).

By virtue of its capacity for mosquito-borne, sexual, and vertical transmission, as well as its association with congenital Zika syndrome (CZS), ZIKV remains a significant global public health risk. Mounting evidence identifies the male reproductive tract as a significant ZIKV reservoir; however, data regarding the duration of ZIKV persistence, potential for sexual transmission, and male genitourinary sequelae remain sparse. Furthermore, while microcephaly is a well-documented, extreme manifestation of CZS, there are cases of normocephalic newborns with confirmed prenatal ZIKV exposure but no observable congenital defects exhibiting neurologic deficits and behavioral abnormalities over time. These and other long-term developmental sequelae to prenatal ZIKV infection are not well described.

I addressed these gaps in knowledge using archived tissues from 1) 51 ZIKV-inoculated male macaques from past collaborative research projects; and 2) two juvenile rhesus macaque infants exposed prenatally to ZIKV. In the male macaque cohort, I identified persistent ZIKV RNA and infectious virus in testis, epididymis, seminal vesicle, and prostate gland of sexually mature male macaques, with detection as late as 60 days post-inoculation. ZIKV RNA localized primarily to testicular stem cells/sperm precursors and epithelial cells, including Sertoli cells, epididymal duct epithelium, and glandular epithelia of the seminal vesicle and prostate gland. ZIKV infection was associated with microscopic evidence of inflammation in the epididymis and prostate gland of sexually mature males, which could have significant effects on male fertility. In the two juvenile

macaques, I identified CNS microcalcifications and macrostructural developmental abnormalities within the CNS visual pathway, specifically disorganization, blending of layers, laminar discontinuities, and regions of low cell density within the lateral geniculate nucleus.

COVID-19 disease, caused by SARS-CoV-2, varies from asymptomatic to severe respiratory disease, progressing to acute respiratory distress syndrome (ARDS), multiorgan dysfunction, and death in a subset of patients. Clinical evidence of coagulopathy and microscopic indicators of pulmonary vascular damage are increasingly reported; however, published autopsy data in human patients remain relatively scarce and SARS-CoV-2 induced vascular lesions have not been fully characterized. I used a previously described Syrian golden hamster model of COVID-19 disease to demonstrate that regions of active SARS-CoV-2 induced pulmonary inflammation exhibit ultrastructural evidence of endothelial injury with platelet marginalization and marked perivascular and subendothelial mononuclear inflammation composed primarily of macrophages. SARS-CoV-2 antigen/RNA was not associated with affected blood vessels. Taken together, these findings suggest that the prominent microscopic vascular lesions in SARS-CoV-2 inoculated hamsters (and by extrapolation, humans) are primarily due to indirect endothelial damage, likely secondary to immune dysfunction.

These studies emphasize the importance of animal models such as nonhuman primates and hamsters to study pathogenesis of emerging viral diseases.

**CHAPTER 1**

**LITERATURE REVIEW**

**Zika virus and SARS-CoV-2**

# 1 Flavivirus and coronavirus precipitate two major 21<sup>st</sup> century pandemics

## 1.1 What is a pandemic?

According to epidemiologists, the emergence of novel infectious disease pathogens is increasing in frequency (1). Emerging infectious diseases refer to novel infectious agents causing human disease for the first time, to increased incidence of previously identified infectious agents, or to infectious agents reported in new geographic areas with naïve populations (2). The observed or expected baseline level of a disease found in a particular geographic area is referred to epidemiologically as the endemic level (3). If the disease occurs at persistent, high levels it may be referred to as hyperendemic, while a sudden, significant increase in disease prevalence above the expected baseline is known as an epidemic (3). The occurrence of an epidemic requires that both the host and the pathogen are present in the same geographic area in adequate numbers, and that the infectious agent is transmitted effectively from the reservoir or vector to the susceptible host (**Figure 1**). Factors commonly associated with epidemics include increased pathogen virulence or transmissibility, increased host susceptibility, introduction of the pathogen to a naïve population, or any factors that increase host exposure to the pathogen (3).

The majority of this century's pandemics have been zoonotic in origin (i.e., the pathogen is transmitted from animals to humans) (1). Mammals, and to a lesser extent, avian species, are the most common reservoirs for zoonotic pathogens (excluding invertebrate vectors/intermediate hosts such as mosquitoes) (4). The reservoir for a zoonotic pathogen can come into contact with and infect a novel host population in a process known as cross-species transmission, or spillover (5). Pandemics are typically caused by spillover of zoonotic viruses (particularly wildlife

zoonoses) into naïve human populations and tend to be driven not simply by virus biology, but also by ecological, behavioral, and socioeconomic factors (1,6).

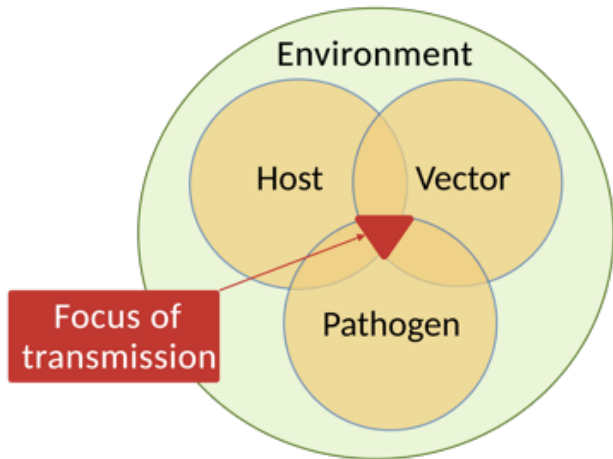


**Figure 1.** The epidemiological triad. Interactions between susceptible host, competent vector, and infectious pathogen in a permissive environment determine disease and pathogen ecology. Adapted from Hueffer K, *et al.* 2011 (7) using BioRender.com.

Studies of recent pandemic zoonoses have revealed repeated patterns. In addition to the drivers discussed above (such as changes in the ecology of the host, and/or pathogen, and/or vector) there is a strong correlation between emerging diseases and increased human population density with encroachment into wildlife habitat. Most emerging pathogens originate at regions of interface between humans, wildlife and/or livestock (where viruses coevolve with new hosts), supporting the hypothesis that anthropogenic factors such as agricultural expansion, changing land use patterns, trade and travel routes are principal contributors to contemporary infectious disease outbreaks (1,8). Global climate change is another major driver behind emerging infectious diseases (6). For instance, expansion of the geographic ranges of various mosquito vectors may explain the emergence/re-emergence of arboviruses such as dengue and Zika virus (9). A recent study identified the phylogenetic proximity of wildlife reservoirs to humans as an important predictor of emerging zoonoses, and further showed that RNA viruses in general and bat viruses in particular are predisposed toward zoonoses (8). This finding is not surprising in light of the number of

contemporary viruses that have been traced back to bat reservoirs, including Ebola and Marburg viruses, Hendra and Nipah viruses, severe acute respiratory syndrome coronavirus (SARS-CoV) and, Middle East respiratory syndrome coronavirus (MERS-CoV) (5,8).

## 1.2 Introduction to arboviruses

Arboviruses (arthropod-borne viruses) comprise more than 500 species (9) from multiple viral genera that are transmitted to vertebrate hosts either biologically from infected arthropod vectors (e.g., mosquitoes, ticks, sandflies, midges) or mechanically by contaminated mouthparts during blood feeding (10). Arboviruses circulate within wildlife populations; humans and domestic animals are typically considered incidental or dead-end hosts in that they do not develop viremia of sufficient magnitude to infect later vectors. However, some arboviruses, such as dengue and chikungunya viruses, have escaped this requirement for enzootic amplification and are instead able to maintain urban transmission cycles involving only humans and mosquito vectors (9,10). Biological transmission of an arbovirus to a susceptible vertebrate host follows viral replication within the infected arthropod vector and is typically horizontal, though vertical (from an infected female to her offspring) and venereal (from an infected male directly to a female vector or vice versa) transmission may also occur at low levels (10).

Vector competence refers to the ability of a vector to become orally infected and transmit a pathogen, while the extrinsic incubation period is the time it takes for successful transmission of a pathogen such as an arbovirus to a susceptible vertebrate host following ingestion of an infectious blood meal (11,12). Vectorial capacity is a measure of the transmission potential of a pathogen which takes into account both vector competence and the extrinsic incubation period; it represents

the number of cases resulting from the introduction of a single infectious person (12). Effective horizontal transmission of an arbovirus involves ingesting a viremic blood meal of sufficient titer to infect the vector (e.g., mosquito) midgut epithelium, subsequent viral dissemination within the hemocoel (body cavity) via hemolymph (the arthropod version of blood), viral replication within the salivary glands, and infection of the vertebrate host upon feeding (e.g., expectoration during mosquito probing and feeding) (**Figure 2**) (10,11,13). In addition to physical barriers, vector competence and the extrinsic incubation period are affected by environmental factors (especially temperature), innate immune responses, and indirect immune system effects associated with the arthropod microbiome (11,12).

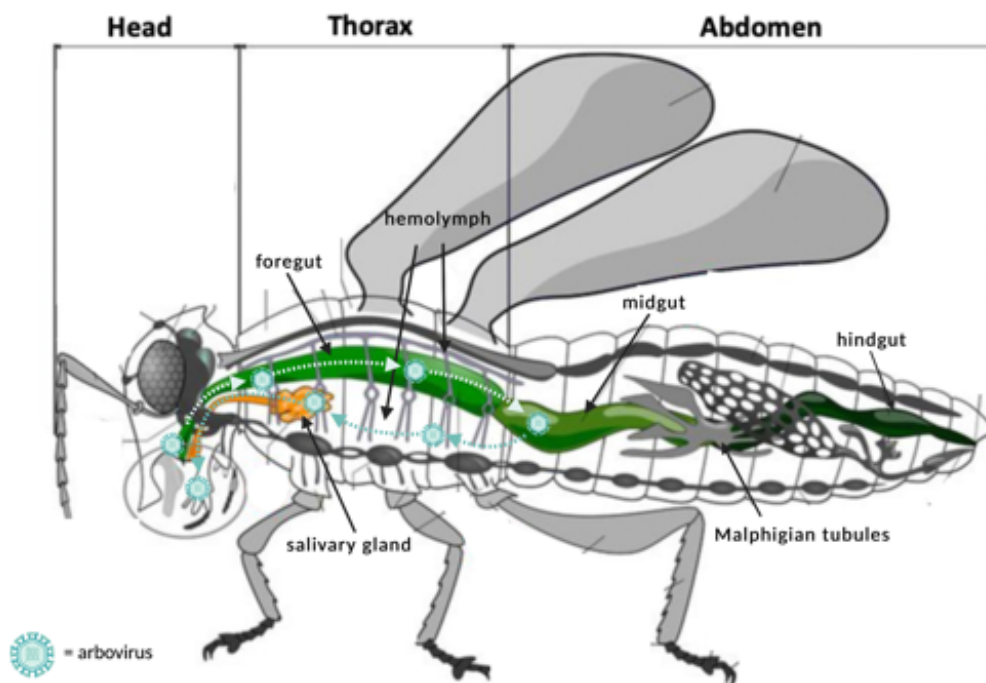


**Figure 2.** Schematic representation of arbovirus dissemination in a mosquito vector. Following an infectious blood meal, virions infect the midgut epithelium and disseminate via hemolymph to replicate in secondary tissues, eventually reaching the salivary glands, where infectious virus is released into salivary ducts for horizontal transmission in saliva to a susceptible vertebrate host. Viruses may also infect reproductive tissues for vertical transmission to offspring. Adapted from Piotr Jaworski, Creative Commons ([www.thoughtco.com](http://www.thoughtco.com)), 2019 (14) using BioRender.com

As noted above for emerging infectious diseases in general, arboviruses generally persist at endemic levels. Progression to epidemic levels requires that adequate numbers of competent vectors and susceptible hosts overlap within a permissive environment. This is typically facilitated by alterations in host, vector or viral biology and/or by anthropogenic changes such as human expansion into rural areas or wildlife habitat, climate-change induced expansion of vectorial geographic ranges, or increased urbanization resulting in heat islands that can expedite arboviral amplification/transmission (10). There are three major mechanisms underlying most human outbreaks of mosquito-borne arboviruses (**Figure 3**): 1) direct spillover from the enzootic host to humans; 2) human spillover following amplification in domestic animal species (see Japanese encephalitis and West Nile viruses below), where humans generally fail to develop sufficient viremias to carry on transmission and are thus considered dead-end hosts; and 3) urban transmission cycles (see dengue and Zika viruses below) between anthropophilic mosquitoes (e.g., *Aedes aegypti* and *Ae. albopictus*) and humans, who act as amplification hosts. It is the third mechanism, with its potential for rapid urban spread, that is one of the most important in terms of threat to human health (15). Globally, arboviral infections are on the rise, frequently emerging in areas with no previous history of local transmission or causing more severe manifestations of clinical disease in regions known to be endemic (9). For most arboviruses there are no approved vaccines or antiviral treatments (9).

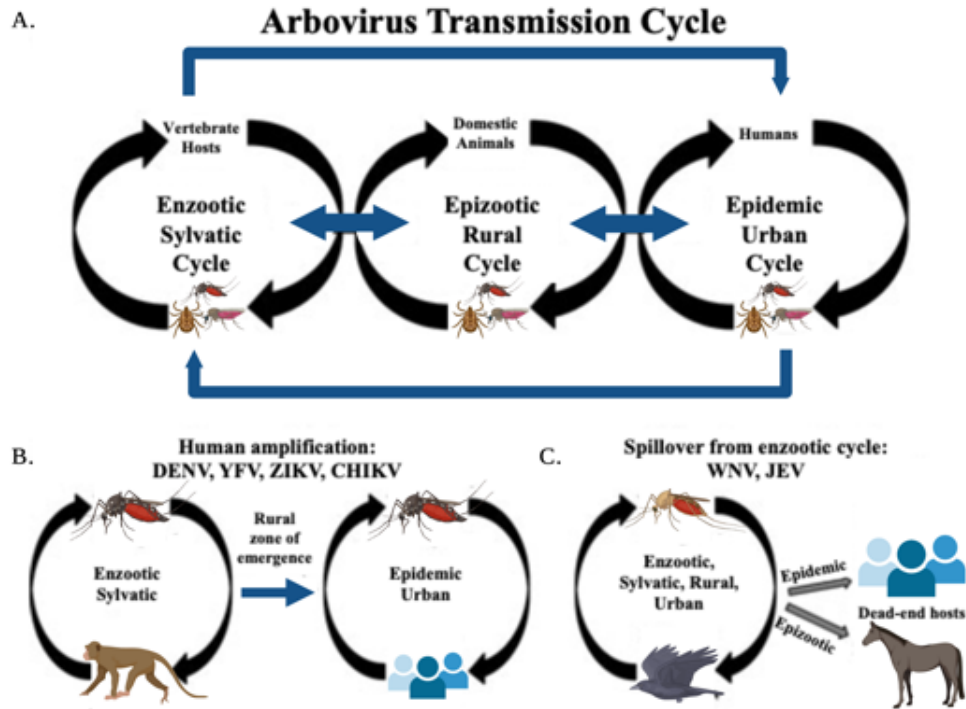


**Figure 3.** Typical arbovirus transmission cycles. DENV= dengue virus; YFV= yellow fever virus; ZIKV= Zika virus; CHIKV= chikungunya virus. Adapted from Anez G, *et al.* 2012 (9) using BioRender.com.

Arboviruses are comprised of a range of primarily RNA viruses, including (but not limited to) flaviviruses (e.g., dengue, West Nile, Zika, Japanese encephalitis, yellow fever, and tick-borne encephalitis viruses), alphaviruses (e.g., chikungunya, Mayaro, Venezuelan/Eastern/Western equine encephalitis viruses), bunyaviruses (e.g., Rift Valley fever virus), and orbiviruses (bluetongue virus). The only known DNA arbovirus is an asfarvirus, African swine fever virus. Almost all arboviruses are RNA viruses which often have higher mutation rates than DNA viruses because, for the most part, the arbovirus RNA polymerase lacks proof-reading ability. Error prone replication results in the random generation of viral variants, some of which possess the inherent ability to adapt to variable host/vector environments. Variants that survive in both vertebrate and invertebrate hosts are perpetuated in natural cycling (10,11). As mosquitoes are very common and well-described arthropod vectors, the remainder of this section will focus on mosquito-borne

arboviruses, specifically flaviviruses, though other non-mosquito-borne arboviruses are also significant causes of disease in both humans and domestic animals (10,11).

### **1.3 Mosquito-borne flaviviruses of public health concern**

The *Flavivirus* genus is comprised of more than 70 enveloped, positive-sense, single-stranded RNA viruses that, with few exceptions, require hematophagous (blood-feeding) arthropods such as mosquitoes or ticks to complete their horizontal transmission cycle (16,17). Members include yellow fever virus (YFV), dengue virus (DENV), Japanese encephalitis virus (JEV), West Nile virus (WNV), St. Louis encephalitis virus (SLEV), Zika virus (ZIKV), and tick-borne encephalitis virus ([TBEV] not discussed in this review), all of which are pathogenic in humans, domestic animals, and/or birds. These viruses have the potential to emerge in non-endemic regions with naïve human populations and thus pose a significant global public health concern (16,17). Among global arboviral activity over the last few decades, mosquito-borne flaviviruses are overrepresented; specifically, YFV, DENV, JEV, WNV, and ZIKV have been reported as emerging or re-emerging in various regions around the world (9). Most (50-80%) of human flavivirus infections are asymptomatic (18). When symptomatic, clinical signs are generally self-limiting and non-specific, and can include flu-like symptoms such as fever, arthralgia, myalgia, headache, and maculopapular rash. More severe clinical disease manifestations are also reported and include vascular damage, neuroinvasive disease, and death, depending on the virus, its pathogenesis, cellular and tissue tropisms, and the host immune responses (16,18). Based on these possible severe manifestations, flaviviruses are sometimes grouped as either those with the capacity to cause visceral disease, including vascular leakage and hemorrhage (e.g., YFV, DENV, and ZIKV) and those that can cause neurotropic disease (e.g., JEV, WNV and ZIKV) (18).

### 1.3.1 Yellow fever virus (YFV)

YFV (so named for the jaundice associated with severe cases) is the prototypical flavivirus; both humans and nonhuman primates (NHPs) are highly susceptible (1). Historical evidence and phylogenetic data suggest that this virus originated in Africa and spread to port cities of Americas by the 16<sup>th</sup> century, probably due to onboard human transmission cycles on slave ships which carried both the *Aedes aegypti* vector and naïve humans (19). Although mosquito control and the development of an effective vaccine have greatly reduced YFV in North America, it is considered a reemerging disease and a significant cause of morbidity and mortality in parts of Africa and South America, which tend to lack routine immunization programs (19). In 2013, World Health Organization (WHO) models estimated the global YFV burden at 84,000-170,000 cases annually, with 29,000-60,000 deaths (20). Enzootic, sylvatic transmission cycles in South/Central America involving nonhuman primates and canopy-dwelling mosquitoes such as *Hemagogus janthinomys* may also contribute to YFV spillover into nearby human settlements (known as ‘jungle’ yellow fever). Additionally, humans in urban areas can serve as viremic hosts when bitten by the anthropophilic, daytime-biting mosquito vector *Ae. aegypti* (known as ‘urban’ yellow fever) (1,21).

While African models estimate that only 12% of infections are symptomatic, mortality can range from 20 - 60% in severe symptomatic cases of YFV infection (18). When symptomatic, YFV is associated clinically with a hemorrhagic fever syndrome. Early symptoms are typical for a flavivirus (acute febrile illness), but can quickly progress to jaundice, hemorrhagic diathesis, shock, and death in severe cases. This is due to viral replication in hepatocytes (liver cells) with

subsequent liver and kidney damage, resulting in coagulopathy, disseminated intravascular coagulation (DIC), widespread hemorrhage, and eventually multi-organ failure and death (18,21).

### 1.3.2 Dengue virus (DENV)

In contrast to other flaviviruses, contemporary human DENV outbreaks are not zoonotic (1). Ancestral DENV strains maintained an enzootic transmission cycle between sylvatic canopy mosquitoes (i.e., *Aedes aegypti formosus*) and NHPs (a mechanism that continues today in the forests of West Africa and Southeast Asia); however, present-day DENV epidemics are largely characterized by independent urban transmission cycles between anthropophilic mosquito vectors and humans, who serve as both reservoir and amplification hosts (**Figure 3B**) (1,16). The primary vector, *Aedes aegypti aegypti*, evolved in Africa but was later transported all over the world (**Figure 4A**) (16). Females live in close proximity to humans (particularly in urban areas), rely exclusively on blood (vs. carbohydrates) for both oogenesis and energy needs, and oviposit desiccation-resistant eggs in artificial water containers. Additionally, the hematophagous females are day-biters. These factors result in frequent host contacts during a single mosquito gonotrophic cycle and likely contribute significantly to the success of *Ae. aegypti* as an arbovirus vector (16).

Unsurprisingly, poverty-stricken areas that lack municipal water services and trash collection are predisposed to significant DENV outbreaks (1). *Ae. albopictus*, another day-biting mosquito that evolved in Asia but was introduced to the Americas by the international used tire trade, serves as a secondary DENV vector in some areas (1). This invasive species is highly adaptable, with a relatively wide geographic range due to its tolerance of cooler temperatures (**Figure 4B**). *Ae. albopictus* is found both in urban areas and near dense vegetation (e.g., rubber and palm oil

plantations) (22). Both *Ae. aegypti* and *Ae. albopictus* also serve as vectors for CHIKV, YFV and ZIKV (22).

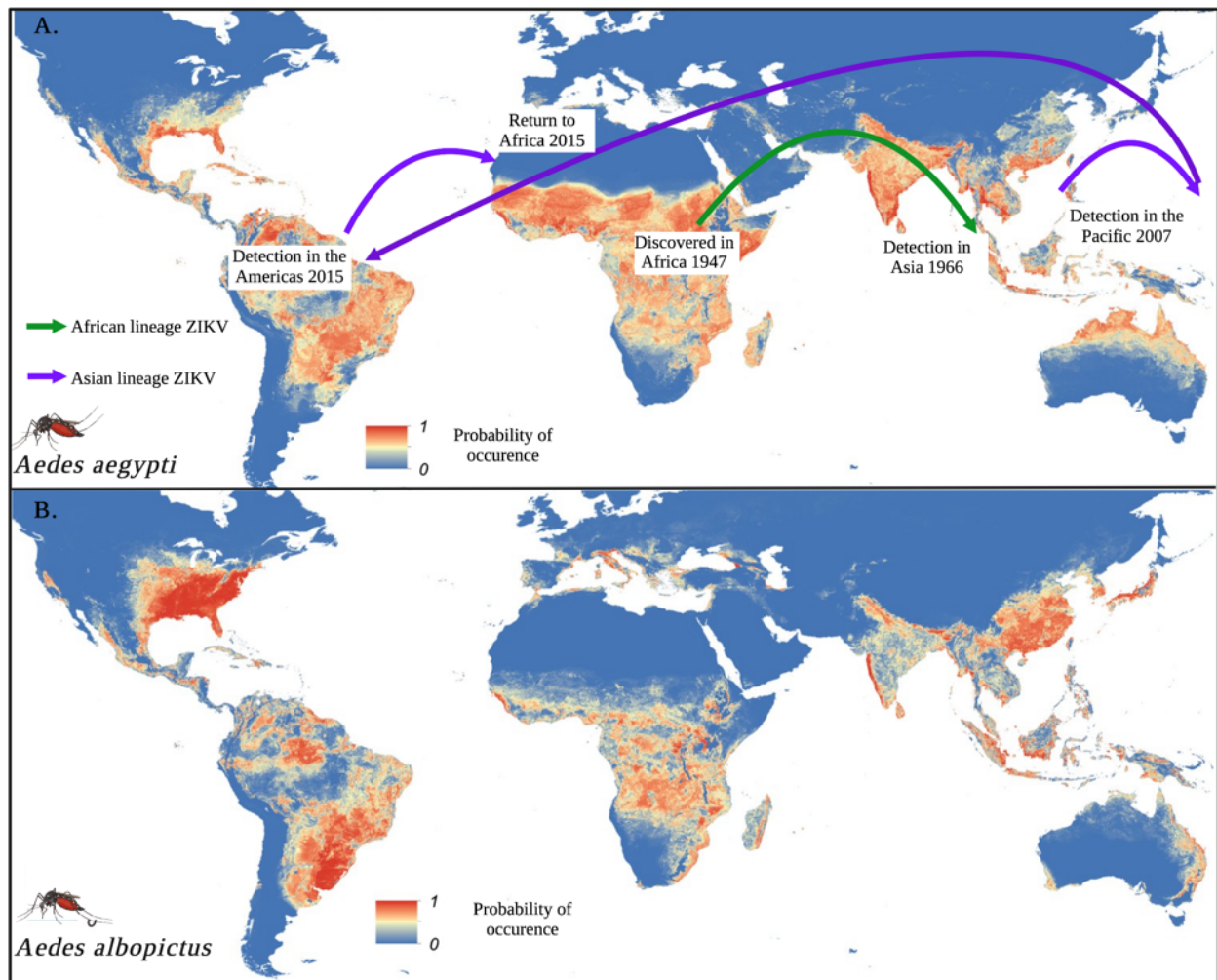


**Figure 4.** Global map showing the predicted distribution of *Ae. aegypti* (A) and *Ae. albopictus* (B), along with the timeline of Zika virus emergence (A). Legend depicts the probability of occurrence, ranging from 0 (blue) to 1 (red) at a spatial resolution of 5 km × 5 km. Adapted from Kraemer M, *et al.* 2015 (23) using BioRender.com.

Among flaviviruses, DENV is associated with the highest human morbidity and mortality (16). Due to urbanization, climate change, failures in mosquito control, and increased shipping/travel (9), both the global incidence and geographic range of DENV have increased dramatically over the past 20 years (22). The WHO estimates an approximate frequency of 390 million DENV

infections per year of which ~96 million are symptomatic, with 3.9 billion people in 129 tropical and subtropical countries (particularly in Asia) at risk for DENV infection (22). Like other flaviviruses, most DENV infections are subclinical, though it is notable that both pre-symptomatic and asymptomatic patients can develop sufficient viremia for human-to-mosquito transmission of DENV (9,22). Patients with symptomatic DENV can be any age and typically exhibit non-specific, febrile illness following a 4-10 day incubation period (22). A subset of patients develop severe dengue, which is also referred to as dengue hemorrhagic fever. Severe dengue is strongly associated with previous DENV infection, is characterized by vascular leakage/hemorrhage, and can result in widespread edema, respiratory distress, hypotension, organ dysfunction and death (1,22). Though most DENV infections are mosquito-borne, vertical transmission during pregnancy and transmission via blood transfusion or organ donation are also infrequently reported (22).

There are four DENV serotypes (DENV-1 to 4) which co-circulate simultaneously in dengue endemic countries; many countries are hyperendemic for all four serotypes (9). While recovery from DENV infection results in lifelong immunity against the infecting serotype, there is only partial, temporary cross-immunity to the remaining serotypes (24). Secondary infection by a different serotype is associated with severe dengue (22). A proposed mechanism for severe dengue is known as antibody-dependent enhancement where non-neutralizing antibodies from the initial DENV infection bind to a heterotypic serotype during secondary infection. Rather than neutralizing the virus, the antibody-virus complexes bind monocyte Fc $\gamma$  receptors, resulting in more efficient entry into monocytes and a higher risk of developing severe dengue (16,24,25). There is no specific treatment for dengue fever and supportive care is used to mitigate disease. A dengue vaccine (Dengvaxia®) was released by Sanofi Pasteur in 2015; however, vaccination of

seronegative individuals, particularly children, was later shown to be associated with a high risk of developing severe dengue. As a result, vaccination with Dengvaxia® is only recommended for individuals between 9 and 45 years old who reside in DENV-endemic areas and have had at least one previous episode of DENV infection (22).

### 1.3.3 Japanese encephalitis virus (JEV)

First described in Japan in the 1800s, JEV is the most common cause of mosquito-borne encephalitis in Asia. It is also one of the few viral encephalitides for which there is a vaccine (1), although recent studies suggest that the existing vaccine may not be as effective against divergent strains of JEV newly identified in Malaysia, Korea, and China (18). The enzootic transmission cycle is maintained between mosquito vectors of the genus *Culex* and ardeid birds (e.g., black-crowned night herons [*Nycticorax nycticorax*] and Asian cattle egrets [*Bubulcus ibis coromandus*]), which fail to develop clinical disease (1,26). In addition to aquatic bird species, domestic swine serve as important amplification hosts (26,27). This is likely a function of both their propensity for developing prolonged, high-titer viremia and the close proximity of pig farms to human communities (26,27). JEV causes disease in a variety of vertebrate species (e.g., equids) as well as humans (26). Human outbreaks have been closely associated with significant increases in human population density, irrigated rice acreage (which leads to increased abundance of both the mosquito vector and the ardeid bird maintenance hosts), and pig farming (1). Disease distribution reaches from Korea south to Australia and northwest to Pakistan and correlates with the expansion of irrigated crops such as rice and the geographic range of the primary vector (*Culex tritaeniorhynchus*). Currently, over 3 billion people live in geographic regions considered to be at risk for JEV. The vast majority of human and equid JEV infections are transmitted via blood

feeding by infected mosquitoes who previously fed on infected birds. Both humans and equids are considered dead-end hosts as they fail to develop high enough titer viremias to infect mosquitoes (1).

Most adults residing in JEV-endemic areas have protective immunity associated with either natural childhood infection or vaccination, so Japanese encephalitis primarily affects children, and, to a lesser extent, the elderly. Naïve travelers of any age are also at risk (26). The global incidence of Japanese encephalitis is unknown due to incomplete reporting and inadequate diagnostic surveillance in many JEV-endemic countries (27); however, current estimates range from 50,000 to 68,000 cases annually, depending on region, age and immunization status (26,27). Nearly 99% of human JEV infections are asymptomatic. In symptomatic cases, a typical prodromal febrile phase begins after a 5 to 15 day incubation period. For a subset of patients, this may be followed by a range of neurologic lesions, including meningitis, encephalitis, a Parkinson-like syndrome characterized by tremors and hypertonia, and/or acute flaccid paralysis. Clinical Japanese encephalitis is associated with a mortality rate of 20 - 30% (27). Neurologic sequelae are reported in 30 - 50% of survivors and include seizures, movement disorders, cognitive deficits, learning disabilities, and behavioral problems (26,27).

#### **1.3.4 West Nile virus (WNV)**

WNV, one of the most widely distributed arboviruses in the world, is found on all continents except Antarctica (9). The virus first emerged in the United States in New York in the summer of 1999, and over the next 5 years it spread across the continent, reaching the Pacific coast by 2003, causing seasonal epidemics as far north as Canada and as far south as Argentina and Brazil (9,28,29).

Between 1999 and 2020, more than 50,000 human cases of WNV were reported in the United States alone; over 25,000 of these were associated with neuroinvasive disease, resulting in more than 2,000 deaths (30). Cases also continue to emerge in both humans and horses in Europe (18). WNV is maintained via enzootic transmission cycle primarily between mosquito vectors of the genus *Culex* (i.e., *Culex pipiens*, *tarsalis* and *quinquefasciatus*) and passeriform birds (i.e., house sparrows and finches, blue jays, robins, crows) which are ubiquitous, highly competent amplification hosts. American crows in particular develop high magnitude viremias and, due to a mortality rate approaching 100%, they serve as a key indicator species for seasonal North American outbreaks of WNV (31). As with JEV, infected *Culex* mosquitoes tangentially transmit WNV to equids and humans, which are dead-end hosts. Though most human infections are mosquito-borne, transmission via blood transfusion, organ transplants and breast milk are also rarely reported (1,28).

Like JEV and other flaviviruses, the majority (approximately 80%) of human WNV infections are asymptomatic. When symptomatic, following an incubation period averaging 2 to 14 days (29), clinical signs vary from non-specific and flu-like (West Nile fever [WNF]), to severe neuroinvasive disease, including encephalitis, meningitis and/or acute flaccid paralysis (AFP) (24,29). Neuroinvasive disease is associated with a mortality rate of approximately 10% (29,30). Studies in the United States suggest that, while people of any age are equally susceptible to infection with WNV infection, the risk of neuroinvasive disease and death increases significantly with age (60 - 89 years old) (28,29). An effective vaccine is widely used in equids; however, there is currently no licensed vaccine for humans and treatment remains supportive, with prevention strategies focused primarily on mosquito control (29).

### 1.3.5 St. Louis encephalitis virus (SLEV)

SLEV occurs throughout North and South America, as well as in the Caribbean (32). It was first identified in the summer of 1933 during a mosquito-borne viral epidemic in St. Louis, Missouri (33). Its geographic range extends from Canada to Argentina; however, nearly all reported human cases of SLE have been in the U.S.- historically in urban areas within the eastern and central states, but more recently in southwest states (34). Notably, following the emergence of WNV in New York in 1999, SLEV activity in the U.S. decreased significantly (32). Published data indicate that, not only does experimental WNV infection of an amplifying host, the house finch (*Haemorrhous mexicanus*), prevent subsequent infection with SLEV by conferring sterilizing immunity (35), but WNV may actually competitively inhibit SLEV amplification within their shared avian hosts (33,36). Since the 1930s, SLEV activity has been documented continuously in the U.S., primarily in southern and western states, via mosquito and sentinel chicken surveillance, though sporadic, focal human outbreaks have also been reported. In South and Central America, only scattered human cases were reported until 2005 when an SLE outbreak occurred in Córdoba City, Argentina (33). This epidemic was significant not for its magnitude, where only 47 probable or confirmed cases were reported, but for the severity of clinical disease where 45 of these 47 patients were hospitalized and nine died (33). In 2015, there was a small SLE outbreak in Arizona that included a fatal case, and SLEV was identified in local mosquito pools; since then there have also been human cases in California, Arizona and Nevada (32,33). Phylogenetic data suggests that the SLEV in the western U.S. since 2015 is actually due to introduction of a South American lineage of SLEV, rather than re-emergence of previously endemic strains (32). Overall, from 2011 to 2020

there have been about 100 cases of SLE in the U.S., with 25 cases of neuroinvasive disease and six fatalities (34).

Like WNV, SLEV maintains an enzootic transmission cycle between *Culex* mosquitoes and the amplifying hosts, passerine and columbiform birds and particularly house finches, house sparrows, and doves. Birds generally remain asymptomatic; however, spillover into humans and equid species can result in clinical outcomes ranging from mild febrile illness to fatal neurologic disease (32). SLE epidemics have been associated with environmental factors such as temperature, rainfall, snowmelt, and surface water conditions (33). When symptomatic, the clinical presentation of SLEV infection in humans may be indistinguishable from WNV. Following a 4 to 14 day incubation period, patients typically present with non-specific febrile illness similar to other flaviviruses. A subset of SLE patients go on to develop neuroinvasive disease characterized by neurologic symptoms such as stiff neck, disorientation, dizziness, tremors, ataxia, and sometimes coma. As with WNV, SLEV infection tends to be more severe older adults vs. children and young adults (34) and there is a significant correlation between age and neurologic symptom severity (33). This was apparent during the 2015 outbreak in Argentina, where approximately 95% of patients over 60 years old developed encephalomyelitis (vs. 80% of patients less than 20 years old) (33). The mortality rate in patients diagnosed with SLE ranges from 5 to 20% and there is no approved vaccine or antiviral treatment (34).

### **1.3.6 Zika virus (ZIKV) and other emerging flaviviruses**

Mosquito-borne ZIKV, discovered in the Ziika forest of Uganda in 1947, emerged rapidly into urban areas in 2007, initiating epidemics in the Pacific, Southeast Asia, and the Americas (37).

ZIKV is discussed in detail below. Another emerging flavivirus, Usutu virus (USUV), is closely related phylogenetically to JEV and WNV and cycles enzootically in Africa between ornithophilic mosquitoes (primarily *Culex* spp., though it has been detected in some *Aedes* spp. as well) and both passerine (i.e., blackbirds [*Turdus merula*], magpies [*Pica pica*]) and strigiform (e.g., great grey owls [*Strix nebulosa*]) birds, which serve as amplifying hosts (38). USUV has historically been confined to Africa; however, it has recently received attention due to its identification in Europe, primarily via mosquito and bird surveillance. Symptomatic cases have also been reported in Italy and Croatia (39). Though not discussed in this brief review, there are also a number of tick-borne flaviviruses associated with encephalitis and hemorrhagic fever, including tick-borne encephalitis (TBE), Kyasanur Forest Disease (KFD), Alkhurma disease, and Omsk hemorrhagic fever (40).

#### 1.4 Flavivirus structure and replication

Flaviviruses share similar genomic organization and replication strategies. They are small (~50 nm diameter) spherical, enveloped virus particles with a positive sense (+) single stranded RNA (ssRNA) genome of 10–11 kb (18). The genome is comprised of a single open reading frame (ORF) flanked on either side by 5' and 3' untranslated regions (UTRs), with a cap at the 5' end. The ORF is translated into a polyprotein with three structural (capsid [C], precursor of membrane [prM], and envelope [E]) and seven non-structural (NS1, NS2A, NS2B, NS3, NS4A, NS4B and NS5) proteins (**Figure 5**) (18) which are subsequently cleaved by both viral and host proteases, resulting in mature proteins (41). The structural proteins are the first to be translated and are the only ones found in mature, infectious virions, while the non-structural proteins are primarily involved in viral replication (41).

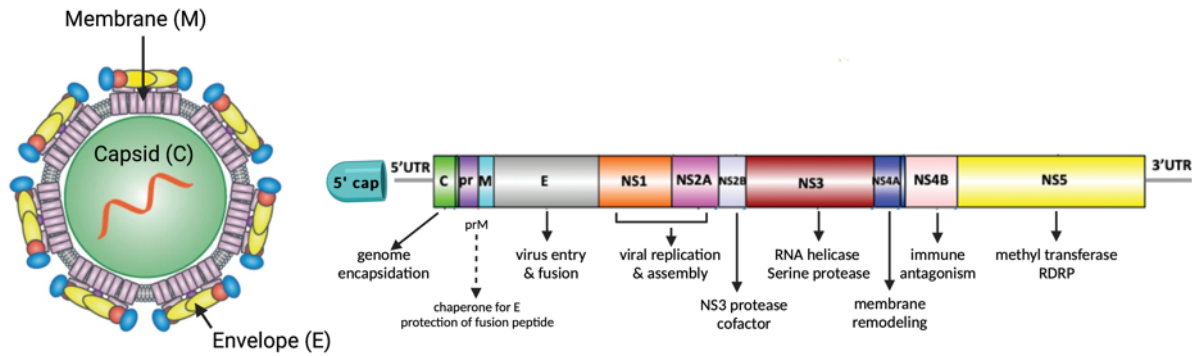


**Figure 5.** General genomic organization of flaviviruses. The flavivirus RNA genome has a 5' cap but lacks a poly A tail and encodes 3 structural proteins (C, prM/M, E) and 7 non-structural proteins (NS1, NS2A, NS2B, NS3, NS4A, NS4B and NS5). The major function is listed for each protein. The gray lines represent 5'- and 3'-untranslated regions (UTR). Adapted from Pierson TC, Diamond MS, 2020 (18), and Sirohi D, Kuhn RJ, 2017 (42) using BioRender.com. RDRP = RNA dependent RNA polymerase.

Flaviviruses enter susceptible host cells (i.e., cells of monocyte-macrophage lineage) via receptor-mediated endocytosis facilitated by structural protein E (24,43), though the precise receptor(s) required for flavivirus entry into different host target cells remain incompletely understood (43) (**Figure 6**). Regardless of specific host-receptor interactions, the ensuing acidic endosomal pH facilitates viral fusion with the host cell membrane and release of the nucleocapsid and single stranded RNA (ssRNA) genome into the cytoplasm (24). After uncoating and translation of the polyprotein and processing into structural and non-structural proteins, RNA synthesis begins. RNA synthesis occurs on double membrane vesicle packets (VP or DMV) derived from the rough endoplasmic reticulum (rER) and Golgi-apparatus (41), where there is protection from innate immune surveillance (18). Genome replication is followed by export into the cytoplasm and virion assembly in the rER. In contrast to mature virions, which are smooth and spherical, immature virus particles are spiky, measuring ~60 nm in diameter, and comprised of the replicated genome surrounded by an inner nucleocapsid and an outer lipid bilayer envelop with embedded E and prM heterodimer complexes (24). These immature, non-infectious virions bud into the rER lumen for

maturation and transport through the trans-Golgi network (TGN) (44). The slightly acidic pH of the TGN stimulates both envelope protein reorganization and furin-induced cleavage of prM into pr and M (45). Exposure to the neutral pH of the extracellular environment following exocytosis results in dissociation of the cleaved prM fragment and emergence of a mature, infectious flavivirus particle (**Figure 6**) (43). Subviral particles (SVPs), which contain both a lipid membrane and prM-E complexes, but lack a capsid and genome, are produced as natural by-products and released in a similar manner to mature virions; however, SVPs are not infectious (24,43).

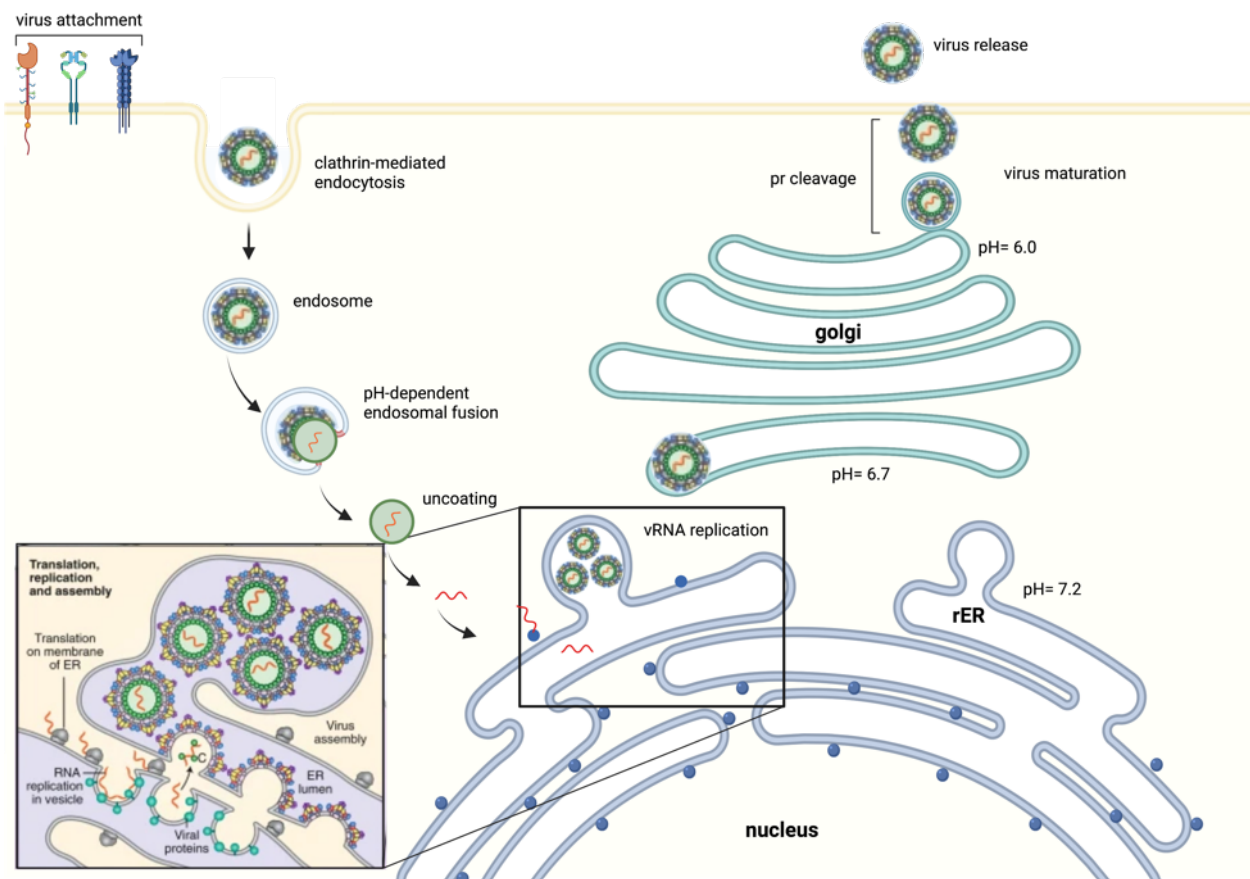


**Figure 6.** Summary of flavivirus replication steps. Flaviviruses enter susceptible host cells via receptor-mediated endocytosis. The acidic endosomal pH facilitates viral fusion with the host cell membrane and cytoplasmic release of the nucleocapsid and ssRNA genome. RNA replication occurs on complex virus-induced double membrane structures, after which immature virus particles assemble in rough endoplasmic reticulum (rER) and then traffic through the trans-Golgi network (TGN). The mildly acidic TGN pH facilitates furin-induced cleavage of prM. The neutral

pH of the extracellular environment following exocytosis results in dissociation of the cleaved pr fragment and emergence of mature, infectious flavivirus particles. Adapted from Pierson TC, Diamond MS, 2020 (18) using BioRender.com.

## 1.5 Coronaviruses as a public health concern

Coronaviruses are zoonotic and capable of causing respiratory and intestinal disease in both humans and domestic animals. There are four genera within the subfamily *Coronavirinae*, including *alpha-*, *beta-*, *gamma-*, and *deltacoronavirus*. Gamma- and deltacoronaviruses predominantly infect birds and rarely mammals. Alpha- and betacoronaviruses infect mammals exclusively, causing respiratory disease in humans and gastroenteritis in domestic animals (e.g., porcine transmissible gastroenteritis virus, porcine enteric diarrhea virus [PEDV] and swine acute diarrhea syndrome coronavirus [SADS- CoV]) (46). Prior to 2003, coronaviruses circulating in humans (HCoV- NL63, HCoV-229E, HCoV- OC43 and HKU1) were primarily associated with mild, seasonal respiratory infections (i.e., the “common cold”) in immunocompetent people, although severe infections were occasionally reported in infants, young children, and the elderly (46–48).

Beginning in 2002-2003 in Guangdong province, China (46), the first SARS-CoV pandemic resulted in more than 8,000 worldwide infections and 775 deaths (49). SARS-CoV infection causes non-specific febrile illness with fever, cough, dyspnea, and headache (50). Since 2012, there have been nearly 2,500 confirmed cases of MERS-CoV in 27 countries and especially in Saudi Arabia, resulting in over 850 deaths (51). In late 2019 betacoronavirus SARS-CoV-2, the etiologic agent behind COVID-19 (discussed in detail below), emerged in Hubei province, China. The resulting COVID-19 pandemic has overwhelmed health care systems and continues to cause devastating economic damage worldwide (47). As of May 2022, there have been more than 500 million

confirmed cases and 6 million deaths globally (52). SARS-CoV, MERS-CoV and SARS-CoV-2 can infect bronchial epithelial cells, pneumocytes and upper respiratory tract cells in humans; thus infected individuals can develop severe, life-threatening respiratory disease (48).

Coronaviruses adapt to infect new host species via genetic recombination and mutation. As with arboviruses, human coronavirus epidemics are typically associated with areas of human-wildlife interaction; in fact, all known pathogenic coronaviruses have wildlife origins, with domestic animals often serving as intermediate hosts and facilitating viral transmission to humans (46). Early in the first SARS-CoV outbreak, the virus was identified in masked palm civets (*Paguma larvata*) in live animal markets; however, further epidemiological investigation indicated that the SARS-CoV strains found in market civets were probably transmitted to them via bats, which are hunted as a food source in many Asian and African countries, and that civets probably served as intermediate hosts rather than the reservoir (46,49). Following its initial introduction, SARS-CoV progressed to human-to-human transmission, eventually spreading globally as far away as Toronto (1). Similarly, while many cases of human MERS-CoV were linked to contact with dromedary camels (*Camelus dromedarius*) (46,51), a closely phylogenetically related coronavirus of bat origin was subsequently identified (although live MERS-CoV has not been isolated from wild bats) (49). Taken together, published data and current sequence databases suggest that SARS-CoV and MERS-CoV, and likely SARS-CoV-2 likely originated in bats (47,49).

## 1.6 Coronavirus structure and replication

Coronaviruses are so named due to the 9 – 12 nm “spikes” (S-protein trimers) projecting from the host-derived viral envelope, which are reminiscent of a solar corona (47). At approximately 30 kb,

the positive ssRNA coronavirus genome is the largest among RNA viruses, significantly larger than that of the flaviviruses discussed above. The coronavirus genome is flanked by two untranslated regions (UTRs): a 5'-cap structure and a 3'-poly-A (polyadenylated) tail, both of which have *cis*- acting secondary RNA structures critical for RNA synthesis (47). The coronavirus genome/subgenomes generally contain at least six ORFs (53). Two large ORFs at the 5' end (ORF1a and ORF1b) occupy two-thirds the genome length and encode two long polypeptides (pp1a and pp1b) that are proteolytically cleaved into 16 non-structural proteins, most of which are essential components of the viral replication and transcription complex (48,53). In contrast to flaviviruses, coronaviruses are capable of proofreading during replication (48). ORFs adjacent to the 3'- terminus encode at least four main structural proteins, including spike (S), envelope (E), membrane (M), and nucleocapsid (N) proteins (**Figure 7**) which are necessary for virion assembly (48). Additionally, different species of coronaviruses have interspersed ORFs encoding a range of accessory proteins (e.g., HE protein, 3a/b protein, and 4a/b protein) which are thought to affect virulence by modulating the host response to infection (48). The various structural and accessory proteins are translated from 3' subgenomic RNAs (sg RNA) to form a characteristic nested set of subgenomic messenger RNAs (sg mRNAs) (48,53).

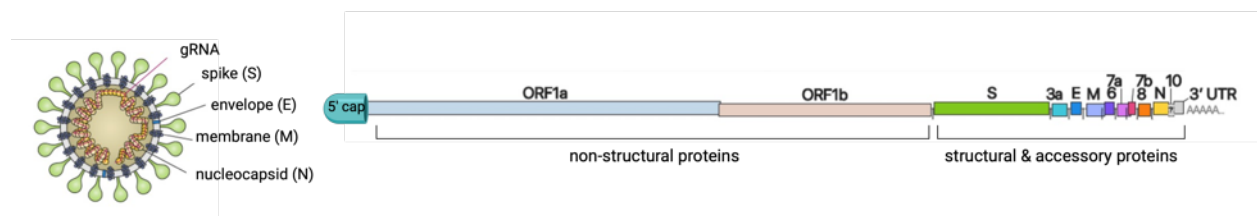


**Figure 7.** General genomic organization of coronaviruses. The large (30 kb) coronavirus RNA genome has a 5' cap and a poly A tail. Two large ORFs at the 5' end (ORF1a and ORF1b) encode two long polypeptides that are proteolytically cleaved into 16 non-structural proteins, most of which are important in viral replication. ORFs at the 3' end encode at least four structural proteins, including spike (S), envelope (E), membrane (M), and nucleocapsid (N) proteins, which are necessary for virion assembly. Additional ORFs encode a range of accessory proteins which may vary based on coronavirus species. Adapted from Kim D, *et al.*, 2020 (54) using BioRender.com.

The first step in any coronavirus infection involves binding of the receptor-binding domain (RBD) of the viral spike (S) protein to the appropriate host cell receptor (55). Distribution and expression of coronavirus receptors are important determinants of pathogenicity. Host receptors have been characterized for several pathogenic coronaviruses, including HCoV-229E (human aminopeptidase N [APN]), MERS-CoV (dipeptidyl peptidase 4 [DPP4]), and SARS-CoV, SARS-CoV-2 and HCoV- NL63 (angiotensin- converting enzyme 2 [ACE2]) (48,56). For both SARS-CoV and SARS-CoV-2, bound S-protein is proteolytically cleaved by host membrane type 2 transmembrane serine protease (TMPRSS2), and to a lesser degree, endosomal cysteine proteases cathepsin B and L (CatB and CatL). Cleavage of S1/S2 by furin-like protease primes the S-protein for cellular entry and ultimately facilitates viral fusion with the host cell endosomal membrane. Alternatively, cleavage may occur by other proteases following fusion of the late endosome with a lysosome (47,56,57). The general replication steps for SARS-related coronavirus (SARS-CoV and SARS-CoV-2) are depicted in **Figure 8**.

Following viral entry and fusion with the cellular or endosomal membrane, coronaviral genomic RNA is released/uncoated and recognized as mRNA by ribosomes, which directly translate the two large ORFs (ORF1a and ORF1b) into two long polyproteins (pp1a and pp1ab). Pp1a and pp1b are co-/post-translationally proteolytically cleaved into 16 non-structural proteins (including RNA-dependent RNA polymerase [RdRp]), which are essential components of the viral replication and transcription complex as well as facilitators of intracellular membrane remodeling (48,53). Viral genomic RNA replication and transcription of sgRNAs occurs in perinuclear DMVs, which, along with convoluted membranes (CMs) and small double-membrane spherules (DMSs), form an interconnected, vesicular structure associated with the ER/Golgi apparatus, known as the

coronavirus replication organelle (RO) (58,59). The RO provides a protective microenvironment hidden from cytosolic innate immune sensors, as well as increasing replicative efficiency by positioning replication factors within close proximity to one another. Structural M, S and E proteins are directly translated onto the ER membrane, while cytosolic N-protein encapsidates newly replicated genomes to form the nucleocapsid. In the ER- to- Golgi intermediate compartment (ERGIC), the nucleocapsid induces invagination of the ER membrane embedded with M-, S- and E-proteins, ultimately resulting in the formation of new viral particles within DMVs (48,57). S-protein homotrimers form spikes on the viral surface and, as noted above, are critical for host cell attachment and entry. M-protein binds to the nucleocapsid, stimulating membrane curvature and shaping virions. E-protein is involved in viral assembly and release, as well as viral pathogenesis (53). Mature, infectious virions are secreted from the infected cell by exocytosis (48).

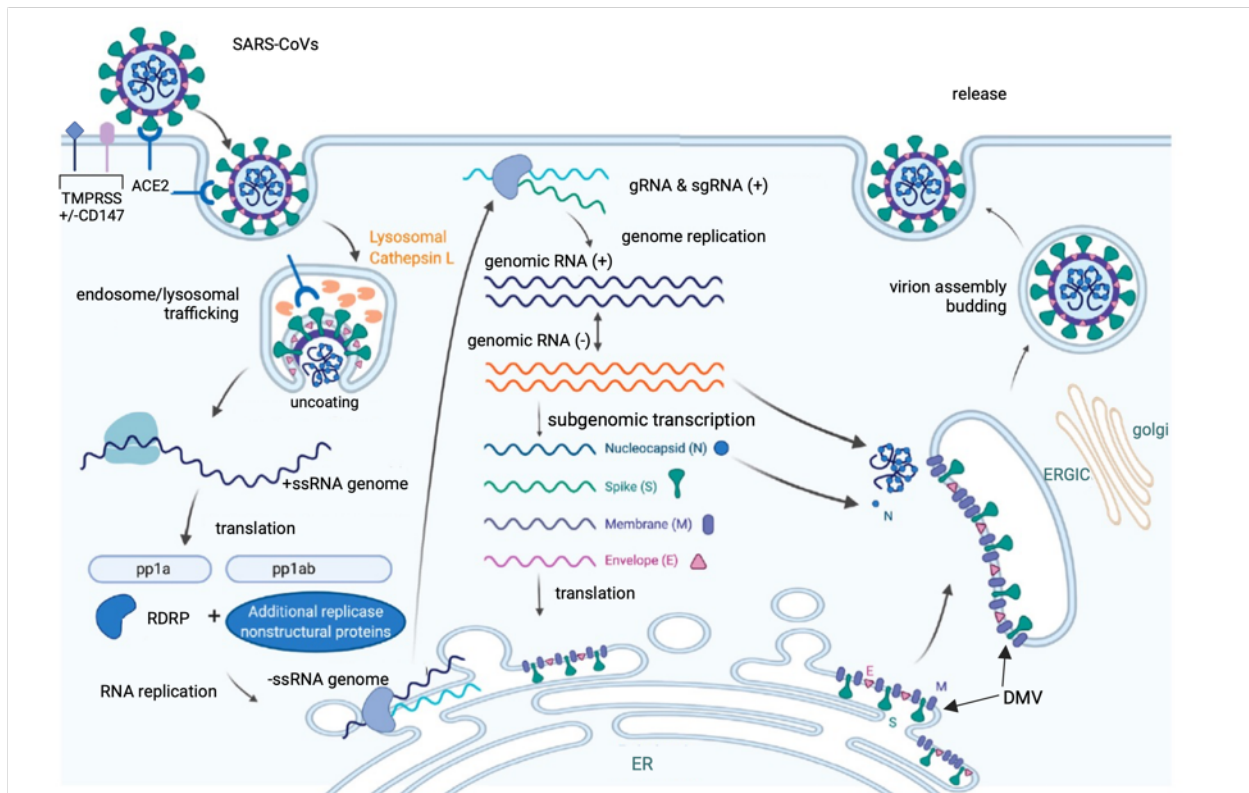


**Figure 8.** SARS-CoV/SARS-CoV-2 lifecycle. To enter a susceptible host cell, the SARS-CoV envelope spike (S) protein binds angiotensin-converting enzyme 2 (ACE2). Surface transmembrane protease serine 2 (TMPRSS2) facilitates cleavage of the S1/S2 site, SARS is shuttled into the endosomal pathway, and endolysosomal cathepsin L mediates virus–cell membrane fusion. Recent studies also suggest that SARS-CoV-2 may alternatively utilize receptor CD147 (also known as basigin) (47). Upon cytosolic release the viral RNA genome, ORF1a/b are translated into polyproteins (pp1a and pp1b), which are cleaved by viral protease into individual replicase complex nonstructural proteins, including the RNA-dependent RNA polymerase (RdRp). Viral genomic RNA replication and transcription of subgenomic (sg)RNAs occurs in complex virus-induced perinuclear double-membrane vesicles (DMVs) associated with the endoplasmic reticulum (ER). Translation of sgRNA produces both structural (spike [S], envelope [E], membrane [M], nucleocapsid [N]) and accessory proteins which are inserted into the ER–Golgi intermediate compartment (ERGIC), where they interact with newly formed positive sense genomic RNA to form a complete virion. Finally, mature, infectious virions are secreted from the infected cell by exocytosis. Adapted from Harrison AG, *et al.*, 2020 (60) using BioRender.com.

## 2 Zika virus

### 2.1 Natural History and Emergence of Zika virus

ZIKV was originally identified in a febrile rhesus macaque (with no other clinical signs) during a YFV surveillance study in the Ziika Forest preserve of Uganda in 1947. Shortly thereafter, ZIKV was isolated from forest dwelling *Aedes africanus* mosquitoes. This African ancestral/ prototypical strain of ZIKV was designated MR-766 (37,61) and transmission was primarily enzootic, circulating between NHPs and sylvatic mosquitoes, with occasional spillover into humans causing small, sporadic urban outbreaks (62). The first documented human ZIKV cases, which were diagnosed via virus isolation and identification of serum antibodies, occurred in Nigeria in 1952 (63–65). Over a decade later, ZIKV was isolated outside of Africa for the first time from domestic *Ae. aegypti* mosquitoes in Malaysia in 1966 (**Figure 4**) (66). By 1977-1978, several human ZIKV infections were reported in Indonesia and were characterized clinically by fever, malaise, gastrointestinal pain and anorexia (67); however, data regarding the incidence of human ZIKV infection in Africa and Asia is largely lacking for this time period. There are only 13 documented

cases of natural human ZIKV infection prior to 2007 (68). However, as ZIKV testing was primarily serologic in nature, and there is cross-reactivity between antibodies produced by ZIKV and infection with other flaviviruses endemic in ZIKV areas, it is likely that human ZIKV infection was misdiagnosed and underreported for years (65). Due to what was thought to be only sporadic association with human infections, ZIKV was not generally considered to be a significant public health threat (and thus little research was performed) until more recently. Unlike ancestral African lineage ZIKV, which is characterized by an enzootic sylvan transmission cycle with occasional human spillover, people infected with emerging Asian lineage ZIKV developed high enough viral titers for a continuous urban cycle between humans and peridomestic/domestic *Aedes* spp. mosquitoes (*Aedes aegypti* and *Ae. albopictus*) (**Figure 3B**) (69). Predictably for a mosquito-borne flavivirus, this urban emergence of ZIKV was likely secondary to a combination of anthropogenic changes including altered land-use patterns, increased urbanization with human expansion into forest habitat, and possibly climate-change induced expansion of vectorial geographic ranges, combined with the modified capacity of Asian lineages to be transmitted by human-adapted domestic mosquito species (1,64).

Mosquito-borne ZIKV rapidly re-emerged into urban areas in 2007, initiating epidemics in the Pacific, Southeast Asia, and the Americas (**Figure 4A**). In Yap State, Federated States of Micronesia, there were 5,000 suspected cases in 2007, affecting 75% of the population. Sequencing and analysis of the viral genome suggested that the virus originated from Southeast Asia via transmission by *Ae. hensilli* (62,65,70). During this time period, scattered cases of ZIKV infection were also reported in Southeast Asian countries including Thailand, Cambodia, Malaysia, Singapore and the Philippines (65,70). French Polynesia reported 28,000 suspected

cases from 2013 to 2014 with suspected transmission by *Ae. aegypti* and *Ae. polynesiensis* and subsequent spread to New Caledonia, the Cook Islands, Easter Island, and the rest of the South Pacific (62,65,70–73). Clinical signs were typically mild in the Yap outbreak, characterized by low-grade fever, rash, arthralgia, and conjunctivitis; however, clusters of the Guillain–Barré syndrome (an autoimmune disorder characterized by flaccid paralysis) were reported for the first time, temporally associated with ZIKV infection during the French Polynesia outbreak (73) (and later in the Americas) (64).

Epidemiologic and virologic data suggest that Asian lineage ZIKV was introduced into Brazil in 2013, resulting in emergence of a new American subclade, though fulminant disease was not recognized until 2015 (**Figure 4A**) (64,65). With the emergence of ZIKV in Brazil, physicians noted a significant increase in the incidence of microcephaly among newborns, although cases were initially overestimated due to lack of a clear, specific clinical definition of microcephaly (64). Since then, medical professionals have begun to utilize the INTERGROWTH-21<sup>st</sup> fetal growth standards (74). Gradually, evidence of ZIKV-induced congenital defects in addition to microcephaly began to emerge, a constellation of fetal lesions now referred to as Congenital Zika Syndrome (CZS) (75–77) (reviewed in section 2.4). After establishing a foothold in Brazil, ZIKV spread quickly to the largely naïve populations of the Americas and the Caribbean, reaching pandemic levels and prompting the WHO to declare a Public Health Emergency of International Concern in February 2016 (78). Prior to the ZIKV pandemic, only sporadic infections were reported in Africa; however, between July 2015 and June 2016 two African countries, Cape Verde and Angola, reported ZIKV cases (including cases of microcephaly) associated with a newly introduced Asian lineage virus, which was confirmed via genome sequencing of RT-qPCR positive

samples (79). Notably, congenital birth defects have only been associated with Asian lineage strains of ZIKV (64). There have been over 40,000 cases of confirmed/probable ZIKV infection in the U.S. and its territories since 2015 (80). ZIKV infections in the continental U.S. were primarily travel associated (though local transmission occurred in Texas and Florida), while the vast majority of cases in U.S. territories were locally acquired (80).

## **2.2 ZIKV structure and replication**

The structure and replication of ZIKV is very similar to that of other flaviviruses, particularly DENV (**Figures 5-6**); however, in contrast to DENV, which has 4 distinct serotypes, there is just one ZIKV serotype with two lineages- African and Asian (81). The prM, E, and NS1 proteins exhibit the greatest sequence divergence from other flaviviruses (82,83).

## **2.3 Life cycle and Transmission of ZIKV**

As noted above, ZIKV historically maintained a sylvatic transmission cycle between *Aedes* spp. mosquitoes and NHPs (primarily in Africa) (69). Like DENV, ZIKV subsequently evolved an urban transmission cycle requiring only humans, who produce high enough viral titers to directly infect mosquitoes, and the two major contemporary domestic/peridomestic mosquito vectors, *Ae. aegypti* and *Ae. albopictus* (**Figure 3B**) (69). *Ae. aegypti* and *Ae. albopictus* are expanding their geographic ranges and are currently present in Africa, South and Central America, India and Singapore, as well as the U.S., where they have been detected in more than 30 states and territories (82,84) (**Figure 4**). Due to common hosts, mosquito vectors, and biology, ZIKV and DENV overlap geographically with similar seasonality, incidence and clinical signs; simultaneous outbreaks and concurrent infections are commonly reported (85). *Aedes aegypti* and *Ae. albopictus*

are susceptible to both coinfection and sequential infection with multiple arboviruses, and results from one study suggest that coinfecting mosquitoes may be more likely to transmit DENV than ZIKV (86). Human case reports, *in vitro* experiments, and *in vivo* studies in mice and NHPs report conflicting conclusions regarding the effects of previous infection and coinfection on flavivirus transmission and virulence in human populations (85,87). Additional controlled experiments in primates as well as large epidemiological cohort studies are necessary.

Coupled with vector-borne spread is the capacity for ZIKV to also be sexually and vertically transmitted, and via blood transfusions (**Figure 9**), although there are currently no diagnostic mechanisms to distinguish sexually transmitted ZIKV infection from blood-borne, mosquito-acquired infection (88). Cases of sexual transmission of ZIKV are likely underreported owing to the number of asymptomatic individuals and may provide a mechanism of viral spread beyond vector geographic ranges into naïve human populations. Male-to-female sexual transmission of ZIKV is highly efficient in humans as well as macaque (89) and immunodeficient mouse (90) models. There are reports of human cases of ZIKV infection in which the seminal viral load two weeks after the onset of symptoms was  $10^3$  -  $10^4$  times higher than that in the blood (88). In sexually mature female rhesus macaques, subcutaneous inoculation rarely resulted in ZIKV detection in the reproductive tract, while direct intravaginal inoculation, which is used as a proxy for male-to-female sexual transmission, led to enhanced viral shedding from vaginal secretions prior to the development of viremia (91). The magnitude and duration of infectious viremia in rhesus macaques suggests that humans with sexually transmitted ZIKV infection could generate sufficient viremia to infect competent mosquito vectors. Thus, sexual transmission of ZIKV could help maintain ZIKV circulation within the population, even in the absence of mosquito-to-human

transmission (89). Taken together, published data suggest that sexual transmission of ZIKV may be responsible for a significant number of human infections and could even serve as mechanism for introducing ZIKV to non-endemic regions lacking mosquito-human-transmission (89,92).

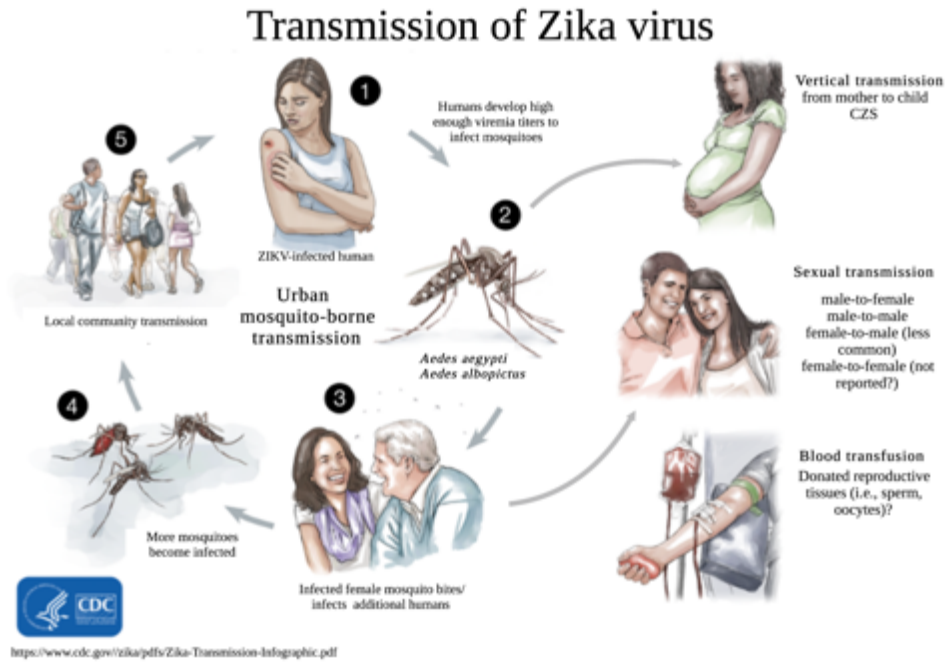


**Figure 9.** Schematic depicting mechanisms of ZIKV transmission. CZS= congenital Zika syndrome. Adapted from [www.cdc.gov](http://www.cdc.gov), 2019 (93) using BioRender.com.

There is strong evidence that the male reproductive tract serves as an important ZIKV reservoir; however, reported durations of viral persistence in semen and male genital tissues vary widely. ZIKV has been identified in the semen of both symptomatic and asymptomatic infected men, as well as in vasectomized men, suggesting that, in addition to the testes and epididymis, the virus likely persists in the bulbourethral glands, prostate gland, and/or seminal vesicles (94,95). Semen obtained from symptomatic, convalescent men can harbor both ZIKV RNA and infectious virus well after the resolution of viremia (96–98). The latest documented report of sexual transmission was 44 days after the onset of symptoms (99). While published data also suggest that ZIKV shedding by infected men can occur prior to the onset of clinical signs, during the symptomatic

period, and in non-symptomatic convalescent men (100,101), the relative contribution of asymptomatic males to sexual transmission has not been determined. One study evaluating ZIKV-infection in men reported that older age, infrequent ejaculation, and the presence of certain symptoms (e.g., conjunctivitis) at the time of initial illness were associated with prolonged sexual shedding of ZIKV RNA (98). Viral RNA has been detected in human semen for up to 370 days after the onset of symptoms, while infectious virus is more short-lived, with positive cultures from semen samples reported for up to 69 days (92,102). It remains unclear whether there is any association of the magnitude/duration of viremia with genital invasion by ZIKV or viral shedding (in semen) and subsequent risks of male-to-female or male-to-male sexual transmission.

The male ejaculate is composed of a cellular and a fluid component. The cellular component comprises spermatozoa, white blood cells, and desquamated germ cells and epithelial cells. Mature spermatozoa develop in stages from germ cells in testicular seminiferous tubules (supported by Sertoli cells), undergo maturation and storage (for 1 - 21 days) (103) in the ducts of the epididymis, and travel via the vas deferens through the accessory sex glands and into the urethra for ejaculation (104,105). The fluid component contains secretions from accessory sex glands, primarily the seminal vesicle and prostate gland, and to a lesser extent, the bulbourethral gland and epididymis. These fluid secretions are important for semen pH and coagulation, suppression of the female immune response, and sperm motility and chromatin stability (104,105). Either component (or both) could harbor infectious ZIKV and contribute to sexual transmission, and published data regarding specific cellular tropisms of ZIKV are conflicting (see section 2.4 for specific details).

Vertical ZIKV transmission from mother to child can result in CZS (described in detail below) (75,76); however, effects of the timing of prenatal infection, as well as the presumed tropism of ZIKV for neural progenitor cells (NPCs) have not been sufficiently evaluated and there are currently no established procedures for predicting adverse fetal outcomes such as CZS in pregnant women who became infected with ZIKV. Overall, the mechanisms by which ZIKV impacts pregnancy outcomes and risk factors associated with fetal pathology are poorly understood. Additionally, it is unknown whether the high seminal viral titers developed by ZIKV-infected men and/or the enhanced intravaginal viral replication/shedding associated with male-to-female sexual transmission are of sufficient magnitude to infect the fetus and induce CZS following sexual intercourse between a ZIKV-infected man and a naïve pregnant woman (106). Similarly, it remains unclear whether ZIKV is capable of directly infecting the oocyte during fertilization (106). A recent study in immunodeficient, naïve female mice showed that sexual transmission of ZIKV resulted in increased morbidity/mortality and higher ZIKV titers in the dam's reproductive tract as well as her fetuses, versus subcutaneous and intravaginal inoculation (107).

ZIKV transmission via laboratory needle-stick injury (108) and blood/platelet transfusion are rarely reported (**Figure 9**) (109,110). Although ZIKV has been isolated from breast milk, there are no confirmed reports of transmission via breast feeding (111). In addition to blood and semen, ZIKV has been detected in urine and saliva, all of which serve as possible alternative sources of non-vector-borne transmission (112,113); however, the prevalence, magnitude and duration of ZIKV persistence in these fluids are unclear. A recent prospective study in humans assessing the persistence of ZIKV in various body fluids reported ZIKV RNA in the urine for up to 34 days after the onset of ZIKV symptoms, while less than 5% of participants had detectable ZIKV RNA in

saliva (114). ZIKV RNA was also demonstrated in cervical swabs from infected women for up to three weeks after symptoms, well after the resolution of viremia (115).

#### **2.4 Clinical human disease, diagnosis, treatment, and prevention**

ZIKV infection is subclinical in approximately 80% of adults. When symptomatic, clinical signs typically last for 2 - 7 days (following a 3 - 14 day incubation period) and include rash, fever, arthralgia, myalgia, and conjunctivitis (116). Clinical infection in adults is rarely accompanied by neurologic disease such as meningoencephalitis or Guillain-Barré syndrome. Guillain-Barré syndrome is an autoimmune disorder that is typically associated with previous infection in which immune system attack of the peripheral nervous system can induce near-total paralysis (64,116).

Published data suggest that ZIKV is gonadotropic in men, but information regarding genitourinary sequelae and effects on fertility are lacking in both humans and animal models of human ZIKV infection. Hematospermia, prostatitis, painful ejaculation, penile discharge, dysuria, low sperm counts and sperm motility issues are occasionally reported in ZIKV-infected men (94,95,117,118). Otherwise, human data are sparse, as obtaining genital biopsy specimens in men is invasive and not typically performed without a significant medical reason (119). The prevalence of ZIKV in semen, associated viral kinetics, factors influencing male sexual transmission, male genitourinary lesions and their potential effects on fertility, as well as risk factors associated with sperm donation/assisted fertility procedures remain largely unknown (94).

Vertical transmission of ZIKV from mother to child can result in a range of possible obstetric outcomes, referred to as CZS, including early fetal death, utero-placental pathology, premature

rupture of membranes, fetal growth restriction, musculoskeletal contracture, and congenital fetal central nervous system (CNS) malformations such as microcephaly, neuropathology, ocular defects, and hearing loss (64,78). Neuroimaging (brain CT and MRI) of congenitally infected neonates has variously revealed a malformed cerebral cortex and corpus callosum, cerebellar and brainstem hypoplasia, ventriculomegaly, an enlarged cisterna magna, and/or multifocal microcalcifications (120). In a U.S. cohort of women infected with ZIKV during pregnancy, CZS affected one in seven babies prenatally exposed to ZIKV (121); however, some infants born to mothers who were ZIKV-infected during pregnancy fail to manifest overt microcephaly or detectable viral RNA in fluids, but go on to develop neurologic problems as they age (122). Following the 2015 - 16 ZIKV epidemic in the Americas, various cohort studies reported delayed onset neurodevelopment and neurosensory alterations in infants prenatally exposed to ZIKV, where language function, vision and hearing, cognition, and motor function are commonly affected components (122–125). The long-term developmental consequences of prenatal ZIKV exposure are otherwise not well described and we lack mechanisms to definitively identify infants likely to develop neurodevelopmental deficiencies (126).

Current guidelines for diagnosing ZIKV vary based on potential exposure, pregnancy status and presence/absence of clinical signs. As antibody-based tests can cross-react with antibodies against other flaviviruses (particularly DENV) (127) and possibly in those individuals vaccinated against YFV (128), diagnosis of ZIKV infection has largely shifted to detection by nucleic acid tests (129). The Centers for Disease Control (CDC) recommend that symptomatic pregnant women with possible ZIKV exposure undergo concurrent testing of serum and urine by nucleic acid amplification tests (NAAT), which are best for diagnosing acute infection, and serum ZIKV IgM

testing for up to 12 weeks after symptom onset (130). For asymptomatic pregnant women with ongoing possible ZIKV exposure as indicated by residence in or frequent travel to an area with risk of ZIKV activity, the CDC recommends NAAT testing three times during pregnancy rather than serology for IgM. Since IgM can persist for months after infection, IgM serology results in this situation cannot reliably determine whether an infection occurred during the current pregnancy (130). Antibody production/seroconversion is clearly an important mechanism for diagnosing ZIKV, thus understanding maternal-fetal-placental immune responses to ZIKV infection is critical to develop diagnostic tools and effective vaccine strategies. However, the host immune response to ZIKV and specific mechanisms underlying protective immunity against vertical transmission are complex and not fully characterized.

Though a safe, effective ZIKV vaccine has the potential to protect over 2 billion people residing in ZIKV endemic areas, there is currently no prophylactic or therapeutic treatment approved for human ZIKV infection, other than supportive care. As of 2020 there were a handful (8 - 9) of vaccine candidates in phase 1 or 2 clinical trials (131), including DNA-based vaccines (where host cells use viral protein-encoding synthetic DNA to produce antigenic viral target proteins), adenovirus vector-based vaccines (which are easy to manufacture and induce a robust immune response), mRNA-based vaccines (which, similar to DNA vaccines, directly translate mRNA molecules into the viral antigens, but do not run the risk of integration into the human genome), live attenuated ZIKV vaccines (which may be contraindicated in pregnant or immune suppressed people), and purified inactivated virus vaccines (which cannot revert to live virus and are thus not contraindicated in pregnant women or immunocompromised people, but may require boosting to ensure long-term protection) (132).

## 2.5 Animal models of ZIKV

### 2.5.1 Rodents

Owing to genetic homogeneity and ease of genomic manipulation, laboratory mice serve as useful, tractable models of many human infectious diseases, including ZIKV; however, due to differing pathophysiology and immune responses, mice generally require immune suppression to become infected with ZIKV (103). ZIKV antagonizes antiviral interferon (IFN) signaling and ultimately dampens the immune response in humans by inhibiting the activation of signal transducer and activator of transcription proteins 1 and 2 (STAT1 and STAT2) (133,134). As this ZIKV-induced degradation of STAT1/2 does not occur in mice (135), an effective murine model of ZIKV pathogenesis (like DENV) must use mice with a deficient IFN response (136). One commonly utilized lethal murine model of ZIKV utilizes an inbred strain (typically either the 129/Sv or C57BL/6 genetic background) with knockout of receptors for type I ( $IFN\alpha 1^{-/-}$ ) and type II ( $IFN\gamma 1^{-/-}$ ) interferons, referred to as A129 and AG129 for single or double knockouts, respectively (137). Pharmacological immune suppression with an IFNAR1-blocking antibody also results in viremia and limited tissue detection of ZIKV RNA in B6 wild type (WT) mice inoculated with ZIKV; however, this is not considered a lethal model and mice do not generally develop any appreciable clinical signs of disease (138,139).

Subcutaneous (SC) or intraperitoneal (IP) inoculation of immunosuppressed mice with both ZIKV lineages results in viremia and clinical signs of illness, including hunched posture, lethargy, ruffled fur, and weight loss. A subset of mice, and particularly those inoculated with Asian lineage ZIKV, may also exhibit neurologic signs, such as tremors, ataxia and/or paralysis. Most ZIKV-inoculated, immunosuppressed mice reach euthanasia criteria within a week. Tissue analyses indicate that the

highest magnitude ZIKV RNA tends to occur in the brain and testes (90,137,138,140–142), though ZIKV can also infect the cells lining the blood-retinal barrier in immunosuppressed mice, resulting in chorioretinal atrophy (143). Additional studies indicate that the overall severity of ZIKV pathology may be inversely proportional to age, with highest mortality in pups  $\leq 3$  weeks old, and that Asian lineage ZIKV tends to be associated with more severe clinical signs and higher viremia than African (139,140). In addition to morbidity and mortality as described above, immediate postnatal inoculation of newborn mice is associated with clinical indications of neurologic disease, including tremors, seizures, hyperactivity, limb collapse (144), and variable encephalomyelitis (145). ZIKV RNA was detected in pup brains for up to 15 dpi (144), while viral antigen was identified within both neurons and astrocytes (145).

Studies in mice support the widely held hypothesis that the male reproductive tract serves as a significant ZIKV reservoir in humans. ZIKV RNA is routinely recovered from the murine testis and epididymis, with evidence of viral tropism for spermatogenic precursors, Sertoli cells, and epididymal epithelia, along with scattered luminal cell debris, and low numbers of inflammatory cells (90,139,146,147). Lazear *et al.* further demonstrated persistent, high levels of testicular ZIKV replication in IFNAR-deficient (*Ifnar1<sup>-/-</sup>*) male mice 6 dpi (138). ZIKV inoculation of immunosuppressed male mice has been reported to induce testicular and/or epididymal damage progressing to atrophy, with low serum testosterone and evidence of decreased fertility. Reported microscopic genital lesions include orchitis with seminiferous tubule necrosis, testicular atrophy and oligospermia and/or epididymitis (90,139,147–153). The prostate gland and seminal vesicles are typically spared (149,152), though ZIKV-associated prostatitis is infrequently reported (154). ZIKV RNA has been reported to persist in the murine testis for over 4 weeks, with infectious virus

detected in semen of both intact and vasectomized males for 7 - 21 dpi (though infectious virus titers were significantly reduced in vasectomized mice), and ZIKV RNA for up to 5 weeks after vasectomy (90).

Published data overwhelmingly demonstrate that immunosuppressed female mice are susceptible to sexual transmission of ZIKV. Following intravaginal (IVG) ZIKV inoculation of immunosuppressed (90,155,156) and WT (156) female mice, both ZIKV RNA (155,156) and infectious virus (90,156) were detected in serum (90) and/or vaginal washes (155,156) from 4 - 10 dpi, indicating that the vaginal mucosa is permissive to viral replication. Only immune suppressed mice developed viremia or evidence of clinical disease (155–157), including hind limb paralysis in *Ifnar1<sup>-/-</sup>* mice challenged with high dose [ $5.2 \times 10^5$  PFU] ZIKV (156). ZIKV RNA was variably detected in the vagina, uterus, and ovaries as well as systemically in the spleen and brain (90,156), while ZIKV NS2B, a marker of viral replication, was identified by immunohistochemistry (IHC) in the vagina, local draining lymph nodes, spleen, and brain (155). Similarly, mating both intact and vasectomized ZIKV infected AG129 male mice with naïve females between 7 and 19 dpi (where 7 dpi was the first time point with detectable infectious virus in male seminal fluids), resulted in systemic female infection and sporadic vertical transmission. Infectious virus was cultured from vaginal washes, uterus, placenta and brain, and those female mice who became pregnant exhibited significantly higher mean infectious ZIKV titers in the uterus when compared to IVG inoculated non-pregnant females (90). Furthermore, *in utero* ZIKV transmission was documented in 2 out of 11 fetuses born to one of the pregnant females resulting from this mating (90). Taken together, published data suggest that ZIKV can be sexually transmitted from immunosuppressed males to both pregnant and non-pregnant immunosuppressed females, with

systemic spread, vertical transmission to the fetus and/or lethal disease. Notably, clinical disease in one of these studies was only observed in those mice challenged during induced diestrus, while mice in induced-estrus were resistant to disease (155). This indicates that, in addition to pregnancy, the estrus cycle may exert significant effects on female susceptibility to vaginal ZIKV transmission and viral persistence in the female reproductive tract (155). The significance of this finding in the context of human ZIKV infection remains unclear, as the menstrual cycle of human females differs significantly from the mouse estrus cycle.

Depending on the strain, mouse gestation typically lasts 19 to 21 days (158) (vs. 280 days in humans). Despite differences in timing and gross/microscopic organization, basic placental development, structure, and function is well conserved between rodents and humans. Both species have a hemochorial discoid placenta (159); however, the mouse placenta is labyrinthine with fetal blood flowing in a “labyrinth” of anastomosing structures while the human placenta is villous, with fetal blood flowing centrally (160). Blastocyst implantation, an invasive process in which embryo-derived trophoblast cells invade the decidualizing maternal uterus, occurs early in gestation in both species (~7 - 9 days post-fertilization in humans and ~E4.5 in mice). The amnion, chorion, and allantois form beginning at mouse E6.5 and 12 - 15 days post-fertilization in humans. As placental development progresses, embryonic chorio-allantoic fusion (which occurs ~21 days post-fertilization in humans and ~E8.5 in mice) allows invagination of fetal blood vessels into the chorionic trophoblast layer, where they interdigitate with trophoblast lined maternal blood sinuses. Further differentiation and proliferation generate interdigitating placental villi, each composed of a mesenchymal core containing fetal blood vessels and lined by syncytiotrophoblast cells. In humans these are typically formed by the fourth week of gestation, with establishment of the

maternal blood supply between weeks 10 and 12 (vs. E10 to E14.5 in mice). This closely apposed countercurrent fetal-maternal blood flow ensures efficient nutrient and gas exchange and is critical for normal embryonic development going forward (161). There are also well documented dissimilarities between human and murine embryologic neural development. For instance, neurogenesis begins later but lasts significantly longer in primates compared to rodents (162).

Various studies have documented vertical transmission of ZIKV to fetal mice following SC, IP (90,163), and, importantly, IVG inoculation of pregnant dams, which suggests that sexually transmitted ZIKV can infect the developing embryo (156). Fetal infection is significantly more likely when the dam is infected prior to E12, which roughly corresponds with gestation days 4 – 48 in the first trimester for humans; later in gestation direct inoculation of the mouse fetus is necessary to assure productive, clinically apparent ZIKV infection. This is in contrast to congenital human infection, which has also been documented in newborns exposed to ZIKV during the second and third trimesters of pregnancy (145). Similar to humans, *in utero* ZIKV infection of fetal mice typically results in detection of infectious ZIKV and viral RNA in both the placenta (163,164) and fetal brain (156,163), and is associated with placental insufficiency, intrauterine growth restriction, and/or early fetal death (156,163,165). *In utero* injection of Asian lineage ZIKV into the lateral ventricles of fetal mice led to cerebral cortical thinning, microcephaly and high viral titers within neural progenitor cells (NPCs) (166,167), while intracerebral or SC inoculation of newborn mice with a 2015 Brazilian ZIKV isolate produced clinical signs of ZIKV infection, including lethargy, ataxia and paralysis, with cerebral cortical encephalitis (144,167), ocular lesions (165), and an apparent tropism for radial glial cells (a type of NPC) (164).

Overall, mouse models of ZIKV pathogenesis recapitulate many aspects of natural human infection. Studies have variously shown that genetically immunodeficient adult mice develop clinical disease, while infection of pregnant dams early in gestation can result in early fetal death or pups with neurologic disease and/or congenital growth abnormalities. The major limitation is that effective murine models of ZIKV pathogenesis require mice with a deficient IFN response.

SC ZIKV inoculation of both pregnant and non-pregnant STAT2 knock-out (KO) hamsters resulted in weight loss and approximately 40% mortality. Viral RNA was detected in the uterus, placenta, brain, spinal cord, and testis, while infectious virus was only detected in the testes, placenta, fetal brain, and (rarely) in adult brain. No clinical signs (beyond weight loss) or significant histopathologic lesions were observed. Conversely, inoculation of wild type hamsters failed to result in detectable ZIKV infection (168). In contrast to hamsters, SC inoculation of immunocompetent guinea pigs resulted in transient viremia, seroconversion, detection of neutralizing antibody, and variable clinical signs of infection (i.e., fever, lethargy, hunched back, ruffled fur, and decreased mobility) (169,170). ZIKV RNA was detected in the spleen and brain (suggesting that the virus may also be neurotropic in guinea pigs) (169), as well as the testis, where it was associated with inflammation and necrosis (170). Notably, one study further reported significant shedding of ZIKV RNA in both saliva and tears, with efficient transmission to naïve co-caged animals as well as productive infection with similar viral kinetics following intranasal (IN) ZIKV inoculation (170). Taken together, these data suggest that both immune suppressed hamsters and immunocompetent guinea pigs are susceptible to ZIKV infection and recapitulate some of the clinical features and viral kinetics described in ZIKV-infected patients.

### 2.5.2 Non-human primates

Owing to their close phylogenetic relationship to humans, old world monkeys, such as rhesus and cynomolgus macaques, are susceptible to ZIKV infection without immune intervention (171). *In vivo* viral kinetics, including the length and magnitude of viremia, ZIKV RNA and infectious virus levels within tissues, tissue tropism, and protective immunity following re-challenge with a homologous viral strain are similar in non-pregnant adult macaques and humans (172–175). Similarly, ZIKV inoculation of adult male and non-pregnant female olive baboons (*Papio anubis*) resulted in mild clinical signs similar to human infection, including rash and conjunctivitis, with viremia, a ZIKV-specific IgM and IgG antibody response, and sporadic detection of ZIKV RNA in saliva, urine and CSF (176). Thus, extrapolating data from translational ZIKV studies utilizing old world monkeys is a useful method for understanding the pathogenesis of and risk factors associated with human ZIKV infection. One limitation of NHP models is the small sample size (typically limited to N = 1 - 5) due to the high costs and limited availability of animals. A recent report estimated that the sample size required to identify statistically significant differences in neurodevelopmental lesions between ZIKV-infected and control groups is approximately 14 animals per group (126).

Long term data regarding the duration and magnitude of infectious virus within the male genital tract, as well as any tropism for specific cell types, are sparse in non-human primates, including macaques. In contrast to mice, genitourinary lesions and infertility are usually not major features reported in macaques inoculated with ZIKV (175,177,178). This discrepancy may have to do with the use of immunodeficient knockout mice vs immune competent macaques and/or the low sample sizes typically used in NHP studies, which often do not provide sufficient statistical power for

accurate evaluation. Male rhesus and cynomolgus macaque models have demonstrated ZIKV RNA in the semen for up to 28 dpi, three weeks after the resolution of viremia (179). ZIKV RNA has also been demonstrated in the testes (177,179), prostate gland, and seminal vesicles (178,179) from 4 to 35 dpi; however, the time points noted above for viral RNA detection in macaque semen and male genital tissues represent the end of the various studies, so viral shedding may be more prolonged than suggested by the published data. ZIKV-associated prostatitis is occasionally identified in ZIKV-infected male macaques (154). Overall, the duration of ZIKV persistence in the male reproductive tract, specific viral tissue and/or cellular tropisms, and potential effects of ZIKV on male genitourinary symptoms remain unclear in both humans and animal models, making it difficult to develop coherent guidelines regarding risks of male sexual transmission and infertility. These gaps in knowledge also affect the field of assisted reproductive technology (ART). There are no documented instances of human ZIKV transmission due to assisted fertility procedures; however, ZIKV transmission via sperm, oocytes or embryos is theoretically possible (180), and fetal ZIKV infection has been documented following IVG inoculation of pregnant mice (156).

Published data indicate that, like immunosuppressed mice, macaques are susceptible to sexual transmission of ZIKV. IVG and intrarectal ZIKV inoculation of macaques resulted in seroconversion and viremia of sufficient magnitude to infect competent mosquito vectors, suggesting that sexual transmission of ZIKV could serve as mechanism for introducing ZIKV into non-endemic regions (89). Following SC inoculation ZIKV RNA can be detected in vaginal secretions even after the resolution of viremia, though, similar to both mice and humans, detection is sporadic and does not typically persist for as long as in the male genital tract (174).

Gestation time in macaques is approximately 160 days (vs. 280 days in humans) (160). Despite minor differences in gestational and developmental timelines, humans and macaques have very similar reproductive anatomy and physiology, including placental development, structure, function. The villous, hemochorial, single-discoid, deciduate placenta of humans is very similar to that of the macaque, although macaque placentas are usually bi-discoid (181). Like humans, basic macaque placental development (including blastocyst apposition to the uterus, trophoblast adhesion followed by migration through the uterine wall, endometrial blood vessel penetration, villar development, and establishment of the communication with maternal blood) occurs within the first two weeks of gestation (160). Early studies, including some of our work, validate pregnant rhesus macaques as a model for ZIKV in human pregnancy (75,182–188), where approximately one out of four animals infected with Asian/American ZIKV in early gestation experienced early abortion/stillbirth despite few clinical signs of infection (184). In addition to prolonged maternal viremia and detection of infectious ZIKV and viral RNA in the amniotic fluid, placenta and fetal brain (75,186), these studies have variously demonstrated placental damage/dysfunction (185), microscopic brain lesions (including ependymal cell loss, gliosis, and microcalcifications) (75,182,188,189), and abnormal fetal neurodevelopment (190); however, none have reproduced microcephaly. This suggests that, like humans, only a subset of NHP maternal ZIKV infections result in severe fetal outcomes. Other possible explanations for the generalized failure of various studies to reproduce microcephaly in NHP models include lack of power due to low Ns and/or that pregnant NHP in a laboratory setting are inoculated with ZIKV upon confirmation (via ultrasound) of pregnancy (after GD 20), while in humans, infection can occur at any time.

As previously noted, long-term sequelae of *in utero* ZIKV exposure (e.g., neurodevelopmental defects) are not well described in humans or NHP models. Beckman *et al.* recently conducted quantitative neuroanatomical analyses of brains from nearly full-term fetuses exposed to ZIKV *in utero*. ZIKV antigen was detected in the frontal lobe by IHC, along with activated microglia and increased apoptotic immature neurons in comparison to age-matched, uninfected control animals. There were also significant macrostructural changes within visual pathways, which tracked temporally with CNS development. These findings led the authors to hypothesize that ZIKV-induced neocortical inflammation results in a wave of NPC death and subsequent morphological/neurodevelopmental defects, which may explain why ZIKV-exposed infants without appreciable evidence of growth restriction or microcephaly can still manifest developmental abnormalities over time (190). Postnatal ZIKV inoculation of two infant rhesus macaques was similarly associated with neurologic lesions, including ventriculomegaly, inflammatory infiltrates, astrogliosis, and Wallerian degeneration. MRI also revealed aberrant functional connectivity between brain areas associated with emotional reactivity, resulting in significant behavioral alterations (191). Importantly, most animal studies of CZS, whether in mice or NHPs, are terminated at some point near the end of gestation, and very few live births have been described (145).

Macaque models of human ZIKV infection are also useful for testing medical countermeasures against ZIKV. Several groups have shown that prophylactic co-administration of two monoclonal antibodies in non-pregnant and pregnant rhesus macaques, followed by high-dose ZIKV challenge, reduced viremia as well as limiting vertical transmission from mother to fetus and protecting the fetus from neurologic damage associated with CZS (192,193). Moreover, Van Rompay *et al.*

recently demonstrated the production of vaccine-induced neutralizing antibody, as well as a reduction in viremia magnitude/duration, incidence of fetal infection, adverse fetal outcomes, and placental and fetal brain pathology in rhesus macaques vaccinated with a novel DNA vaccine and then challenged 3 times with ZIKV (194).

Historically, old world primates (e.g., macaques) were considered the primary maintenance hosts for sylvatic African transmission cycles of ZIKV; however, recent data suggest that new world primates (e.g., marmosets [*Callithrix* sp.], capuchins [*Sapajus* sp.], squirrel [*Saimiri* sp.] and owl [*Aotus* sp.] monkeys) are susceptible to ZIKV infection and may act as reservoirs (195–197). Although typically asymptomatic, marmosets experimentally inoculated SC or IV with ZIKV developed viremia and neutralizing antibodies, with ZIKV RNA variably detected in saliva (which also had infectious virus), urine and/or semen even after the resolution of viremia (195,197–199). There were no obvious brain or testicular lesions (as evaluated by ultrasonography and MRI-histopathology was not performed) (198). Similar to both macaques and humans, intramuscular (IM) ZIKV inoculation of two pregnant marmoset dams (at gestation days equivalent to the second trimester in humans) resulted in prolonged viremia, viruria, and asymptomatic seroconversion, with early fetal death in both animals at 16 - 18 dpi, and neuropathology of the developing fetal brain and eye. ZIKV RNA was detected in the dam placenta (which also exhibited evidence of viral replication), lymph node, brain and eye (200). Taken together, these studies suggest that like old world primates, neotropical/new world species are also naturally susceptible to ZIKV infection and may serve as reservoirs and/or amplification hosts in South/Central American urban transmission cycles (195–197). Furthermore, marmosets recapitulate a number of features of

human disease and may prove a relevant model for ZIKV and CZS, especially considering their smaller size and lower zoonotic risk in comparison to old world species (198).

## **2.6 ZIKV pathogenesis**

### **2.6.1 Tissue/cellular viral tropism and host receptor interactions**

Because the most common mechanism of ZIKV transmission is via mosquito feeding, skin cells are a probable initial target for viral infection. Dermal fibroblasts, epidermal keratinocytes, and immature dendritic cells are all permissive to ZIKV (201); infection of dendritic and other monocyte/macrophage lineage cells (103) likely facilitates hematogenous viral spread to peripheral tissues (201–203). In contrast to most other flaviviruses, ZIKV can cross the placental barrier, resulting in fetal brain infection, early fetal death, and/or CZS. Numerous cell types from a variety of tissues are reported to be permissive to ZIKV infection, including NPCs, astrocytes, microglia, neurons, retinal and optic nerve cells, endothelial cells (i.e., those contributing to the blood-brain-barrier), and various placental cells, such as macrophages (Hofbauer cells) and trophoblasts (42,204–206). Overall, susceptibility to ZIKV infection appears to be highly cell type specific.

Although the specific receptors required for viral entry into different host target cells remain incompletely understood, ZIKV is thought to utilize dendritic cell-specific intracellular adhesion molecule 3-grabbing nonintegrin (DC-SIGN) (201) and the phosphatidyl serine (PS)- and phosphatidyl ethanolamine (PE)-binding transmembrane T-cell immunoglobulin and mucin (TIM) and TAM (Tyro3-AXL-Mertk) family receptors (particularly AXL) to facilitate host cell entry (201,207–210). TIM and TAM family membrane receptors are found in various mammalian tissues whose major functions are to mediate phagocytosis of apoptotic germ cells and contribute

to immune homeostasis via negative regulation of innate immunity (211); they also interact with PS-binding proteins (i.e., Gas6 and Protein S) which can bind to the surface of enveloped viruses such as flaviviruses (212). AXL is highly expressed by human NPCs (210) and some types of trophoblasts (205), both of which are important targets of ZIKV (213), though only a subset of monocyte/macrophage lineage cells express AXL (214). Human testis, epididymis, seminal vesicle, prostate gland and ductus deferens all express AXL RNA, with the highest protein expression in Sertoli cells and, to a lesser extent, epididymal epithelial cells and Leydig cells (215).

Data concerning the role of TIM/TAM receptors (and others) in ZIKV entry into host cells is conflicting, suggesting that the precise receptors/co-receptors required for viral entry are cell type specific and that there is some redundancy (216–218). AXL appears to be required for productive infection of human skin cells, endothelial cells, astrocytes, and microglia (201,216–219); however, AXL alone was shown to be unnecessary for ZIKV infection of human NPCs and cerebral organoids (220). Recent *in vitro* studies in human Sertoli cells and testicular organoids further demonstrated that human Sertoli cells express high levels of AXL and that pharmacologic inhibition of AXL significantly reduces ZIKV replication (209,221). The apparent tropism of ZIKV for stem-like cells also correlates with AXL expression in both humans and mice. A recent mouse study used IHC to demonstrate that spermatogonia, some testicular peri-tubular myoid cells, and epididymal epithelial cells exhibited AXL expression (weaker positive signals were also noted in Sertoli cells); however, there was no AXL expression in the prostate gland or seminal vesicle (149). Recent work also suggests that Tyro3 receptors expressed by human spermatozoa may play a role in ZIKV-binding (136).

In the placenta, cytotrophoblasts, endothelial cells, fibroblasts, and Hofbauer cells (macrophages) of the chorionic villi, as well as epithelial cells and trophoblast progenitors of the amniochorionic membranes strongly express suspected cofactors for ZIKV entry including AXL, Tyro3, and/or TIM1. TIM1 in particular appears to be highly expressed in maternal decidua, chorionic villi, and fetal amniochorionic membranes (205). The relative susceptibility of these cells to ZIKV infection seems to be at least partly gestation day dependent. First trimester (but not term) mesenchymal cells, cytotrophoblasts, and Hofbauer cells support ZIKV replication, which can result in villitis (205,222), while second and third trimester infection is limited primarily to Hofbauer cells (145). It is not surprising then, that advanced *in vivo* imaging studies have documented abnormal placental oxygen transport (185) and that placental dysfunction has been implicated as a mechanism contributing to adverse fetal outcomes and CZS (213). Additionally, a recent study showed that ZIKV infection of human placenta trophoblast cells resulted in proteasomal degradation of ZO-1 and occludin (components of cellular tight junctions), which suggests that ZIKV crosses the placental barrier by disrupting cellular tight junctions (223).

ZIKV is also thought to utilize AXL (among other receptors) for viral entry into immune-privileged sites such as the brain, the eye, and the testes (209). These tissues are considered immune-privileged in that they are separated from the immune system by the blood-brain barrier (BBB), the blood-retina barrier (BRB), and the blood-testis barrier (BTB)/blood-epididymis barrier (BEB), respectively (106).

The BTB is formed by specialized junctions between adjacent testicular Sertoli cells, near the basement membrane of the seminiferous tubule epithelium, and allows protection of developing

sperm from immune system attack (224). The blood-epididymis barrier (BEB) similarly sequesters spermatozoa from the immune system and helps regulate the local microenvironment via ductular epithelial tight junctions (153). *In vitro* experiments using a human Sertoli cell barrier model showed that ZIKV can pass through the blood-testis-barrier without directly altering its permeability, though ZIKV infection of Sertoli cells was associated with enhanced leukocyte adhesion and exposure of Sertoli cells to inflammatory mediators, which likely increased BTB permeability indirectly (211). Similarly, *in vivo* studies in immunosuppressed mice have shown that ZIKV can penetrate both Sertoli cell tight junctions of the BTB (150) and epididymal duct tight junctions of the BEB, with downregulation of both tight junction proteins and secreted proteins critical for the absorption and secretion functions of the epididymis (153).

The BBB maintains CNS homeostasis and protects the brain from pathogens and toxins by regulating molecular/cellular movement. It is composed of endothelial cells with tight junctions, pericytes closely associated with the endothelial basement membrane, and astrocytes with polarized cellular processes whose end-feet (or podocytes) completely ensheath the vascular tube and link blood vessels with adjacent neuronal circuits (**Figure 10**) (225). Although its function is essentially the same as the BBB, the BRB has 2 barrier layers. The outer barrier is formed by the retinal pigment epithelial (RPE) cell layer and regulates the movement between the choroid and the sub-retinal space. The inner barrier is associated with the retinal microvasculature and, similar to the BBB, is composed of endothelial cells with tight junctions (226). Reports regarding mechanisms used by ZIKV to penetrate the BBB are conflicting and the specific means has yet to be fully defined. Chiu *et al.* recently reported that, despite productive infection of human brain-derived endothelial cells and release of viral particles into the basal portion of their BBB model,

ZIKV infection failed to disrupt the BBB permeability or alter the expression of tight junction proteins; however, fluorescence-labeled ZIKV particles could cross the BBB model via transcytosis (223). In contrast, other groups have reported that ZIKV infection does alter endothelial cell barrier function, resulting in increased BBB permeability and vascular leakage (227,228).

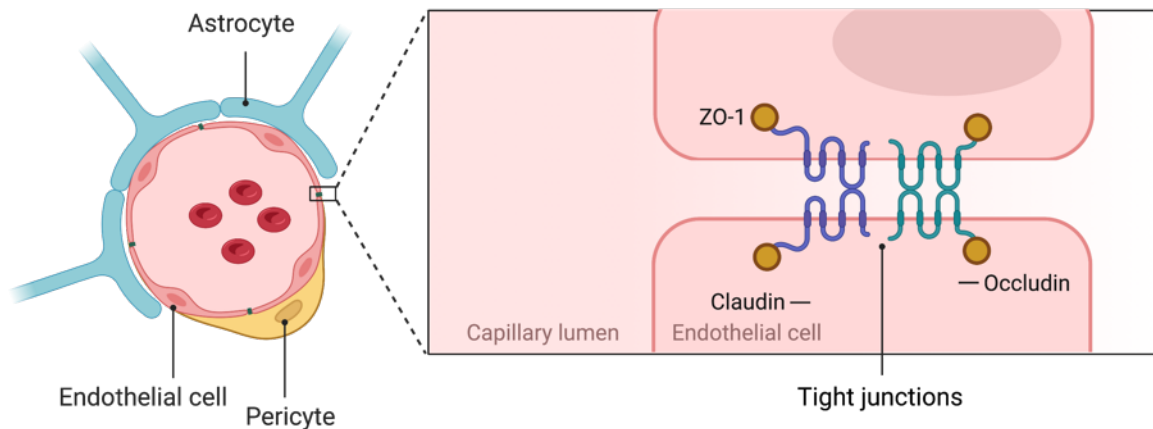


**Figure 10.** Schematic of the normal blood-brain-barrier (BBB). Created using BioRender.com.

### 2.6.2 Infection of the CNS

NPCs are primary stem cells capable of differentiation into various CNS cell types, including neurons. Essentially, NPCs are responsible for populating the brain with neurons. Proliferation, migration, and differentiation of NPCs into neurons and glia is a tightly regulated process that ultimately results in formation of the highly structured mammalian neocortex. In primates, these cellular differentiation pathways are active primarily during embryogenesis and persist through prenatal and some postnatal development (162,229). The mammalian neocortex is composed of a thin layer of gray matter (GM) surrounding underlying white matter (WM). GM is made up of interconnecting columns of neurons arranged in 6 layers, along with supporting glial cells and

blood vessels, while WM is composed of myelinated axons running to or from the overlying GM. In contrast to mice, which are lissencephalic, the surface of the primate neocortex is gyrencephalic, characterized by a complex pattern of gyri and sulci (162,229). In primates, the developing fetal brain is comprised primarily of NPCs, particularly within the first trimester (162). Published data report that ZIKV is neurotropic, specifically targeting embryonic NPCs (though it can also replicate to some degree in mature neurons) (230).

*In vitro* models using human stem cells (165,230,231) and brain organoids (165,232) have shown that ZIKV can infect and replicate in human NPCs, resulting in transcriptional dysregulation, attenuated cell growth, apoptosis, defective neurogenesis, reduced organoid volume, and/or cortical neuroanatomical abnormalities. As previously described, ZIKV exhibits a similar tropism for NPCs in fetal and neonatal mice. ZIKV infection of fetal or newborn mice by vertical transmission or direct intracerebral inoculation results in decreased cell migration, impaired neurogenesis and cell death, with defective development of the cortical layer and congenital defects including microcephaly, hydrocephalus, encephalitis, and ocular lesions (144,164–167). One group reported abnormal vascular density and diameter along with increased BBB permeability, astrogliosis, and widespread microglial activation in the CNS of intracerebrally inoculated embryonic mice (167). Loss of NPCs and perturbations in hippocampal neuron maturation and patterning has also been reported in fetal macaques exposed to ZIKV (75,189).

### **2.6.3 Host immune response**

The human innate immune system detects viral infections via sensors such as pattern recognition receptors (PRRs), which recognize pathogen-associated molecular patterns (PAMPs). Detection

of PAMPs by PRRs ultimately results in upregulation of type I IFN stimulated genes (ISGs) and pro-inflammatory cytokines, which facilitate innate antiviral responses and play a role in initiation of the adaptive immune response (including activation of T- and B-lymphocytes, production of neutralizing antibody, etc) (233). ZIKV dampens the human immune response by using viral NS5 to promote ubiquitin-mediated proteasomal degradation of STAT1 and STAT2, which are critical transcription factors involved in antiviral IFN signaling and host resistance to ZIKV infection (234).

### **3 SARS-CoV-2**

#### **3.1 Natural history and emergence**

In December 2019, a novel betacoronavirus (subgenus *Sarbecovirus*), SARS-CoV-2, emerged in Wuhan, Hubei province, China with an outbreak of pneumonia of unknown origin. Symptoms were suggestive of viral pneumonia, similar to those reported with previous outbreaks of SARS-CoV and MERS-CoV (235). The earliest cases were epidemiologically linked to the Huanan Seafood Wholesale Market in Wuhan, which deals in seafood as well as poultry and wildlife (236), though patients with no history of exposure to this market, including several familial clusters, were also identified (235,237). As hospitalizations increased, so did documented cases of nosocomial infection in health care workers, indicating that this novel coronavirus was capable of human-to-human transmission (235,237). On December 31, 2019, the Wuhan Municipal Health Commission notified the WHO of a pneumonia outbreak of suspected viral etiology (236). Within a month the virus had spread to all 34 provinces of China (235). On 30 January 2020, the WHO declared the outbreak a Public Health Emergency of International Concern (238). As SARS-CoV-2 shares 75-80% genome sequence identity with SARS-CoV

(239,240), the International Committee on Taxonomy of Viruses named the novel coronavirus ‘SARS- CoV-2’, and the WHO named the disease coronavirus disease 2019 (COVID-19) in February 2020 (241).

Highly efficient transmission in combination with the frequency of international travel resulted in rapid worldwide spread of SARS-CoV-2; on March 11, 2020 the global COVID-19 outbreak was officially classified by the WHO as a pandemic (242). As of May 2022, there have been more than 500 million confirmed cases and 6 million deaths globally (52) (**Figure 11**).

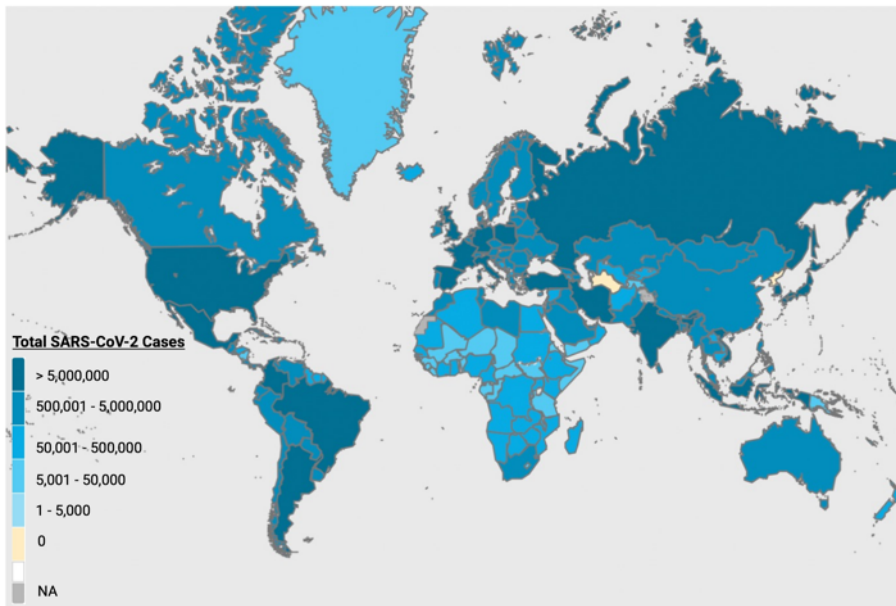


**Figure 11.** Map showing the number of confirmed global cases of COVID-19 as of May 2022. Adapted from the World Health Organization (WHO) Coronavirus Dashboard (52) using BioRender.com.

### 3.2 Virus structure and replication

For the most part, SARS-CoV-2 genome organization, protein characteristics and replication mechanisms are similar to other betacoronaviruses, as previously described (**Figure 7-8**). Notably, while most of the structural genes of SARS- CoV-2 share 85 - 90% amino acid identity with SARS-CoV, the S protein receptor-binding domain (RBD) has just 73% amino acid similarity (243).

SARS-CoV-2 has four amino acid residues (PRRA) inserted at the junction of S protein subunits S1 and S2, which generates a cleavage site for furin and other proteases (244,245). The identification of similar amino acid insertions in bat coronaviruses suggests that similar insertion events may occur naturally in animal betacoronaviruses (246). Furin cleavage at this site is thought to result in S protein instability and facilitate the conformational change necessary for RBD binding to ACE2. Overall, this RBD modification facilitates viral S protein interactions with ACE2, resulting in increased binding affinity compared to other betacoronaviruses (60,247). Host cell receptor neuropilin-1 (NRP1) binds the resulting furin-cleaved substrates and is thought to increase SARS-CoV-2 infectivity by providing a pathway into the central nervous system (CNS). SARS-CoV-2 may also utilize the alternative receptor CD147, which is expressed at high levels in the human brain, to infect cerebral nervous system (248). Another distinction is that the SARS-CoV-2 protein encoded by accessory gene ORF8 shares only 40% amino acid identity to ORF8 of SARS-CoV. In contrast to SARS-CoV, the novel ORF8 protein of SARS-CoV-2 fails to trigger intracellular stress pathways, which could have important consequences in the context of diminishing the host innate immune response (243).

By transmission electron microscopy (TEM), SARS-CoV-2 particles are reportedly similar in appearance to other coronaviruses, particularly SARS-CoV. Ellipsoidal to spherical enveloped viral particles range in diameter from 60 to 140 nm and are located within DMVs, the continuous membrane system formed by rER and the Golgi complex, or adherent to the cell surface, pending release (50,56,300). The viral lumen is typically packed with electron dense ribonucleoproteins (RNPs) (248). While TEM studies have also identified extracellular virions, these are often difficult to distinguish morphologically from subcellular organelles such as coated vesicles,

multivesicular bodies, perichromatin granules, glycocalyceal bodies, and cellular projections (50). Characteristic surface projections (the so-called “solar corona”) are typically indistinct in standard TEM thin-preparations but may be visualized following tannic acid treatment (50,301).

Like all viruses, SARS-CoV-2 continuously evolves, largely due to genetic mutations during replication. Throughout the pandemic, novel SARS-CoV-2 variants (e.g., omicron and delta) containing one or more mutations relative to the original virus have emerged to replace the previously dominant ancestral variant, and will likely continue to incite new outbreaks (249). The WHO closely monitors emerging variants and may classify one as a variant of concern (VOC) based on the following criteria: increased transmissibility and/or virulence, significantly reduced efficacy of neutralizing antibodies from previous infection/vaccination, vaccine or treatment failure, or ineffectiveness of standard diagnostic/detection methods (249).

### **3.3 Transmission**

Overall, genetic evidence suggests that SARS-CoV-2 probably originated in animals, although exactly how and when the virus first entered humans remains unclear. Likewise, the precise reservoir and/or intermediate animal host(s) have not been clearly established (235). Current phylogenetic analyses indicate that SARS-CoV-2 clusters with SARS-CoV, SARS-related coronaviruses (SARSr-CoVs) in bats and recently identified coronaviruses in pangolins (235). Bats are strongly suspected to serve as a natural reservoir (235), and pangolins have been suggested as an intermediate host (47). As noted above, there is a clear epidemiological link to the Wuhan seafood/live animal market; however, patients with no history of exposure to the market, including several familial clusters, were also identified in the first wave of the pandemic, indicating that the market may not be the initial source of human infection (235).

Sequencing of the SARS-CoV-2 viral genome reveals a 75 - 80% similar genome identity to SARS-CoV, and an even closer genetic relationship to several bat coronaviruses (55,240). Bats serve as natural hosts for a number of alpha- and betacoronaviruses. Currently, the closest identified relatives to SARS-CoV-2 are bat coronaviruses identified in China. One was isolated from *Rhinolophus affinis* and provisionally named ‘RaTG13;’ it shares 96.2% complete genome sequence identity and 92.9% S-gene sequence identity with SARS-CoV-2 (250). The other, ‘RmYN02,’ was detected in *Rhinolophus malayanus* and shares 93.3% complete genome identity with SARS-CoV-2 and 97.2% sequence identity specifically in ORF1ab. Despite low sequence identity (61.3%) to the SARS-CoV-2 RBD, RmYN02 also exhibits similar amino acid insertions at the S1-S2 subunit junction in the S protein (246). Even with these genetic similarities, the level of divergence between similar bat coronaviruses and SARS-CoV-2 is estimated to represent over 20 years of sequence evolution, indicating that, while a bat coronavirus may undeniably be an evolutionary precursor of SARS-CoV-2, it is unlikely to be the direct predecessor (251).

Besides bats, pangolins are also tentatively linked with SARS-CoV-2 emergence and transmission. Malayan pangolins (*Manis javanica*) smuggled into China from Southeast Asia between 2017 and 2019 carry a SARS-CoV-2- related virus with 92.4% genome sequence similarity and a receptor binding motif with just one amino acid variation from human SARS-CoV-2 (252). However, in contrast to bats, infected pangolins exhibit clinical signs and histopathological lesions (including interstitial pneumonia) of respiratory disease. This observation suggests that, rather than playing a significant role in the emergence of SARS-CoV-2 in humans, pangolins were most likely infected via spillover from the natural hosts (252). Overall, these data suggest that assorted coronaviruses

similar to SARS-CoV-2 are likely circulating in wildlife populations (251). Widespread surveillance of SARS-CoV-2-related viruses in bats, pangolins and other wildlife species in Asia is required if we hope to pinpoint the specific zoonotic origin of SARS-CoV-2. It is also possible that a number of recombination events between severe acute respiratory syndrome-related coronaviruses coexisting in bats facilitated the eventual emergence of SARS-CoV-2 (48).

The human-to-human transmissibility of SARS-CoV-2 is higher than SARS-CoV or MERS-CoV (60). The basic reproduction number ( $R_0$ ) refers to the average number of people subsequently infected by each currently infected person. If  $R_0 \leq 1$ , the number of secondary cases should decrease over time and the outbreak will eventually die out without human interference (253). In 2020, the mean  $R_0$  for SARS-CoV-2 was estimated to be  $\sim 2.71$  (based on averaging data from approximately 50 independent global studies); however, published estimates vary widely, ranging from  $\sim 0.5$ - $6.5$  (253). Notably, many emerging VOCs, including delta (5.08 average with a range of 3.2 - 8) (254) and omicron (9.5 average with a range of 5.5 - 24) (255), have higher  $R_0$  values than ancestral strains from 2019 and early 2020.

Transmission of SARS-CoV-2 typically follows close contact, when respiratory ( $>5\mu\text{m}$  diameter) and/or aerosol ( $<5\mu\text{m}$  diameter) droplets come into contact with mucus membranes of the upper respiratory tract (57,60,256–258). As ACE2 and TMPRSS2 are both highly expressed by the enterocyte microvillar brush border in the human intestinal tract (259), it is not surprising that SARS-CoV-2 also utilizes the fecal-oral transmission route. Gastrointestinal symptoms are frequently reported and SARS-CoV-2 RNA is detected in stool samples from  $\sim 20\%$  of patients with COVID-19 (260). As asymptomatic individuals can also shed the virus in their feces (261),

wastewater surveillance serves as a useful early warning system for community spread of SARS-CoV-2 (261). The relative contribution of fomites (e.g., contaminated door handles or personal protective equipment [PPE]) remains under investigation but is likely less significant than respiratory droplets and direct contact (258,262). SARS-CoV-2 RNA shedding generally declines with resolution of symptoms, though it may continue at lower levels for days to weeks. That being said, detection of viral RNA during convalescence does not necessarily indicate infectious, replication-competent virus (263).

Studies suggest that SARS-CoV-2 is less lethal and more transmissible than SARS-CoV and MERS-CoV (60). The incubation period, or time between exposure and the appearance of clinical signs, for COVID-19 disease ranges from 4 – 14 days (versus 2 – 11 days for SARS-CoV), with an average of 4 - 5 days (60). High viral RNA titers and infectious virus are reported in nasal swabs/saliva specimens from both asymptomatic and presymptomatic patients, and transmission of SARS-CoV-2 by pre- and asymptomatic patients has been documented, though the frequency is unknown (263–267). Reinfection is also widely reported, particularly with newly emerging variants; however, the length of immunity, antibody titers required for protection, and frequency of reinfection also remain unclear (263).

At the outset of the pandemic, there was significant concern that domestic animals (i.e., livestock and companion animals) might be susceptible to SARS-CoV-2 and serve as a reservoir for human infection. SARS-CoV-2 RNA has been detected in the respiratory tract of pet dogs (268) and cats (269,270) housed with COVID-19 patients, farmed mink (271,272), and a handful of large zoo felids (lions and tigers) (273). Dogs with detectable viral RNA were generally asymptomatic (268)

while domestic cats, lions and tigers (269,270,273) exhibited variable, mild clinical signs of respiratory disease. Experimental SARS-CoV-2 inoculation of dogs failed to result in clinical disease (274) while inoculation of domestic cats caused mild, nonfatal respiratory disease with bronchointerstitial pneumonia (275) and evidence of airborne transmission to a subset of naïve, co-housed cats (274). A large serologic survey failed to detect SARS-CoV-2 specific antibodies in any companion animals, including dogs and cats (276). Following experimental inoculation of chickens, ducks, and pigs, no SARS-CoV-2 RNA or infectious virus was detected in virus-inoculated or naïve co-housed animals, and all animals remained seronegative, indicating that these species are not naturally susceptible to SARS-CoV-2 (274).

Mustelids, including ferrets (*Mustela putorius furo*) and mink (*Neovison vison*) are susceptible to a number of coronaviruses, including SARS-CoV-2 (272,277) and ferrets are often used as a translational model for human COVID-19 disease (see section 3.5) (278). In a series of high morbidity/mortality COVID-19 outbreaks in farmed mink in the Netherlands, likely introduced by infected humans (271), a 2 - 3 day clinical course of dyspnea, mucoid nasal discharge and inappetence was typically followed by death (272). SARS-CoV-2 RNA and antigen were detected in the lung of affected mink, and histopathologic pulmonary features, including interstitial pneumonia and diffuse alveolar damage with hyaline membranes, were similar to reports in human patients with severe COVID-19 (272). Whole genome sequencing provided evidence of animal-to-human transmission, resulting in the culling of millions of farmed mink (271).

Overall, published reports indicate that SARS-CoV-2 replicates poorly or not at all in most domestic species/companion animals. While cats appear to be susceptible, natural infection

resulting in transmission to humans has not been definitively documented in either cats or dogs. In contrast, mustelid species such as ferrets and mink are susceptible to infection and capable of viral transmission (274). Recent research also indicates that a variety of free-living wildlife species are susceptible to SARS-CoV-2, including deer mice (*Peromyscus maniculatus*) (279), bushy-tailed woodrats (*Neotoma cinerea*) (279), bank voles (*Myodes glareolus*) (280), Chinese tree shrews (*Tupaia belangeri chinensis*) (281), common marmosets (*Callithrix jacchus*) (282), Egyptian fruit bats (*Rousettus aegyptiacus*) (283), racoon dogs (*Nyctereutes procyonoides*) (284), striped skunks (*Mephitis mephitis*) (279,285), raccoons (*Procyon lotor*) (285), and white-tailed deer (*Odocoileus virginianus*) (286). Coronaviruses (including SARS-CoV-2) clearly have a broad host range, and as noted in section 1, many emerging pathogens originate or mutate at regions of interface between humans and wildlife/livestock. Spillback from humans could lead to the establishment of a wildlife reservoir, jeopardizing infection control and impeding wildlife management, welfare and conservation efforts (287).

### **3.4 Clinical human disease, treatment, and prevention**

In contrast to common cold coronaviruses (e.g., HCoV-229E) (48), which produce only mild upper respiratory tract symptoms, symptomatic SARS-CoV-2 infection initially presents with flu-like symptoms and may progress to severe respiratory disease with radiographic evidence of pneumonia (47,60,288). Clinical signs of COVID-19 disease are variable. While some infections remain asymptomatic, most patients develop some or all of the following symptoms: fever, chills, fatigue, headache, muscle aches (myalgia), sore throat, nasal congestion, cough, dyspnea, loss of smell (anosmia), loss of taste (ageusia), nausea/vomiting, and diarrhea (53,267,288). Although the

prevalence of asymptomatic infections is not clear, RT-PCR and serologic studies suggest that they may be relatively common and that the total number of cases is likely underreported (267).

A subset of COVID-19 patients, particularly those who are more than 60 years old or have pre-existing co-morbidities (such as obesity, diabetes, cardiovascular disease, renal damage, liver dysfunction, and cancer), progress to atypical, severe manifestations of COVID-19 disease, including acute respiratory distress syndrome (ARDS) (235,288) and/or a systemic hyperinflammatory state (the so-called ‘cytokine storm’) (289). There is no widely agreed-upon definition of the cytokine storm, as it has been associated with variable underlying etiologies, cytokines are a normal component of the immune response, and it is unclear exactly when an inflammatory reaction crosses the line from appropriate to dysregulated. However, a recently proposed unifying definition broadly describes the cytokine storm as immune dysregulation characterized by high levels of circulating cytokines, immune-cell hyperactivation, and systemic inflammation, which, if left untreated can result in multiorgan failure and death (289).

In addition to continuing deficiencies in pulmonary function, a subset of recovered COVID-19 patients go on to develop long-term clinical sequelae, including shortness of breath, intermittent fever, anosmia, ageusia, myocardial dysfunction, gastrointestinal distress, and neurocognitive deficits such as anxiety, insomnia, depression, and a chronic fatigue-like syndrome often referred to as “brain fog.” These post-viral complications, initially referred to as “long COVID” but now collectively designated “post-acute sequelae of SARS-CoV-2 infection” (PASC), vary in severity and chronicity, and often develop well after the resolution of infection (47,60,290,291). PASC is also frequently reported in patients with asymptomatic/mild forms of COVID-19 (292).

Among a cohort of more than 44,000 Chinese COVID-19 patients, disease severity was categorized as mild (81%), severe (14%, dyspnea/hypoxia, or > 50% lung involvement by imaging), or critical (5%, respiratory failure, ARDS, multiorgan dysfunction). All deaths occurred in patients classified as having critical illness, and the case fatality ratio (CFR) within this group was 49%. The overall CFR was 2.3%. CFR was highest among those of advancing age; mortality among patients of 80 years or older was 14.8%, 70 – 79 years was 8.0%, 60 – 69 years was 3.6%, 50 – 59 years was 1.3%, 40 – 49 years was 0.4%; and for patients younger than 40 years dropped to 0.2%. CFR was also higher for patients with the comorbidities described above. Disease severity was reduced among children, where 94% were asymptomatic or had mild to moderate disease, while 5% and 1% exhibited severe or critical disease, respectively (293). Accounting for age and comorbidities, the mortality reported in the United States appears similar to reports from China (263).

Hematologic and serum chemistry abnormalities, including lymphopenia (reported in up to 83% of hospitalized patients), neutrophilia, mild thrombocytopenia, elevations in D-dimer (reported in up to 45% of patients), elevated fibrin(ogen) degradation products (FDPs), elevated serum alanine aminotransferase (ALT), aspartate aminotransferase (AST), and lactate dehydrogenase (LDH) levels, high C-reactive protein (CRP), and high ferritin levels are reported in patients with COVID-19 disease, and are typically associated with increased disease severity and/or mortality (263,294). Similar laboratory abnormalities are associated with the cytokine storm, in addition to high levels of circulating cytokines, particularly IL-1 $\beta$ , IL-6, and TNF (289). Increased numbers of neutrophils and macrophages with corresponding elevations in proinflammatory cytokines (IL-6 and IL-8) and

chemokines (CCL2) have also been reported in the bronchoalveolar lavage fluid (BALF) of patients with severe COVID-19 disease (60). Overall, patients with critical disease tend to exhibit high plasma levels of proinflammatory markers, suggesting potential immune dysregulation (i.e., cytokine storm) (263,295). Notably, elevated plasma IL-6 correlates directly with fibrinogen levels in COVID-19 patients (296).

D-dimer levels represent an independent risk factor for death where mortality in COVID-19 patients with D-dimer values greater than 1000 ng/mL is approximately 20 times more likely when compared to patients with lower values (294). Aberrations in D-dimer and FDP levels are reminiscent of disseminated intravascular coagulation (DIC), a condition characterized by unrestrained coagulation, ongoing consumption of clotting factors, and widespread microvascular thrombosis. Laboratory features of DIC typically include some combination of thrombocytopenia, prolonged prothrombin times (PT) and activated partial thromboplastin times (aPTT), hypofibrinogenemia, and decreased antithrombin III and/or protein C, in addition to elevated D-dimer and FDPs (297). In contrast, patients with severe COVID-19 disease often exhibit normal to minimally prolonged PT, normal or slightly decreased aPTT, mild thrombocytopenia to mild thrombocytosis, normal to increased fibrinogen, increased protein C (294,296). Rather than DIC, these laboratory findings are suggestive of a distinct coagulopathy characterized by a combination of hypercoagulable and severe inflammatory pathophysiological states (290,294,295). This makes sense given the crossover between host immune, inflammatory and hemostatic processes, where infiltrating leukocytes play a role in activating both endothelial cells and platelets (298,299). Thromboelastography (TEG) in COVID-19 ICU patients is also reported to be consistent with a

hypercoagulable state (295), which could predispose affected individuals to both venous and arterial thrombosis (296).

As the pandemic progressed, clinical evidence of coagulopathy, including arterial and venous thromboembolism and myocardial infarction, as well as microscopic indicators of pulmonary vascular damage (described in detail below) became increasingly evident (60,290,300–302).

Although published autopsy results from COVID-19 patients are somewhat lacking, pulmonary microscopic features are generally consistent with widespread alveolar damage, including alveolar septal necrosis with hemorrhage, edema, fibrin deposition and formation of hyaline membranes, with reparative changes such as type II pneumocyte hyperplasia and alveolar septal fibrosis developing later in the course of disease. Vascular lesions, including perivascular inflammation, endotheliitis (characterized by sub- and intra-endothelial inflammatory cell infiltration with variable transmigration of the vessel wall) (303), and venous, arterial, and microvascular thrombosis are also documented in association with acute COVID-19 disease, primarily within the lungs, but also in peripheral tissues such as skin, heart, brain, liver, intestine, and kidneys (290,302,304).

Diagnosis of current COVID-19 infection requires detection of SARS-CoV-2 RNA via NAAT (e.g., qRT-PCR) or antigen in respiratory specimens. NAATs are highly sensitive and specific tests that have been designed to detect viral RNA genes, but detection does not necessarily indicate the presence of replication competent infectious virus. Antigen tests are immunoassays that detect the presence of a specific viral antigen (e.g., N protein). They are highly specific, though less sensitive than most NAATs. Rapid-antigen tests can provide rapid results in minutes and are available for

self-testing, thus these tests are very useful for screening, keeping in mind that it may prove necessary to confirm with a laboratory-based NAAT. Thoracic computed tomography (CT) scans are also widely used to confirm a COVID-19 diagnosis; lesions typically include parenchymal ground-glass opacities (80%) and subpleural lesions (20%) (263,288). Antibody tests (e.g., ELISA) are useful for detecting previous infection with SARS-CoV-2, though they are not recommended for diagnosis of current infection. SARS-CoV-2 S- and N-proteins are the primary antigenic targets for antibody detection. Serum IgM antibodies are typically detectable during the early (~two weeks) post-infection period, followed by isotype switching, after which IgG predominates. Antibody (serology) tests are often used for public health and epidemiological surveillance (263,288).

As transmission of SARS-CoV-2 occurs primarily via exposure to respiratory droplets, face coverings, frequent hand washing, physical distancing and quarantine were the mechanisms of disease prevention prior to vaccine development (308). Currently within the U.S., vaccination with one of two FDA approved mRNA vaccines (BNT162b2 [Pfizer-BioNTech] or mRNA-1273 [Moderna]) is considered the most effective way to prevent clinical disease due to SARS-CoV-2 infection (308). A third vaccine (Ad26.COV2.S [Johnson & Johnson/Janssen]) is also available but has been associated with severe adverse events (thrombosis with thrombocytopenia syndrome) (309).

Treatment of COVID-19 disease is generally supportive, though several drugs have been approved or are under evaluation for use in the United States. Remdesivir, which prevents viral replication via binding of viral RNA-dependent RNA polymerase, is the only FDA approved antiviral drug

for the treatment of COVID-19. Ritonavir-boosted nirmatrelvir (Paxlovid), molnupiravir, and some anti-SARS-CoV-2 monoclonal antibodies (e.g., sotrovimab) have also received Emergency Use Authorizations from the FDA (310). In addition to antivirals, which are most useful during acute COVID-19, a variety of anti-inflammatory therapies have received EUAs. For instance, baricitinib (Janus kinase [JAK] inhibitor) and tocilizumab (IL-6 inhibitor) are effective in the later disease stages which are characterized by a hyperinflammatory state (310).

### **3.5 Animal models**

Various animal models of SARS-CoV-2, including mice, hamsters, non-human primates, and ferrets, have been described and are useful for studying viral pathogenesis and evaluating the efficacy of medical countermeasures. As noted previously, ACE2 is a critical host membrane receptor for the spike protein of SARS-CoV-2. Structural analyses of ACE2 in various species reveal that the ACE2 S-protein interface region in rhesus macaques is identical to that of humans, and that hamster ACE2 exhibits a very high binding affinity for the SARS-CoV-2 spike protein (311). However, owing to structural variation in mouse ACE2, SARS-CoV-2 inoculation fails to produce significant disease in conventional inbred laboratory mice. Thus, mouse models of COVID-19 typically utilize K18-hACE2-transgenic mice, originally developed for investigation of SARS-CoV pathogenesis, which express humanized ACE (hACE2) (312).

Intranasal (IN) SARS-CoV-2 inoculation results in consistent infection with efficient viral replication in the upper and lower respiratory tract of both hACE2 mice (312–314) and Syrian golden hamsters (311,315–319). Infectious virus and viral RNA are generally detectable in the lung as early as two dpi and are cleared by seven dpi (311–319), though hamsters typically develop higher magnitude and longer duration lung viral titers than transgenic mice (317). When present,

clinical signs include weight loss, lethargy, ruffled fur, hunched back posture, and tachypnea (311,313,319). Similar to humans, infected hamsters demonstrate peripheral ground glass opacities and areas of lung consolidation on micro-computed tomographic (micro-CT) imaging (315). Infected hamsters and mice mount post-challenge neutralizing antibody responses and are generally resistant to short-term re-challenge; they can also infect naïve cage-mates (311–318).

SARS-CoV-2 RNA/antigen initially localizes to airway epithelial cells, with subsequent extension into surrounding type I and II pneumocytes and scattered alveolar macrophages (316,318). Though similar, histopathologic lesions in hamsters tend to be more variable, progressive, and severe than those reported in hACE2 transgenic mice. Both hamsters and hACE2 mice develop progressive microscopic pulmonary lesions beginning as early as two dpi. Mice initially present with bronchiolitis which develops into mononuclear interstitial pneumonia, while early bronchiolitis in hamsters progresses to marked alveolar septal damage and neutrophilic to histiocytic bronchointerstitial pneumonia (311,314–316,319). Both hamsters and transgenic mice have scattered multinucleated syncytial cells, and by 10 - 14 dpi both exhibit microscopic evidence of pulmonary repair and regeneration, including type II pneumocyte and bronchiolar epithelial hyperplasia. Notably, SARS-CoV-2 infection can be lethal in hACE2 mice and tends to be non-lethal in hamsters, despite more severe histopathologic pulmonary lesions in this species (311–313,315–319).

Ferrets are naturally susceptible to SARS-CoV-1 and -2 and recapitulate some aspects of human disease; they are also capable of both direct and airborne viral transmission (277,320). SARS-CoV-2 inoculated ferrets are often asymptomatic but can develop clinical signs of mild respiratory

disease such as fever, inappetence and weight loss. Viremia is not reported, though viral RNA is detected in oropharyngeal swabs, nasal washes, BALF, saliva, and occasionally urine and feces (277,278,321). Aged ferrets ( $\geq 3$  years old) in particular can have high viral loads with prolonged nasal shedding of virus (322). Microscopic pulmonary lesions are typically mild and may include bronchiolitis, alveolar histiocytosis, suppurative pneumonia and perivascularitis with subendothelial inflammation (277,278,321).

SARS-CoV-2 causes mild to moderate respiratory disease in rhesus macaques. SARS-CoV-2 inoculated macaques generally fail to become viremic, though a subset develop clinical signs of disease including fever, inappetence, hunched posture, and weight loss, with detectable viral RNA from one to three dpi in nasal and oropharyngeal swabs and BALF, and radiographic evidence of pulmonary infiltrates, particularly within caudal lung lobes. Seroconversion and neutralizing antibodies are detectable in these animals by 10 dpi. Microscopic pulmonary lesions are variable in severity. Early in the course of disease lesions are characterized by mild inflammatory infiltrates (primarily mononuclear cells with fewer neutrophils and occasional syncytial cells) centered on terminal bronchioles and few foci of alveolar damage. By 7 - 10 dpi lesions have typically progressed to patchy mild to moderate interstitial pneumonia. Similar to rodents, SARS-CoV-2 RNA and antigen are identified in bronchiolar epithelial cells, type I and II pneumocytes, and scattered alveolar macrophages (192,323–325). Mortality is not generally observed. Although age does not appear to affect disease outcome, prolonged viral shedding from the upper respiratory tract has been reported in aged animals (324). Rechallenge following initial viral clearance results in reduced viral loads within BALF and nasal mucosa with high SARS-CoV-2 specific antibody and neutralizing antibody titers, suggesting protective immunity against re-exposure (325).

Hamsters, transgenic mice, ferrets and NHPs are susceptible to SARS-CoV-2, and variably recapitulate the clinical, virological, and histopathological features associated with COVID-19 disease. When choosing the appropriate model, the advantages and disadvantages of each species should be considered in the context of the type and purpose of the study, research goals, and anticipated practical applications.

### **3.6 Pathogenesis**

Unlike SARS-CoV, SARS-CoV-2 can infect and replicate in naso- and oropharyngeal tissues of the upper respiratory tract, which may account for its increased transmissibility and likely plays a role in presymptomatic transmission (60). Upper and lower respiratory tract cells targeted by SARS-CoV-2 include tracheal/bronchial/bronchiolar epithelial cells, type I and II alveolar pneumocytes, and to a lesser extent, alveolar macrophages (326–328). ACE2 receptor binding is critical for viral entry into susceptible host cells and differences in binding affinity for host ACE2 receptors likely account (at least in part) for the variable infectivity reported among emerging SARS-CoV-2 variants (47). ACE2 is a component of the renin-angiotensin system (RAS) which maintains blood pressure homeostasis via regulation of fluid and salt balance (328). ACE2 specifically catalyzes the production of angiotensin II, a peptide which triggers vasoconstriction (329). RAS hyperactivation has been proposed as a contributing factor to atherosclerosis, heart failure, hypertension, diabetes, renovascular disorders, pulmonary hypertension, pneumonia, fibrosis, and sepsis (329).

Recent studies have also identified novel proteases which may act as additional SARS-CoV-2 receptors/co-receptors, including TMPRSS and basigin (BSG, also known as CD147 or extracellular matrix metalloproteinase inducer [EMMPRIN]) (47,296). Notably, CD147 is also expressed by endothelial cells, and upregulation of CD147 during inflammation stimulates metalloproteinase expression; this has led to the suggestion that CD147 may partially mediate the cardiovascular damage associated with severe COVID-19 disease (330). Overall, SARS-CoV-2 infection in combination with the subsequent inflammatory response damages airways, alveolar septa and pulmonary vasculature, resulting in reduced surfactant production, vascular leakage, impaired oxygen exchange, and respiratory distress (57).

Endothelial injury is a likely underlying mechanism linking inflammation and hypercoagulability in severe cases of COVID-19 disease (290); however, it remains unclear whether vascular complications in COVID-19 disease are mediated by direct viral effects (e.g., infection of endothelial cells with subsequent vascular endothelial dysfunction), indirectly via immune hyperactivation or dysregulation (302), or some combination. As noted in section 3.4, some patients exhibit clinical signs and laboratory results consistent with a systemic hyperinflammatory state known as the cytokine storm. Neutrophil extracellular traps (NETs) are another potential contributor to the pathogenesis of severe COVID-19. NETs are scaffolds of extracellular DNA with attached histones, neutrophil granule proteins and antimicrobial peptides that are released in response to microbes, cytokines (IL-8, TNF), and complement components, among other stimuli. Although their main functions are antimicrobial (i.e., killing, entrapping or hindering dissemination of microorganisms), NETs can also cause ‘innocent bystander’ damage, and,

considering the complex interactions between inflammation and coagulation, both the cytokine storm and NETosis can promote a hypercoagulable state and thrombosis (298).

In a non-inflamed environment, endothelial cells maintain vascular homeostasis and barrier functions by limiting vascular permeability, coagulation, and inflammation. Platelets in this environment are quiescent and do not interact with the endothelium (299). Endothelial cell activation due to damage or infection results in a pro-coagulant, pro-inflammatory state characterized by increased vascular permeability, production of cytokines, leukocyte adhesion molecules, and coagulation factors, and activation of platelets and leukocytes (299). Platelets are crucial for both vascular homeostasis and repair of vascular injury; they also play a role in inflammation and the immune response. Platelets interact with leukocytes, endothelial cells, and associated vascular support cells, both directly and indirectly through the induction and/or release of hemostatic and inflammatory mediators (331). Activated platelets release vasoactive substances, and both activated platelets and endothelial cells release Von Willebrand factor (vWF) which facilitates platelet aggregation and adhesion to the damaged endothelium (296). While direct coronaviral infection of platelets has not been definitively documented (296), oxidative stress, hypoxia (i.e., caused by inflammation or COPD) and other stressors associated with severe SARS-CoV-2 infection alter platelet mitochondrial function and may result in platelet hyperactivation (332). Activated platelets can induce the formation of NETs, leading to immunothrombosis (333), thus hyperactivated platelets are yet another possible contributor to immune dysregulation and microthrombosis in severe COVID-19 disease (296). Activation of the complement cascade may also facilitate a hypercoagulable state via induction of platelet activation and aggregation (296).

Taken together, published data are most consistent with an indirect mechanism of endothelial injury mediated by the local and/or systemic inflammatory response and resulting in disrupted vascular homeostasis. Activation of the inflammatory response results in a great deal of crosstalk between platelets, endothelial cells and leukocytes, which may ultimately result in endothelial damage, parallel activation of the coagulation cascade, and thrombosis (334). Further supporting this theory, biomarkers of endothelial dysfunction/injury, including thrombomodulin, vWF, and P-selectin, are often elevated in patients afflicted with severe COVID-19 disease (290,296).

#### **4 Conclusions and hypotheses**

ZIKV and SARS-CoV-2 are the etiologic agents responsible for the two major pandemics of the 21<sup>st</sup> century. ZIKV spread since 2015 led to establishment of urban epidemic cycles involving humans and *Aedes* mosquitoes. ZIKV is also unique among mosquito-borne flaviviruses in its capacity for both sexual and vertical transmission. Vertical transmission from mother to child can result in a range of severe obstetric outcomes and a constellation of fetal lesions known as CZS, which affects one in seven babies prenatally exposed to ZIKV. These features, together with anthropogenic factors facilitating expansion of vectorial geographic ranges, ensure that ZIKV remains a significant global public health risk.

Recent evidence indicates that sexual transmission of ZIKV may be responsible for a significant number of human infections and could also serve as mechanism for introducing ZIKV to non-endemic regions lacking mosquito-human-mosquito transmission. Although mounting evidence identifies the male reproductive tract as a significant ZIKV reservoir, data regarding the duration of ZIKV persistence, potential for sexual transmission, and male genitourinary sequelae remain

sparse. By virtue of similar reproductive anatomy and physiology to humans, macaques serve as a useful model for ZIKV infection, and extrapolating data from macaque models of ZIKV is a useful method for understanding the pathogenesis of and risk factors associated with human ZIKV infection. However, macaque studies to date have been limited by small sample size, typically one to five animals. Based on published data in mouse and macaque models and using archived reproductive tissues from 51 ZIKV-inoculated male macaques from past collaborative research projects, **I hypothesize that ZIKV will persist in the male macaque genital tract for longer than detectable viremia, where it will localize to germ cells and epithelial cells and associate with genital lesions.** This hypothesis is addressed in Chapter 2.

Microcephaly is an extreme manifestation of CZS; however, over time, normocephalic newborns with confirmed ZIKV infection but no observable congenital defects can also exhibit visual and neurologic deficits reminiscent of CZS. These and other long-term developmental consequences of prenatal ZIKV exposure remain poorly understood. Furthermore, most animal studies of CZS, whether in mice or NHPs, are terminated at some point near the end of gestation, and very few live births have been described. My second hypothesis, addressed in Chapter 3, is that **early prenatal ZIKV exposure results in developmental abnormalities in the lateral geniculate nucleus (LGN) of two year old rhesus macaques when compared to age-matched controls.**

COVID-19 disease varies from asymptomatic to severe respiratory disease, progressing to ARDS, multiorgan dysfunction, and death in a subset of patients. Clinical evidence of coagulopathy and microscopic indicators of pulmonary vascular damage are increasingly reported, particularly in severe cases. Comprehensive pathological examination is critical for understanding any emerging

infectious disease; however, biosafety concerns in combination with the sudden nature of the pandemic and health care personnel shortages significantly limited both ante-mortem procedures and autopsies in COVID-19 patients. Thus, while there is an urgent need to better define the full range of SARS-CoV-2 pathologies, published data in human patients remain relatively scarce. Syrian golden hamsters closely recapitulate the clinical, virological, and histopathological features associated with severe COVID-19 disease. Based on published data, **I hypothesize that Syrian golden hamsters inoculated with SARS-CoV-2 will develop microscopic pulmonary vascular lesions comparable to those reported in humans with severe COVID-19, and that these lesions are secondary to indirect “innocent bystander” damage due immune dysregulation rather than direct viral infection of endothelial cells.** This hypothesis is addressed in Chapter 4.

## **CHAPTER 2**

### **Zika virus persistence in the male macaque reproductive tract**

Submitted *PLOS Neglected Tropical Diseases*

## **Zika virus persistence in the male macaque reproductive tract**

Erin E. Ball<sup>1,7</sup>, Patricia Pesavento<sup>1</sup>, Koen K. A. Van Rompay<sup>1,2</sup>, M. Kevin Keel<sup>1</sup>, Anil Singapuri<sup>1</sup>, Jose P. Gomez-Vazquez<sup>3</sup>, Dawn M. Dudley<sup>4</sup>, David H. O'Connor<sup>4</sup>, Meghan E. Breitbach<sup>4</sup>, Nicholas J. Maness<sup>5,6</sup>, Blake Schouest<sup>5</sup>, Antonito Panganiban<sup>5,6</sup>, Lark L. Coffey<sup>1\*</sup>

<sup>1</sup>Department of Pathology, Microbiology, and Immunology, University of California, Davis, CA

<sup>2</sup>California National Primate Research Center, University of California, Davis, CA, USA

<sup>3</sup>Center for Animal Disease Modeling and Surveillance, University of California, Davis, CA

<sup>4</sup>Department of Pathology and Laboratory Medicine, University of Wisconsin, Madison, WI

<sup>5</sup>Division of Microbiology, Tulane National Primate Research Center, Covington, LA, USA

<sup>6</sup>Department of Microbiology and Immunology, Tulane University School of Medicine, New Orleans, LA, USA

<sup>7</sup>United States Army, Veterinary Corps

\* Corresponding author

### **Abstract**

Zika virus (ZIKV) is unique among mosquito-borne flaviviruses in that it is also vertically and sexually transmitted by humans. The male reproductive tract is thought to be a ZIKV reservoir; however, the reported magnitude and duration of viral persistence in male genital tissues vary widely in humans and non-human primate models. ZIKV tissue and cellular tropism and potential effects on male fertility also remain unclear. The objective of this study was to resolve these questions by analyzing archived genital tissues from 51 ZIKV-inoculated male macaques and correlating data on plasma viral kinetics, tissue tropism, and ZIKV-induced pathological changes in the reproductive tract. We hypothesized that ZIKV would persist in the male macaque genital tract for longer than there was detectable viremia, where it would localize to germ and epithelial cells and associate with lesions. We detected ZIKV RNA and infectious virus in testis, epididymis, seminal vesicle, and prostate gland. In contrast to prepubertal males, sexually mature macaques were significantly more likely to harbor persistent ZIKV RNA or infectious virus somewhere in the genital tract, with detection as late as 60 days post-inoculation. ZIKV RNA localized primarily to testicular stem cells/sperm precursors and epithelial cells, including Sertoli cells, epididymal

duct epithelium, and glandular epithelia of the seminal vesicle and prostate gland. ZIKV infection was associated with microscopic evidence of inflammation in the epididymis and prostate gland of sexually mature males, pathologies that were absent in uninfected controls, which could have significant effects on male fertility. The findings from this study increase our understanding of persistent ZIKV infection which can inform risk of sexual transmission during assisted reproductive therapies as well as potential impacts on male fertility.

### **Author Summary**

Zika virus (ZIKV) spread since 2015 led to establishment of urban epidemic cycles involving humans and *Aedes* mosquitoes. ZIKV is also sexually and vertically transmitted and causes congenital Zika syndrome. Together, these features show that ZIKV poses significant global public health risks. By virtue of similar reproductive anatomy and physiology to humans, macaques serve as a useful model for ZIKV infection. However, macaque studies to date have been limited by small sample size, typically 1 to 5 animals. Although mounting evidence identifies the male reproductive tract as a significant ZIKV reservoir, data regarding the duration of ZIKV persistence, potential for sexual transmission, and male genitourinary sequelae remain sparse. Here, we analyzed archived genital tissues from more than 50 ZIKV-inoculated male macaques. Our results show that ZIKV can persist in the male macaque reproductive tract after the resolution of viremia, with virus localization to sperm precursors and epithelial cells, and microscopic evidence of inflammation in the epididymis and prostate gland. Our findings help explain cases of sexual transmission of ZIKV in humans, which also carries a risk for transmission via assisted fertility procedures, even after resolution of detectable viremia.

## **Introduction**

Mosquito-borne Zika virus (ZIKV) rapidly emerged into urban areas in 2007 (1), initiating epidemics in the South Pacific and the Americas since 2015 and resulting in over 40,000 ZIKV cases in the U.S. and its territories (2). As of December 2021, 89 countries and territories have had documented mosquito-borne transmission of ZIKV (3). Coupled with this swift global vector-borne spread is the capacity for ZIKV to also be sexually and vertically transmitted, although there are currently no diagnostic mechanisms to distinguish sexually transmitted ZIKV from mosquito-acquired infection (4). Cases of sexual ZIKV transmission are likely underreported owing to a high number of asymptomatic individuals, where passive surveillance shows that 4 out of 5 infections do not produce disease (5). Recent evidence indicates that sexual transmission of ZIKV may be responsible for a significant number of infections and could also serve as mechanism for introducing ZIKV to non-endemic regions lacking mosquito-human-mosquito transmission (6–8).

There is strong evidence that the male reproductive tract serves as an important ZIKV reservoir. Infectious ZIKV and ZIKV RNA have been identified in the semen of symptomatic and asymptomatic men, as well as in vasectomized men, suggesting that, in addition to the testes and epididymis, the virus likely persists in the bulbourethral glands, prostate gland, and/or seminal vesicles (9,10). However, reported durations of viral persistence in semen and male genital tissues vary widely. Viral RNA has been detected in human semen for up to 370 days after the onset of symptoms, while infectious virus is more short-lived, with positive cultures from semen samples reported for up to 69 days (6,11). It remains unclear whether there is an association between the magnitude and duration of viremia and genital invasion by ZIKV, viral shedding in semen, and subsequent risk of male-to-female or male-to-male sexual transmission. Genitourinary sequelae in

ZIKV infection are not well described, apart from hematospermia, prostatitis, and low sperm counts, which are occasionally reported in ZIKV-infected men (9,10).

While the laboratory mouse serves as a useful, tractable model of human infectious diseases, including ZIKV infection, rhesus and cynomolgus macaques have a closer genetic relationship and comparable reproductive anatomy and physiology comparable to humans, with the same primary and secondary sex organs, similar stages of spermatogenesis, and comparable levels of male sex hormones (12,13). Thus, extrapolating data from macaque models of ZIKV is a useful method for understanding the pathogenesis of and risk factors associated with human ZIKV infection. *In vivo* viral kinetics, including the length and magnitude of viremia, ZIKV RNA and infectious virus levels within tissues, and tissue tropism, are similar in adult macaques and humans (14–16), validating macaques as a useful model for human ZIKV infection. Unfortunately, long-term data regarding the duration and magnitude of ZIKV in the male genital tract, as well as tropism for specific cell types, are sparse in non-human primates (NHP). ZIKV RNA in rhesus and cynomolgus macaques has been detected in the semen for up to 28 days post-inoculation (DPI), after the resolution of viremia (17). ZIKV RNA has also been detected in the testes (17,18), prostate gland and seminal vesicles (17,19) of 6 macaques from 4 to 35 DPI. These time points represent the end of studies, so viral persistence in male macaque genital tissues and shedding in semen may be more prolonged than suggested in published data.

Although significant lesions and evidence of infertility are infrequently reported in NHP, mouse models have variously demonstrated ZIKV-induced orchitis with seminiferous tubule necrosis, testicular atrophy, oligospermia, viral tropism for spermatogenic precursors and Sertoli cells (20–

22). Overall, the duration of ZIKV persistence in the male reproductive tract, specific viral tissue and cellular viral tropisms, and potential effects of ZIKV on male genitourinary symptoms remain unclear in both humans and animal models. Further information on ZIKV persistence in the male reproductive tract can improve guidelines regarding risks of male sexual transmission and infertility. These gaps in knowledge also affect the field of assisted reproductive technology (ART). There are no documented instances of ZIKV transmission due to assisted fertility procedures; however, ZIKV transmission via sperm, oocytes, or embryos is theoretically possible (23). Notably, there is one documented case of congenital Zika syndrome in a fetus associated with sexual transmission from an asymptomatic man with a history of travel to a ZIKV endemic area to his pregnant wife (24).

Based on published data (15,17,19–22), we hypothesized that ZIKV would persist in the male genital tract of macaques for longer than detectable viremia, where it would localize to germ cells and epithelial cells and associate with lesions. We used archived reproductive tissues from 51 ZIKV-inoculated male macaques from past collaborative research projects at 4 National Primate Research Centers (NPRC) for this study. These animals, aged 2 to 15 years old, were each inoculated once or multiple times with different doses, using varied routes and strains of ZIKV. They were euthanized and necropsied at times ranging from 1 to 60 DPI. Using tissues from these animals, we quantified ZIKV RNA and infectious virus in genital tissues using qRT-PCR and plaque assays, localized ZIKV RNA to specific cell types using *in-situ* hybridization (ISH), and evaluated histomorphology in testes, epididymis, seminal vesicle, and prostate gland. Our results suggest that the male macaque reproductive tract indeed serves as a reservoir for ZIKV, where the epididymis and seminal vesicle are most likely to harbor virus. We further demonstrate that ZIKV

RNA localizes primarily to stem cells (spermatogonia), sperm precursors (1° and 2° spermatocytes) and various epithelial cells, including Sertoli cells, epididymal duct epithelium, and glandular epithelium of the seminal vesicle and prostate gland. Finally, we show that ZIKV infection is associated with microscopic lesions in the epididymis and prostate gland, which could have significant effects on male fertility.

## Results

**Samples from 51 experimentally ZIKV inoculated male macaques were used to evaluate ZIKV tropism and disease in the male reproductive tract.** Archived reproductive tissues and fluids from previous research projects, including testes, epididymis, seminal vesicle, prostate gland and/or semen from 51 ZIKV-inoculated and 8 uninfected male rhesus (*Macaca mulatta*) and cynomolgus (*Macaca fascicularis*) macaques ranging from 2 to 15 years old were provided by the California (CNPRC), Tulane (TNPRC), Wisconsin (WNPRC), and Washington (WaNPRC) National Primate Research Centers (**Table 1**). All uninfected control tissues were from rhesus macaques (N = 7 from CNPRC, N = 1 from WaNPRC). Of the ZIKV-inoculated animals, 5 were cynomolgus macaques from TNPRC, while the remaining 46 were rhesus macaques from CNPRC, WNPRC and TNPRC. Twenty-two animals (all rhesus macaques) were inoculated intravenously (IV) and 28 (including the 5 cynomolgus macaques) were inoculated subcutaneously (SC) with Brazilian (N = 20), Puerto Rican (N = 23), or French Polynesian (N = 2 [semen samples]) strains of ZIKV and necropsied between 1 and 60 DPI. Five ZIKV-inoculated rhesus macaques were inoculated with plasma from a ZIKV-infected human for which specific strain information was not available, and the duration of infection was not available for 2 rhesus macaques for which frozen semen was the only submitted sample. Animals lacking specific metadata were not included

in statistical analyses. Among macaques from CNPRC and TNPRC, 4 were immune suppressed via CD8<sup>+</sup> -cell depletion to assess the impact of these cells on acute ZIKV infection immediately prior to (N = 2 cynomolgus macaques) or 4 weeks after (N = 2 rhesus macaques) ZIKV inoculation. Seven sexually immature rhesus macaques received anti-ZIKV antibody prior to inoculation (5 of 7 animals for which viremia data was available had reduced or delayed viremia), while 9 animals that failed to become viremic upon initial inoculation were reinoculated with a higher dose to ensure infection. Plasma and serum and or viremia data was available from only a subset of the animals, N = 36. There was a single vasectomized from CNPRC and a single splenectomized cynomolgus macaque from TNPRC.

**Table 1: Male macaques and the ZIKV treatments used on animals in this study.** A macaque was considered ZIKV-infected if ZIKV RNA was detected in any fluid or genital tissue. \* Reinoculated animals; (V) vasectomized animal; # received anti-ZIKV antibody prior to inoculation; + immune suppressed animals; ∇splenectomized animal; (semen) frozen semen was the only submitted sample; ‘- ‘data not available; RM= rhesus macaque; CM is cynomolgus macaque; IV is intravenous; SC is subcutaneous; ZIKV is Zika virus; PFU is plaque forming units; DPI is days post inoculation the animal was euthanized. For ZIKV strains, Brazil SPH2015 is GenBank accession KU321639.1, Brazil ZIKV Rio-U1 is GenBank accession KU926309, Puerto Rico PRVABC-59 is GenBank accession KU501215.1, PRVABC-59 clone is PRVABC-59 clone virus (pjW236-C1 P0), PRVABC-59 WT clone is PRVABC-59 clone virus (pW232-WT P0), French Polynesia Zika virus/*H.sapiens*-tc/FRA/2013/FrenchPolynesia/3328 is GenBank accession KJ776791.2. CNPRC is California National Primate Research Center; TNPRC is Tulane National

Primate Research Center; WNPRC is Wisconsin National Primate Research Center; FFPE is formalin fixed paraffin embedded tissues; w/ is with, aa is amino acid.

Animal #	Origin	Species	Age in years	Route	Inoculum	Dose	DPI	Sampled Tissues	ZIKV infected
318059	CNPRC	RM	3.6	IV	Brazil SPH2015	100,000 PFU	1	Testis, epididymis, seminal vesicle, prostate (RNA later, snap frozen, FFPE)	Yes
322042	CNPRC	RM	2.5	IV	Brazil SPH2015	100,000 PFU	1	Testis, epididymis, seminal vesicle, prostate (RNA later, snap frozen, FFPE)	Yes
267274*	CNPRC	RM	12.6	IV	Puerto Rico PRVABC-59	10,000 PFU	4	Testis, epididymis, seminal vesicle, prostate (RNA later, snap frozen, FFPE)	Yes
268506	CNPRC	RM	10.8	IV	Plasma from RM infected with Brazil SPH2015	100 PFU	6	Testis, epididymis, seminal vesicle, prostate (RNA later, snap frozen, FFPE)	Yes
298725*	CNPRC	RM	7.6	IV	Puerto Rico PRVABC-59	10,000 PFU	7	Testis, epididymis, seminal vesicle, prostate (RNA later, snap frozen, FFPE)	Yes
314587*	CNPRC	RM	4.7	IV	Puerto Rico PRVABC-59	10,000 PFU	10	Testis, epididymis, seminal vesicle, prostate (RNA later, snap frozen, FFPE)	Yes
294028 (V)	CNPRC	RM	8.3	IV	Plasma from ZIKV infected human	1,800 RNA copies	11	Testis, epididymis, seminal vesicle, prostate (RNA later, snap frozen, FFPE)	Yes
303583*	CNPRC	RM	6.7	IV	Puerto Rico PRVABC-59	10,000 PFU	14	Testis, epididymis, seminal vesicle, prostate (RNA later, snap frozen, FFPE)	Yes
317415*	CNPRC	RM	4.7	IV	Puerto Rico PRVABC-59	75 PFU	14	Testis, epididymis, seminal vesicle, prostate (RNA later, snap frozen, FFPE)	Yes
313992*	CNPRC	RM	4.8	IV	Puerto Rico PRVABC-59	75 PFU	14	Testis, epididymis, seminal vesicle, prostate (RNA later, snap frozen, FFPE)	Yes
283199	CNPRC	RM	8.8	SC	Brazil SPH2015 w/ mixture of M and I at polyprotein aa 1404	1,000 PFU	14	Testis, epididymis, seminal vesicle, prostate (RNA later, snap frozen, FFPE)	Yes
249788	CNPRC	RM	8.8	SC	Brazil SPH2015 w/ mixture of M and I at polyprotein aa 1404	1,000 PFU	14	Testis, epididymis, seminal vesicle, prostate (RNA later, snap frozen, FFPE)	Yes
434 <sup>+</sup>	TNPRC	CM	8.6	SC	Brazil ZIKV Rio-U1	10,000 PFU	14	Testis, seminal vesicle, prostate (snap frozen, FFPE)	Yes
441 <sup>+</sup>	TNPRC	CM	8.7	SC	Brazil ZIKV Rio-U1	10,000 PFU	14	Testis, seminal vesicle, prostate (snap frozen, FFPE)	Yes
448	TNPRC	CM	8.7	SC	Brazil ZIKV Rio-U1	10,000 PFU	14	Testis, seminal vesicle, prostate (snap frozen, FFPE)	Yes
455	TNPRC	CM	8.7	SC	Brazil ZIKV Rio-U1	10,000 PFU	14	Testis, seminal vesicle, prostate (snap frozen, FFPE)	Yes

462 <sup>v</sup>	TNPRC	CM	9.1	SC	Brazil ZIKV Rio-U1	10,000 PFU	14	Testis, seminal vesicle, prostate (snap frozen, FFPE)	Yes
91056	WNPRC	RM	3.8	SC	Puerto Rico PRVABC-59 WT clone	10,000 PFU	15	Testis, seminal vesicle, prostate (RNA later)	Yes
317338*	CNPRC	RM	4.7	IV	Puerto Rico PRVABC-59	75 PFU	15	Testis, seminal vesicle, prostate (snap frozen, FFPE)	Yes
317254*	CNPRC	RM	4.7	IV	Puerto Rico PRVABC-59	75 PFU	15	Testis, seminal vesicle, prostate (snap frozen, FFPE)	Yes
98154	WNPRC	RM	2.5	SC	Puerto Rico PRVABC-59	10,000 PFU	15	Testis, seminal vesicle, prostate (RNA later)	Yes
70070	WNPRC	RM	6.9	SC	Puerto Rico PRVABC-59 clone	10,000 PFU	18	Testis, seminal vesicle, prostate (RNA later)	Yes
297479	CNPRC	RM	5.5	IV	Brazil SPH2015	100,000 PFU	21	Testis, epididymis, seminal vesicle, prostate (RNA later, snap frozen, FFPE)	Yes
288239	CNPRC	RM	7.4	IV	Brazil SPH2015	100,000 PFU	21	Testis, epididymis, seminal vesicle, prostate (RNA later, snap frozen, FFPE)	Yes
70392	WNPRC	RM	6.4	SC	Puerto Rico PRVABC-59 clone	10,000 PFU	21	Testis, seminal vesicle, prostate (RNA later)	Yes
316897 <sup>#</sup>	CNPRC	RM	2.8	SC	Puerto Rico PRVABC-59	1,000 PFU	22	Testis, epididymis, seminal vesicle, prostate (RNA later, snap frozen, FFPE)	Yes
317317 <sup>#</sup>	CNPRC	RM	2.8	SC	Puerto Rico PRVABC-59	1,000 PFU	22	Testis, epididymis, seminal vesicle, prostate (RNA later, snap frozen, FFPE)	No evidence
325479 <sup>#</sup>	CNPRC	RM	1.8	SC	Puerto Rico PRVABC-59	1,000 PFU	23	Testis, epididymis, seminal vesicle, prostate (RNA later, snap frozen, FFPE)	Yes
300489	CNPRC	RM	5.3	IV	Plasma from ZIKV infected human	42 PFU	24	Testis, epididymis, seminal vesicle, prostate (RNA later, snap frozen, FFPE)	Yes
318297	CNPRC	RM	3	SC	Puerto Rico PRVABC-59	1,000 PFU	26	Testis, epididymis, seminal vesicle, prostate (RNA later, snap frozen, FFPE)	Yes
318570	CNPRC	RM	3	SC	Puerto Rico PRVABC-59	1,000 PFU	26	Testis, epididymis, seminal vesicle, prostate (RNA later, snap frozen, FFPE)	Yes
313999 <sup>#</sup>	CNPRC	RM	3.3	SC	Puerto Rico PRVABC-59	1,000 PFU	28	Testis, epididymis, seminal vesicle, prostate (RNA later, snap frozen, FFPE)	Yes
315091 <sup>#</sup>	CNPRC	RM	3.2	SC	Puerto Rico PRVABC-59	1,000 PFU	28	Testis, epididymis, seminal vesicle, prostate (RNA later, snap frozen, FFPE)	Yes
314818 <sup>#</sup>	CNPRC	RM	3.2	SC	Puerto Rico PRVABC-59	1,000 PFU	29	Testis, epididymis, seminal vesicle, prostate (RNA later, FFPE)	Yes
315833 <sup>#</sup>	CNPRC	RM	3.2	SC	Puerto Rico PRVABC-59	1,000 PFU	29	Testis, epididymis, seminal vesicle, prostate (RNA later, FFPE)	Yes

7 <sup>+</sup>	TNPRC	RM	11.9	SC	Brazil ZIKV Rio-U1	10,000 PFU	30	Testis, seminal vesicle, prostate (snap frozen, FFPE)	Yes
119 <sup>+</sup>	TNPRC	RM	9.8	SC	Brazil ZIKV Rio-U1	10,000 PFU	30	Testis, seminal vesicle, prostate (snap frozen, FFPE)	Yes
609	TNPRC	RM	9.8	SC	Brazil ZIKV Rio-U1	10,000 PFU	30	Testis, seminal vesicle, prostate (snap frozen, FFPE)	Yes
406	TNPRC	RM	6.7	SC	Brazil ZIKV Rio-U1	10,000 PFU	30	Testis, seminal vesicle, prostate (snap frozen, FFPE)	Yes
297402*	CNPRC	RM	5.8	IV	Plasma from RM infected with Brazil SPH2015	<12 PFU	31	Testis, epididymis, seminal vesicle, prostate (RNA later, snap frozen, FFPE)	Yes
298151	CNPRC	RM	5.4	IV	Plasma from RM infected with Brazil SPH2015	21 PFU	32	Testis, epididymis, seminal vesicle, prostate (RNA later, snap frozen, FFPE)	Yes
275240	CNPRC	RM	10	IV	Plasma from RM infected with Brazil SPH2015	2,000 RNA copies	35	Testis, epididymis, seminal vesicle, prostate (RNA later, snap frozen, FFPE)	Yes
248500	CNPRC	RM	15.3	IV	Plasma from RM infected with Brazil SPH2015	57 RNA copies	35	Testis, epididymis, seminal vesicle, prostate (RNA later, snap frozen, FFPE)	Yes
290990	CNPRC	RM	7.4	IV	Plasma from ZIKV infected human	5 PFU	36	Testis, epididymis, seminal vesicle, prostate (RNA later, snap frozen, FFPE)	Yes
262017	CNPRC	RM	11	IV	Plasma from ZIKV infected human	64 PFU	38	Testis, epididymis, seminal vesicle, prostate (RNA later, snap frozen, FFPE)	Yes
273651	CNPRC	RM	9.8	IV	Plasma from ZIKV infected human	633 RNA copies	51	Testis, epididymis, seminal vesicle, prostate (RNA later, snap frozen, FFPE)	Yes
309442 <sup>+</sup>	CNPRC	RM	4	SC	Puerto Rico PRVABC-59	1,000 PFU	60	Testis, epididymis, seminal vesicle, prostate (RNA later, snap frozen, FFPE)	Yes
318479 <sup>+</sup>	CNPRC	RM	2.8	SC	Puerto Rico PRVABC-59	1,000 PFU	60	Testis, epididymis, seminal vesicle, prostate (RNA later, snap frozen, FFPE)	Yes
42217	WNPRC	RM	10	SC	French Polynesia	1,000,000 PFU	-	Semen (snap frozen)	Yes
77560	WNPRC	RM	6	SC	French Polynesia	100,000 PFU	-	Semen (snap frozen)	Yes

**A subset of differing experimental conditions exert significant effects on ZIKV detection and histopathologic lesion severity in male macaque reproductive tissues.** We first assessed the effects of different experimental conditions, including the frequency and route of ZIKV inoculation, viral strain, dose, macaque species, administration of anti-ZIKV antibody, and immune suppression, on whether ZIKV RNA, infectious ZIKV, and microscopic lesions were detected in male genital tissues. Viremia and detection of ZIKV in male reproductive tissue were significantly associated with the dose and route (IV versus SC) of inoculation (**Supplemental Table 1**). A higher ZIKV inoculation dose resulted in higher peak viremia (Kruskal Wallis,  $p = 0.032$ ). IV inoculation was also associated with significantly higher peak viremia ( $p = 0.02$ ; 0.21, 1.89 95% confidence interval [CI]) than SC inoculation, and was 8.71 (1.52, 94.17 95% CI) times more likely than SC inoculation to result in ZIKV detection somewhere in the male reproductive tract; 13.5 (2.23, 115.66 95% CI) times more likely in the epididymis, and 6.11 (1.41, 31.35 95% CI) more likely in the seminal vesicle. Route of inoculation was not significantly associated with the likelihood of detecting ZIKV in the prostate or testis. Likewise, the IV route of inoculation was associated with a higher histology severity score in the epididymis (0.36, 1.70 95% CI) and prostate gland (0.01, 1.10 95% CI). Of the 7 animals treated with anti-ZIKV antibody, all 5 animals for whom plasma was available had detectable viremia, although peak viremia was delayed and reduced in magnitude when compared to untreated controls. Administration of anti-ZIKV antibody was also associated with a decreased likelihood of detecting of ZIKV RNA within the epididymis (Fisher's exact,  $p = 0.01$ ) and significantly lower histology severity scores within the prostate gland (simple logistic regression,  $p < 0.0001$ ). Reinoculation with a second dose of ZIKV after no infection was detected as a result of the first inoculation resulted in a higher viremia area under the curve (AUC;  $p = 0.002$ ; 10.68, 43.94 95% CI) and significantly affected histology severity

scores in sexually mature macaques, increasing the epididymis score by 1.62 (0.88, 2.6 95% CI) and the prostate gland score by 0.95 (0.30, 1.61 95% CI). Immune-suppression by CD8 T-cell depletion and viral inoculum strain (Brazil vs. Puerto Rico) did not significantly affect presence of ZIKV RNA or histology severity scores within male reproductive tissues. The limited sample size for cynomolgus (5 animals) versus rhesus (46 animals) macaques precluded statistical assessments of associations between species and the dependent variables. The experimental conditions exerting a significant effect on the dependent variables (including the presence of ZIKV RNA, infectious ZIKV and microscopic lesion severity in genital tissues) were subsequently incorporated into the appropriate logistic or linear regression model.

**ZIKV-inoculated male macaques become viremic.** A macaque was considered ZIKV-infected if viremia or ZIKV RNA was detected in any other fluid or tissue besides serum or plasma (**Table 1**). Viremia was assessed from ZIKV RNA in sera or plasma in 36 of the adult male macaques and was detected in 34 of the 36 animals. Viremia in macaques, excluding animals that were pre-treated with anti-ZIKV antibody that showed delayed and reduced magnitudes, typically lasted for 4 to 14 DPI with a peak between 4 and 8 log<sub>10</sub> RNA copies/mL and occurring, on average, at 4 to 5 DPI (**Figure 1**). Of the 15 animals for which viremia data was unavailable and the one animal without detectable viremia, ZIKV RNA was detected in at least one genital tissue or fluid (including semen) for 14 animals, confirming ZIKV infection. The single remaining rhesus macaque did not have detectable viral RNA in any fluid or tissue, so ZIKV infection could not be definitively confirmed. Viremia kinetics did not correlate with ZIKV RNA, infectious ZIKV levels, or histologic lesion severity in male genital tissues (**Supplemental Table 1**). Overall, ZIKV-

inoculated male macaques from this study become viremic with similar magnitude and duration to published data from other macaque models.

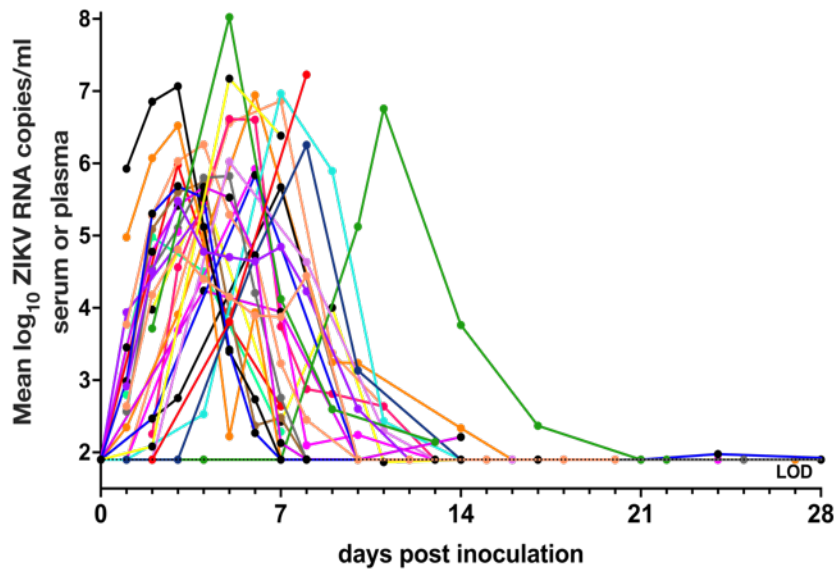


**Figure 1.** Zika virus viremia in adult male macaques lasts for 4 to 25 days post-inoculation with a peak from 4 - 8  $\log_{10}$  RNA copies/mL at 4 - 5 days post-inoculation (DPI). ZIKV RNA levels in serum or plasma, reported as mean  $\log_{10}$  RNA copies/ml and assayed in triplicate. Each line/symbol represents an individual macaque (N=36). Viremia data was not available for each of the 51 animals. Rhesus macaques

pre-treated with anti-ZIKV antibody were not included in calculations of average viremia duration and magnitude and are not shown on this graph. The dotted line denotes the average limit of detection (LOD), 1.9  $\log_{10}$  RNA copies/ml.

**ZIKV RNA is detectable in the testis, epididymis, seminal vesicle, prostate gland and/or semen of male macaques and can persist for at least 60 days.** Both ZIKV RNA and infectious virus were detected in the male macaque reproductive tract. ZIKV RNA was detected in at least one reproductive tissue or fluid including the testis, epididymis, seminal vesicle, prostate gland, or semen in 34 out of 48 macaques (71%). Overall ZIKV RNA was most frequently detected in the seminal vesicle (46%, 22/48) and epididymis (55%, 21/38), while the prostate gland (32%, 15/46) and testes (31%, 16/51) were less frequently ZIKV RNA positive (**Figure 2A**). The highest absolute magnitude of ZIKV RNA was detected in the epididymis at 31 DPI. ZIKV RNA was detected as early as 1 DPI and late as 60 DPI in the testis. The single vasectomized rhesus macaque

had detectable ZIKV RNA in all four genital tissues. Previously, 35 DPI was the longest documented duration of ZIKV RNA in male macaque genital tissues (19).

To identify the presence of infectious ZIKV in the male reproductive tract, we performed plaque assays on available frozen samples for tissues with detectable ZIKV RNA. Infectious ZIKV was detected in at least one reproductive tissue in 18 out of 27 macaque tissues (67%), as early as 4 DPI, and as late as 50 DPI in the epididymis (**Figure 2B**). Infectious ZIKV was cultured most frequently from the seminal vesicle (63%, 12/19), followed by epididymis (27%, 5/18) and testis (30%, 4/13). Infectious ZIKV was rarely cultured from the prostate gland (16%, 2/12). While both available semen samples contained detectable ZIKV RNA, there was no evidence of infectious virus in either sample.

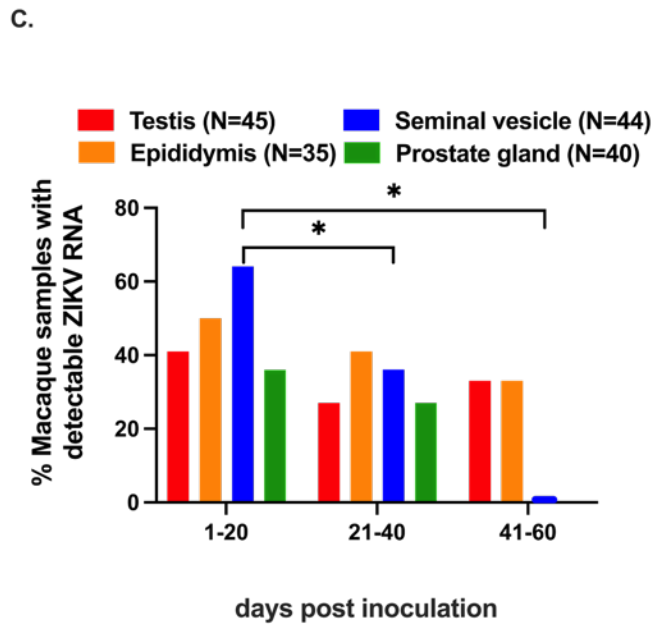
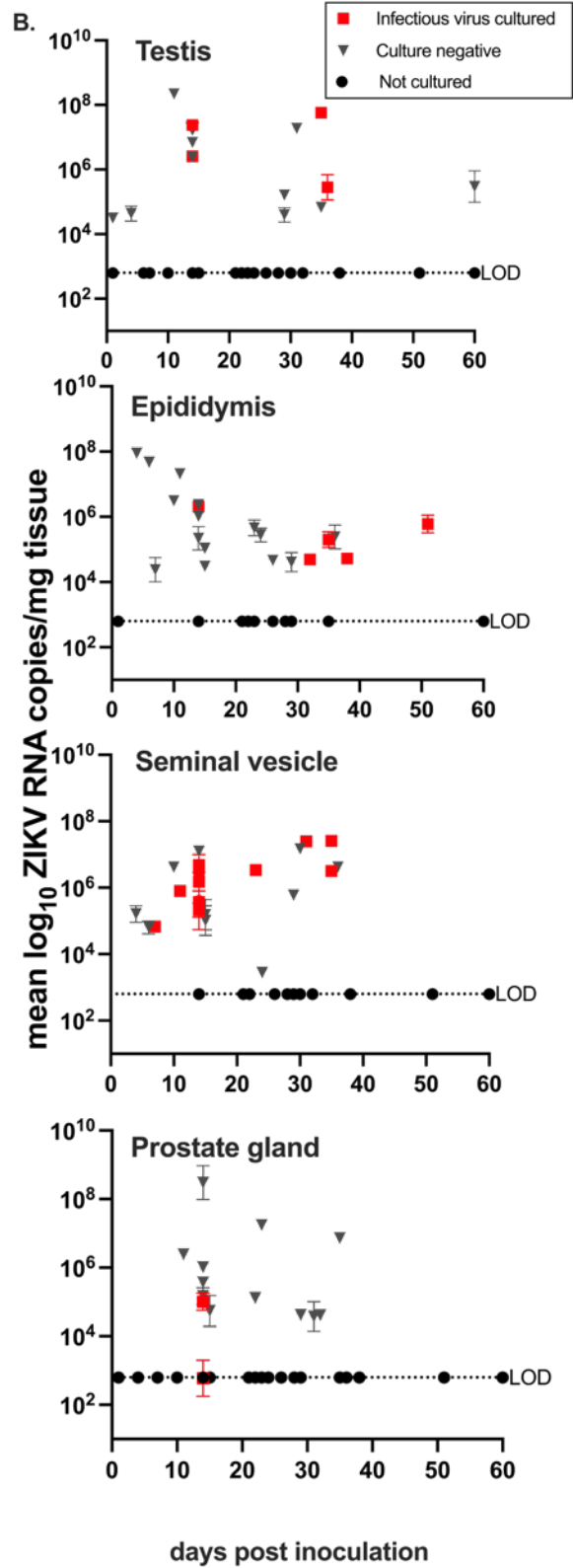
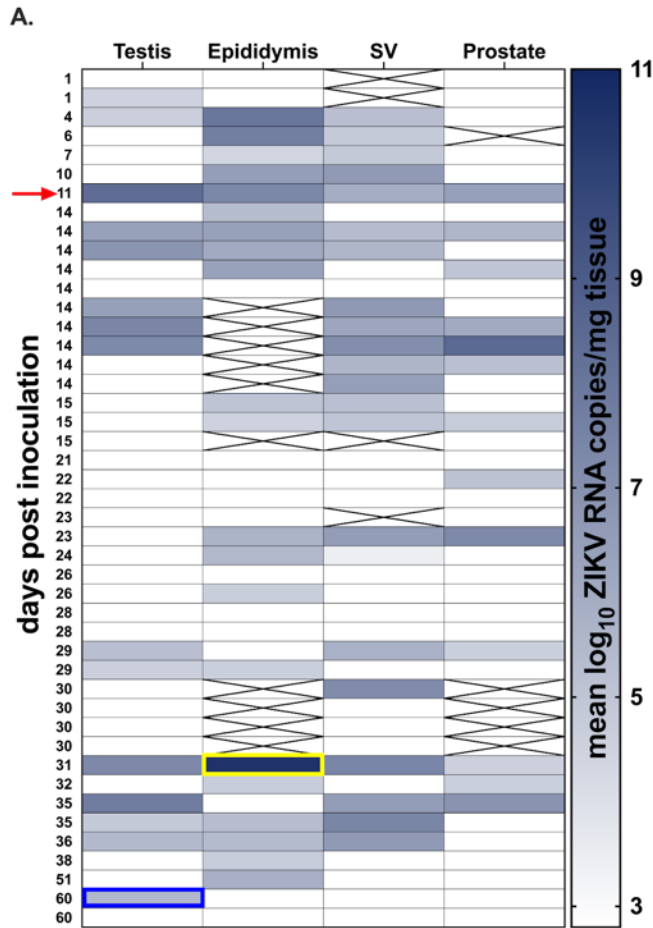


**Figure 2. ZIKV RNA and infectious virus are detected in testis, epididymis, seminal vesicle, and prostate gland of male macaques.** (A) Heatmap categorizing ZIKV RNA by male macaque genital tissue type. The color intensity correlates with the magnitude of ZIKV RNA detected by qRT-PCR and is shown as mean  $\log_{10}$  RNA copies/mg tissue. A full complement of genital tissues was not collected for every animal and tissues that were not available are crossed out. The highest absolute magnitude was detected in the epididymis (yellow box) and the latest day post inoculation of ZIKV detection occurred in the testis (blue box). There was one vasectomized macaque who had detectable ZIKV RNA in all four genital tissues (red arrow). SV is seminal vesicle. (B) ZIKV RNA levels in male macaque genital tissues, reported as mean  $\log_{10}$  RNA copies/mg tissue and assayed in triplicate with error bars showing standard deviations. Each symbol represents an individual macaque. ZIKV RNA positive samples that also contained detectable infectious ZIKV are denoted with red squares. Black triangles indicate PCR-positive samples which were negative for infectious virus. Black circles denote PCR-negative samples that were not cultured. Titers ranged from 1 - 10 PFU/mg tissue. Average LODs for ZIKV RNA and infectious virus were 2.8  $\log_{10}$  RNA copies/mg and 40 PFU/mg tissue, respectively. (C) ZIKV RNA was significantly more likely to be detected in the seminal vesicle (blue bars) at 1-20 DPI (vs. 21-40 DPI and 41-60 DPI). Mann-Whitney: ns, p value > 0.05; \*, p value < 0.05.

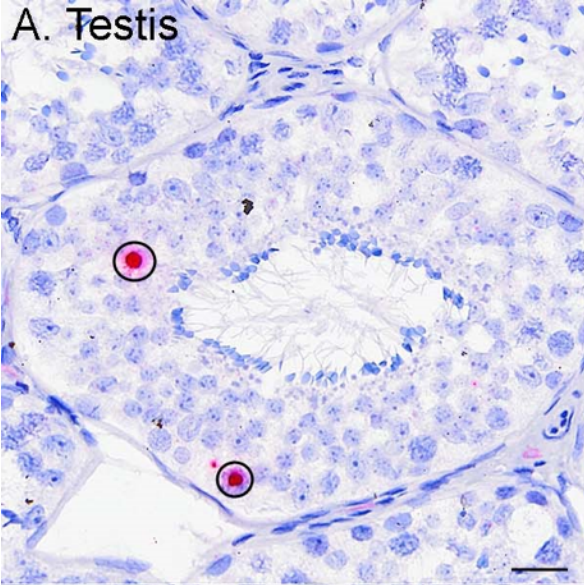
The duration of detection of ZIKV RNA in this study ranged from 1 to 60 DPI and shorter study endpoints did not correlate with detection of ZIKV RNA in all male genital tissues. However, macaques euthanized at earlier times (between 1 and 20 DPI) were significantly more likely to harbor ZIKV RNA in the seminal vesicle when compared to those euthanized between 21 and 40 DPI (Mann-Whitney,  $p = 0.02$ ) or 41 to 60 DPI (Mann-Whitney,  $p = 0.03$ ) (**Figure 2C**; **Supplemental Table 2**). Taken together, these data indicate that ZIKV can persist in multiple male genital tissues and most frequently and at the highest magnitude in the epididymis and seminal vesicle for up to 60 DPI, 1 month after the end of detectable viremia.

***In-situ* hybridization (ISH) of genital tissues from ZIKV-inoculated male macaques demonstrates ZIKV RNA in the testis, epididymis, seminal vesicle, and prostate gland.** To visualize specific cellular tropism of ZIKV, we next performed ISH on male macaque genital tissues where  $\geq 5$  RNA copies/mg tissue were detected (N = 20 sexually mature; N = 2 sexually immature). ISH staining was consistent with qRT-PCR data. All sections of sexually mature testis,

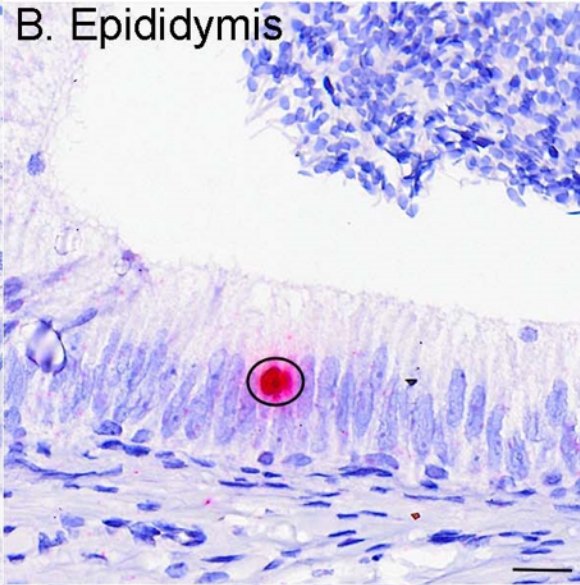
seminal vesicle, and prostate gland that contained detectable ZIKV RNA were also ISH-positive, where positivity was identified as red cytoplasmic/peri-nuclear signal. Both sexually immature animals with detectable ZIKV RNA also had ISH positive tissues. The same was generally true for the epididymis; however, epididymal tissue sections from 2 out of 17 examined samples lacked a visible ISH signal while demonstrating detectable ZIKV RNA. This may be a function of the very small tissue sample sizes, rather than a true disparity between the two RNA detection methods. No ISH signal was observed in tissues from non-inoculated macaques.

In the testis, ZIKV RNA was detected primarily within 1° and 2° spermatocytes (**Figure 3A**), spermatogonia (germ cells), and Sertoli cells (modified epithelial cells), with rare signal in interstitial Leydig cells and peri-tubular cells. For the epididymis, seminal vesicle, and prostate gland, ZIKV RNA was detected most frequently within ductal (epididymis) and glandular (seminal vesicle and prostate gland) epithelial cells (**Figure 3B-D**). In all 4 tissues, spindle cells located within interstitial or capsular connective tissue also occasionally harbored ZIKV RNA. While these cells cannot be definitively identified without special stains, they are most consistent with being migrating macrophages, fibroblasts or possibly mesenchymal stem cells based on cellular morphology and anatomic location. Overall, ZIKV demonstrated a tropism for stem-like cells and epithelial cells of the male macaque reproductive tract. ZIKV RNA was also detected in scattered macrophages associated with epididymal inflammation in 1 macaque (**Figure 3E**).

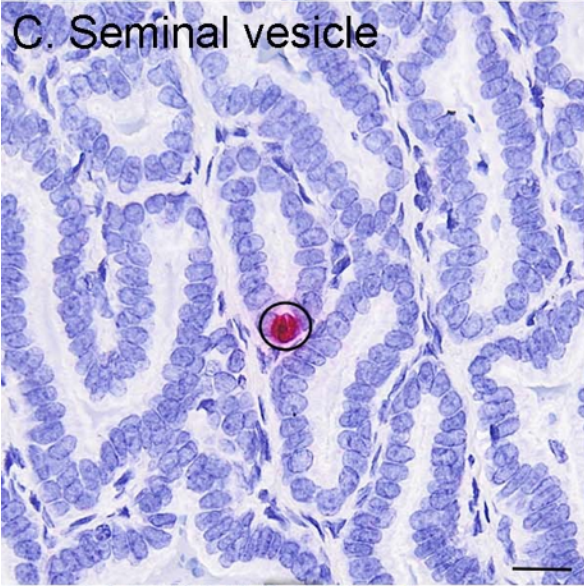
A. Testis



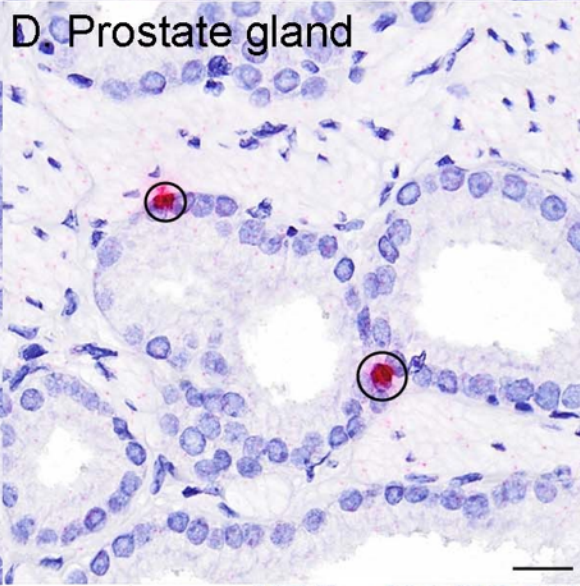
B. Epididymis



C. Seminal vesicle



D. Prostate gland



E. Epididymitis

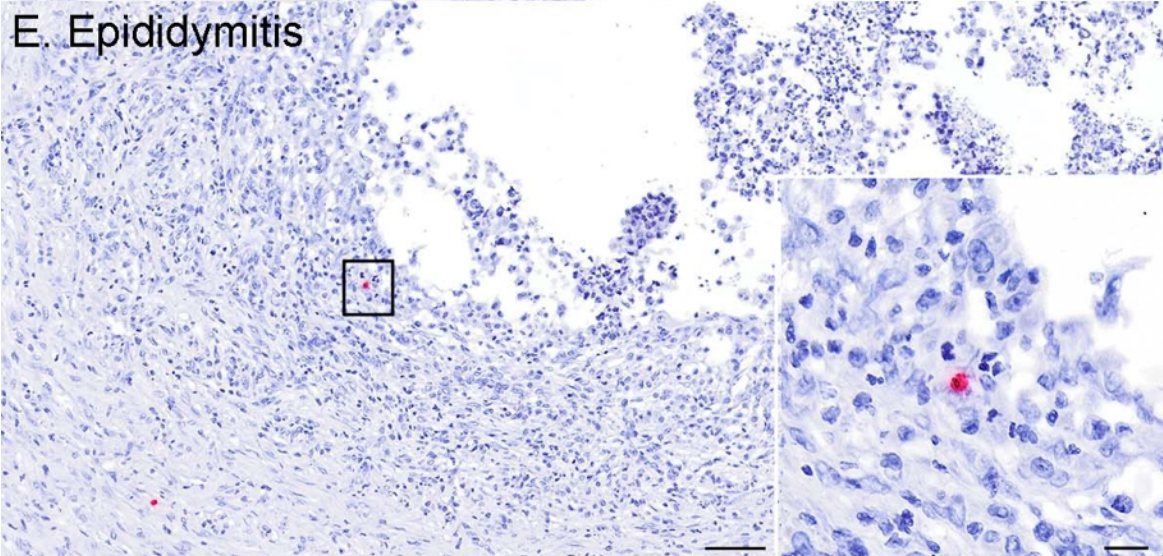


**Figure 3. *In-situ* hybridization (ISH) of genital tissues from ZIKV-inoculated male macaques demonstrates ZIKV RNA in the testis, epididymis, seminal vesicle, and prostate gland.** Photomicrographs of tissues from ZIKV-inoculated males after ISH where positive cells exhibit an intracytoplasmic/perinuclear red signal (circled). See Figure 7 for normal histology of testis, epididymis, seminal vesicle, and prostate gland. (A) Within the testis ZIKV RNA localized most frequently to sperm precursors, including germ cells, 1<sup>o</sup>/2<sup>o</sup> spermatocytes (circled), less frequently to Sertoli cells, and rarely to peritubular spindle cells and Leydig cells (images not shown here). Within the (B) epididymis, (C) seminal vesicle, and (D) prostate gland, ZIKV RNA localized primarily to ductular or glandular epithelial cells (circled). In one animal with epididymitis (E), intralesional ZIKV RNA was detected in mononuclear cells consistent with macrophages (black box denotes areas depicted in inset). In all 4 tissues, spindle cells (likely fibroblasts or migrating macrophages) located within interstitial or capsular connective tissue, also occasionally harbored ZIKV RNA (images not shown here). No ZIKV staining was observed in tissues from non-inoculated macaques (data not shown). Bar (A – D, inset) = 20  $\mu$ m; Bar (E) = 0.1 mm.

**Sexual maturity impacts detection of ZIKV in male macaque reproductive tissues.** Male macaques typically reach sexual maturity around 4 years of age (12,25). Here, 29 out of 36 (81%) sexually mature macaques older than 4 years inoculated with ZIKV had detectable viral RNA in at least one reproductive tissue or fluid, versus just 6 out of 14 (43%) sexually immature macaques. ZIKV RNA was detected more frequently within the reproductive tract of sexually mature male macaques (**Figure 4A, Supplemental Table 2**) (logistic regression,  $p = 0.004$ ), and specifically in the epididymis (logistic regression,  $p < 0.0001$ ) and seminal vesicle (logistic regression,  $p = 0.0005$ ) (**Figure 4B**). Similarly, infectious ZIKV was cultured exclusively from male genital tissues of sexually mature macaques. We also assessed effects of sexual maturity on absolute ZIKV RNA magnitude (mean RNA copies/mg tissue); however, due to relatively low Ns and lack of normality, the model resulted in a better fit when overall ZIKV RNA presence or absence in genital tissues was assessed instead. These data demonstrate that sexually mature male macaques are significantly more likely to harbor ZIKV RNA and/or infectious virus somewhere in the reproductive tract.

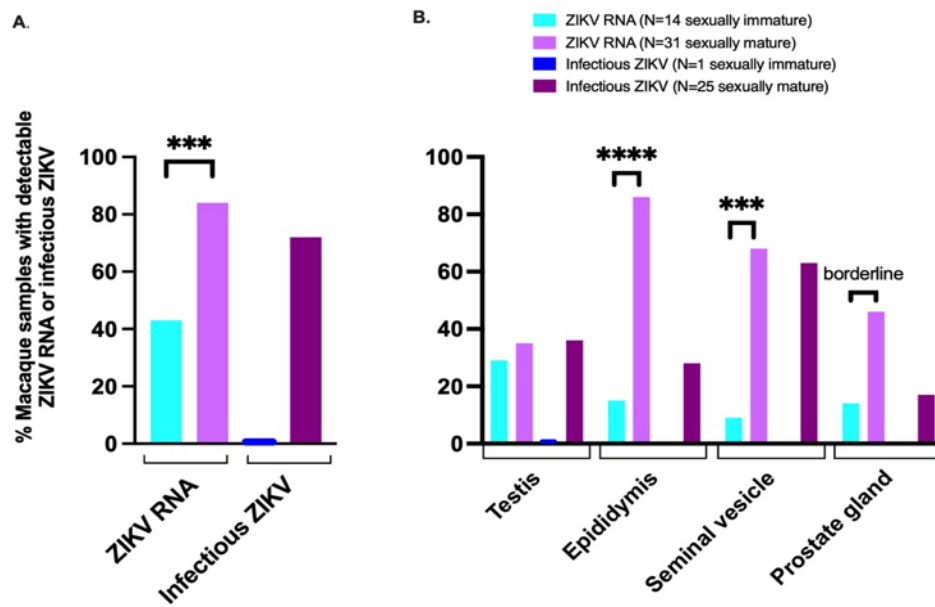


**Figure 4. Sexually mature male macaques are more likely to harbor persistent ZIKV RNA and infectious virus in at least one genital tissue (A), in the epididymis and seminal vesicle (B). Only one tissue (testis) from a sexually immature macaque had detectable ZIKV RNA and no infectious virus was cultured; statistical**

tests were not performed on infectious ZIKV data. Sexually immature = 0 - 4 years old; sexually mature = > 4 years old. Logistic regression: ns, p value > 0.08; borderline, p value between 0.05 and 0.08; \*, p value ≤ 0.05; \*\* p value ≤ 0.01; \*\*\*, p value ≤ 0.001; \*\*\*\*p value ≤ 0.0001.

**ZIKV inoculation of sexually mature male macaques is associated with microscopic lesions in the epididymis and prostate gland.** Overall, histopathologic lesions were relatively uncommon within the reproductive tract of male macaques inoculated with ZIKV. When present, histopathologic lesions in testis, epididymis, seminal vesicle, and prostate gland were scored according to quantitative criteria (**Supplemental Table 3**). Sexually mature ZIKV-inoculated male macaques had significantly higher severity scores than uninfected, age-matched controls in the epididymis (Mann-Whitney,  $p = 0.02$ ) and prostate gland (Mann-Whitney,  $p < 0.001$ ) (**Figure 5A**). Similarly, sexually mature ZIKV-inoculated macaques had significantly more severe microscopic lesions than sexually immature ZIKV-inoculated macaques in the epididymis (linear regression,  $p = 0.02$ ), and prostate gland (linear regression,  $p = 0.0001$ ). No significant lesions were noted in the seminal vesicle. As with ZIKV RNA, macaques euthanized at earlier timepoints

(between 1 and 20 DPI) were more likely to have significant microscopic lesions resulting in higher histology scores in the epididymis and prostate gland when compared to those euthanized between 21 and 40 DPI (Mann-Whitney,  $p = 0.01$  and  $p = 0.02$ , respectively) or 41 to 60 DPI (Mann-Whitney,  $p = 0.08$  trend and  $p = 0.05$ , respectively) (**Figure 5B, Supplemental Table 2**).

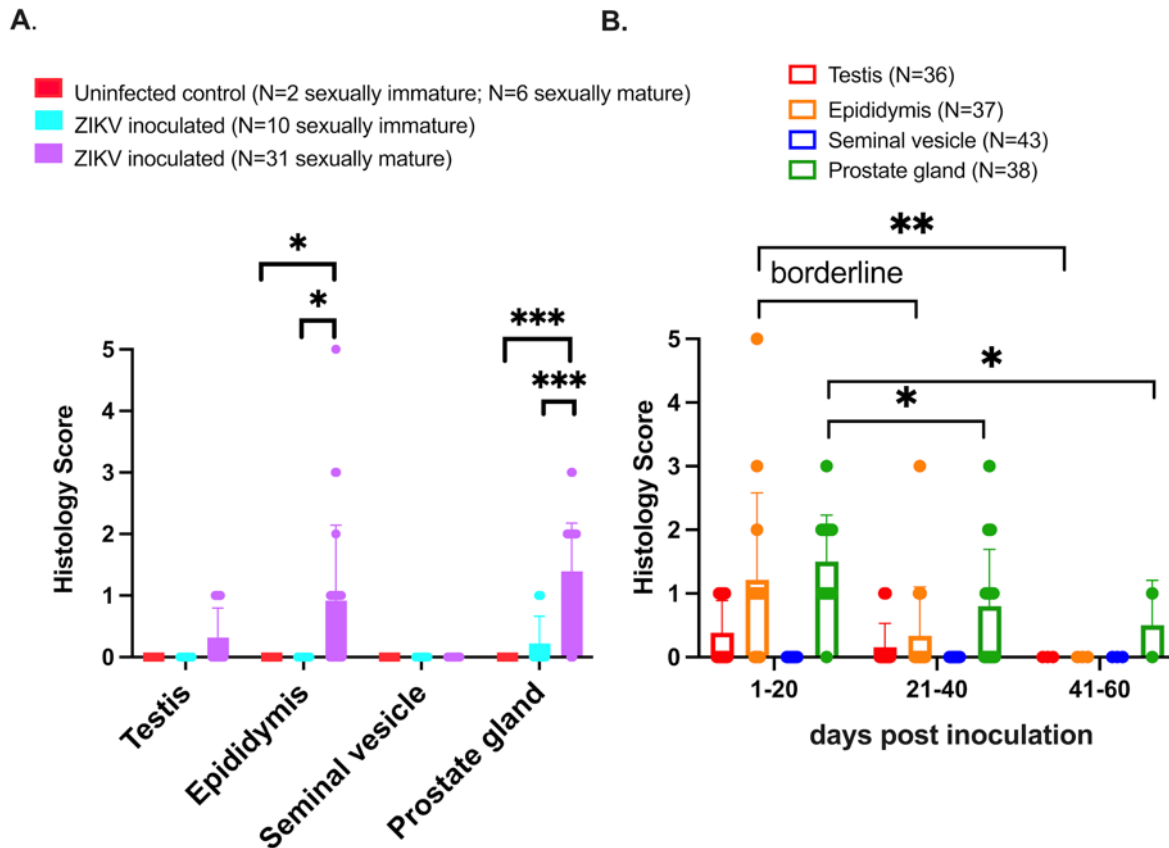


**Figure 5. Sexual maturity and duration of ZIKV infection impact histopathologic lesion severity in male macaque reproductive tissues.** Macaque genital tissues were scored histologically from 0 (normal) to 5 (markedly abnormal). **(A)** Pathology severity scores for sexually mature and immature ZIKV-inoculated male macaques and uninfected, age-matched controls **(B)** Pathologic lesions were more likely to occur between 1 and 20 DPI in the epididymis and prostate gland (vs. 21 - 40 and 41 - 60 DPI). Each dot represents an individual macaque. Bars show the mean histology score, and error bars show standard deviation. Sexually immature = 0 - 4 years old; sexually mature = > 4 years old. Mann-Whitney: ns,  $p$  value > 0.08; borderline,  $p$  value between 0.05 and 0.08; \*,  $p$  value  $\leq 0.05$ ; \*\*,  $p$  value  $\leq 0.01$ ; \*\*\*,  $p$  value  $\leq 0.001$ .

Sporadic epididymal and prostatic inflammation were noted exclusively within sexually mature males. Three out of 25 sexually mature macaques exhibited epididymal microscopic lesions with a histology severity score of  $\geq 3$ . Lesions ranged from mild lymphohistiocytic periductal infiltrates to severe pyogranulomatous epididymitis with duct rupture, multinucleated giant cells containing engulfed spermatozoa, multifocal mineralization, fibroplasia, and sperm stasis with dilated/tortuous epididymal ducts (**Figure 6A, B**). This correlates with the virology data reported above, where macaques with detectable ZIKV RNA in the epididymis exhibited higher histology scores indicative of more severe lesions than those without detectable virus (linear regression,  $p = 0.01$ , **Supplemental Table 2**).

The most common histologic finding in the prostate gland was mild to moderate prostatic inflammation (4/28 animals) characterized by periglandular aggregates of lymphocytes, macrophages, and scattered neutrophils. Affected glands were often expanded by sloughed cells, necrotic debris, neutrophils, and macrophages (**Figure 6C, D**). While both ZIKV RNA and infectious virus were frequently detected within the seminal vesicle, no significant microscopic lesions were noted in this tissue in ZIKV-inoculated animals. There was variably severe mineralization of secretory product; however, this was also present in control tissues and is a very common, clinically insignificant background lesion in the seminal vesicle of sexually mature macaques (26).

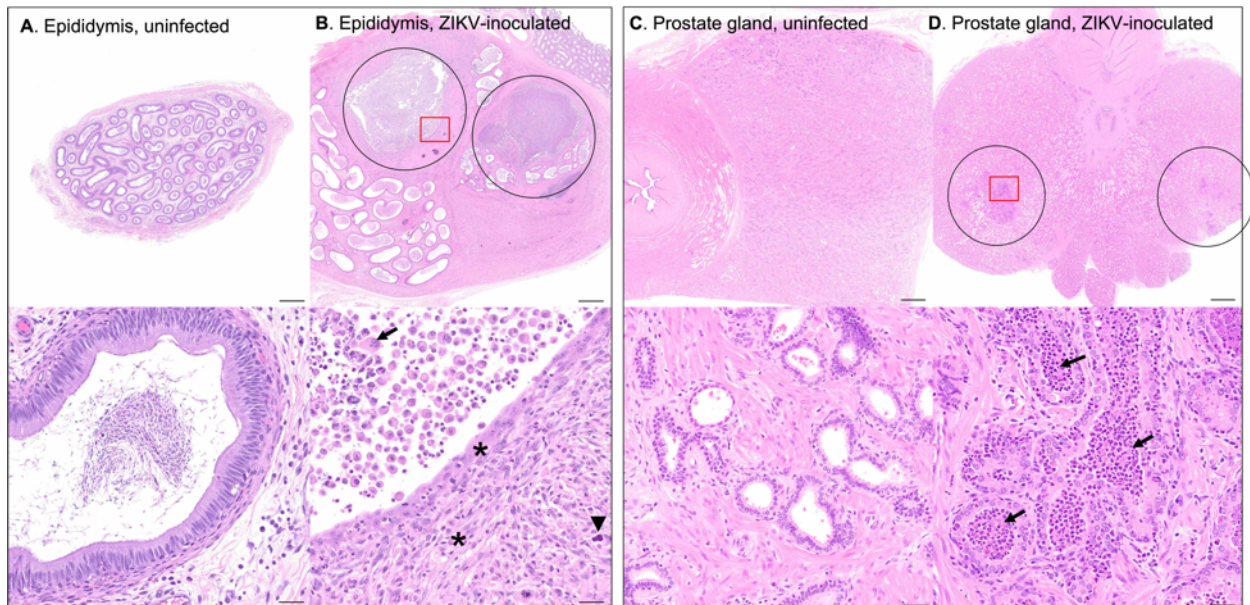


**Figure 6. Photomicrographs of H&E-stained genital tissues from uninfected & ZIKV-inoculated male rhesus macaques** (A) Normal epididymis from an uninfected control animal. (B) Epididymis from a ZIKV-inoculated rhesus macaque with duct rupture and pyogranulomatous epididymitis (circled). Remaining epididymal ducts are dilated and tortuous with sperm stasis. In the 20X image (lower panel, area denoted by red box in upper panel) normal duct epithelial architecture is lost with replacement by fibroplasia (asterisks) and mineralization (arrowhead) with neutrophils, multinucleated giant cells (arrow), and necrotic debris. This correlates with virology data, where macaques with detectable epididymal ZIKV RNA exhibited higher histology scores than those without detectable virus (data not shown, linear model,  $p = 0.008$ ). (C) Normal prostate gland from an uninfected control animal. (D) Prostate gland from a ZIKV-inoculated macaque with mild to moderate prostatitis (circled). In the 20X image (lower panel, area denoted by red box in upper panel) glandular lumens are expanded or replaced by sloughed cells, necrotic debris, neutrophils, and macrophages (arrows). Scale bars: upper images 1mm; lower images 20  $\mu\text{m}$ .

Microscopic evaluation of macaque testes was complicated by using conventional formalin fixation (where special fixatives are preferred) (27), lack of serial sectioning, small sample size, poor preservation and/or crush artifact in some samples (N = 6 samples of testis, which were discarded for data analysis). Furthermore, rhesus macaques, in contrast to cynomolgus macaques, are seasonal breeders (27), which results in reduced spermatogenesis and low hormone levels out of season (28). As a result of these complicating factors, only significant testicular lesions, including inflammation, necrosis, or evidence of sperm stasis (as evidenced by luminal aggregation of spermatozoa within seminiferous tubules or rete testes and/or luminal macrophages

with engulfed spermatozoa) were scored for statistical analyses. Using these criteria, testicular lesions were uncommon and mild in ZIKV-inoculated animals.

In summary, we identified a significant association between ZIKV-infected, sexually mature male macaques and pathologic microscopic lesions in the epididymis and prostate gland, predominantly between 1 and 20 DPI, that were absent in non-infected animals.

## **Discussion**

In this study, we investigated a poorly understood aspect of human ZIKV infection. We evaluated role of the male reproductive tract in the context of viral persistence in genital tissues, potential for sexual transmission, and microscopic lesions with their probable effects on fertility. This study further emphasizes the utility and relevance of macaque models of ZIKV infection, as we were able to evaluate archived reproductive tissue samples from more than 50 male macaques, which are generally very difficult to obtain from ZIKV-infected men. Intravenous or subcutaneous inoculation of Brazilian or Puerto Rican ZIKV of male rhesus and cynomolgus macaques produced asymptomatic infection with viremia lasting from 4 to 14 DPI and peaking at 4 to 5 DPI. These findings are consistent with those from adult, non-pregnant ZIKV-infected humans (29,30), as well as published data from NHP models of ZIKV infection (14–16,19,31–33).

Our findings, including the detection of both ZIKV RNA and infectious virus in male macaque genital tissues, and ZIKV RNA (but not infectious virus) in the two available semen samples, support the hypothesis that male reproductive tract serves as a reservoir for ZIKV (34). Our findings are also consistent with published data in NHP, which, while sparse, have demonstrated

ZIKV RNA in macaque semen for up to 28 DPI (31), and in the testis (18,31), seminal vesicle (19,31), and prostate gland (19,31,35) from 4 to 35 DPI, frequently after the resolution of viremia. We detected ZIKV RNA most frequently in the epididymis and seminal vesicle, with the highest absolute magnitude occurring in the epididymis. A higher peak ZIKV viremia, larger viremia AUC, and detection of ZIKV RNA in the epididymis and seminal vesicle correlated with sexual maturity in macaques. Infectious ZIKV was cultured from at least one genital tissue, most frequently in the seminal vesicle and epididymis, in 38% (18/48) of ZIKV-inoculated macaques. ZIKV RNA persisted in male macaque genital tissues for up to 60 DPI, about 6 weeks after the resolution of viremia at 14 DPI in most animals in this study. Our results extend knowledge on the duration of persistence since 35 DPI was the longest previously documented duration of ZIKV RNA in male macaque genital tissues (19). As 60 DPI was the latest time point assessed in this study; it is possible that persistence of ZIKV RNA in male macaque genital tissues may be even more prolonged. This finding suggests that the potential for sexual transmission of ZIKV remains even after viremia has resolved, which raises significant concerns regarding the risks of male sexual transmission to both men and periconceptional and non-pregnant women, as well as in the context of assisted fertility procedures such as sperm donation. Except for one reported case of congenital Zika syndrome arising from sexual transmission of ZIKV from an infected man to his naïve, pregnant wife (24), the relationship between sexual and vertical transmission from mother to fetus is poorly understood, and further studies are needed.

Semen obtained from symptomatic convalescent men can harbor both ZIKV RNA and infectious virus after the resolution of viremia (36–38). The latest documented report of human sexual transmission was 44 days after the onset of symptoms (39). It is unclear whether the absence of

infectious virus from semen samples in the present study denotes a lack of transmission potential, prior infection followed by clearance below the limit of detection, or a methodological artifact of infectious virus decay after a freeze-thaw cycle that would result in a false negative in a sample of low titer. Unfortunately, metadata (including age, ZIKV strain/dose, route of inoculation, and duration of infection) were unavailable for the animals from which these samples were collected, so it is possible that viral migration to the male reproductive tract occurred early during infection, and by the time of necropsy, when a “snapshot” is taken, ZIKV RNA or infectious virus levels declined to low or undetectable levels.

The male ejaculate is composed of both cellular and fluid components. The cellular component comprises spermatozoa, and white blood, desquamated germ, and epithelial cells. The fluid component contains secretions from accessory sex glands, primarily the seminal vesicle and prostate gland, and to a lesser extent, the bulbourethral gland and epididymis (**Figure 7**). Either or both components could harbor infectious ZIKV and contribute to sexual transmission. Published data regarding specific cellular tropisms of ZIKV are somewhat conflicting, as detailed below. *In vitro* studies using human cells have variously demonstrated that primary testicular germ cells (41–43), Sertoli cells (42–46), peritubular myoid cells (43), epididymal epithelial cells (47), fibroblasts (42), and epithelial and mesenchymal stem cells of the prostate gland (48) are susceptible to ZIKV infection. Following ZIKV inoculation of *ex vivo* testicular explants, macrophages, and peritubular cells are most frequently infected, with fewer Leydig and Sertoli cells infected (34). ZIKV inoculation of human testicular organoids (HTO) results in productive ZIKV infection, with decreased HTO survival and reduced expression of spermatogonial, Sertoli, and Leydig cell markers (49). *In vivo* studies using immunodeficient mice have similarly demonstrated virus

localization to sperm precursors (20), Sertoli cells (20,50), interstitial Leydig cells (20,22), epididymal epithelium (22,50–53), prostatic epithelium (35), and the cell-free seminal plasma fraction of the murine ejaculate (50), from 3 to 33 DPI (51–53).

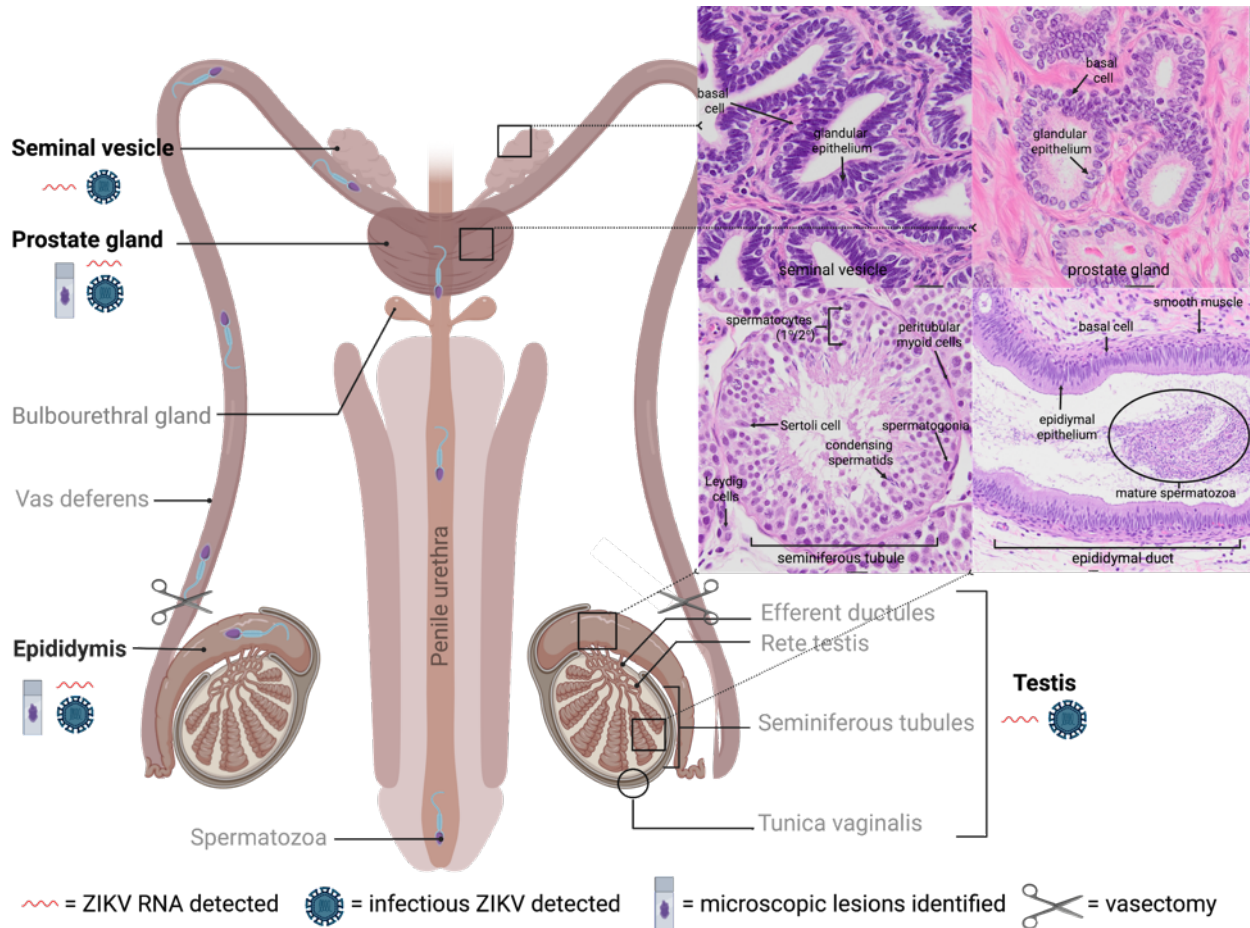


**Figure 7. Normal anatomy and histology of the sexually mature male primate reproductive tract with summary of results.** Tissues that were sampled are in bold. Insets (denoted by black boxes on diagram) depict normal microscopic features of each tissue. Mature spermatozoa develop in stages from germ cells (spermatogonia) in testicular seminiferous tubules (supported by Sertoli cells), undergo maturation and storage in the ducts of the epididymis, and travel via the vas deferens through the accessory sex glands and into the urethra for ejaculation (75,76). Both ZIKV RNA and infectious virus were detected in the testis, epididymis, seminal vesicle, and prostate gland. Microscopic lesions were noted in the sexually mature epididymis and prostate gland. Created with BioRender.com.

Viral antigen was identified in mature spermatozoa from the semen sample of a ZIKV-infected man (54), and ZIKV shedding in human semen has been shown to correspond with the duration required for the human spermatogonial life cycle, which is approximately 74 days (55). Infectious virus and ZIKV RNA have been isolated from the semen of vasectomized men for up to 69 and 96 days after symptom onset, respectively (56,57) ZIKV RNA and infectious virus levels are significantly reduced in vasectomized versus non-vasectomized ZIKV-infected men (38). The single vasectomized rhesus macaque in the present study had detectable ZIKV RNA in all 4 genital tissues, and infectious virus was cultured from the seminal vesicle (semen was not available from this animal). A vasectomy is a surgical sterilization procedure that entails cutting the vas deferens to prevent sperm from leaving the epididymis and entering the male ejaculate (58). Detection of ZIKV within semen and/or accessory sex glands of vasectomized males suggests that infected spermatozoa are not required for sexual transmission and that infectious cells/fluids from the seminal vesicle and/or prostate gland may also play a significant role in sexual transmission. Furthermore, mature spermatozoa lack endoplasmic reticula, Golgi apparatus, and tRNAs and are considered transcriptionally inactive (59) and therefore could not be expected to be infected with and produce ZIKV.

Results from *in vitro* and *in vivo* experiments as well as observations in humans suggest that chronic ZIKV infection in males could result in sexual transmission of virus; however, while germ cells and later sperm precursors harbor ZIKV, mature spermatozoa are probably not the only source of infectious ZIKV in semen or the sole contributor to sexual transmission. Rather, epididymal epithelial cells, leukocytes like macrophages, and other transcriptionally active cells are more probable sources of replicating ZIKV in semen and likely play a crucial role in sexual

transmission of ZIKV (52). Our results support this conclusion. Using ISH we showed that, in addition to testicular germ cells and 1<sup>o</sup>/2<sup>o</sup> spermatocytes, ZIKV RNA localized to macaque Sertoli cells (which are modified epithelial cells), epididymal epithelial cells, and glandular epithelial cells within the seminal vesicle and prostate gland during both acute and chronic stages of disease. Taken together, our findings and published data suggest that ZIKV is capable of breaching blood-testis and/or blood-epididymal-barriers to replicate in multiple cell types and persist in the male reproductive tract, though specific mechanisms by which ZIKV enters these cells and establishes persistence remain undefined. Additionally, our observation that ZIKV RNA localized most frequently to testicular stem-like cells including germ cells and spermatocytes is in agreement with previous macaque studies demonstrating an apparent viral preference for stem cells, such as fetal neural precursor cells in macaque fetuses exposed to ZIKV prenatally (60).

ZIKV is clearly gonadotropic in men, but information regarding genitourinary sequelae and effects on fertility are lacking in both humans and animal models of human ZIKV infection. Hematospermia, prostatitis, painful ejaculation, penile discharge, dysuria, low sperm counts and sperm motility issues are occasionally reported in ZIKV-infected men (9,10,61,62); however, human data remain sparse, as obtaining genital biopsy specimens from men is invasive and not typically performed without a significant medical reason (63). Up to 80% of ZIKV-infected humans remain asymptomatic, and gauging the true prevalence of ZIKV in semen, understanding associated viral kinetics, recognizing factors influencing male sexual transmission, characterizing male genitourinary lesions, and identifying potential effects on fertility and risk factors associated with sperm donation and assisted fertility procedures have proven quite difficult (9).

In the present study, microscopic lesions were relatively uncommon in the reproductive tract of ZIKV-inoculated male macaques; however, microscopic lesion severity scores for both the epididymis and prostate gland were significantly higher in sexually mature ZIKV-inoculated male macaques versus uninfected, age-matched controls and ZIKV-inoculated, sexually immature animals. Specifically, ZIKV-inoculated sexually mature macaques exhibited sporadic, variably severe epididymitis and/or prostatic inflammation. Statistically, the macaques with detectable ZIKV RNA in the epididymis exhibited significantly higher histology scores than those without detectable virus. These findings further underscore the potential importance of the epididymis in the context of ZIKV persistence and shedding, sexual transmission, and associated genitourinary pathology.

The occasionally noted moderate to severe epididymitis associated with a detectable ISH signal within these ZIKV-inoculated macaques is suggestive of possibly ZIKV-induced epithelial damage. With subsequent epididymal duct rupture and exposure of luminal contents including sperm to the surrounding tissue, a severe inflammatory response (sperm granuloma) ensues. Epididymitis in primates has several documented etiologies, including sexually transmitted or ascending urinary bacterial or fungal infections, trauma/obstruction and, less commonly, viral infection as caused by orthorubulaviruses (mumps), adenoviruses, or enteroviruses (65). Prostatic periglandular and/or perivascular lymphocytic infiltrates are common, clinically insignificant background findings in macaques, however, the presence of neutrophilic inflammation and necrotic debris, as seen here, are not (26). As noted for epididymitis, ascending bacterial infection associated with recurrent urinary tract infection is the most frequently reported cause of prostatitis in humans (66). The same is likely also true in macaques, although prostatic inflammation is much

less common in NHP (67). Although ascending bacterial infection is a more commonly reported cause of both epididymitis and prostatitis than viral infection (65), the macaques in this study lived controlled environments, underwent regular physical examinations and blood work, and exhibited no evidence of trauma or infection (other than ZIKV) at necropsy or by microscopic evaluation. While we cannot definitively prove causation, there is an association between ZIKV and histologic genital lesions which warrants further study. Furthermore, epididymitis is associated clinically with male infertility (65), and chronic prostatitis in humans is a well-known precursor to prostatic carcinoma (68), so developing a thorough understanding of potentially ZIKV-induced pathologic lesions can inform long-term implications for the health of men in ZIKV-endemic regions. Further study, including detailed analysis of semen from ZIKV infected macaques and humans, is necessary.

Sexual maturity also had a significant effect on our results. Sexually mature male macaques were more likely to harbor persistent ZIKV in the reproductive tract, particularly in the epididymis or seminal vesicle. Furthermore, significant histopathologic lesions only occurred in sexually mature male macaques inoculated with ZIKV. The explanation for this observation likely relates to anatomic and physiologic differences between sexually immature and mature males, such as the types and relative differentiation of cells present in genital tissues and accessory sex glands, receptor expression, and/or hormone production. In contrast to the post-pubertal macaque testis, sexually immature seminiferous tubules possess smaller diameter lumens and contain only Sertoli cells and undifferentiated spermatogonia (12). Epididymal ducts are similarly reduced in diameter, lined by small, flattened epithelial cells, and surrounded by increased fibrous connective tissue

(12). Glands of the sexually immature seminal vesicle and prostate gland are also narrowed, lack luminal secretions, and are lined by low cuboidal to flattened epithelial cells (12).

A major limitation of this study is that, despite having data from more than 50 animals, macaques were from different experiments which were not designed specifically for the analysis presented here. As a result, statistical adjustments for multiple experimental conditions and robust parametric statistics were not possible due to the violation of normality assumptions. As such, we used non-parametric statistics (except for ordinal regression). Although some confidence intervals are large, our results suggest relationships between the experimental conditions analyzed, and as such, could support future research.

In conclusion, we show here that the male macaque reproductive tract serves as a reservoir for ZIKV RNA and infectious virus, that epithelial cells and mesenchymal/stem cells of the testis, epididymis, seminal vesicle, and prostate gland can harbor ZIKV RNA, and that ZIKV infection is associated with microscopic lesions in the epididymis and prostate gland. The immune-privileged, inherently immunosuppressive nature of the testes and epididymis (69) likely promotes ZIKV persistence and sexual transmission of infectious virus beyond the acute stage of infection. Overall, sexually mature males are at significantly higher risk for genital ZIKV persistence and urogenital sequelae, though mechanisms of viral entry into the male reproductive tract and the pathogenesis of injury to genital tissues remain unclear. Taken together, our results support the hypotheses that 1) the male genital tissues including accessory sex glands such as the seminal vesicle and prostate gland serve as a reservoir and probable replication site for ZIKV, and 2) that genital lesions and impaired male fertility are possible, if not likely, sequelae to ZIKV infection.

Furthermore, our identification of ZIKV RNA in frozen semen samples, and detection of ZIKV RNA and infectious virus in frozen genital tissue samples (for up to 60 DPI and 50 DPI respectively), has significant implications for the safety of assisted fertility procedures involving donated reproductive tissues such as sperm, oocytes and embryonic tissue, where ZIKV screening and testing is recommended but not required by the U.S. Food and Drug Administration and is performed at the discretion of individual clinics (23,70).

By extrapolating our findings from ZIKV-infected macaques, we can increase our understanding of persistent ZIKV infection in men. This was an opportunistic study as our research team leveraged archived macaque tissues originating from multiple different studies where the animals were exposed to variable experimental conditions. Additional, controlled experiments are clearly needed, particularly to define: 1) mechanisms of viral entry into the male reproductive tract; 2) effects of ZIKV infection on the histomorphology of genital tissues and fertility, including detailed analysis of semen, in sexually mature ZIKV-infected males; and 3) the relationship between sexual transmission to naïve periconceptional woman and risks of vertical transmission to the fetus.

## **Methods**

**Study Design.** The tissues evaluated in this study were from healthy male rhesus (*Macaca mulatta*) and cynomolgus (*Macaca fascicularis*) macaques, born at their respective National Primate Research Centers (**Table 1**). All studies were approved by the appropriate Institutional Animal Care and Use Committees (IACUC). Archived reproductive tissues, including testes, epididymis, seminal vesicle, and prostate gland, from 51 ZIKV-infected and 8 age-matched, uninfected, male rhesus and cynomolgus macaques from past or ongoing collaborative research projects were kindly

donated by the California (N = 35) (14,32,33), Tulane (N = 10) (71), Wisconsin (N = 6) (72,73), and Washington (N = 1 uninfected control rhesus macaque) NPRCs. These animals, aged 2 to 15 years old, were inoculated IV or SC with variable ZIKV strains and doses, humanely euthanized, and necropsied at 1 to 60 DPI. When possible, testis, epididymis, seminal vesicle, and prostate gland were examined; however, a full complement of genital tissues was not collected from each animal. Among rhesus macaques from the CNPRC, 9 animals that failed to become viremic upon initial inoculation were reinoculated, and 4 animals were immune suppressed via CD8+ T-cell depletion 4 weeks after inoculation to evaluate the potential for viremia resurgence, which did not occur. Plasma/serum and or viremia data was available from only a subset of these animals (N = 36). Uninfected, age-matched control tissue was obtained from colony management culls at the California and Washington NPRCs.

**Necropsy, tissue collection and histopathology.** All necropsies were performed by a board-certified veterinary pathologist and 1 to 2 technicians. Macaques were euthanized with an overdose of sodium pentobarbital. The veterinary pathologist evaluated each tissue *in situ* prior to excision. Technicians trimmed each tissue using separate forceps and razor blades to minimize risks for cross-contamination. Male reproductive tissues, including testis, epididymis, seminal vesicle, and prostate gland were collected. Tissues were collected for viral analyses in RNAlater (Thermo Fisher Scientific, Waltham, MA) according to the manufacturer's instructions. Extra available samples were snap-frozen and stored at -70°C. Tissues for histopathology were preserved in 10% neutral-buffered formalin (Thermo Fisher Scientific), paraffin-embedded, thin sectioned (5 µm), routinely stained with hematoxylin and eosin (H&E) and evaluated by a board certified veterinary

anatomic pathologist, generating a cumulative abnormality score from 0 (normal) to 5 (markedly abnormal) (**Supplemental Table 3**).

**Isolation and quantification of viral RNA from plasma and male genital tissues.** ZIKV RNA was isolated from samples and measured in triplicate by qRT-PCR according to methods described previously (14). Briefly, EDTA-anticoagulated whole blood was centrifuged for 10 minutes at 800 g and the resulting plasma fraction was stored at -70°C. RNA was extracted from plasma according to the manufacturer's instructions using the MagMAX Express-96 Deep Well Magnetic Particle Processor (Thermo Fisher Scientific). Solid tissues frozen in RNAlater (including frozen samples of whole semen) were thawed and homogenized to a liquid state using a 5 mm steel ball, Qiazol lysis reagent and the Qiagen/Retsch TissueLyser II (all from Qiagen, Germantown, MD). RNA was extracted from homogenized tissue supernatants using the viral RNA universal mini kit (Qiagen) or the automated QIAcube (Qiagen). All RNA extracts were eluted in 60 µL of diethyl pyrocarbonate (DEPC)-treated water for storage at -70°C prior to quantification and were tested in triplicate using an Applied Biosystems ViiA 7 RT-qPCR machine (Thermo Fisher Scientific). Viral RNA levels were calculated in RNA copies by comparing the average of each triplicate from a sample to the standard curve generated with each PCR plate. Levels of ZIKV RNA in samples are expressed as mean  $\log_{10}$  RNA copies per mL fluid or mg tissue. The limit of detection (LOD) varied depending on the volume/weight of tissue sampled and volume of Qiazol needed to homogenize to liquefaction, with means of 1.9  $\log_{10}$  RNA copies/mL and 2.8  $\log_{10}$  RNA copies/mg tissue. A sample was considered positive when 2 of 3 or all 3 replicates yielded an RNA copy value. When a sample exhibited an inconsistent qRT-PCR signal (1 of 3 replicates positive) retesting was performed, generally on a different aliquot, if available. If the retest result was

negative (3 of 3 replicates), the sample was considered negative. If 1 of 3 replicates remained positive but was within 1 log<sub>10</sub> RNA copies/mg tissue or mL fluid of the LOD, the sample was also considered negative.

**Infectious Zika virus quantification by plaque assay.** Infectious ZIKV was detected using a Vero cell (American Type Culture Collection, Manassas, VA) plaque assay, as described previously (14). Briefly, confluent 12-well Vero plates were inoculated with 250 µL of 1:10 and 1:20 dilutions of macaque tissue homogenate in Dulbecco's Modified Eagle Medium (DMEM) (Thermo Fisher Scientific) supplemented with 2% fetal bovine serum and allowed to adsorb at 37°C for 1 hour. After incubation, each cell monolayer was overlaid with 1 ml 0.4% agarose (liquefied 10% agar, ultrapure agarose [Invitrogen, Carlsbad, CA] diluted in 42°C DMEM) and allowed to solidify. The plates were incubated at 37°C for 7 days. Cell monolayers were then fixed with 4% formalin for 30 minutes, agar plugs were gently removed, and viable cells were stained with 0.05% crystal violet (Sigma, St. Louis, MO) in 20% ethanol. Plaque assays were only performed on tissues that tested positive via qRT-PCR and were not performed on samples that contained less than 3 log<sub>10</sub> genomes/mg tissue since our previous work showed those samples were not likely to contain infectious ZIKV. Two replicate titrations were performed for each sample, the number of plaques per plate was averaged, and results were reported as ‘presence’ or ‘absence’ of infectious virus. The limit of detection of the assay was 40 PFU/mg tissue.

**Viral RNA detection by *in-situ* hybridization (ISH).** Colorimetric *in-situ* hybridization (ISH) was performed manually on superfrost plus slides (Thomas Scientific, Swedesboro, NJ), according to the manufacturer’s instructions (74), using the RNAscope 2.5 HD Red Reagent Kit (Advanced

Cell Diagnostics, Newark, CA) and RNAscope Probe V-ZIKVsph2015 (Advanced Cell Diagnostics). Briefly, each 5  $\mu\text{m}$  section of formalin-fixed, paraffin embedded tissue was pretreated with heat and protease, followed by ZIKV probe (GenBank accession number KU321639.1 [complete genome]; 70 pairs; target region 130-4186) hybridization for 2 hours at 40°C, a cascade of signal amplification molecules, and signal detection. Slides were counterstained with hematoxylin and mounted with xylene based EcoMount (BioCare Medical, Pacheco, CA). A probe designed to detect bacterial *dapB* (Advanced Cell Diagnostics, Newark, CA) was used as a negative control. A section of spleen from a ZIKV-infected rhesus macaque euthanized 4 DPI was used as a positive control. ISH was only performed on tissues that tested positive via qRT-PCR and was not performed on samples that contained less than 5  $\log_{10}$  genomes/mg tissue. Positive staining was identified as red cytoplasmic or perinuclear staining. When possible, ISH-positive cell types were identified by the pathologist based on tissue location and cell morphology.

**Data analyses.** A noteworthy feature of this project is that it leverages existing, archived tissues, including tissues from various studies performed at three other primate centers in addition to our CNPRC (Tulane, Wisconsin, and Washington NPRCs). While no additional animals were infected to conduct this project, samples originated from macaques exposed to differing experimental conditions, including frequency and route of inoculation, viral strain and dose, primate species, and immune-suppression via CD8<sup>+</sup> T-cell depletion (**Table 1**). To account for these differing experimental conditions, we investigated the association between the variables with tests for independence. Due to the limitations of small sample size, we conducted a univariate analysis using non-parametric methods including Wilcoxon rank test for continuous variables, Fisher's exact test for categorical, and univariate regression models for the histology scores. Further

analysis to assess confounders was not possible due to restricted sample size. All the statistical analyses were performed in R-studio. Graphs were created using GraphPad Prism. P-values of less than or equal to 0.05 were considered statistically significant.

## Supplemental Material

**Supplemental Table 1:** Experimental conditions exerting a significant effect on dependent variables in ZIKV inoculated male macaques. All statistical tests performed using R. Only significant and borderline P-values reported here. P value  $\leq 0.05$  is significant, P value 0.05-0.08 is borderline. CI is confidence interval; Ab is antibody; DPI is days post-inoculation; AUC is area under the curve. <sup>1</sup>Intravenous (IV) as reference.

DEPENDENT VARIABLE	EXPERIMENTAL CONDITION	TEST	ESTIMATE (95%CI)	P-VALUE
Viremia positive/negative	Administration of anti-ZIKV Ab	Fisher's exact	0 (0.0, 1.19)	0.03
Peak viremia magnitude	Administration of anti-ZIKV Ab	t-test	2.03 (0.93, 3.07)	0.02
Peak viremia (DPI)	Administration of anti-ZIKV Ab	t-test	-9.23 (-20.90, -11.49)	0.0005
Overall viremia duration	Administration of anti-ZIKV Ab	t-test	-7.69 (-15.86, -8.35)	0.0001
Peak viremia magnitude	ZIKV Dose	Kruskal Wallis	19.73 (chi square)	0.03
Peak viremia magnitude	Route of inoculation <sup>1</sup>	t-test	2.62 (0.21, 1.89)	0.02
Viremia AUC	Reinoculation	t-test	3.89 (10.68, 43.94)	0.002
Detection of ZIKV RNA in the male reproductive tract	Route of inoculation <sup>1</sup>	Fisher's exact	8.71 (1.52, 94.17)	0.01
Detection of ZIKV RNA in epididymis	Route of inoculation <sup>1</sup>	Fisher's exact	13.5 (2.23, 115.66)	0.001
Detection of ZIKV RNA in epididymis	Administration of anti-ZIKV Ab	Fisher's exact	0.073 (0.001, 0.73)	0.01
Detection of ZIKV RNA in seminal vesicle	Route of inoculation <sup>1</sup>	Fisher's exact	6.11 (1.41, 31.35)	0.01
Histology score, epididymis	Route of inoculation <sup>1</sup>	Simple logistic regression	1.03 (0.36, 1.70)	0.004
Histology score, prostate gland	Route of inoculation <sup>1</sup>	Simple logistic regression	0.56 (0.01, 1.10)	0.05
Histology score, epididymis	Reinoculation	Simple logistic regression	1.62 (0.88, 2.36)	0.002
Histology score, prostate gland	Reinoculation	Simple logistic regression	0.95 (0.30, 1.61)	0.01
Histology score, prostate gland	Administration of anti-ZIKV Ab	Simple logistic regression	-1.32 (-1.96, -0.68)	<0.0001

**Supplemental Table 2:** Table summarizing statistically significant variables in ZIKV inoculated male macaques. Statistical tests performed using R-studio or Graphpad Prism. Only significant P-values reported here. P value  $\leq 0.05$  is significant, P value of 0.05-0.08 is borderline; CI is confidence interval; DPI is days post-inoculation.

DEPENDENT VARIABLE	INDEPENDENT VARIABLE	TEST	ESTIMATE (95% CI)	P-VALUE
Detection of ZIKV RNA in epididymis	Magnitude peak viremia	Ordered logistic regression model	0.24 (0.11, 0.37)	0.0007
Detection of ZIKV RNA in male reproductive tract	Sexual maturity	Ordered logistic regression model	0.33 (0.06, 0.61)	0.02
Detection of ZIKV RNA in epididymis	Sexual maturity	Ordered logistic regression model	0.71 (0.46, 0.95)	<0.0001
Detection of ZIKV RNA in seminal vesicle	Sexual maturity	Ordered logistic regression model	0.59 (0.28, 0.88)	0.0005
Detection of ZIKV RNA in seminal vesicle	Days post-inoculation	Ordered logistic regression model	-0.02 (-0.02, -0.006)	0.005
Detection of ZIKV RNA in seminal vesicle from 1-20 DPI	Detection of ZIKV RNA in seminal vesicle from 21-40 DPI	Mann-Whitney	-	0.02
Detection of ZIKV RNA in seminal vesicle from 1-20 DPI	Detection of ZIKV RNA in seminal vesicle from 41-60 DPI	Mann-Whitney	-	0.03
Histology score epididymis (ZIKV-inoculated)	Histology score epididymis (uninfected controls)	Mann-Whitney	-	0.02
Histology score prostate (ZIKV-inoculated)	Histology score prostate (uninfected controls)	Mann-Whitney	-	<0.0001
Histology score epididymis	Sexual maturity	Linear model	0.92 (0.15, 1.68)	0.02
Histology score prostate	Sexual maturity	Linear model	1.17 (0.62, 1.71)	0.0001
Histology score epididymis	Detection of ZIKV RNA in epididymis	Linear model	1.09 (0.34, 1.84)	0.01
Histology score epididymis	Days post-inoculation	Linear model	-0.03 (-0.05, -0.007)	0.02
Histology score prostate	Days post-inoculation	Linear model	-0.02 (-0.05, -0.003)	0.03

**Supplemental Table 3:** Histologic scoring criteria for the male macaque genital tissues

	Testis	Epididymis	Seminal vesicle	Prostate gland
<b>0 (none)</b>	No significant lesions	No significant lesions	No significant lesions	No significant lesions
<b>1 (minimal)</b>	Lesions minimal and significance questionable (affecting <5% of the visible surface area): Rare perivascular/ peritubular mononuclear infiltrates (less than 3 small foci); and/or mild evidence of sperm stasis (rete testes or efferent ducts exhibit sperm aggregation with debris, macrophages, and multinucleated giant cells +/- engulfed sperm)	Lesions minimal and significance questionable (affecting <5% of the visible surface area): Rare perivascular/ periductular mononuclear infiltrates (less than 3 small foci); and/or mild evidence of sperm stasis (dilated epididymal ducts lacking sperm with replacement by debris, macrophages, and multinucleated giant cells +/- engulfed sperm)	Lesions minimal and significance questionable: Rare perivascular/ peritubular mononuclear infiltrates (less than 3 small foci)	Lesions minimal and significance questionable (affecting <5% of the visible surface area): Rare perivascular/periglandular mononuclear infiltrates (less than 3 small foci); and/or foci of increased fibrous connective tissue
<b>2 (mild)</b>	Mild lesions not observed in control animals (affecting 5-10% of the visible surface area): As above with more frequent perivascular/peritubular mononuclear infiltrates; and/or mild mixed inflammation,	Mild lesions not observed in control animals (affecting 5-10% of the visible surface area): As above with more frequent perivascular/periductular mononuclear infiltrates; and/or mild mixed inflammation,	Mild lesions not observed in control animals (affecting 5-10% of the visible surface area): As above with more frequent perivascular/peritubular mononuclear infiltrates; and/or mild mixed	Mild lesions not observed in control animals (affecting 5-10% of the visible surface area): As above with more frequent perivascular/ periglandular mononuclear infiltrates; and/or mild mixed inflammation, hemorrhage/edema; and/or

	hemorrhage/edema; and/or mild evidence of seminiferous tubule degeneration	hemorrhage/edema; and/or mild evidence of ductular epithelial degeneration	inflammation, hemorrhage/edema	expansion of glandular lumens by necrotic debris, neutrophils, and mononuclear inflammatory cells; and/or occasional foci of mineralization
3 (moderate)	Moderate lesions not observed in control animals (affecting 10-20% of the visible surface area): As above with multiple larger foci of mixed inflammation; and/or rare, small granulomas; and/or scattered foci of mineralization; and/or seminiferous tubule necrosis	Moderate lesions not observed in control animals (affecting 10-20% of the visible surface area): As above with multiple larger foci of mixed inflammation; and/or rare, small granulomas; and/or scattered foci of mineralization; and/or ductular epithelial necrosis	Moderate lesions not observed in control animals (affecting 10-20% of the visible surface area): As above with multiple larger foci of mixed inflammation; and/or rare, small granulomas; and/or glandular epithelial necrosis	Moderate lesions not observed in control animals (affecting 10-20% of the visible surface area): As above with multiple larger foci of mixed inflammation; and/or rare, small granulomas; and/or scattered foci of mineralization; and/or ductular epithelial necrosis
4 (severe)	Widespread moderate to severe mixed inflammation, necrosis, mineralization and/or granulomas (affecting greater than 20% of the visible surface area)	Widespread moderate to severe mixed inflammation, necrosis, ductular rupture, mineralization and/or granulomas (affecting greater than 20% of the visible surface area)	Widespread moderate to severe mixed inflammation, necrosis, mineralization and/or granulomas (affecting greater than 20% of the visible surface area)	Widespread moderate to severe mixed inflammation, necrosis, glandular rupture, mineralization and/or granulomas (affecting greater than 20% of the visible surface area)
5 (severe +)	Same as "4" but with evidence of chronicity such as frequent, extensive mineralization, replacement of necrotic testicular architecture with fibrous connective tissue, or large, well-organized granulomas or abscesses	Same as "4" but with evidence of chronicity such as frequent, extensive mineralization, replacement of necrotic epididymal architecture with fibrous connective tissue, or large, well-organized granulomas or abscesses	Same as "4" but with evidence of chronicity such as replacement of necrotic seminal vesicular architecture with fibrous connective tissue, or large, well-organized granulomas or abscesses	Same as "4" but with evidence of chronicity such as replacement of necrotic prostatic architecture with fibrous connective tissue, or large, well-organized granulomas or abscesses

**Acknowledgements.** We thank K. Jackson for assistance completing *in-situ* hybridization; J. Vidal for assistance with histopathology interpretation; J. Go and the Washington National Primate Research Center Tissue Distribution Program, and the pathology staff at the UC Davis School of Veterinary Medicine and the California National Primate Research Center.

### **CHAPTER 3**

**Early prenatal Zika virus exposure is associated with CNS neuroanatomical abnormalities in juvenile rhesus macaques.**

## **Early prenatal Zika virus exposure is associated with CNS neuroanatomical abnormalities in juvenile rhesus macaques**

Erin E. Ball<sup>1,4</sup>, Jeff Bennett<sup>2,3</sup>, Rebekah Keesler<sup>2,5</sup>, Koen K. A. Van Rompay<sup>1,2</sup>, Lark L. Coffey<sup>1</sup>, Eliza Bliss-Moreau<sup>2,3\*</sup>

<sup>1</sup>Department of Pathology, Microbiology and Immunology, University of California, Davis, CA,

<sup>2</sup>California National Primate Research Center, University of California, Davis, CA,

<sup>3</sup> Department of Psychology, University of California, Davis, CA,

<sup>4</sup>United States Army, Veterinary Corps

<sup>5</sup>Currently Charles River Laboratories, Reno, NV

\* Corresponding author

### **Abstract**

**Background.** CZS affects one in seven babies prenatally exposed to ZIKV. Microcephaly is an extreme manifestation of CZS; however, over time, normocephalic newborns with no observable congenital defects and confirmed ZIKV infection can also exhibit neurologic deficits and behavioral abnormalities consistent with CZS. These and other long-term developmental consequences of prenatal ZIKV infection are not well described. The rhesus macaque model of fetal ZIKV infection, which recapitulates many features of ZIKV and CZS in pregnant humans, can be useful to study the long-term impacts of fetal ZIKV exposure on the development of the central nervous system. We hypothesize that first trimester fetal ZIKV exposure will result in central nervous system abnormalities in juvenile rhesus macaques.

**Methods.** We used histological techniques to evaluate brains from two juvenile two year old rhesus macaques exposed *in utero* to ZIKV during the first trimester.

**Results.** Early fetal ZIKV exposure resulted in macrostructural developmental abnormalities within the CNS visual pathway, specifically disorganization, blending of layers, laminar discontinuities, and regions of low cell density within the lateral geniculate nucleus (LGN).

**Conclusion.** Normocephalic juvenile rhesus macaques exposed prenatally to ZIKV may exhibit significant neuropathology. This is the first description of postnatal neuroanatomical defects in rhesus macaques identified two years after fetal ZIKV exposure.

**Funding.** NIH Award Numbers: R01 HD096436, R21 NS104692 (EBM), R21AI129479 (KKAVR), Office of Research Infrastructure Program P51OD011107 (CNPRC) and T32 OD 011147 (EEB); U.C. Davis Graduate Student Support Program (EEB); U.S. Army Long Term Health Education & Training Program (EEB).

## **Introduction**

ZIKV is unique among mosquito-borne flaviviruses in its capacity for sexual and vertical transmission (202). Vertical transmission from mother-to-child can result in a range of possible obstetric outcomes, including utero-placental pathology, premature rupture of membranes, fetal growth restriction, musculoskeletal contracture, congenital fetal central nervous system malformations, including microcephaly, skull deformation, abnormally small cerebral cortices, retinal lesions, hearing loss, and early fetal death (64,75–77). This constellation of fetal lesions is now referred to as Congenital Zika Syndrome (CZS) and, in a U.S. cohort of pregnant women, affected one in seven babies prenatally exposed to ZIKV (121). Microcephaly is an extreme manifestation of CZS; however, over time, normocephalic newborns with confirmed ZIKV infection but no observable congenital defects can also exhibit neurologic deficits and behavioral abnormalities reminiscent of CZS (122). These and other long-term developmental consequences of prenatal ZIKV infection are not well understood.

ZIKV was originally identified in a sentinel rhesus macaque in the Ziika Forest preserve of Uganda in 1947 (61) where it circulated between NHPs and sylvatic mosquitoes (62). Its emergence into urban areas beginning in 2007 (73) and subsequent association with birth defects prompted the development of captive NHP models of human ZIKV infection. Rhesus macaques (*Macaca mulatta*) have similar reproductive physiology, anatomy, placentation (160), and neuroanatomy and neurodevelopment (335,336) to humans. ZIKV infection in pregnant macaques, including the length and magnitude of viremia, tissue levels of ZIKV RNA and infectious virus levels, and tissue tropism, recapitulates many features of ZIKV infection and CZS in pregnant humans (75,76,182,184–186,188,189). Existing rhesus macaque models of ZIKV, including our own work, have variously demonstrated placental damage/dysfunction, early fetal death (**Figure 1A**), and central nervous system (CNS) lesions consistent with abnormal brain development, though none have reproduced microcephaly (75,76,182,184–186,188,189), suggesting that, like humans, only a subset of NHP maternal ZIKV infections result in this manifestation.

Data from studies using human stem cells and brain organoids (165,230–232) and pregnant mouse models overwhelmingly indicate that ZIKV is neurotropic and that it targets embryonic neural progenitor cells (NPCs) in the developing brain (144,164–167). This tropism can result in NPC transcriptional dysregulation, decreased cell migration, impaired neurogenesis and/or cell death, with defective embryonic development of the cortical layer and congenital defects such as microcephaly, hydrocephalus, and ocular lesions (144,164–167). Loss of NPCs and perturbations in hippocampal neuron maturation and patterning have also been reported in fetal macaques exposed prenatally to ZIKV *in utero* (75,187). To date, NHP studies evaluating neuroanatomical abnormalities associated with CZS have assessed fetuses or animals sacrificed shortly after birth

(182,187,188). Thus, consequences of prenatal ZIKV infection beyond childhood remain largely unknown.

Given the frequency of ocular abnormalities and visual impairment in human infants with CZS (337–340), our previous work demonstrating abnormalities within the lateral geniculate nucleus (LGN) of fetal rhesus macaques exposed to ZIKV and harvested at end of gestation (190), and the postnatal ocular developmental lesions previously documented in one of the *in utero* ZIKV-exposed juvenile rhesus macaque from this study (341), we hypothesized that the visual pathway, specifically the LGN, would be similarly compromised in older animals. The LGN is a six-layered structure located in the ventral thalamus, which receives retinal input from the optic tract and projects axons to synapse in the primary visual cortex (V1) of the occipital lobe (**Figure 1B-C**) (342). Here, our histological evaluation of brains from two year old rhesus macaques exposed to ZIKV *in utero* during the first trimester demonstrates that early prenatal fetal ZIKV exposure results in CNS microcalcifications and macrostructural developmental abnormalities in the LGN when compared to age-matched controls.

## **Results**

**Study design and validation of the pregnant rhesus macaque ZIKV model.** Using a previously validated model of CZS (75), six pregnant rhesus macaque dams were inoculated intravenously (IV) and intraamniotically (IA) with ZIKV between gestation days (GD) 42 and 53, which, given the macaque gestation period of approximately 160 days (343), corresponds to the first trimester of pregnancy. Dams exhibited prolonged viremia with detection of ZIKV RNA in amniotic fluid samples throughout gestation, and adverse fetal outcomes (e.g., early fetal death) in four of six

dams (344). ZIKV RNA was isolated from maternal reproductive/fetal extraembryonic and fetal tissues, including fetal brain, as previously reported (184), implicating ZIKV as underlying etiology. Each of the two remaining pregnant dams (dam one and dam two) gave birth to a live female (animal 1 and animal 2) by natural delivery on GD 168 or 171, respectively (**Figure 1A**).

Animals one and two appeared normal at birth, with normal birth weight (460 g and 500 g for animal one and animal two, respectively, where the mean birth weight of captive colony-born female macaques is reported as 488 g) (345) and normal body measurements relative to archived data from other newborn macaques at the facility (344). There was no gross or ultrasonographic evidence of microcephaly, which we defined as a biparietal diameter  $\geq 2$  SD below the colony mean for uninfected animals (344). Both neonates had detectable anti-ZIKV IgG titers which gradually declined to undetectable levels, suggesting passive transfer of maternal anti-ZIKV antibodies and lack of postnatal viral replication (344). Animals one and two were maternally reared until 17 months old, then separated from their mothers and then housed together until euthanasia, at approximately two years old. Over these two years these two macaques were monitored clinically, receiving physical, ophthalmologic and neurologic/behavior examinations (**Figure 1A**).

Physical exams and routine bloodwork were normal, and serial blood ( $\geq 15$  time points), urine, and CSF samples collected between two days post-delivery and euthanasia failed to yield detectable ZIKV RNA (344). Neither animal exhibited any obvious postnatal behavioral or neurological defects. Overall eye growth appeared normal; however, animal one had postnatal ocular

developmental abnormalities characterized by bilateral, progressive colobomatous chorioretinal atrophic lesions, which were previously described by Yiu *et al.* (344).

Animals one and two were humanely euthanized at approximately two years old and a board-certified veterinary pathologist performed post-mortem examinations, with collection of tissue and fluid samples as previously described (344) and fixation of the right brain hemisphere from each animal in paraformaldehyde for 48 hours. ZIKV RNA was not detected in spleen or inguinal lymph node from either ZIKV-exposed juvenile macaque (344), though this does not preclude previous infection. There were no significant macro- or microscopic lesions in the spleen, lymph nodes, lung, heart, jejunum, liver, kidney, spinal cord, or middle ear of either animal (344). Taken together, our previous reports (75,184,344) indicate that combined IV and IA ZIKV inoculation of pregnant rhesus macaques during the first trimester can result in fetal infection, with detection of ZIKV RNA in fetal brains and congenital ocular developmental abnormalities in surviving juvenile macaques. There was no evidence of ZIKV infection in either animal at the time of euthanasia. Two age-matched juvenile male macaques who were not exposed prenatally to ZIKV served as controls. These animals were nursery reared and were euthanized at two years old, with post-mortem examination and tissue collection and processing as described above.

**Juvenile rhesus macaques exposed prenatally to ZIKV exhibit cerebral cortical microcalcifications and structural abnormalities in the lateral geniculate nucleus.**

Microscopic evaluation of Nissl-stained slides revealed scattered cerebral cortical microcalcifications in animals one and two (**Figure 1D**), particularly at the thalamic gray-white matter junction, and most frequently animal one; however, the loss of ependymal lining cells with underlying gliosis observed in our previous fetal study (75) was not a prominent feature here. Next,

we compared serial Nissl-stained sections of brain from animals one and two to those from the two uninfected age-matched controls.

Using imaging analysis software, we computed the proportion of LGN surface area occupied by the magno-, parvo- and koniocellular layers, but because of the very small sample size did not carry out formal hypothesis testing statistics. Evaluation of the descriptive statistics suggested that the mean areas were comparable between controls and prenatally ZIKV-exposed macaques, though there was a trend toward decreased parvocellular and increased koniocellular surface area in both prenatally ZIKV-exposed animals (**Figure 1E**). Microscopic evaluation of Nissl-stained sections of brain from animals one and two revealed structural abnormalities within the LGN comparable to what we previously reported in fetal brains (190), while the two control subjects appeared normal (**Figure 1F-G**). Normally, the magno- and parvocellular layers of the LGN are separated by a thin layer of koniocellular tissue (**Figure 1C,F,G**). However, in animals one and two there was blurring of these boundaries, laminar discontinuities, and regions of low cell density, particularly affecting the rostral portion of the LGN. In animal one these defects occurred primarily within the parvocellular layers at the level of the hilum (**Figure 1H**), while the ventrolateral aspect of the magnocellular layers was more severely affected in animal 2 (**Figure 1I**).

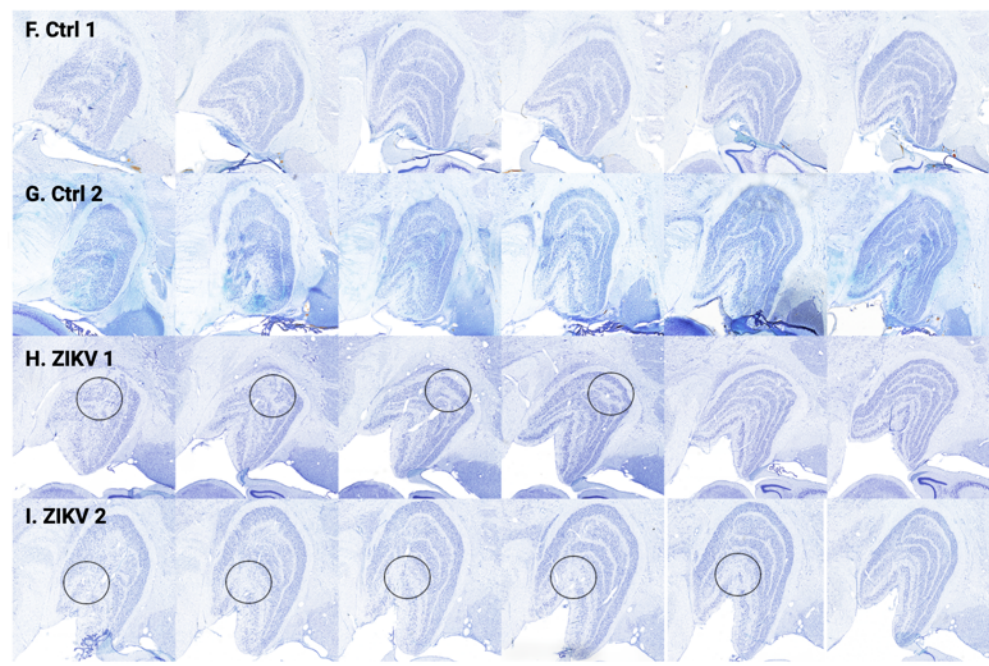
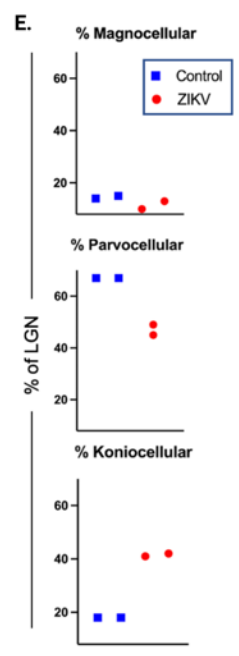
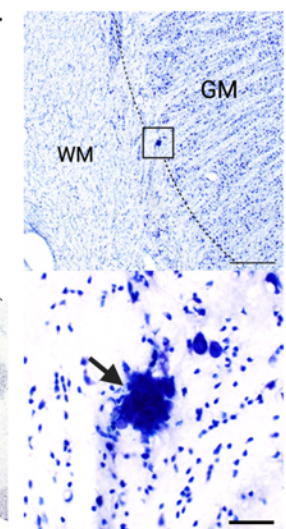
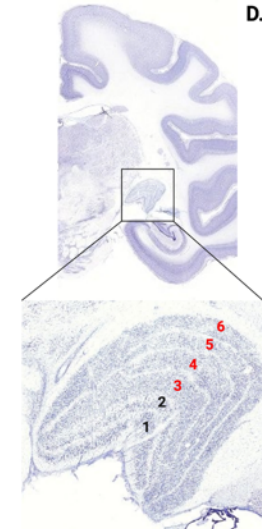
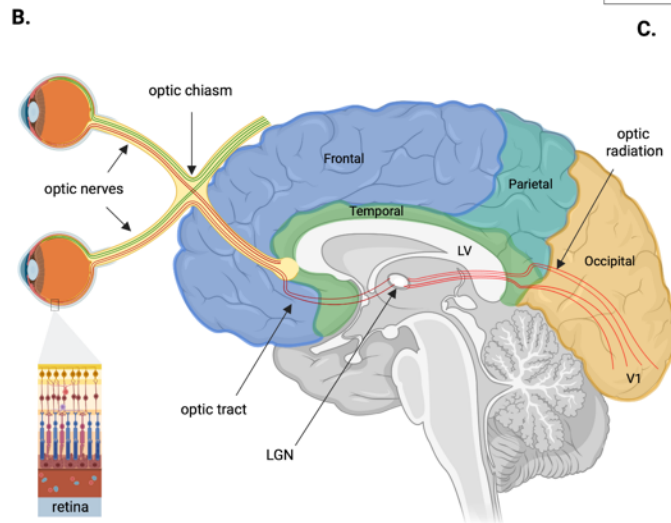
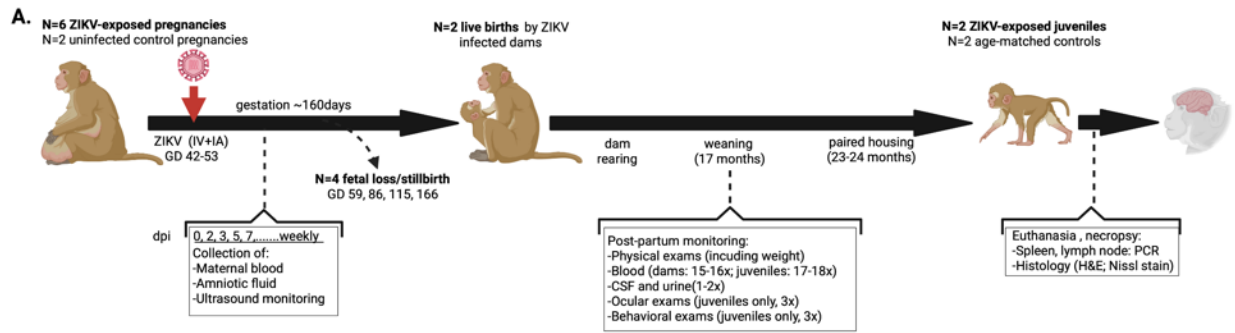


**Figure 1.** (A) Experimental design; GD = gestation day; dpi = days post-inoculation; CSF = cerebral spinal fluid, IV= intravenous, IA = intraamniotic. Adapted from Yiu, *et al.* 2020 (37) using BioRender.com. (B) Pathway of visual information from the retina through the lateral geniculate nucleus (LGN) to the primary visual cortex (V1) in the primate occipital lobe; LV = lateral ventricle. (C) Nissl-stained coronal section of a normal juvenile rhesus macaque brain depicting the anatomic location of the LGN (box). The boxed area is a normal Nissl-stained section of LGN with layers labeled as follows: 1 - 2 = magnocellular layers (contra- and ipsilateral inputs, respectively); 3 - 6 = parvocellular layers (alternating ipsi- and contralateral inputs). Magno- and parvocellular layers are separated by a thin layer of koniocellular tissue. Adapted from [www.blueprintnhpatlas.org](http://www.blueprintnhpatlas.org) (39) using BioRender.com. (D) Nissl-stained coronal section of brain from animal one demonstrating a focal microcalcification at the grey matter (GM)-white matter (WM) junction (denoted by dotted line in upper panel). The lower panel (area denoted by black box in upper panel) shows a higher magnification view of the same microcalcification (arrow); scale bars = 500  $\mu\text{m}$  (upper panel) and 50  $\mu\text{m}$  (lower panel). (E) The mean proportion of LGN surface area occupied by magno-, parvo- and koniocellular layers and calculated using ImageJ was comparable between controls and prenatally ZIKV-exposed juvenile macaques, though there was a trend toward decreased parvocellular and increased koniocellular surface area in both prenatally ZIKV-exposed animals. (E - H) Photomicrographs of Nissl-stained sections of right LGN from two year old uninfected control animals (E - F) and rhesus macaques exposed prenatally to ZIKV (G - H). Black ovals indicate areas of structural abnormalities. Uninfected control LGNs (Ctrl 1 and Ctrl 2) appear within normal limits. LGNs from prenatally ZIKV-exposed animals one (ZIKV 1) and two (ZIKV 2) exhibit areas of undifferentiated lamination with blending of layers, laminar discontinuities, and regions of low cell density.

**Discussion.** This study documents that fetal ZIKV exposure can generate long-term neuroanatomical abnormalities that persist into childhood in a rhesus monkey model of ZIKV infection. Based on our previous work in fetal ZIKV infected brains, we anticipated that we might find anatomical disorganization of the LGN, which we confirmed in these two juvenile macaques who were exposed prenatally to ZIKV but were normocephalic at birth and afterwards. Specifically there was disorganization, blending of layers, laminar discontinuities, and regions of low cell density within the LGN. This is consistent with our recently reported findings in near-term fetal macaques from a similar cohort of animals who were exposed to ZIKV in the first or second trimester, where neuroanatomical evaluation of specific brain regions revealed a number of macrostructural neurodevelopmental abnormalities within the cerebral cortex, including the LGN, likely secondary to neuroinflammatory mechanisms (190). Despite these qualitative

abnormalities, there was no significant difference in proportion of the histological section occupied by the LGN or the relative proportions of magno-, parvo- or koniocellular surface area between controls and the ZIKV-exposed fetuses (190). In the two juvenile macaques described here, evaluation of the mean surface areas of the magno-, parvo- and koniocellular layers revealed decreased relative parvocellular and increased relative koniocellular surface area in both ZIKV-exposed animals; however, the very small sample size precluded drawing conclusions about statistical significance of the differences between the ZIKV-exposed and control animals.

Ependymal cell loss with underlying gliosis, a frequently reported microscopic feature of fetal ZIKV infection (75,188,189), was not observed within the lateral ventricles of these animals; however, the cerebral cortical microcalcifications previously described by our group (75) and others (182) were also present within these two juvenile macaques, two years post-ZIKV exposure. CNS microcalcifications occurred most frequently within the thalamic white matter and at the gray-white matter junction, which is consistent with CZS in humans (347). Until recently, ZIKV-associated fetal brain microcalcifications were widely supposed to occur as a result of cellular necrosis (185). Current data suggest instead that ZIKV infection of pericytes triggers aberrant bone morphogenic protein (BMP)-mediated osteogenic activation and perivascular calcification in the subcortical white matter of the developing fetal brain (348).

Lesions within the visual system appear to be a repeatable feature of CZS in both humans (337–340) and animal models (76,190). The LGN is a bilateral six-layered structure located in the ventral thalamus that is present at birth and continues to develop postnatally. It receives retinal input from the optic nerve through optic projections, and then sends output to the primary visual cortex (V1)

via axons of the optic radiation (342,349). Appropriate anatomic and functional organization of these elements is critical for normal neural and ocular development (342,349). Notably, in addition to the neuroanatomic abnormalities within the LGN, animal one exhibited postnatal ocular developmental lesions which were described previously (344). Taken together, these findings are consistent with published reports of delayed childhood neurodevelopment and neurosensory alterations in infants and children prenatally exposed to ZIKV, where language function, vision and hearing, cognition, and motor function are commonly affected components (122–125).

Lack of power due to small sample size (N=2) precludes robust statistical analysis in this observational study; however, there is clear association between prenatal ZIKV exposure and structural neurodevelopmental abnormalities in the LGN which warrants further investigation. Additional, controlled experiments evaluating the long-term neurologic consequences of both prenatal and postnatal ZIKV infection are undoubtedly needed. To our knowledge, this is the first description of postnatal CNS microcalcifications and neuroanatomical defects in normocephalic rhesus macaques identified two years after fetal ZIKV exposure. Our findings may help explain why some normocephalic newborns whose mothers were ZIKV-infected during pregnancy, but who exhibit no observable congenital defects, develop ocular lesions and visual deficits over time.

## **Methods**

**Study Design:** The study design and methods, including PCR and ELISA, are described in detail by Yiu *et al.* (37). Briefly, pregnant rhesus macaques were inoculated IV and IA with 2000 plaque forming units of ZIKV on GD 51 (dam one) or GD 53 (dam 2) which represented a combination 1000 PFU of Puerto Rico 2015 (PRVABC-59; GenBank, KU501215) and 100 PFU of Brazil 2015

(Zika virus/H.sapiens-tc/BRA/2015/Brazil\_SPH2015; GenBank, KU321639.1). Dams were clinically evaluated daily for the duration of the study and sedated for ultrasound monitoring and sample collection according to the schedule in **Figure 1A**. Dams one and two gave birth to live females (animals one and two) by natural delivery on GDs 168 and 171, respectively. Infants one and two were maternally reared until 17 months old, then separated from their mothers and housed together until euthanasia, at approximately two years of age. Over these two years the infants received regular physical, ophthalmologic and neurologic/behavior examinations. Serial blood ( $\geq 15$  time points), urine, and CSF samples were collected between two days post-delivery and euthanasia (**Figure 1A**). Routine isolation and quantitation of viral RNA from fluids and tissues was performed and ZIKV-specific binding IgG was detected using a whole virion ELISA, as previously described (37). Two ZIKV-exposed infants and two age-matched uninfected control animals were euthanized and necropsied at approximately 2 years old.

**Necropsy tissue processing, sectioning, Nissl staining and histopathology:** Processing and analysis of paraformaldehyde-fixed, Nissl-stained tissues sections is described in depth by Beckman *et al.* (33). Briefly, uninfected control and ZIKV-exposed animals were euthanized with an overdose of pentobarbital (FatalPlus, VOrtech Pharmaceuticals, Dearborn, MI, USA), followed by immediate collection of spleen and inguinal lymph node specimens preserved in RNALater (ThermoFisher, Waltham MA, USA) for RT-PCR. In contrast to the methods described by Beckman *et al.* (190). where fetal brain hemispheres were immersion fixed, here the upper body was perfused with 4% paraformaldehyde (EMS, Hatfield, PA USA) in 0.1 M sodium phosphate buffer (ThermoFisher, Waltham MA, USA) for optimal preservation of brains and eyes for histological analysis. The right hemisphere of the brain and both eyes were further fixed in 4% paraformaldehyde for 48 hours, while the left hemisphere and other tissues were fixed in a 10-fold

volume of 10% neutral buffered formalin (ThermoFisher, Waltham MA, USA). Formalin fixed tissues were subsequently embedded in paraffin, thin-sectioned (5  $\mu\text{m}$ ), stained routinely with hematoxylin and eosin (H&E), and evaluated by two board-certified anatomic pathologists.

The paraformaldehyde-fixed right brain hemisphere was cryoprotected in 10% glycerin (FisherScientific, Waltham, MA USA) with 2% DMSO (Sigma-Aldrich, St Louis, Mo USA) in 0.1 M sodium phosphate buffer overnight then 20% glycerin with 2% DMSO in 0.1 M sodium phosphate buffer for 72 hours. The right hemisphere was then frozen in isopentane (FisherScientific, Waltham, MA USA) following standard laboratory procedures (350) and sectioned on a sliding freezing microtome (Fisher Scientific Microm HM430, Waltham, MA, USA) into eight series (seven at 30  $\mu\text{m}$  and one at 60  $\mu\text{m}$ ). The 30  $\mu\text{m}$  tissue sections were placed in a cryoprotectant solution (composed of Ethylene glycol, glycerin in 0.1 M phosphate buffer) and stored at  $-20^{\circ}\text{C}$ . The 60  $\mu\text{m}$  tissue sections were postfixated for two weeks in 10% neutral buffered formalin and stored at  $4^{\circ}\text{C}$ . The 60  $\mu\text{m}$  sections were mounted on gelatin subbed slides, Nissl stained using 0.25% thionin (FisherScientific, Waltham, MA USA) (according to our standard protocols) (350) and finally coverslipped using DPX mounting medium (Millipore Sigma, St. Louis, MO, USA). Nissl-stained sections were scanned (TissueScope LE; Huron Digital Pathology; St. Jacobs, ON, Canada) and digital images were used for blinded analyses. Due to animal availability for this study, uninfected controls were nursery-reared, while prenatally ZIKV exposed rhesus macaques were maternally reared in a semi-natural social environment. Studies have shown that nursery-reared macaques can exhibit altered physiology (351), behavior, and even brain development, with a comparatively smaller corpus callosum and cognitive deficits when

compared to maternally reared juveniles (352); however, defects specifically within the LGN are not reported.

**Analysis of Nissl-stained brain sections:** We first reviewed each Nissl-stained section to qualitatively identify abnormalities and regions of interest across brains. Based on published data (190) and our previous identification of congenital ocular lesions in this cohort (344) we elected to quantitatively evaluate the lateral geniculate nucleus (LGN), which is located in the ventral thalamus where it serves as part of the visual pathway (**Figure 2**). Anatomical boundaries were determined by comparing Nissl-stained tissue to reference atlases (346,353) and all anatomical analyses were performed using ImageJ (Fiji, NIH). The 3 largest complete sections of LGN from each subject were evaluated. Using ImageJ, the total LGN surface area in each section and then the magnocellular (layers 1 and 2) and parvocellular (layers 3 - 6) surface areas were measured three times. The koniocellular surface area was calculated as the total LGN surface area minus the magnocellular and parvocellular areas. Measurements were first averaged within a section, then between sections, for each animal.

**Data analysis:** Quantitative measurements of Nissl-stained sections were performed using ImageJ (Fiji, NIH).

**Study Approval:** All procedures were conducted on protocols #19211 and 20959 approved by the institutional animal care and use committee (IACUC) at the University of California, Davis. The University of California, Davis, is accredited by the Association for Assessment and Accreditation

of Laboratory Animal Care (AAALAC). All rhesus macaque work adhered to the 2011 NIH Guide for the Care and Use of Laboratory Animals.

### **Acknowledgements**

We thank Bhakti Patwardhan and Jala Atufa for assistance with sectioning and the pathology staff at the California National Primate Research Center and the UC Davis School of Veterinary Medicine.

## **CHAPTER 4**

### **SARS-CoV-2 vasculopathy in a Syrian golden hamster model.**

## **SARS-CoV-2 vasculopathy in a Syrian golden hamster model.**

Erin E. Ball<sup>1,3</sup>, Christopher M. Weiss<sup>1,4</sup>, Hongwei Liu<sup>1</sup>, Ken Jackson<sup>1</sup>, M. Kevin Keel<sup>1</sup>, Christopher Miller<sup>2</sup>, Timothy Carroll<sup>2</sup>, Koen K. A. Van Rompay<sup>1,2</sup>, Lark L. Coffey<sup>1</sup>, Patricia Pesavento<sup>1\*</sup>

<sup>1</sup>Department of Pathology, Microbiology and Immunology, University of California, Davis, CA,

<sup>2</sup>California National Primate Research Center, University of California, Davis, CA,

<sup>3</sup>United States Army, Veterinary Corps

<sup>4</sup>Current address: Meissa Vaccines, Inc., Redwood City, CA

\* Corresponding author

### **Abstract**

Clinical evidence of vascular dysfunction and hypercoagulability as well as pulmonary vascular damage and microthrombosis are frequently reported in severe cases of human COVID-19 disease. Syrian golden hamsters recapitulate histopathologic pulmonary vascular lesions reported in COVID-19 patients. Here, we use an established Syrian golden hamster model to define SARS-CoV-2 induced vascular pathologies. We show that regions of active pulmonary inflammation and SARS-CoV-2 infection are characterized by ultrastructural evidence of endothelial damage with platelet marginalization and both perivascular and subendothelial macrophage infiltration. SARS-CoV-2 antigen/RNA was not associated with affected blood vessels. Taken together, these findings suggest that the prominent microscopic vascular lesions in SARS-CoV-2 inoculated hamsters are likely due to indirect endothelial damage followed by platelet and macrophage infiltration, which may also be occurring in people.

### **Introduction**

SARS-CoV-2 infection in humans varies from asymptomatic to severe respiratory disease, progressing to acute respiratory distress syndrome, multiorgan dysfunction and death in a subset of patients. As the pandemic has progressed, there have been increasing reports documenting

clinical evidence of coagulopathy and microscopic indicators of pulmonary vascular damage, including endotheliitis, defined as subendothelial leukocyte infiltration with lifting and/or damage to endothelial cells (303), vasculitis, and microthrombosis associated with severe cases of COVID-19 (294–296,354). Syrian golden hamsters (*Mesocricetus auratus*) are naturally susceptible to SARS-CoV-2 and closely recapitulate the clinical, virological, and histopathological features of human COVID-19 disease (311,315,317–319,355). Here, we used Syrian golden hamsters to define SARS-CoV-2 induced vascular pathologies, which have not been fully characterized in this animal model. Specifically, we show for the first time in hamsters that regions of active SARS-CoV-2 induced pulmonary inflammation exhibit ultrastructural evidence of endothelial damage, with platelet marginalization and marked perivascular and subendothelial mononuclear inflammation composed primarily of macrophages, and that SARS-CoV-2 antigen/RNA is not associated with affected blood vessels. These findings suggest that the microscopic vascular lesions in SARS-CoV-2 inoculated hamsters are primarily due to indirect endothelial damage followed by platelet and macrophage infiltration and not direct viral infection of the endothelium.

## **Results**

**Validation of the model.** The experimental design is summarized in **Supplemental figure S1A**. Briefly, animals were inoculated intranasally with SARS-CoV-2 alpha (B.1.1.7) or mock inoculated with DPBS on day 0, monitored daily for weight loss and clinical disease and to swab the oropharyngeal cavity, and euthanized on three, six, or seven dpi. A subset of hamsters inoculated with SARS-CoV-2 exhibited mild weight loss from two to three dpi (**Supplemental figure S1B**), though none reached euthanasia criteria (loss of 20% of day zero weight) or displayed clinical signs of illness. Infectious virus was recovered from the upper respiratory tract between one and three dpi and from the lung at three dpi (**Supplemental figure S1C - D**). Most hamsters

did not become viremic, though infectious virus was detected in the plasma of one female hamster, which also had a very low infectious virus titer in the duodenum at three dpi. Otherwise, infectious virus was not detected in hamster tissues. Overall, SARS-CoV-2 inoculated hamsters developed non-lethal infection with infectious virus recoverable until three dpi from the upper airway and lung. All hamsters inoculated with SARS-CoV-2 developed moderate to severe microscopic pulmonary lesions (**Figure 1**). No significant microscopic abnormalities were noted in the brain, heart, spleen, liver, gastrointestinal tract, kidneys, or male/female reproductive tissues of any hamster. Inoculation of additional hamsters with emerging SARS-CoV-2 variants, including delta (B.1.617.2) and epsilon (B.1.427 and B.1.429) variants, produced similar histopathologic lesions and is described elsewhere (316,356).

**Syrian golden hamsters inoculated with SARS-CoV-2 develop progressive, broncho-interstitial pneumonia with prominent vascular lesions.** SARS-CoV-2 induced lung pathology in hamsters was assessed using two methods. First, we used ImageJ to quantify the approximate lung surface area exhibiting microscopic lesions consistent with COVID-19 disease (defined as inflammation, necrosis, hemorrhage and/or edema visible at subgross magnification) as a proxy for the overall extent and severity of pulmonary lesions. We then scored pathologic lesions specifically affecting pulmonary vasculature according to the criteria outlined in **Supplemental Table S1**. Both scores were significantly higher in SARS-CoV-2 inoculated hamsters when compared to uninfected controls (**Figure 1A**). SARS-CoV-2 inoculated hamsters exhibited a progressive increase in the extent and severity of lung lesions from three to seven dpi (**Figure 1A-D**). At three dpi there was patchy neutrophilic and histiocytic inflammation centered upon large airways (bronchitis and bronchiolitis), as well as variable bronchiolar epithelial and alveolar septal

necrosis with replacement by fibrin, hemorrhage, edema, necrotic debris, numerous neutrophils and macrophages, and scattered multinucleated syncytial cells (**Figure 1C**). By six dpi, lesions progressed to widespread necrotizing broncho-interstitial pneumonia (**Figure 1D**). Reparative changes, consisting of bronchiolar epithelial hyperplasia (**Figure 1D**) and prominent type II pneumocyte hyperplasia were also common by six dpi. Vascular lesions, including marked perivascular cuffing and subendothelial mononuclear inflammatory cell infiltration (endotheliitis) with variable transmigration of the vessel wall, were noted frequently at both evaluated time points (**Figure 1C - D**); however, necrotizing vasculitis and thrombosis were not prominent features. These histologic features are consistent with published data from hamster models (311,315,317–319), including lesions reported in association with emerging SARS-CoV-2 variants (316,356).

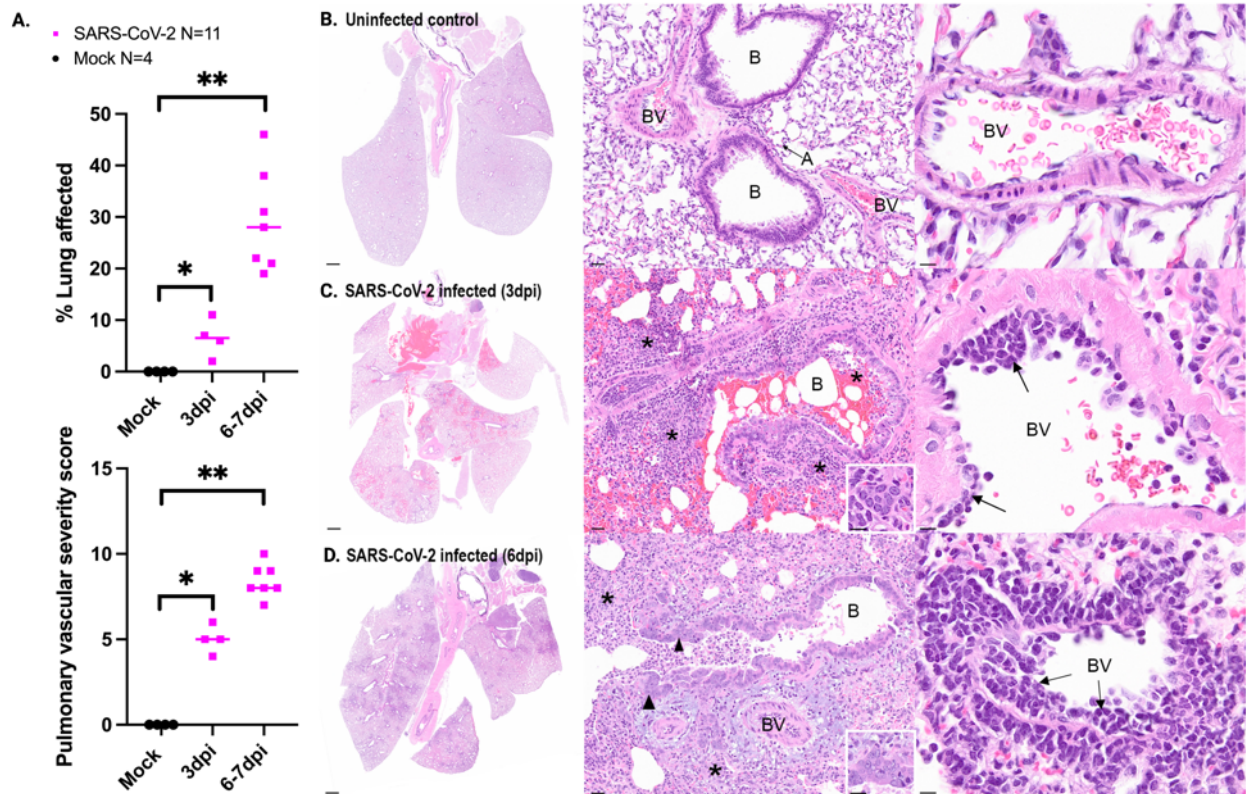


**Figure 1. Pulmonary pathology severity score summary and photomicrographs of H&E-stained lung sections from uninfected and SARS-CoV-2 inoculated hamsters at three and six dpi.** (A) The proportion of lung surface area exhibiting SARS-CoV-2 induced microscopic lesions (top graph) and the mean pulmonary vascular histology severity score (bottom graph) increased from three to seven dpi in SARS-CoV-2 inoculated hamsters. Scores were significantly higher in SARS-CoV-2 inoculated hamsters than mock-infected control animals (Mann-Whitney). Horizontal lines denote means. Each dot/square indicates an individual hamster; dpi = days post-inoculation; \* p value  $\leq 0.05$ ; \*\* p value  $\leq 0.01$ . (B) Normal lung from uninfected hamster. (C) Lung from a SARS-CoV-2 inoculated hamster euthanized three dpi. There is patchy necrohemorrhagic bronchiolitis and alveolar septal necrosis with replacement by hemorrhage, fibrin, an inflammatory infiltrate composed primarily of neutrophils and macrophages (asterisks, middle panel), with scattered multinucleated syncytial cells (inset, middle panel), and mononuclear endotheliitis (arrows, right panel) with perivascular inflammation. (D) Lung from a SARS-CoV-2 inoculated hamster euthanized six dpi. There is widespread broncho-interstitial pneumonia (asterisks, middle panel) with bronchiolar epithelial hyperplasia (arrowheads, middle panel) and multinucleated syncytial cells (inset, middle panel). Endotheliitis (arrows, right panel) and perivascular inflammation remain prominent. Hematoxylin and eosin (H&E) stain. B = bronchiole; A = alveolar septa; BV = blood vessel. Left column (B – D), scale bar = 1 mm; middle column (B – D), scale bar = 30  $\mu\text{m}$  (inset, scale bar = 20  $\mu\text{m}$ ); right column (B – D), scale bar = 20  $\mu\text{m}$ .

**Pulmonary subendothelial inflammation in SARS-CoV-2 inoculated hamsters is characterized by endothelial damage with macrophage and platelet infiltration.** We used immunohistochemistry (IHC), immunofluorescence (IFA), *in-situ* hybridization (ISH), and transmission electron microscopy (TEM) to further characterize foci of endotheliitis identified on H&E-stained slides. IHC staining with antibodies against Von Willebrand Factor/Factor 8 (endothelial cells) (**Figure 2A**), Iba1 (macrophages), CD-3 (T-lymphocytes), and CD79a (B-lymphocytes) revealed that, at both time points, the mononuclear cells adhered to the endothelial surface or infiltrating subendothelial vascular layers are consistent primarily with macrophages (**Figure 2B**). There are also low numbers of T-lymphocytes (**Figure 2C**) and few B-lymphocytes (**Figure 2D**).

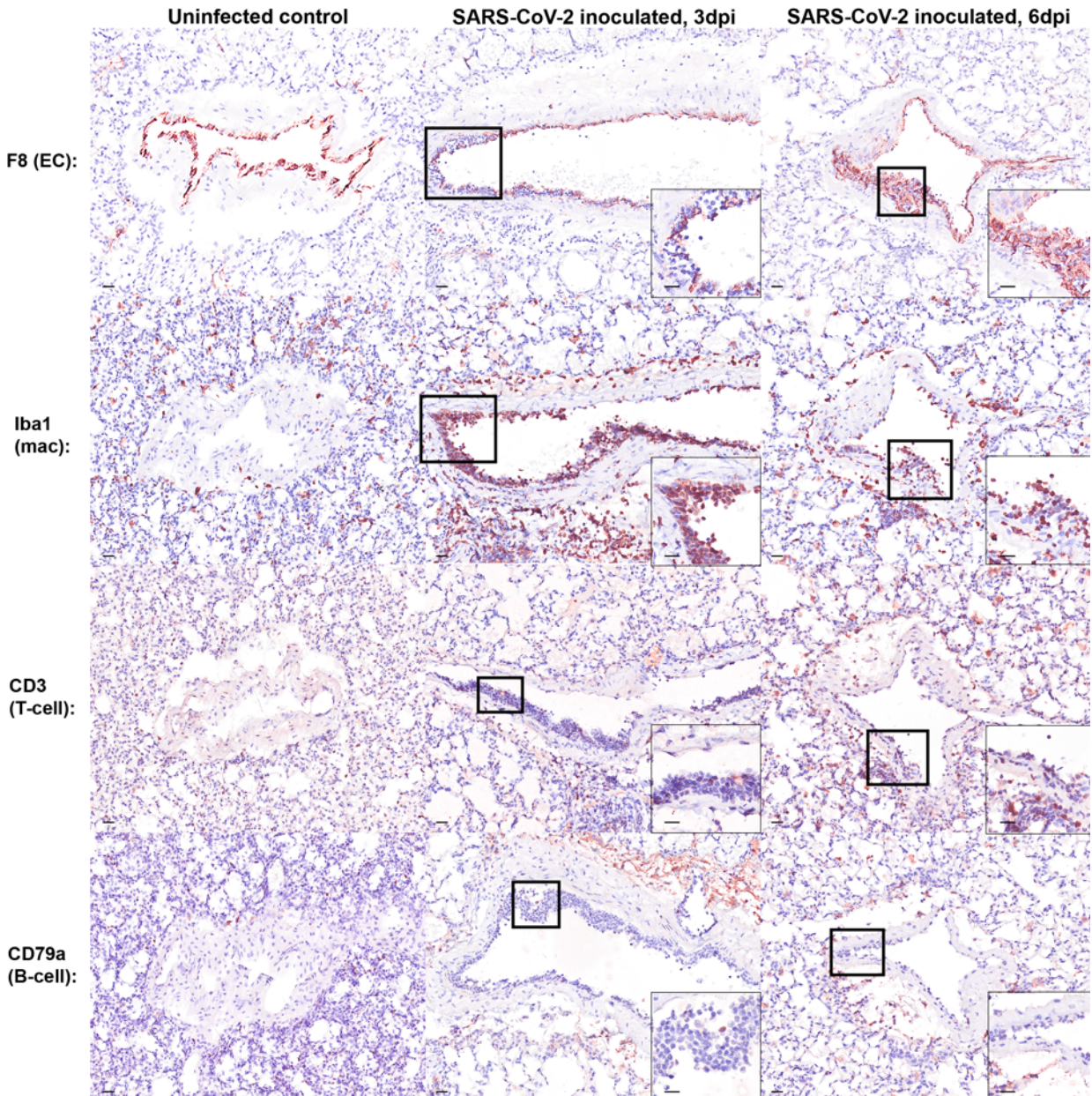


**Figure 2. Photomicrographs of immunohistochemically (IHC) stained lung sections from uninfected and SARS-CoV-2 inoculated hamsters.** IHC staining using antibodies against endothelial cells (Von Willebrand factor/Factor 8 [vWF/F8]) (A), macrophages (Iba1) (B), T-lymphocytes (CD3) (C), and B-lymphocytes (CD79a) (D), where positive cells exhibit intracytoplasmic or membranous brown staining. Insets show higher magnification views of the areas denoted by black boxes. EC = endothelial cell; macs = macrophages; T-cell = T-lymphocytes; B-cell = B-lymphocytes. Overall, IHC indicates that the subendothelial mononuclear cell infiltrate is composed primarily of macrophages. Scale bars = 20  $\mu$ m. See **Supplemental Figure S2** for internal controls.

Immunofluorescent antibodies against SARS-CoV-2 nucleocapsid protein (NP) demonstrated viral antigen in hamster terminal bronchiolar epithelium, type I pneumocytes, and, less commonly, alveolar macrophages at three dpi (**Figure 3A - C**). Viral NP was not identified within or near blood vessels. **Figure 3A** shows lifting of the vascular endothelium (green) by infiltrating mononuclear cells (likely macrophages based on IHC results above). In **Figure 3B**, green anti-platelet antibody (CD41) localization along the arteriolar endothelium highlights areas of platelet marginalization, while the presence of intracytoplasmic green signal within mononuclear cells (**Figure 3B - C**) is consistent with platelet phagocytosis by activated macrophages. We next used ISH to assess the cellular tropism of SARS-CoV-2 in the hamster respiratory tract (**Figure 3D – L**), where “positive” cells demonstrate intracytoplasmic red signal. Overall, SARS-CoV-2 RNA was observed primarily at three dpi (**Supplemental figure S3**), within bronchial/bronchiolar epithelial cells, type I and II pneumocytes, and (less frequently) alveolar macrophages, where it corresponded with areas of inflammation. Notably, viral RNA was not identified within or associated with the pulmonary vasculature (**Figure 3F, I, L**).

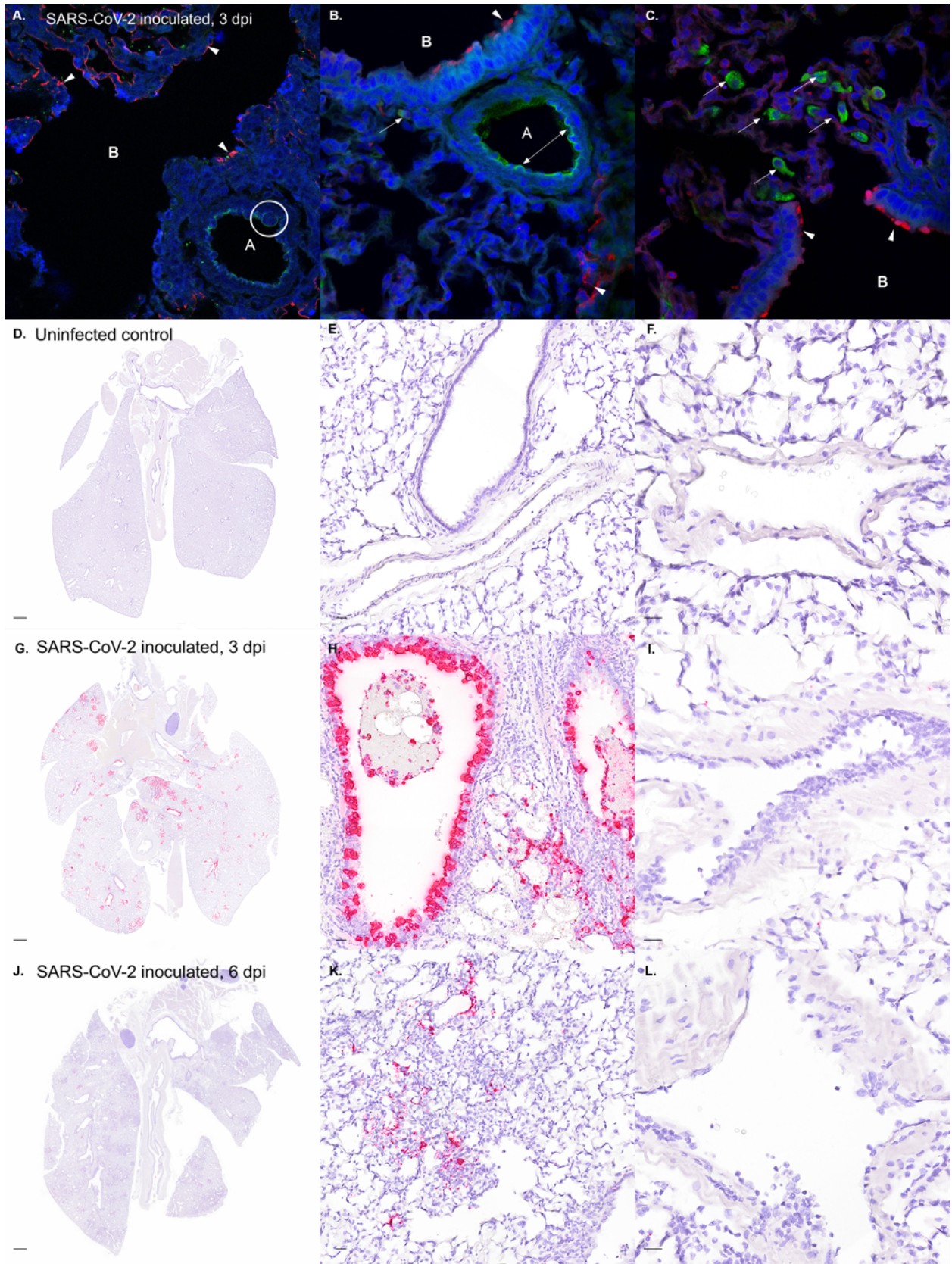


**Figure 3. Photomicrographs of immunofluorescent antibody (IFA)- and in-situ hybridization (ISH)-labeled sections of lung from uninfected and SARS-CoV-2 inoculated hamsters. (A-C)** IFA with antibodies against SARS-CoV-2 nucleocapsid (red) at three dpi shows the presence of viral antigen (arrowheads) within hamster terminal bronchiolar epithelium type I pneumocytes, and, less commonly, alveolar macrophages. **(A)** Anti-endothelial cell antibody CD31 (green) demonstrates lifting of the arteriolar endothelium by infiltrating mononuclear cells (circled). **(B-C)** Anti-platelet antibody CD41 (green) highlights platelet marginalization along the arteriolar endothelium (double-headed arrow) **(B)**, and the presence of intracytoplasmic green signal within mononuclear cells **(B-C)** is consistent with platelet phagocytosis by alveolar macrophages (arrows). B = bronchiole; A = arteriole. **(D-L)** Distribution of SARS-CoV-2 RNA positive cells in ISH-labeled sections of lung. Cells labeled by riboprobe in-situ hybridization stain red. **(D - F)** Lung from uninfected hamster is negative for ISH signal. **(G - I)** In lung sections from a SARS-CoV-2 inoculated hamster euthanized three dpi, SARS-CoV-2 RNA is most prominent within airways **(G - H)**, extending from mainstem bronchi to bronchiolar epithelial cells of smaller airways and multifocally into type I and II pneumocytes of peribronchiolar alveolar septa. **(J - L)** In lung sections from a SARS-CoV-2 inoculated hamster euthanized six dpi, the number of positive cells has decreased dramatically, with scattered signal in type I and II pneumocytes lining alveolar septa, and occasional weak signal remaining in airway epithelial cells **(J - K)**. No signal is identified within pulmonary vessels **(F, I, L)**. Scale bar = 1 mm (D,G,J); scale bar = 20  $\mu$ m (E, F, H, I, K, L).

Ultrastructurally, there was significant evidence of endothelial activation and injury in the pulmonary vasculature of SARS-CoV-2 inoculated hamsters. Activated endothelial cells bulged into the vascular lumen (**Figure 4A**), often with irregular, frond-like filopodia (**Figure 4B**), long, thick, dense tight junctions, and thickened, irregular basal laminae (**Figure 4C**). Damaged, degenerating endothelial cells exhibited cytoplasmic vacuolation with partial detachment from the basal lamina (**Figure 4D**). Consistent with the findings reported above, mononuclear cells, including macrophages and lymphocytes (**Figure 4A**), as well as activated platelets (**Figure 4C - D**) were often associated with the resulting perivascular spaces. There were no viral particles noted within or associated with affected endothelial cells. Taken together, our results are suggestive of vascular endothelial damage with mononuclear subendothelial inflammation (endotheliitis) and infiltration of platelets into areas of active pulmonary infection and inflammation.

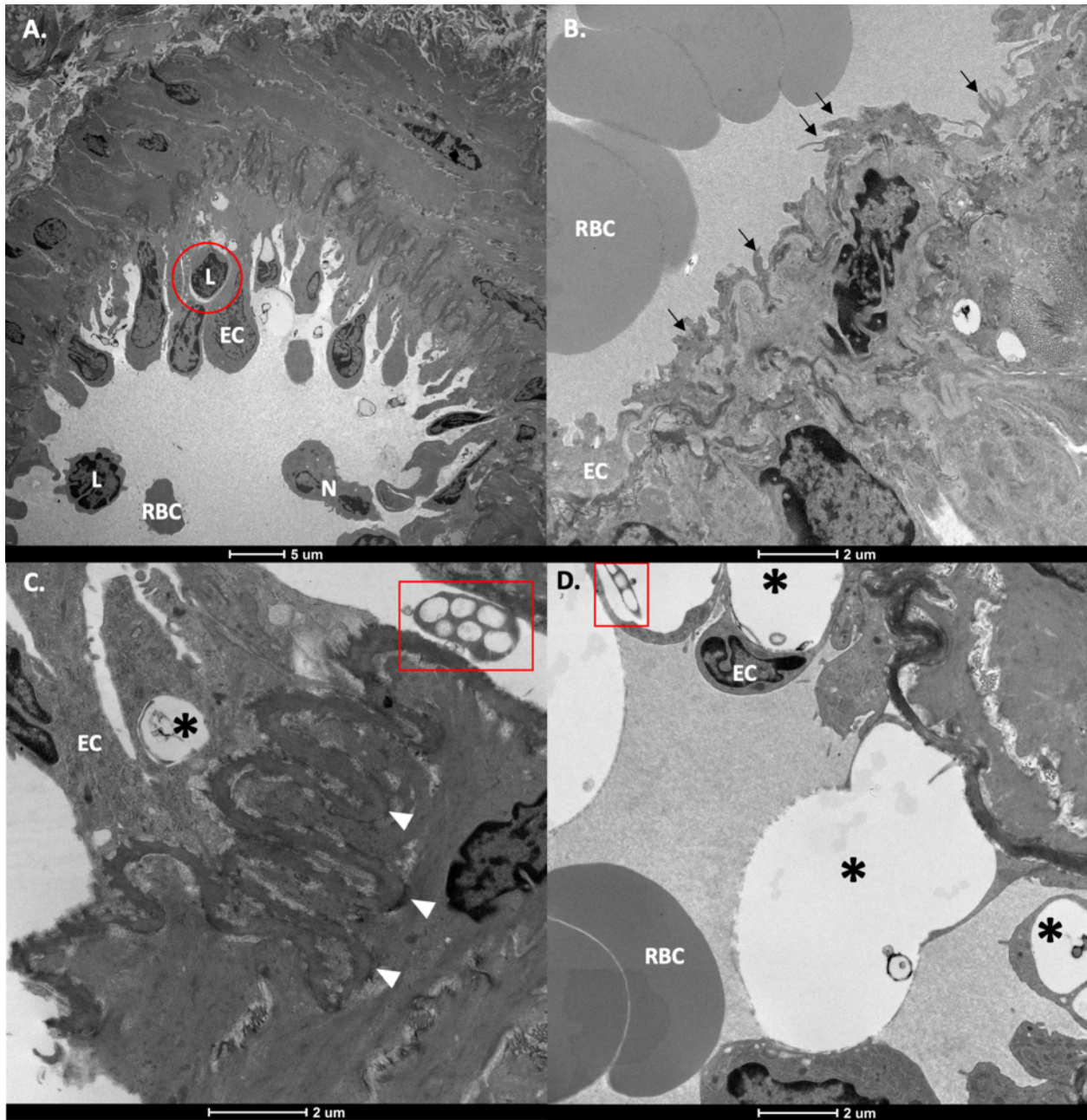


**Figure 4. Transmission electron microscopy images of hamster pulmonary blood vessels six days after inoculation with SARS-CoV-2.** (A) Activated endothelial cells lining a small pulmonary arteriole and bulging into the vascular lumen with a subintimal lymphocyte (red circle); (B) Activated venular endothelial cell with frond-like filopodia (arrows); (C) Vacuolated (asterisk) endothelial cell with a thickened, irregular basal lamina (arrowheads); activated, degranulated platelets (C/D, red box) are associated with the resulting perivascular spaces; (D) Damaged, degenerating endothelial cells with marked cytoplasmic vacuolation (asterisks) resulting in partial detachment from the underlying, thickened basal lamina. RBC = red blood cell; EC = endothelial cell; L = lymphocyte; N = neutrophil. Scale bar = 5  $\mu\text{m}$  (A); Scale bar = 2  $\mu\text{m}$  (B-D).

## Discussion

The histopathologic pulmonary lesions reported here, including moderate to severe broncho-interstitial pneumonia and alveolar damage with prominent perivascular and subendothelial inflammation, are comparable with the limited published autopsy data available from severe COVID-19 patients (354,357–359), although hyaline membranes, and vasculitis with microthrombi (also frequently reported in humans) were not prominent features in these hamsters. This disparity may reflect the timing of disease progression, the presence of co-morbidities and/or other host-specific factors. *In vivo* hamster studies employ healthy animals and are terminated by 10-14 dpi (311,315,317,318). In contrast, human autopsy data largely derives from hospitalized patients with severe COVID-19 exacerbated by co-morbidities and extensive exposure to medications, with a median duration between symptom onset and death exceeding 15 days (360,361). Supporting this hypothesis, lung specimens from two pulmonary adenocarcinoma patients retrospectively diagnosed with SARS-CoV-2 infection also lacked hyaline membranes and microthrombi, presumably because COVID-19 disease was an unexpected, ancillary diagnosis and the lobectomies happened to capture the acute stage of disease (359).

Using TEM and special staining techniques we demonstrate that endotheliitis in SARS-CoV-2 inoculated hamsters is associated with endothelial cell damage, characterized by marked cytoplasmic vacuolation with thickened irregular basement membranes, platelet marginalization, and infiltration of macrophages. In contrast, previously documented cases of non-COVID-19 associated endotheliitis, including hepatic sinusoidal (associated with acute cellular rejection of liver allografts) (1) and corneal (secondary to herpesviral infection or corneal graft rejection) (303)

and corneal (secondary to herpesviral infection or corneal graft rejection) (362) endotheliitis, tend to be lymphocytic in nature.

Both direct and indirect mechanisms of endothelial damage have been implicated in the pathogenesis of COVID-19 induced vasculopathy/coagulopathy (19). Various reports have documented the presence of viral antigen and/or RNA in association with endothelial cells both *in vitro* (363) and in autopsy tissues (290,354), and “virus-like” particles have been identified ultrastructurally within endothelial cells (304,354,364–366). However, studies utilizing molecular techniques to identify endothelial viral antigen or RNA (290,354) generally fail to exclude staining of vascular support cells such as pericytes and vascular smooth muscle cells, which are closely associated with the endothelium and also express the SARS-CoV-2 receptor ACE2 (330,367,368). Overall, attempts to localize viral antigen/RNA to endothelial cells have been largely unsuccessful, or, at best, equivocal (304,365,369–372). Recent studies report that endothelial cells do not express high levels of ACE2 and that they are capable of only very low levels of viral replication, even when exposed to high titers of SARS-CoV-2 (368,373). Furthermore, the ultrastructural studies described above are underscored by a collective lack of reproducibility (302), and critics have suggested that some of the “viral particles” reported in the literature may actually be subcellular organelles such as coated vesicles (50,307). Together, these data and ours support an indirect mechanism of SARS-CoV-2 induced vascular damage.

Systemic inflammation generates crosstalk between platelets, endothelial cells and leukocytes, ultimately resulting in endothelial damage, platelet hyperactivation, parallel activation of the coagulation cascade, and thrombosis (334). The so-called “cytokine storm” (289) produces a self-

amplifying loop where activated endothelial cells promote leukocyte and platelet adherence, microvascular obstruction, extensive vascular inflammation, and subsequent release of production of toxic reactive oxygen species and pro-inflammatory cytokines, including IL-6, IL-1 $\beta$  (a key cytokine associated with endothelial dysfunction) and TNF $\alpha$ . Endothelial cell activation results in a pro-coagulant, pro-inflammatory state characterized by increased vascular permeability, further production of pro-inflammatory cytokines, leukocyte adhesion molecules, and coagulation factors, and activation of platelets and leukocytes (299). Activated platelets release vasoactive, hemostatic, and inflammatory mediators from granules, trigger the coagulation cascade and provide a procoagulant surface for secondary hemostasis (331,374).

With chronicity, pro-inflammatory cytokines can trigger further endothelial injury and platelet hyperactivation, exacerbating the existing inflammatory milieu and creating a hypercoagulable state. Importantly, recent studies suggest that perturbations of vascular support cells may also contribute to COVID-19 associated coagulopathy, as *in vitro* exposure of human pericytes to SARS-CoV-2 spike (S) protein resulted in dysfunctional pericyte signaling, secretion of pro-inflammatory cytokines, and endothelial cell death (330,367). Cytokines (e.g., IL-8), complement components (e.g., C5a), and activated platelets can additionally induce release of neutrophil extracellular traps (NETs), scaffolds of extracellular DNA with attached histones, neutrophil granule proteins and antimicrobial peptides that function to trap, immobilize, and/or kill pathogens (296,298,333) and are also known to initiate immunothrombosis (333). Notably, Becker *et al.* recently demonstrated the presence of NETosis markers, but not viral antigen, associated with microscopic vascular lesions in a hamster model of COVID-19 disease (355). A human cohort study similarly reported elevated serum markers for NETosis, microscopic evidence of extensive

neutrophil-platelet infiltration, and NET-containing pulmonary microthrombi in severe COVID-19 patients (333). This precarious clinical situation is exacerbated by both ageing and pre-existing cardiovascular risk factors such as obesity, hypertension, and diabetes (296), which are also known to prime platelets for hyperreactivity (374).

Immune dysregulation resulting in excessive production of pro-inflammatory cytokines, endothelial damage, and platelet hyperactivation is likely a major driving force behind the hypercoagulable state and microthrombosis observed in some COVID-19 patients. Although this was an observational study lacking sufficient power for statistical analysis, our findings, particularly the lack of viral association with inflamed vessels, and published data (290,296,355,374–377) collectively support an indirect mechanism linking inflammation and hypercoagulability in severe cases of COVID-19 disease. While further study regarding viral effects on pericytes and endothelium-platelet-leukocyte interactions is necessary to fully understand the pathogenesis of SARS-CoV-2 associated coagulopathy and thrombosis, our results suggest that novel therapeutics targeting the dysregulated immune system (i.e., cytokine production or NETosis) may prove effective medical countermeasures against COVID-19 disease. To our knowledge, this is the first use of TEM and special histologic staining techniques to demonstrate endothelial damage with marginalization of activated platelets and lack of viral association with affected blood vessels in regions of active pulmonary SARS-CoV-2 infection in a Syrian golden hamster model of human COVID-19 disease.

## Methods

**Hamsters:** All hamster work was conducted on protocol #21868 approved by the UC Davis institutional animal care and use committee (IACUC). Infectious virus was handled in certified animal biosafety level 3 laboratory (ABSL-3) spaces in compliance with approved institutional biological use authorization #R2813. The University of California, Davis, is accredited by the AAALAC. All hamster work adhered to the NIH Guide for the Care and Use of Laboratory Animals. Seven male and eight female 8 to 10-week-old Syrian golden hamsters (Charles River Laboratories, Wilmington, MA) were housed in ABSL-3 conditions and acclimated for up to 6 days at 22 - 25°C and a 12:12 hour light: dark cycle. Rodent chow with 18% protein content and sterile bottled water was provided ad libitum for the duration of the experiment.

**SARS-CoV-2 challenge, monitoring, and euthanasia:** SARS-CoV-2/human/USA/CA-CZB-59X002/2020 (GenBank #MT394528) from a 2020 COVID-19 patient in Northern California (provided by Dr. Christopher Miller, UC Davis) was passaged twice in Vero-E6 (American Type Culture Collection [ATCC], Manassas, VA) cells to achieve a titer of  $2.2 \times 10^7$  plaque forming units (PFU)/mL and stored at -80°C. Hamsters were anesthetized with isoflurane and administered 30  $\mu$ L of PBS (Thermo Fisher Scientific, Waltham, MA) or SARS-CoV-2 diluted in PBS at a dose of  $10^4$  PFU intranasally (IN) by a hanging drop over both nares. Inocula were back-titrated to confirm the target dose. Hamsters were monitored daily for clinical signs through the experimental endpoint (six or seven dpi) and euthanized if weight loss exceeded 20% or if they appeared moribund. Hamsters were anesthetized daily with isoflurane, weighed, and throat-swabbed (Puritan, Thermo Fisher). Swabs were vortexed in 400  $\mu$ L of Dulbecco's Modified Eagles Medium (DMEM, Thermo Fisher) and stored at -80°C. Prior to euthanasia, whole blood was collected via

submandibular vein puncture, allowed to clot at room temperature for >10 min, and centrifuged for five min at 8,000 x g. Serum was also stored at -80°C. Following euthanasia by isoflurane overdose and cervical dislocation, hamsters were perfused with cold sterile PBS. At necropsy, tissues were divided/processed for virology assays and histopathology. Lung was homogenized in 1-10 µL/mg DMEM with a sterile glass bead using a Qiagen TissueLyser (Germantown, MD) at 30 Hz for four min, centrifuged at 10,000 x g for five min and stored at -80°C.

**Plaque assay:** Infectious SARS-CoV-2 was detected using a Vero cell plaque assay. Briefly, samples were serially diluted 10-fold in DMEM with 1% bovine serum albumin (BSA) (both from Thermo Fisher) starting at an initial dilution of 1:8. 12-well plates of confluent Vero CCL-81 cells (ATCC) were inoculated with 125 µL of each dilution and incubated at 37°C and 5% CO<sub>2</sub> for one hr. After incubation, each cell monolayer was overlaid with 0.5% agarose (Invitrogen, Carlsbad, CA) diluted in DMEM with 5% fetal bovine serum (FBS) and 1X antibiotic-antimycotic (both from Thermo Fisher) and incubated for three days at 5% CO<sub>2</sub> and 37°C in a humidified incubator. Cell monolayers were then fixed with 4% formalin for 30 min, agar plugs were gently removed, and viable cells were stained for 10 min with 0.05% crystal violet (Sigma, St. Louis, MO) in 20% ethanol, then rinsed with water. Plaques were counted in each well. Viral titers were recorded as the reciprocal of the highest dilution where plaques were noted (PFU per swab or mg tissue).

**Necropsy tissue processing and histopathology:** At necropsy, lung was inflated and tissues were fixed for 48 hrs at room temperature (RT) with a 10-fold volume of 10% neutral buffered formalin (Thermo Fisher). A subset of tissues, including lung, brain, liver, spleen, heart, peripheral lymph nodes, eyes and nasal cavity, were embedded in paraffin, thin-sectioned (four µm) and stained

routinely with hematoxylin and eosin (H&E). H&E slides were scanned to 40x magnification using an Aperio slide scanner with a magnification doubler and a resolution of 0.25  $\mu\text{m}/\text{pixel}$ . Image files were uploaded on a Leica hosted web-based site and a board certified veterinary anatomic pathologist blindly evaluated sections for SARS-CoV-2 induced histologic lesions. Using ImageJ (Fiji, NIH), the total lung surface area in each section and then approximate affected area (i.e., the surface area of lung that appeared abnormal at subgross magnification due to inflammation, necrosis, hemorrhage and/or edema) were measured twice, measurements were averaged, and the percent of affected lung surface area was calculated. For immunofluorescence, fixed tissue was cryoprotected by rinsing overnight in PBS at 4°C, followed by transfer into 30% sucrose (Thermo Fisher) in 1X PBS overnight, frozen on dry ice in Andwin Scientific Tissue-Tek cryomolds filled with Tissue-plus OCT compound, wrapped in parafilm (all Thermo Fisher), and stored at -20°C.

**In situ hybridization (ISH):** Colorimetric ISH was performed according to the manufacturer's instructions (44), using the RNAscope 2.5 HD Red Reagent Kit (Advanced Cell Diagnostics [ACD], Newark, CA) and RNAscope Probe - V-nCoV2019-S (ACD, cat #526 848561). RNAscope Negative Control Probe - DapB (ACD, cat #310043) and lung tissue from a SARS-CoV-2 uninfected control animal hybridized with the SARS-CoV-2 probes served as negative controls. RNAscope Probe - Mau-Ppib (ACD, cat #890851) served a positive control. Briefly, each five  $\mu\text{m}$  deparaffinized section was pretreated with 1x Target Retrieval Buffer at 100°C for 15 min and Protease Plus at 40°C for 30 min prior to hybridization at 40°C for two hrs. This was followed by a cascade of signal amplification and signal detection using a Fast Red solution for 10 min at RT. Slides were counterstained with hematoxylin, dehydrated, cover-slipped, and scanned to 40x

magnification as described above. Positive staining was identified as red cytoplasmic staining. ISH-positive cells were identified based on location and cell morphology.

**Immunohistochemistry (IHC):** Slides were deparaffinized in xylene and 100% ETOH. Endogenous peroxidases were blocked by placing slides in 3% H<sub>2</sub>O<sub>2</sub> in methanol (all Thermo Fisher) for 30 min. After rehydration, Iba1, CD3 and CD79a slides underwent heat-induced antigen retrieval for 30 min using dH<sub>2</sub>O (Iba1) or citrate solution (CD3, CD79a) composed of 20 mL 10X stock solution (12.9 g citric acid, trisodium salt, anhydrous, 500 mL dH<sub>2</sub>O, 10 mL 1N HCl to adjust pH to 6.1, 2.5 mL tween 20 [all Thermo Fisher]) and 180 mL dH<sub>2</sub>O. vWF slides were incubated for 10 min with proteinase K (Agilent Dako, Santa Clara, CA cat #S3020). Following antigen retrieval, all slides were blocked for 20 min in 20 mL normal horse serum (Vector Laboratories, Burlingame, CA) diluted in 180 mL PBS. Antibodies used for IHC were: Rabbit polyclonal anti-Iba1 at 1:600 dilution (Wako Chemicals, USA, Richmond, VA, cat #19-19741); anti-rat CD3 clone CD3-12 at 1:10 dilution (supplied by Dr. Peter Moore, University of California, Davis); mouse anti-human CD79a clone HM57 at 1:100 dilution (Bio Rad, Hercules, CA, cat #MCA2538H); rabbit polyclonal anti-vWF at 1:2000 dilution (Agilent Dako, cat #A0082). Slides were incubated with primary antibodies at RT for one hr with gentle agitation, then allowed to incubate at RT for 30 minutes with rat-on-canine (CD3), mouse-on-canine (CD79a), or rabbit-on-canine (Iba1 and vWF) horseradish peroxidase-polymer (all from BioCare Medical, Pacheco, CA). Colorimetric detection was performed according to manufacturer's instructions using Vector® NovaRED® peroxidase substrate kit (Vector) and slides were counterstained with hematoxylin and bluing reagent (both from Thermo Fisher) prior to mounting.

**Immunofluorescence (IFA):** 12  $\mu\text{m}$  frozen sections of cryoprotected lung tissue were cut using a Leica CM1860 cryotome (Leica Biosystems, Deer Park, IL) and slides were placed in blocking buffer composed of 2% BSA, 0.3% Triton x-100 (Thermo Fisher) and 10% normal donkey serum (Jackson Laboratories, West Grove, PA) in 1X PBS for one hr at RT. Slides were incubated overnight with primary antibodies at 4°C, including: Mouse anti-pan cytokeratin (Lu5) at 1:100 dilution (BioCare Medical, cat #CM043C); mouse anti-CD31/PECAM-1 antibody (JC/70A) at 1:20 dilution (Novus Biologicals, Littleton, CO, cat #NB600-562); rat anti-mouse CD41 (MWReg30) at 1:100 dilution (BD Pharmingen, Franklin Lakes, NJ, cat #553847); mouse anti-human CD61 (Y2/51) at 1:50 dilution (BioRad, Hercules, CA, cat #MCA2588); and rabbit polyclonal anti-SARS2 NP at 1:10,000 dilution (Sino Biologicals, Waye, PA, cat #40143-R019). Next, slides were washed in PBS and allowed to incubate with secondary antibodies, including donkey anti-rabbit AF-594 (Invitrogen, Waltham, MA, cat #A21207), donkey anti-mouse AF-488 (Invitrogen, cat #A21202), and goat anti-rat AF-488 (Invitrogen, cat #A48262) diluted 1:250 in PBS + 10% donkey serum, for one hr. Slides were washed again in PBS and mounted using prolong Gold antifade with DAPI (Thermo Fisher, cat #P36931). Images were acquired on a Leica SP8 STED 3X confocal microscope controlled by Leica LAS X software using a 20x/0.75 mm HC PL APO CS2 objective. Z-stacks were acquired with a 1.04  $\mu\text{m}$  step size. Images were processed using Fiji (ImageJ 1.53c) (378).

**Transmission electron microscopy (TEM):** After fixation in 2.5% glutaraldehyde (Ted Pella, Redding, CA) and 2% paraformaldehyde (Ted Pella) in 0.1 M sodium phosphate buffer (Thermo Fisher), tissues were post-fixed in 1% osmium tetroxide (Electron Microscopy Sciences [EMS], Hatfield, PA) in 0.1 M sodium phosphate buffer for one hr, dehydrated for 30 min each in 50%

EtOH, 75% EtOH and 95% EtOH, and finally dehydrated twice for 20 min in 100% EtOH and placed in propylene oxide (EMS) twice for 15 min. Samples were pre-infiltrated overnight in a 1:1 ratio of propylene oxide to resin (composed of 450 mL dodecenyl succinic anhydride, 250 mL araldite 6005 [both from EMS], 82.5 mL Epon 812 [Polysciences Inc, Warrington, PA], 12.5 ml dibutyl phthalate [Ted Pella], and 450 L benzyldimethylamine [EMS]). The following day tissues were infiltrated in 100% resin for 5 hrs, embedded with fresh resin, and polymerized at 60°C overnight. Embedded tissues were sectioned with a Leica EM UC6 ultramicrotome (Leica Biosystems, Deer Park, IL) at a thickness of 90 nm, collected on copper mesh grids (EMS), and stained with 4% aqueous uranyl acetate for 20 min and for two min in 0.2% lead citrate (both from Ted Pella) in 0.1 N NaOH (Thermo Fisher). TEM imaging was done on FEI Talos L120C at 80 kv using a Ceta-M 16MP camera (both from Thermo Fisher).

**Data analysis:** Quantitative measurements of abnormal lung surface area were performed using ImageJ. GraphPad Prism was used for statistical analyses and to create graphs. P-values of less than or equal to 0.05 were considered statistically significant.

## Supplemental Material

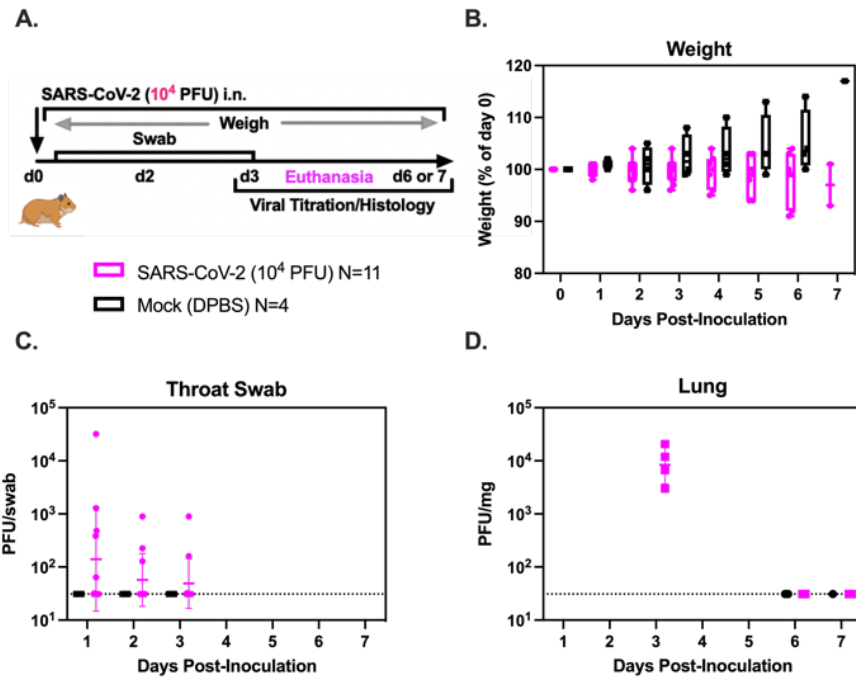


**Figure S1. Validation of the Syrian golden hamster model.** (A) Summary of experimental design. 8 to 10-week-old (N = 11) Syrian golden hamsters were inoculated intranasally with  $10^4$  PFU SARS-CoV-2/human/USA/CA-CZB-59X002/2020 (GenBank #MT394528) a representative viral strain isolated from the U.S. west coast early in the pandemic that had not previously been tested in animals (now referred to as ancestral B.1.1.7 [614G]), or the same volume of DPBS (N=4). Hamsters were weighed and oropharyngeally swabbed daily, then euthanized at three, six, or seven days post inoculation (dpi). (B) Hamster body weight over time (dpi) shown as percent of weight at day zero. Infectious virus recovered from daily oropharyngeal swabs (C) and from lung at necropsy (D). Infectious virus was recovered from the upper respiratory tract of 6 out of 11 SARS-CoV-2 inoculated hamsters between one and three dpi (6 out of 11 hamsters inoculated with SARS-CoV-2 had at least one positive swab). Infectious virus was only detected in the lung of hamsters at three dpi. PFU = plaque forming units; i.n. = intranasal.

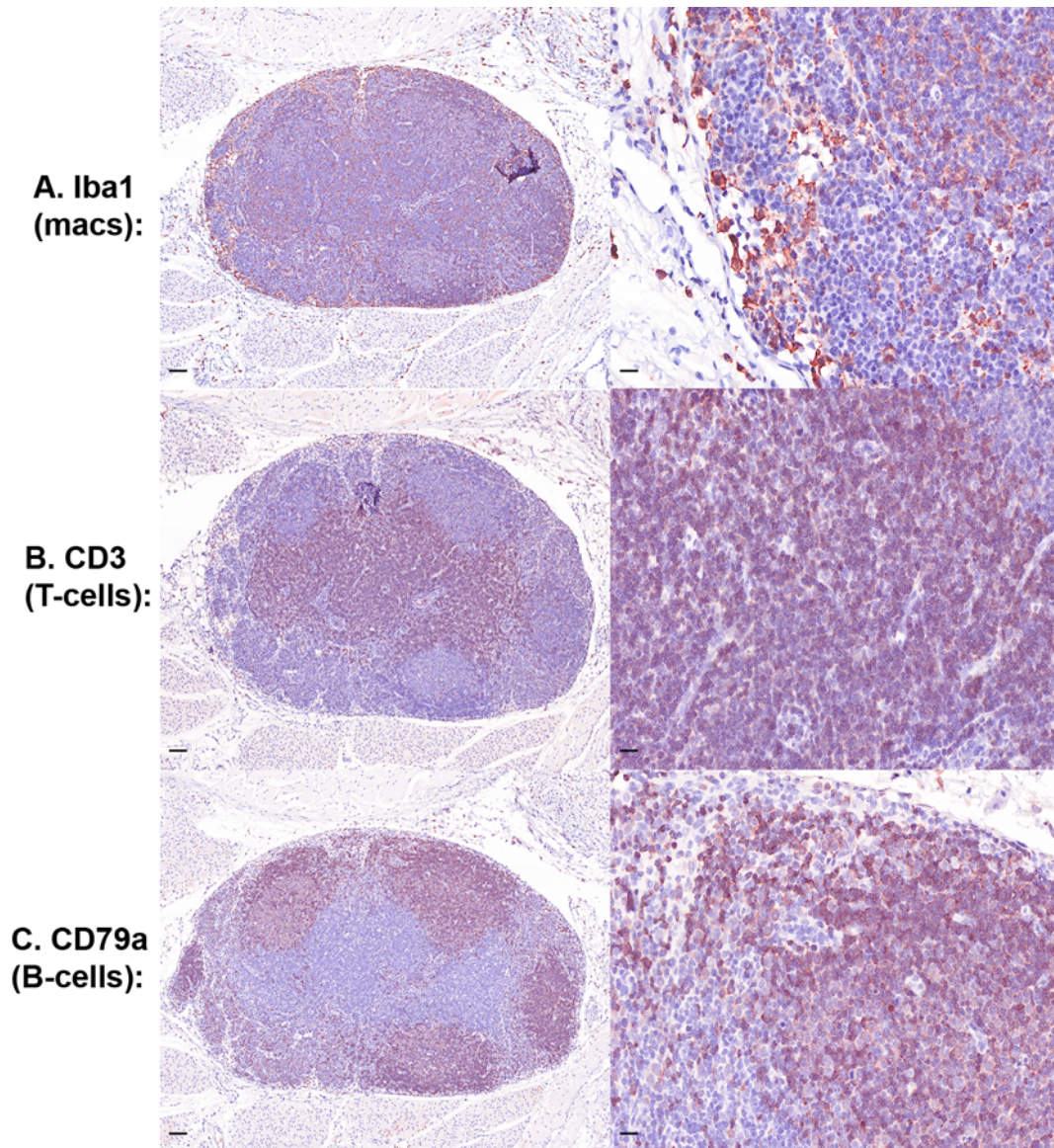


**Figure S2. Immunohistochemistry (IHC) internal control tissue from a SARS-CoV-2 inoculated hamster.** Mediastinal lymph node serves as the internal control for IHC staining with antibodies against macrophages (Iba1) (A), T-lymphocytes (CD3) (B), and B-lymphocytes (CD79a) (C). Positive cells exhibit intracytoplasmic or membranous brown staining; macs = macrophages; T-cell = T-lymphocytes; B-cell = B-lymphocytes; scale bars, left column = 0.1mm; scale bars, right column = 20  $\mu$ m.

**Supplemental Table 1. Histopathology scoring criteria for pulmonary vasculature**

<b>Perivascular edema/fibrin (0-3)</b>	(1) rare perivascular edema/fibrin affecting <10% of the section's vessels (2) mild to mod perivascular edema affecting 10-25% of the section's vessels (3) widespread perivascular edema affecting >25% of the section's vessels
<b>Perivascular inflammation (0-3)</b>	(1) mild perivascular primarily mononuclear inflammation (composed primarily of macs, lymphs +/- few scattered neuts) affecting <10% of the section's vessels (2) Moderate mononuclear to mixed perivascular inflammation affecting 10-25% of the section's vessels (3) widespread severe mononuclear to mixed perivascular inflammation affecting >25% of the section's vessels and/or frequently expanding/osbscuring vessel wall
<b>Endotheliitis (0-3)</b>	(1) rare endothelialitis affecting <10% of the section's vessels (2) mild to mod endothelialitis affecting 10-25% of the section's vessels (3) widespread endothelialitis affecting >25% of the section's vessels
<b>Vasculitis/thrombi (0,1)</b>	(0) absent; (1) present
<b>Total vascular score</b>	<b>0-10</b>

### **Acknowledgements**

We thank Bradley Shibata for assistance with transmission electron microscopy, Zhong Min-Ma for assistance with ISH, and the pathology staff at the UC Davis School of Veterinary Medicine.

**Financial Support:** This work was supported by intramural funding from the Center for Immunology and Infectious Diseases, UC Davis and NIH/R01-AI118590 (CJM); the Graduate Student Support Program, UC Davis (EEB); the University of California Davis Office of Research, and Schools of Medicine and Veterinary Medicine (LLC); and the U.S. Army Medical Center of Excellence Long Term Health Education and Training Program (EEB).

## **EPILOGUE**

ZIKV and SARS-CoV-2 instigated two significant 21st century pandemics, and both remain important public health threats. A variety of animal models have been validated to investigate mechanisms of ZIKV and SARS-CoV-2 dissemination, pathogenesis, and host immune response. Here, I used two well-documented animal models of human disease (male and pregnant female rhesus macaques and Syrian golden hamsters, respectively) to further define several long-term sequelae to ZIKV infection and COVID-19 disease in humans.

The male macaque reproductive tract, including accessory sex organs, serves as a reservoir for ZIKV RNA and infectious virus. ZIKV RNA localized to epithelial cells and stem cells of the testis, epididymis, seminal vesicle, and prostate gland, and persisted in the male reproductive tract for up to 60 dpi. This suggests that the potential for sexual transmission of ZIKV remains even after viremia has resolved and raises significant concerns regarding the risks of male sexual transmission to both men and periconceptional and non-pregnant women, as well as in the context of assisted fertility procedures such as sperm donation. ZIKV infection was associated with inflammation in the epididymis and prostate gland, with viral RNA detected in infiltrating macrophages associated with foci of epididymal duct rupture and epididymitis. Overall, sexually mature males were at significantly higher risk for genital ZIKV persistence and urogenital sequelae, though mechanisms of viral entry into the male reproductive tract and the pathogenesis of injury to genital tissues remain unclear.

Two 24 month old juvenile rhesus macaques who were exposed prenatally to ZIKV but were normocephalic at birth exhibited neuroanatomic developmental abnormalities within the visual

pathway of the CNS, specifically the LGN. This is consistent with recently reported findings in fetal macaques from a similar cohort of animals who were exposed to ZIKV during the first or second trimester, where neuroanatomical quantification of specific brain regions revealed macrostructural neurodevelopmental abnormalities within the cerebral cortex, including the LGN, likely secondary to neuroinflammatory mechanisms. Notably, in addition to the structural abnormalities within the LGN, one infant exhibited postnatal ocular developmental lesions. Our findings may help explain why some normocephalic newborns whose mothers were ZIKV-infected during pregnancy, but who exhibit no observable congenital defects, develop ocular lesions and visual deficits over time.

Taken together, these results support the hypotheses that 1) the male genital tissues including accessory sex glands such as the seminal vesicle and prostate gland serve as a reservoir for ZIKV; 2) that genital lesions and impaired male fertility are possible, if not likely, sequelae to ZIKV infection; and 3) that early prenatal ZIKV exposure is associated with developmental abnormalities in the CNS of juvenile rhesus macaques. Furthermore, both our identification ZIKV RNA and infectious virus in frozen genital tissue samples (for up to 60 dpi and 50 dpi respectively) and our detection of ZIKV RNA in frozen semen, have significant implications for the safety of assisted fertility procedures involving donated reproductive tissues such as sperm, oocytes, and embryonic tissue.

By extrapolating our findings from ZIKV-infected macaques, we can significantly increase our understanding of persistent ZIKV infection in men and long-term neurodevelopmental sequelae in children infected *in utero*. Additional, controlled experiments are clearly needed, particularly to

define: 1) mechanisms of viral entry into the male reproductive tract; 2) effects of ZIKV infection on the histomorphology of genital tissues and fertility, including detailed analysis of semen, in sexually mature ZIKV-infected males; 3) the relationship between sexual transmission to naïve periconceptional woman and risks of vertical transmission to the fetus; and 4) long-term neurologic consequences of both prenatal and postnatal ZIKV infection.

COVID-19 disease varies from asymptomatic to severe respiratory disease, progressing to ARDS, multiorgan dysfunction, and death in a subset of patients. Clinical evidence of coagulopathy and microscopic indicators of pulmonary vascular damage are increasingly reported; however, published autopsy data in human patients remain relatively scarce and SARS-CoV-2 induced vascular lesions have not been fully characterized in humans or animal models. Here, I used the well-established Syrian golden hamster model to define SARS-CoV-2 induced vascular pathologies. Specifically, I show for the first time in hamsters that regions of active SARS-CoV-2 induced pulmonary inflammation exhibit ultrastructural evidence of endothelial damage, with platelet marginalization and marked perivascular and subendothelial mononuclear inflammation composed primarily of macrophages, and that SARS-CoV-2 antigen/RNA is not associated with affected blood vessels.

The histopathologic pulmonary lesions identified in SARS-CoV-2 inoculated hamsters, including progressive, moderate to severe broncho-interstitial pneumonia and alveolar damage with prominent perivascular and subendothelial inflammation, are comparable with the limited published autopsy data available from severe COVID-19 patients. This further supports the hamster as a useful model for human COVID-19 disease. TEM and a variety of special staining

techniques indicate that regions of active pulmonary inflammation and endotheliitis in SARS-CoV-2 inoculated hamsters are characterized by ultrastructural evidence of endothelial damage with platelet marginalization and perivascular/subendothelial macrophage infiltration. SARS-CoV-2 antigen/RNA was not identified within endothelial cells. Taken together, these findings suggest that the prominent microscopic vascular lesions in SARS-CoV-2 inoculated hamsters (and by extrapolation, humans) are likely due to indirect endothelial damage followed by platelet and macrophage infiltration.

Immune dysregulation resulting in excessive production of pro-inflammatory cytokines, endothelial damage, and platelet hyperactivation is likely a major driving force behind the hypercoagulable state and microthrombosis observed in severe COVID-19 disease. Although this was an observational study lacking sufficient power for statistical analysis, both the lack of viral association with inflamed vessels and published data support an indirect mechanism linking inflammation, endothelial damage and platelet hyperactivation in severe cases of COVID-19 disease. Our results suggest that novel therapeutics targeting the dysregulated immune system (i.e., cytokine production or NETosis) may prove effective medical countermeasures against COVID-19 disease. Further study regarding viral effects on pericytes and endothelium-platelet-leukocyte interactions is necessary to fully understand the pathogenesis of COVID-19 associated coagulopathy and thrombosis. To our knowledge, this is the first in-depth microscopic and ultrastructural evaluation of COVID-19 associated vascular lesions in Syrian golden hamsters.

## References

1. Morse SS, Mazet JAK, Woolhouse M, Parrish CR, Carroll D, Karesh WB, et al. Prediction and prevention of the next pandemic zoonosis. 2012;380.
2. Cleaveland S, Laurenson MK, Taylor LH. Diseases of humans and their domestic mammals: Pathogen characteristics, host range and the risk of emergence. *Philos Trans R Soc B Biol Sci.* 2001;356(1411):991–9.
3. Centers for Disease Control and Prevention (CDC). Principles of Epidemiology in Public Health Practice: An introduction to applied epidemiology and biostatistics. 3rd ed. U.S. DEPARTMENT OF HEALTH AND HUMAN SERVICES. Atlanta; 2012. 1–547 p.
4. Taylor LH, Latham SM, Woolhouse MEJ. Risk factors for human disease emergence. *Philos Trans R Soc B Biol Sci.* 2001;356(1411):983–9.
5. Alexander KA, Carlson CJ, Lewis BL, Getz WM, Marathe M V., Eubank SG, et al. The Ecology of Pathogen Spillover and Disease Emergence at the Human- Wildlife- Environment Interface. *Connect Between Ecol Infect Dis.* 2018;5(April):267–98.
6. Daszak P, Cunningham AA, Hyatt AD. Emerging infectious diseases of wildlife - Threats to biodiversity and human health. *Science (80- ).* 2000;287(5452):443–9.
7. Hueffer K, O’Hara TM, Follmann EH. Adaptation of mammalian host-pathogen interactions in a changing arctic environment. *Acta Vet Scand.* 2011;53(1):1–8.
8. Olival KJ, Hosseini PR, Zambrana-Torrel C, Ross N, Bogich TL, Daszak P. Host and viral traits predict zoonotic spillover from mammals. *Nature [Internet].* 2017;546(7660):646–50. Available from: <http://dx.doi.org/10.1038/nature22975>
9. Anez G, Chancey C, Grinev A, Rios M. Dengue virus and other arboviruses: a global view of risks. *ISBT Sci Ser.* 2012;7(1):274–82.
10. Weaver SC, Reisen WK. Present and future arboviral threats. 2010;85:328–45.
11. Kenney JL, Brault AC. The Role of Environmental, Virological and Vector Interactions in Dictating Biological Transmission of Arthropod-Borne Viruses by Mosquitoes. Vol. 89. Elsevier Inc.; 2014. 39–83 p.
12. Mayton EH, Tramonte AR, Wearing HJ, Christofferson RC, Christofferson RC. Age-structured vectorial capacity reveals timing, not magnitude of within-mosquito dynamics is critical for arbovirus fitness assessment. *Parasites and Vectors [Internet].* 2020;13(1):1–13. Available from: <https://doi.org/10.1186/s13071-020-04181-4>
13. Franz AWE, Kantor AM, Passarelli AL, Clem RJ. Tissue barriers to arbovirus infection in mosquitoes. *Viruses.* 2015;7(7):3741–67.
14. Jaworski P (Creative C. Internal Anatomy of an Insect [Internet]. 2019 [cited 2022 Jan 24]. Available from: <https://www.thoughtco.com/internal-anatomy-of-an-insect>
15. Weaver SC, Charlier C, Vasilakis N, Lecuit M. Zika, Chikungunya, and Other Emerging Vector-Borne Viral Diseases.
16. Vasilakis N, Weaver SC. Chapter 1 The History and Evolution of Human Dengue Emergence. *Adv Virus Res.* 2008;72(08):1–76.
17. Fernandez-Garcia MD, Mazzon M, Jacobs M, Amara A. Pathogenesis of Flavivirus Infections: Using and Abusing the Host Cell. *Cell Host Microbe [Internet].* 2009;5(4):318–28. Available from: <http://dx.doi.org/10.1016/j.chom.2009.04.001>
18. Pierson TC, Diamond MS. The continued threat of emerging flaviviruses. *Nat Microbiol [Internet].* 2020;5(6):796–812. Available from: <http://dx.doi.org/10.1038/s41564-020-0714-0>

19. Bryant JE, Holmes EC, Barrett ADT. Out of Africa: A molecular perspective on the introduction of yellow fever virus into the Americas. *PLoS Pathog.* 2007;3(5):0668–73.
20. World Health Organization (WHO). Yellow Fever [Internet]. [cited 2022 Jan 11]. Available from: <https://www.who.int/news-room/fact-sheets/detail/yellow-fever>
21. Monath TP, Vasconcelos PFC. Yellow fever. *J Clin Virol* [Internet]. 2015;64:160–73. Available from: <http://dx.doi.org/10.1016/j.jcv.2014.08.030>
22. World Health Organization (WHO). Dengue and severe dengue [Internet]. [cited 2022 Jan 11]. Available from: <https://www.who.int/news-room/fact-sheets/detail/dengue-and-severe-dengue>
23. Kraemer MUG, Sinka ME, Duda KA, Mylne AQN, Shearer FM, Barker CM, et al. The global distribution of the arbovirus vectors *Aedes aegypti* and *Ae. Albopictus*. *Elife.* 2015;4(JUNE2015):1–18.
24. Chong HY, Leow CY, Abdul Majeed AB, Leow CH. Flavivirus infection—A review of immunopathogenesis, immunological response, and immunodiagnosis. *Virus Res* [Internet]. 2019;274(June):197770. Available from: <https://doi.org/10.1016/j.virusres.2019.197770>
25. Katzelnick LC, Gresh L, Halloran ME, Mercado JC, Kuan G, Gordon A, et al. Antibody-dependent enhancement of severe dengue disease in humans. *Science* (80- ). 2017;358(6365):929–32.
26. Yun SI, Lee YM. Japanese encephalitis: The virus and vaccines. *Hum Vaccines Immunother.* 2014;10(2):263–79.
27. Campbell GL, Hills SL, Fischer M, Jacobson JA, Hoke CH, Hombach JM, et al. Estimated global incidence of Japanese encephalitis: A systematic review. *Bull World Health Organ.* 2011;89(10):766–74.
28. Hayes EB, Komar N, Nasci RS, Montgomery SP, Leary DRO, Campbell GL. Epidemiology and transmission dynamic of West Nile Virus Disease. *Emerg Infect Dis* [www.cdc.gov/eid](http://www.cdc.gov/eid). 2005;11(8):1167–73.
29. Petersen LR, Brault AC, Nasci RS. West Nile virus: Review of the literature. *JAMA - J Am Med Assoc.* 2013;310(3):308–15.
30. ArboNET, Arboviral Diseases Branch C for DC and P (CDC). West Nile Virus: Statistics and Maps [Internet]. 2020 [cited 2022 Jan 11]. Available from: <https://www.cdc.gov/westnile/statsmaps/cumMapsData.html#seven>
31. Wheeler SS, Taff CC, Reisen WK, Townsend AK. Mosquito blood-feeding patterns and nesting behavior of American crows, an amplifying host of West Nile virus. *Parasites and Vectors* [Internet]. 2021;14(1):1–12. Available from: <https://doi.org/10.1186/s13071-021-04827-x>
32. Swetnam DM, Stuart JB, Young K, Maharaj PD, Fang Y, Garcia S, et al. Movement of St. Louis encephalitis virus in the western United States, 2014–2018. *PLoS Negl Trop Dis* [Internet]. 2020;14(6):1–22. Available from: <http://dx.doi.org/10.1371/journal.pntd.0008343>
33. Diaz A, Coffey LL, Burkett-Cadena N, Day JF. Reemergence of St. Louis encephalitis virus in the Americas. *Emerg Infect Dis.* 2018;24(12):2150–7.
34. Centers for Disease Control and Prevention (CDC). St. Louis Encephalitis [Internet]. [cited 2022 Jan 11]. Available from: <https://www.cdc.gov/sle/index.html>
35. Fang Y, Reisen WK. Previous infection with West Nile or St. Louis encephalitis viruses provides cross protection during reinfection in house finches. *Am J Trop Med Hyg.*

- 2006;75(3):480–5.
36. Ottendorfer CL. Impact of the West Nile virus on the natural history of St. Louis encephalitis virus in Florida [Internet]. ProQuest Dissertations and Theses. 2008. Available from: [http://sfx.scholarsportal.info/guelph/docview/304461002?accountid=11233%5Cnhttp://sfx.scholarsportal.info/guelph?url\\_ver=Z39.88-2004&rft\\_val\\_fmt=info:ofi/fmt:kev:mtx:dissertation&genre=dissertations+%2526+theses&sid=ProQ:ProQuest+Dissertations+%2526+These](http://sfx.scholarsportal.info/guelph/docview/304461002?accountid=11233%5Cnhttp://sfx.scholarsportal.info/guelph?url_ver=Z39.88-2004&rft_val_fmt=info:ofi/fmt:kev:mtx:dissertation&genre=dissertations+%2526+theses&sid=ProQ:ProQuest+Dissertations+%2526+These)
  37. Song BH, Yun SI, Woolley M, Lee YM. Zika virus: History, epidemiology, transmission, and clinical presentation. *J Neuroimmunol* [Internet]. 2017;308:50–64. Available from: <http://dx.doi.org/10.1016/j.jneuroim.2017.03.001>
  38. Clé M, Beck C, Salinas S, Lecollinet S, Gutierrez S, Van de Perre P, et al. Usutu virus: A new threat? *Epidemiol Infect.* 2019;147:1–11.
  39. Holbrook MR. Historical perspectives on flavivirus research. *Viruses.* 2017;9(5):1–19.
  40. Centers for Disease Control and Prevention (CDC). Viral Hemorrhagic Fevers (VHFs): Flaviviridae [Internet]. [cited 2022 Jan 14]. Available from: <https://www.cdc.gov/vhf/virus-families/flaviviridae.html>
  41. Mackenzie J. Wrapping things up about virus RNA replication. *Traffic.* 2005;6(11):967–77.
  42. Sirohi D, Kuhn RJ. Zika Virus Structure, Maturation, and Receptors. Vol. 216, *Journal of Infectious Diseases.* 2017.
  43. Heinz FX, Stiasny K. The Antigenic Structure of Zika Virus and Its Relation to Other Flaviviruses: Implications for Infection and Immunoprophylaxis. *Microbiol Mol Biol Rev.* 2017;81(1).
  44. Mackenzie JM, Westaway EG. Assembly and Maturation of the Flavivirus Kunjin Virus Appear To Occur in the Rough Endoplasmic Reticulum and along the Secretory Pathway, Respectively. *J Virol.* 2001;75(22):10787–99.
  45. Yu I, Zhang W, Holdaway HA, Li L, Kostyuchenko VA, Chipman PR, et al. Structure of the Immature Dengue Virus at Low pH Primes Proteolytic Maturation. 2008;13(March):1834–8.
  46. Cui J, Li F, Shi ZL. Origin and evolution of pathogenic coronaviruses. *Nat Rev Microbiol* [Internet]. 2019;17(3):181–92. Available from: <http://dx.doi.org/10.1038/s41579-018-0118-9>
  47. Wiersinga WJ, Rhodes A, Cheng AC, Peacock SJ, Prescott HC. Pathophysiology, Transmission, Diagnosis, and Treatment of Coronavirus Disease 2019 (COVID-19): A Review. *JAMA - J Am Med Assoc.* 2020;324(8):782–93.
  48. V'kovski P, Kratzel A, Steiner S, Stalder H, Thiel V. Coronavirus biology and replication: implications for SARS-CoV-2. *Nat Rev Microbiol* [Internet]. 2021;19(3):155–70. Available from: <http://dx.doi.org/10.1038/s41579-020-00468-6>
  49. Su S, Wong G, Shi W, Liu J, Lai ACK, Zhou J, et al. Epidemiology, Genetic Recombination, and Pathogenesis of Coronaviruses. *Trends Microbiol* [Internet]. 2016;24(6):490–502. Available from: <http://dx.doi.org/10.1016/j.tim.2016.03.003>
  50. Goldsmith CS, Tatti KM, Ksiazek TG, Rollin PE, Comer JA, Lee WW, et al. Ultrastructural Characterization of SARS Coronavirus. *Emerg Infect Dis.* 2004;10(2):320–6.
  51. World Health Organization. Middle East respiratory syndrome coronavirus (MERS-CoV)

- [Internet]. 2019 [cited 2022 Jan 6]. Available from: [https://www.who.int/news-room/fact-sheets/detail/middle-east-respiratory-syndrome-coronavirus-\(mers-cov\)](https://www.who.int/news-room/fact-sheets/detail/middle-east-respiratory-syndrome-coronavirus-(mers-cov))
52. World Health Organization (WHO). WHO Coronavirus (COVID-19) Dashboard [Internet]. 2022 [cited 2022 Feb 7]. Available from: <https://covid19.who.int>
  53. Chen Y, Liu Q, Guo D. Emerging coronaviruses: Genome structure, replication, and pathogenesis. *J Med Virol*. 2020;92(4):418–23.
  54. Kim D, Lee JY, Yang JS, Kim JW, Kim VN, Chang H. The Architecture of SARS-CoV-2 Transcriptome. *Cell* [Internet]. 2020;181(4):914–921.e10. Available from: <https://doi.org/10.1016/j.cell.2020.04.011>
  55. Lee PI, Hsueh PR. Emerging threats from zoonotic coronaviruses—from SARS and MERS to 2019-nCoV. *J Microbiol Immunol Infect* [Internet]. 2020;53(3):365–7. Available from: <https://doi.org/10.1016/j.jmii.2020.02.001>
  56. Hoffmann M, Kleine-Weber H, Schroeder S, Krüger N, Herrler T, Erichsen S, et al. SARS-CoV-2 Cell Entry Depends on ACE2 and TMPRSS2 and Is Blocked by a Clinically Proven Protease Inhibitor. *Cell*. 2020;181(2):271–280.e8.
  57. Hopfer H, Herzig MC, Gosert R, Menter T, Hench J, Tzankov A, et al. Hunting coronavirus by transmission electron microscopy – a guide to SARS-CoV-2-associated ultrastructural pathology in COVID-19 tissues. *Histopathology*. 2021;78(3):358–70.
  58. Du Toit A. Coronavirus replication factories. *Nat Rev Microbiol* [Internet]. 2020;18(8):411. Available from: <http://dx.doi.org/10.1038/s41579-020-0406-z>
  59. Snijder EJ, Limpens RWAL, de Wilde AH, de Jong AWM, Zevenhoven-Dobbe JC, Maier HJ, et al. A unifying structural and functional model of the coronavirus replication organelle: Tracking down RNA synthesis. *PLoS Biol*. 2020;18(6):1–25.
  60. Harrison AG, Lin T, Wang P. Mechanisms of SARS-CoV-2 Transmission and Pathogenesis. *Trends Immunol* [Internet]. 2020;41(12):1100–15. Available from: <https://doi.org/10.1016/j.it.2020.10.004>
  61. Dick GWA, Kitchen SF, Haddow AJ. Zika virus. I. Isolations and serological specificity. *Trans R Soc Trop Med Hyg*. 1952;46(5):509–20.
  62. Weaver SC, Costa F, Garcia-Blanco MA, Ko AI, Ribeiro GS, Saade G, et al. Zika virus: History, emergence, biology, and prospects for control. *Antiviral Res* [Internet]. 2016;130:69–80. Available from: <https://www.sciencedirect.com/science/article/pii/S0166354216301206>
  63. Macnamara F. Zika virus: A report on three cases of human infection during an epidemic of jaundice in Nigeria. *Trans R Soc Trop Med Hyg*. 1954;48(2):139–45.
  64. Musso D, Ko AI, Baud D. Zika Virus Infection — After the Pandemic. *N Engl J Med*. 2019;381(15):1444–57.
  65. Gubler DJ, Vasilakis N, Musso D. History and Emergence of Zika Virus. *J Infect Dis*. 2017;216(January):S860–7.
  66. Marchette NJ, Garcia R, Rudnick A. Isolation of Zika virus from *Aedes aegypti* mosquitoes in Malaysia. *Am J Trop Med Hyg*. 1969;18(3):411–5.
  67. Olson JG, Ksiazek TG, Suhandiman G, Triwibowo V. Zika virus, a cause of fever in central Java, Indonesia. *Trans R Soc Trop Med Hyg*. 1981;75(3):389–93.
  68. Wikan N, Smith DR. Zika virus: History of a newly emerging arbovirus. *Lancet Infect Dis* [Internet]. 2016;16(7):e119–26. Available from: [http://dx.doi.org/10.1016/S1473-3099\(16\)30010-X](http://dx.doi.org/10.1016/S1473-3099(16)30010-X)
  69. Aliota MT, Bassit L, Bradrick SS, Cox B, Garcia-Blanco MA, Gavegnano C, et al. Zika in

- the Americas, year 2: What have we learned? What gaps remain? A report from the Global Virus Network. *Antiviral Res.* 2017;144:223–46.
70. Song BH, Yun SI, Woolley M, Lee YM. Zika virus: History, epidemiology, transmission, and clinical presentation. *J Neuroimmunol.* 2017;308:50–64.
  71. Duffy MR, Chen TH, Hancock WT, Powers AM, Kool JL, Lanciotti RS, et al. Zika virus outbreak on Yap Island, Federated States of Micronesia. *N Engl J Med.* 2009;360(24):2536–43.
  72. Cao-Lormeau VM, Roche C, Teissier A, Robin E, Berry A-L, Mallet H-P, et al. Zika virus, French Polynesia, South Pacific, 2013. *Emerg Infect Dis* [Internet]. 2014;20(6):1085–6. Available from: [https://wwwnc.cdc.gov/eid/article/20/6/14-0138\\_article](https://wwwnc.cdc.gov/eid/article/20/6/14-0138_article)
  73. Musso D, Nilles EJ, Cao-Lormeau VM. Rapid spread of emerging Zika virus in the Pacific area. *Clin Microbiol Infect.* 2014;20(10):O595–6.
  74. Papageorghiou AT, Kennedy SH, Salomon LJ, Altman DG, Ohuma EO, Stones W, et al. The INTERGROWTH-21st fetal growth standards: Toward the global integration of pregnancy and pediatric care. *Am J Obstet Gynecol* [Internet]. 2018;218(2):S630–40. Available from: <http://dx.doi.org/10.1016/j.ajog.2018.01.011>
  75. Coffey LL, Keesler RI, Pesavento PA, Woolard K, Singapuri A, Watanabe J, et al. Intraamniotic Zika virus inoculation of pregnant rhesus macaques produces fetal neurologic disease. *Nat Commun* [Internet]. 2018;9(1):1–12. Available from: <http://dx.doi.org/10.1038/s41467-018-04777-6>
  76. Mohr EL, Block LN, Newman CM, Stewart LM, Koenig M, Semler M, et al. Ocular and uteroplacental pathology in a macaque pregnancy with congenital Zika virus infection. Vol. 13, *PLoS ONE.* 2018.
  77. Russo FB, Jungmann P, Beltrão-Braga PCB. Zika infection and the development of neurological defects. *Cell Microbiol.* 2017;19(6):1–6.
  78. World Health Organization. Zika Virus [Internet]. July 20, 2018. [cited 2021 Sep 29]. Available from: <https://www.who.int/news-room/fact-sheets/detail/zika-virus>
  79. Hill SC, Vasconcelos J, Neto Z, Jandondo D, Zé-Zé L, Aguiar RS, et al. Emergence of the Asian lineage of Zika virus in Angola. *bioRxiv.* 2019.
  80. Centers for Disease Control (CDC) [Internet]. Zika Cases in the United States. 2021 [cited 2022 Jan 19]. Available from: <https://www.cdc.gov/zika/reporting/index.html>
  81. Dowd KA, DeMaso CR, Pelc RS, Speer SD, Smith ARY, Goo L, et al. Broadly Neutralizing Activity of Zika Virus-Immune Sera Identifies a Single Viral Serotype. *Cell Rep* [Internet]. 2016;16(6):1485–91. Available from: <http://dx.doi.org/10.1016/j.celrep.2016.07.049>
  82. Poland GA, Kennedy RB, Ovsyannikova IG, Palacios R, Ho PL, Kalil J. Development of vaccines against Zika virus. *Lancet Infect Dis* [Internet]. 2018 Jul;18(7):e211–9. Available from: <http://www.ncbi.nlm.nih.gov/pubmed/29396004>
  83. Ferraris P, Yssel H, Missé D. Zika virus infection: an update. *Microbes Infect.* 2019;21(8–9):353–60.
  84. Asebe Gulich G. Epidemiology, Driving Factors, Transmission and Control Options of Zika Virus: A Review. *J Infect Dis Ther.* 2016;04(02):1–7.
  85. Vogels CBF, Rückert C, Cavany SM, Perkins TA, Ebel GD, Grubaugh ND. Arbovirus coinfection and co-transmission: A neglected public health concern? *PLoS Biol.* 2019;17(1):1–16.

86. Chaves BA, Orfano AS, Nogueira PM, Rodrigues NB, Campolina TB, Nacif-Pimenta R, et al. Coinfection with zika virus (ZIKV) and dengue virus results in preferential ZIKV transmission by vector bite to vertebrate host. *J Infect Dis.* 2018;218(4):563–71.
87. Olawoyin O, Kribs C. Coinfection, Altered Vector Infectivity, and Antibody-Dependent Enhancement: The Dengue–Zika Interplay. *Bull Math Biol* [Internet]. 2020;82(1):1–20. Available from: <https://doi.org/10.1007/s11538-019-00681-2>
88. Gornet ME, Bracero NJ, Segars JH. Zika Virus in Semen: What We Know and What We Need to Know. *Semin Reprod Med.* 2016;34(5):285–92.
89. Haddow AD, Nalca A, Rossi FD, Miller LJ, Wiley MR, Perez-Sautu U, et al. High infection rates for adult macaques after intravaginal or intrarectal inoculation with zika virus. *Emerg Infect Dis.* 2017;23(8):1274–81.
90. Duggal NK, Ritter JM, Pestorius SE, Chang GJ, Bowen RA, Brault AC, et al. Frequent Zika Virus Sexual Transmission and Prolonged Viral RNA Shedding in an Immunodeficient Mouse Model. *CellReports* [Internet]. 2017;18(7):1751–60. Available from: <http://dx.doi.org/10.1016/j.celrep.2017.01.056>
91. Carroll T, Lo M, Lanteri M, Dutra J, Zarbock K, Silveira P, et al. Zika virus preferentially replicates in the female reproductive tract after vaginal inoculation of rhesus macaques. *PLoS Pathog.* 2017;13(7):1–23.
92. Moreira J, Peixoto TM, Siqueira AM, Lamas CC. Sexually acquired Zika virus: a systematic review. *Clin Microbiol Infect* [Internet]. 2017;23(5):296–305. Available from: <http://dx.doi.org/10.1016/j.cmi.2016.12.027>
93. Centers for Disease Control and Prevention (CDC). Zika virus transmission [Internet]. 2019 [cited 2022 Jan 23]. Available from: <https://www.cdc.gov/zika/prevention/transmission-methods.html>
94. Kurscheidt FA, Mesquita CSS, Damke GMZF, Damke E, Carvalho ARB d. A, Suehiro TT, et al. Persistence and clinical relevance of Zika virus in the male genital tract. *Nat Rev Urol.* 2019;16(4):211–30.
95. Stassen L, Armitage CW, van der Heide DJ, Beagley KW, Frentiu FD. Zika virus in the male reproductive tract. *Viruses.* 2018;10(4):198.
96. Barzon L, Pacenti M, Franchin E, Lavezzo E, Trevisan M, Sgarabotto D, et al. Infection dynamics in a traveller with persistent shedding of Zika virus RNA in semen for six months after returning from Haiti to Italy, January 2016. *Eurosurveillance.* 2016;21(32):1–4.
97. Nicastrì E, Castillettì C, Liuzzi G, Iannetta M, Capobianchi MR, Ippolito G. Persistent detection of Zika virus RNA in semen for six months after symptom onset in a traveller returning from Haiti to Italy, February 2016. *Eurosurveillance.* 2016;21(32):1–4.
98. Mead PS, Duggal NK, Hook SA, Delorey M, Fischer M, McGuire DO, et al. Zika virus shedding in semen of symptomatic infected men. *N Engl J Med.* 2018;378(15):1377–85.
99. Turmel JM, Abgueguen P, Hubert B, Vandamme YM, Maquart M, Le Guillou-Guillemette H, et al. Late sexual transmission of Zika virus related to persistence in the semen. *Lancet.* 2016;387(10037):2501.
100. Musso D, Roche C, Robin E, Nhan T, Teissier A, Cao-Lormeau VM. Potential sexual transmission of zika virus. *Emerg Infect Dis.* 2015;21(2):359–61.
101. Hills SL, Russell K, Hennessey M, Williams C, Oster AM, Fischer M, et al. Transmission of Zika virus through sexual contact with travelers to areas of ongoing transmission — Continental United States, 2016. *Morb Mortal Wkly Rep.* 2016;65(8):215–6.

102. Schwartz AM, Brooks JT, Brault AC, Delorey M, Becksted H, Mead PS, et al. Zika Virus Shedding in Semen of Symptomatic Infected Men. *N Engl J Med.* 2018;378(15):1377–85.
103. Matusali G, Houzet L, Satie A-P, Mahé D, Aubry F, Couderc T, et al. Zika virus infects human testicular tissue and germ cells. *J Clin Invest.* 2018;128(10):4697–710.
104. Wilson AH. The prostate gland: a review of its anatomy, pathology, and treatment. *JAMA - J Am Med Assoc.* 2014;312(5):562.
105. World Health Organization D of RH and R. WHO Laboratory Manual for the Examination and Processing of Human Semen [Internet]. 5th ed. 2010. 1–287 p. Available from: <https://www.who.int/reproductivehealth/publications/infertility/9789241547789/en/>
106. da Silva LRC. Zika virus trafficking and interactions in the human male reproductive tract. *Pathogens.* 2018;7(2).
107. Duggal NK, McDonald EM, Ritter JM, Brault AC. Sexual transmission of Zika virus enhances in utero transmission in a mouse model. *Sci Rep.* 2018;(February):1–8.
108. Gregory CJ, Oduyebo T, Brault AC, Brooks JT, Chung KW, Hills S, et al. Modes of Transmission of Zika Virus. *J Infect Dis.* 2017;216(January):S875–83.
109. Barjas-Castro ML, Angerami RN, Cunha MS, Suzuki A, Nogueira JS, Rocco IM, et al. Probable transfusion-transmitted Zika virus in Brazil. *Transfusion.* 2016;56(7):1684–8.
110. Holda MK, Klimek-Piotrowska W, Holda J. Evidence for Transmission of Zika Virus by Platelet Transfusion. *N Engl J Med.* 2016;375(11):1100.
111. Hamel R, Liégeois F, Wichit S, Pompon J, Diop F, Talignani L, et al. Zika virus: epidemiology, clinical features and host-virus interactions. *Microbes Infect.* 2016;18(7–8):441–9.
112. Barzon L, Percivalle E, Pacenti M, Rovida F, Zavattoni M, Del Bravo P, et al. Virus and Antibody Dynamics in Travelers with Acute Zika Virus Infection. *Clin Infect Dis.* 2018;66(8):1173–80.
113. Grischott F, Puhan M, Hatz C, Schlagenhaut P. Non-vector-borne transmission of Zika virus: A systematic review. *Travel Med Infect Dis [Internet].* 2016;14(4):313–30. Available from: <http://dx.doi.org/10.1016/j.tmaid.2016.07.002>
114. Paz-Bailey G, Rosenberg ES, Doyle K, Munoz-Jordan J, Santiago GA, Klein L, et al. Persistence of Zika virus in body fluids-Final report. *N Engl J Med.* 2018;379(13):1234–43.
115. Prisant N, Breurec S, Moriniere C, Bujan L, Joguet G. Zika virus genital tract shedding in infected women of childbearing age. *Clin Infect Dis.* 2017;64(1):107–9.
116. WHO Zika Virus Fact Sheet [Internet]. 2018 [cited 2018 Oct 9]. Available from: <http://www.who.int/en/news-room/fact-sheets/detail/zika-virus>
117. Joguet G, Mansuy JM, Matusali G, Hamdi S, Walschaerts M, Pavili L, et al. Effect of acute Zika virus infection on sperm and virus clearance in body fluids: a prospective observational study. *Lancet Infect Dis [Internet].* 2017;17(11):1200–8. Available from: [http://dx.doi.org/10.1016/S1473-3099\(17\)30444-9](http://dx.doi.org/10.1016/S1473-3099(17)30444-9)
118. Avelino-Silva VI, Alvarenga C, Abreu C, Tozetto-Mendoza TR, Canto CLM do, Manuli ER, et al. Potential effect of Zika virus infection on human male fertility? *Rev Inst Med Trop Sao Paulo.* 2018;60:e64.
119. Jequier AM. Testicular biopsy: indications and complications. In: Jequier AM, editor. *Male Infertility [Internet].* Cambridge: Cambridge University Press; 2011 [cited 2021 Nov 4]. p. 124–8. Available from: <https://www.cambridge.org/core/product/identifier/9780511997402%23c83147-14->

- 1/type/book\_part
120. De Fatima Vasco Aragao M, Van Der Linden V, Brainer-Lima AM, Coeli RR, Rocha MA, Da Silva PS, et al. Clinical features and neuroimaging (CT and MRI) findings in presumed Zika virus related congenital infection and microcephaly: Retrospective case series study. *BMJ*. 2016;353:1–10.
  121. Rice ME, Galand RR, Roth NM, Ellington SR, Moore CA, Prado MV, et al. Vital Signs: Zika-Associated Birth Defects and Neurodevelopmental Abnormalities Possibly Associated with Congenital Zika Virus Infection — U.S. Territories and Freely Associated States, 2018. *Morb Mortal Wkly Rep*. 2018;67(31):858–67.
  122. Cardoso TF, Santos RS Dos, Corrêa RM, Campos JV, Silva RDB, Tobias CC, et al. Congenital Zika infection: Neurology can occur without microcephaly. *Arch Dis Child*. 2019;104(2):199–200.
  123. Nielsen-Saines K, Brasil P, Kerin T, Vasconcelos Z, Gabaglia CR, Damasceno L, et al. Delayed childhood neurodevelopment and neurosensory alterations in the second year of life in a prospective cohort of ZIKV-exposed children. *Nat Med* [Internet]. 2019; Available from: <http://www.nature.com/articles/s41591-019-0496-1>
  124. Peçanha PM, Gomes Junior SC, Pone SM, Pone MV da S, Vasconcelos Z, Zin A, et al. Neurodevelopment of children exposed intra-uterus by Zika virus: A case series. *PLoS One*. 2020;15(2):e0229434.
  125. Marbán-Castro E, Goncé A, Fumadó V, Martínez MJ, López M, García-Otero L, et al. Zika virus infection in pregnant travellers and impact on childhood neurodevelopment in the first two years of life: A prospective observational study: Zika virus in pregnancy and children’s neurodevelopment. *Travel Med Infect Dis*. 2021;40.
  126. Koenig MR, Razo E, Mitzey A, Newman CM, Dudley DM, Breitbach ME, et al. Quantitative definition of neurobehavior, vision, hearing and brain volumes in macaques congenitally exposed to Zika virus. *PLoS One*. 2020;15(10 October).
  127. (NIAID) NI of A and ID. Zika virus diagnosis [Internet]. 2017 [cited 2022 Jan 19]. Available from: <https://www.niaid.nih.gov/diseases-conditions/zika-diagnosis>
  128. Bernatchez JA, Tran LT, Li J, Luan Y, Siqueira-Neto JL, Li R. Drugs for the Treatment of Zika Virus Infection. *J Med Chem*. 2020;63(2):470–89.
  129. Munoz-Jordan JL. Diagnosis of Zika Virus Infections: Challenges and Opportunities. *J Infect Dis* [Internet]. 2017;216(suppl\_10):S951–6. Available from: [http://academic.oup.com/jid/article/216/suppl\\_10/S951/4753683](http://academic.oup.com/jid/article/216/suppl_10/S951/4753683)
  130. Zika Virus Testing Guidance for Healthcare Providers [Internet]. Centers for Disease Control and Prevention. [cited 2019 Jun 26]. Available from: <https://www.cdc.gov/zika/hc-providers/testing-guidance.html>
  131. (NIAID) NI of A and ID. Zika virus vaccine [Internet]. 2018 [cited 2022 Jan 19]. Available from: <https://www.niaid.nih.gov/diseases-conditions/zika-vaccines>
  132. Makhluף H, Shresta S. Development of Zika Virus Vaccines. *Vaccines* [Internet]. 2018 Jan 18;6(1). Available from: <http://www.ncbi.nlm.nih.gov/pubmed/29346287>
  133. Bowen JR, Quicke KM, Maddur MS, O’Neal JT, McDonald CE, Fedorova NB, et al. Zika Virus Antagonizes Type I Interferon Responses during Infection of Human Dendritic Cells. *PLoS Pathog*. 2017;13(2):1–30.
  134. Grant A, Ponia S, Tripathi S, Balasubramaniam V, Miorin L, Sourisseau M, et al. Zika Virus Targets Human STAT2 to Inhibit Type I Interferon Signaling. *Cell Host Microbe*. 2016;19:882–90.

135. Morrison TE, Diamond MS. Animal Models of Zika Virus Infection. 2017;91(8):1–15.
136. Sakkas H, Bozidis P, Giannakopoulos X, Sofikitis N, Papadopoulou C. An update on sexual transmission of Zika virus. *Pathogens*. 2018;7(3):1–14.
137. Bradley MP, Nagamine CM. Animal models of Zika virus. *Comp Med*. 2017;67(3):242–52.
138. Lazear HM, Govero J, Smith AM, Platt DJ, Fernandez E, Miner JJ, et al. A Mouse Model of Zika Virus Pathogenesis. *Cell Host Microbe* [Internet]. 2016;19(5):720–30. Available from: <http://dx.doi.org/10.1016/j.chom.2016.03.010>
139. Govero J, Esakky P, Scheaffer SM, Diamond MS, Drury A, Fernandez E, et al. Zika virus infection damages the testes in mice. *Nature*. 2016;540(7633):438–42.
140. Rossi SL, Vasilakis N. Modeling Zika Virus Infection in Mice. *Cell Stem Cell*. 2016.
141. Dowall SD, Graham VA, Rayner E, Atkinson B, Hall G, Watson RJ, et al. A Susceptible Mouse Model for Zika Virus Infection. *PLoS Negl Trop Dis*. 2016;10(5):1–13.
142. Zmurko J, Marques RE, Schols D, Verbeke E, Kaptein SJF, Neyts J. The Viral Polymerase Inhibitor 7-Deaza-2'-C-Methyladenosine Is a Potent Inhibitor of In Vitro Zika Virus Replication and Delays Disease Progression in a Robust Mouse Infection Model. *PLoS Negl Trop Dis*. 2016;10(5):1–15.
143. Singh PK, Guest JM, Kanwar M, Boss J, Gao N, Juzych MS, et al. Zika virus infects cells lining the blood-retinal barrier and causes chorioretinal atrophy in mouse eyes. *JCI Insight*. 2017;2(4).
144. Fernandes NCCA, Nogueira JS, Réssio RA, Cirqueira CS, Kimura LM, Fernandes KR, et al. Experimental Zika virus infection induces spinal cord injury and encephalitis in newborn Swiss mice. *Exp Toxicol Pathol* [Internet]. 2017;69(2):63–71. Available from: <http://dx.doi.org/10.1016/j.etp.2016.11.004>
145. Julander JG, Siddharthan V. Small-Animal Models of Zika Virus. *J Infect Dis*. 2017;216(January):S919–27.
146. Chan JFW, Zhang AJ, Chan CCS, Yip CCY, Mak WWN, Zhu H, et al. Zika Virus Infection in Dexamethasone-immunosuppressed Mice Demonstrating Disseminated Infection with Multi-organ Involvement Including Orchitis Effectively Treated by Recombinant Type I Interferons. *EBioMedicine* [Internet]. 2016;14:112–22. Available from: <http://dx.doi.org/10.1016/j.ebiom.2016.11.017>
147. Uraki R, Hwang J, Jurado KA, Householder S, Yockey LJ, Hastings AK, et al. Zika virus causes testicular atrophy. *Sci Adv*. 2017;3(2):e1602899.
148. Robinson C, Chong A, Ashbrook W, Jeng G, Jin J, Chen H, et al. Male germ cells support long-term propagation of Zika virus. *Nat Commun* [Internet]. 2018;9(1):1–11. Available from: <http://dx.doi.org/10.1038/s41467-018-04444-w>
149. Ma W, Li S, Ma S, Jia L, Zhang F, Zhang Y, et al. Zika Virus Causes Testis Damage and Leads to Male Infertility in Mice. *Cell* [Internet]. 2016;167(6):1511–1524.e10. Available from: <http://dx.doi.org/10.1016/j.cell.2016.11.016>
150. Sheng Z-Y, Gao N, Wang Z-Y, Cui X-Y, Zhou D-S, Fan D-Y, et al. Sertoli Cells Are Susceptible to ZIKV Infection in Mouse Testis. *Front Cell Infect Microbiol*. 2017;7(June):1–13.
151. Clancy CS, Van Wettere AJ, Siddharthan V, Morrey JD, Julander JG. Comparative Histopathologic Lesions of the Male Reproductive Tract during Acute Infection of Zika Virus in AG129 and Ifnar  $-/-$  Mice. *Am J Pathol* [Internet]. 2018;188(4):904–15. Available from: <https://doi.org/10.1016/j.ajpath.2017.12.019>

152. McDonald EM, Duggal NK, Ritter JM, Brault AC. Infection of epididymal epithelial cells and leukocytes drives seminal shedding of Zika virus in a mouse model. *PLoS Negl Trop Dis* [Internet]. 2018;12(8):1–22. Available from: <http://dx.doi.org/10.1371/journal.pntd.0006691>
153. Sheng Z, Gao N, Fan D, Wu N, Zhang Y, Han D, et al. Zika virus disrupts the barrier structure and Absorption / Secretion functions of the epididymis in mice. 2021;15(3):e0009211. Available from: <http://dx.doi.org/10.1371/journal.pntd.0009211>
154. Halabi J, Jagger BW, Salazar V, Winkler ES, White JP, Humphrey PA, et al. Zika Virus Causes Acute and Chronic Prostatitis in Mice and Macaques. *J Infect Dis*. 2019;63110:1–12.
155. Tang WW, Young MP, Mamidi A, Regla-Nava JA, Kim K, Shresta S. A Mouse Model of Zika Virus Sexual Transmission and Vaginal Viral Replication. *Cell Rep* [Internet]. 2016;17(12):3091–8. Available from: <http://dx.doi.org/10.1016/j.celrep.2016.11.070>
156. Yockey LJ, Varela L, Rakib T, Khoury-Hanold W, Fink SL, Stutz B, et al. Vaginal Exposure to Zika Virus during Pregnancy Leads to Fetal Brain Infection. *Cell*. 2016;166(5):1247-1256.e4.
157. Duggal NK, Ritter JM, Pestorius SE, Chang GJ, Bowen RA, Brault AC, et al. Frequent Zika Virus Sexual Transmission and Prolonged Viral RNA Shedding in an Immunodeficient Article Frequent Zika Virus Sexual Transmission and Prolonged Viral RNA Shedding in an Immunodeficient Mouse Model. *CellReports*. 2017;18(7):1751–60.
158. Quesenberry KE, Thomas M. Donnelly. Breeding and Reproduction of Mice. In: Aiello SE, Moses MA, editors. *Merck Veterinary Manual*. 11th ed. Merck Manuals; 2016.
159. Malassiné A, Frenzo JL, Evain-Brion D. A comparison of placental development and endocrine functions between the human and mouse model. *Hum Reprod Update*. 2003;9(6):531–9.
160. De Rijk EPCT, Van Esch E. The Macaque Placenta - A Mini-Review. *Toxicol Pathol*. 2008;36(7\_suppl):108S-118S.
161. Hemberger M, Hanna CW, Dean W. Mechanisms of early placental development in mouse and humans. *Nat Rev Genet* [Internet]. 2020;21(1):27–43. Available from: <http://dx.doi.org/10.1038/s41576-019-0169-4>
162. Florio M, Huttner WB. Neural progenitors, neurogenesis and the evolution of the neocortex. *Dev*. 2014;141(11):2182–94.
163. Miner JJ, Cao B, Govero J, Smith AM, Fernandez E, Cabrera OH, et al. Zika Virus Infection during Pregnancy in Mice Causes Placental Damage and Fetal Demise. *Cell* [Internet]. 2016;165(5):1081–91. Available from: <http://dx.doi.org/10.1016/j.cell.2016.05.008>
164. Wu KY, Zuo GL, Li XF, Ye Q, Deng YQ, Huang XY, et al. Vertical transmission of Zika virus targeting the radial glial cells affects cortex development of offspring mice. *Cell Res* [Internet]. 2016;26(6):645–54. Available from: <http://dx.doi.org/10.1038/cr.2016.58>
165. Cugola FR, Fernandes IR, Russo FB, Freitas BC, Dias JLM, Guimarães KP, et al. The Brazilian Zika virus strain causes birth defects in experimental models. *Nature* [Internet]. 2016;534(7606):267–71. Available from: <http://dx.doi.org/10.1038/nature18296>
166. Zhang N, Zhang N, Qin CF, Liu X, Shi L, Xu Z. Zika Virus Disrupts Neural Progenitor Development and Leads to Microcephaly in Mice. *Cell Stem Cell*. 2016;19:120–6.
167. Shao Q, Herrlinger S, Yang S-L, Lai F, Moore JM, Brindley MA, et al. Zika virus infection disrupts neurovascular development and results in postnatal microcephaly with

- brain damage. *Development*. 2016;143:4127–36.
168. Siddharthan V, Van Wettere AJ, Li R, Miao J, Wang Z, Morrey JD, et al. Zika virus infection of adult and fetal STAT2 knock-out hamsters. *Virology* [Internet]. 2017;507(April):89–95. Available from: <http://dx.doi.org/10.1016/j.virol.2017.04.013>
  169. Kumar M, Krause KK, Azouz F, Nakano E, Nerurkar VR. A Guinea pig model of Zika virus infection. *Virol J*. 2017;14(1):1–8.
  170. Deng YQ, Zhang NN, Li XF, Wang YQ, Tian M, Qiu YF, et al. Intranasal infection and contact transmission of Zika virus in Guinea pigs. *Nat Commun* [Internet]. 2017;8(1):1–8. Available from: <http://dx.doi.org/10.1038/s41467-017-01923-4>
  171. Dreef HC, Van Esch E, de Rijk EPCT. Spermatogenesis in the Cynomolgus Monkey (*Macaca fascicularis*): A Practical Guide for Routine Morphological Staging. *Toxicol Pathol*. 2007;35(3):395–404.
  172. Coffey LL, Pesavento PA, Keesler RI, Singapuri A, Watanabe J, Watanabe R, et al. Zika virus tissue and blood compartmentalization in acute infection of rhesus macaques. *PLoS One*. 2017;12(1).
  173. Koide F, Goebel S, Snyder B, Walters KB, Gast A, Hagelin K, et al. Development of a zika virus infection model in cynomolgus macaques. *Front Microbiol*. 2016;7(DEC):1–8.
  174. Dudley DM, Aliota MT, Mohr EL, Weiler AM, Lehrer-Brey G, Weisgrau KL, et al. A rhesus macaque model of Asian-lineage Zika virus infection. *Nat Commun*. 2016;7(May):1–10.
  175. Osuna CE, Lim SY, Deleage C, Griffin BD, Stein D, Schroeder LT, et al. Zika viral dynamics and shedding in rhesus and cynomolgus macaques. *Nat Med*. 2016;22(12):1448–55.
  176. Gurung S, Preno AN, Dubaut JP, Nadeau H, Hyatt K, Reuter N, et al. Translational Model of Zika Virus Disease in Baboons. *J Virol*. 2018;92(16):1–17.
  177. Koide F, Goebel S, Snyder B, Walters KB, Gast A, Hagelin K, et al. Development of a zika virus infection model in cynomolgus macaques. *Front Microbiol*. 2016;7:2028.
  178. Hirsch AJ, Smith JL, Haese NN, Broeckel RM, Parkins CJ, Kreklywich C, et al. Zika Virus infection of rhesus macaques leads to viral persistence in multiple tissues. *PLoS Pathog* [Internet]. 2017;13(3):1–23. Available from: <http://dx.doi.org/10.1371/journal.ppat.1006219>
  179. Osuna CE, Whitney JB. Nonhuman Primate Models of Zika Virus Infection, Immunity, and Therapeutic Development. *J Infect Dis* [Internet]. 2017;216(suppl\_10):S928–34. Available from: [http://academic.oup.com/jid/article/216/suppl\\_10/S928/4753687](http://academic.oup.com/jid/article/216/suppl_10/S928/4753687)
  180. Centers for Disease Control and Prevention (CDC). Exposure, testing and risks with Zika virus [Internet]. 2020 [cited 2021 Nov 5]. Available from: <https://www.cdc.gov/pregnancy/zika/testing-follow-up/exposure-testing-risks.html>
  181. Cline JM, Dixon D, Ernerudh J, Faas MM, Göhner C, Häger JD, et al. The Placenta in Toxicology. Part III: Pathologic Assessment of the Placenta. *Toxicol Pathol*. 2014;42(2):339–44.
  182. Martinot AJ, Abbink P, Afacan O, Prohl AK, Bronson R, Hecht JL, et al. Fetal Neuropathology in Zika Virus-Infected Pregnant Female Rhesus Monkeys. *Cell* [Internet]. 2018;173(5):1111–1122.e10. Available from: <https://doi.org/10.1016/j.cell.2018.03.019>
  183. Magnani DM, Rogers TF, Maness NJ, Grubaugh ND, Beutler N, Bailey VK, et al. Fetal demise and failed antibody therapy during Zika virus infection of pregnant macaques. *Nat Commun*. 2018;9(1):1–8.

184. Dudley DM, Van Rompay KK, Coffey LL, Ardeshir A, Keesler RI, Bliss-Moreau E, et al. Miscarriage and stillbirth following maternal Zika virus infection in nonhuman primates. *Nat Med*. 2018;24(8):1104–7.
185. Hirsch AJ, Roberts VHJ, Grigsby PL, Haese N, Schabel MC, Wang X, et al. Zika virus infection in pregnant rhesus macaques causes placental dysfunction and immunopathology. *Nat Commun* [Internet]. 2018;9(1). Available from: <http://dx.doi.org/10.1038/s41467-017-02499-9>
186. Nguyen SM, Antony KM, Dudley DM, Kohn S, Simmons HA, Wolfe B, et al. Highly efficient maternal-fetal Zika virus transmission in pregnant rhesus macaques. *PLoS Pathog* [Internet]. 2017;13(5):1–22. Available from: <http://dx.doi.org/10.1371/journal.ppat.1006378>
187. Waldorf KMA, Nelson BR, Stencel-Baerenwald JE, Studholme C, Kapur RP, Armistead B, et al. Congenital Zika virus infection as a silent pathology with loss of neurogenic output in the fetal brain. *Nat Med*. 2018;24(3):368–74.
188. Adams Waldorf KM, Stencel-Baerenwald JE, Kapur RP, Studholme C, Boldenow E, Vornhagen J, et al. Fetal Brain Lesions After Subcutaneous Inoculation of Zika Virus in a Pregnant Nonhuman Primate. *Nat Med*. 2016;22(11):1256–9.
189. Adams Waldorf KM, Nelson BR, Stencel-Baerenwald JE, Studholme C, Kapur RP, Armistead B, et al. Congenital Zika virus infection as a silent pathology with loss of neurogenic output in the fetal brain. *Nat Med* [Internet]. 2018;24(3):368–74. Available from: <http://dx.doi.org/10.1038/nm.4485>
190. Beckman D, Seelke AM, Bennett J, Dougherty P, Rompay KA Van, Keesler R, et al. Neuroanatomical abnormalities in a nonhuman primate model of congenital Zika virus infection. *bioRxiv* [Internet]. 2020;2020.11.10.374611. Available from: <https://doi.org/10.1101/2020.11.10.374611>
191. Mavigner M, Raper J, Kovacs-Balint Z, Gumber S, O’Neal JT, Bhaumik SK, et al. Postnatal Zika virus infection is associated with persistent abnormalities in brain structure, function, and behavior in infant macaques. *Sci Transl Med*. 2018;10(435):1–16.
192. Rompay KKA Van, Coffey LL, Kapoor T, Gazumyan A, Keesler RI, Jurado A, et al. A combination of two human monoclonal antibodies limits fetal damage by Zika virus in macaques. Available from: [www.pnas.org/cgi/doi/10.1073/pnas.2000414117](http://www.pnas.org/cgi/doi/10.1073/pnas.2000414117)
193. Keeffe JR, Van Rompay KKA, Olsen PC, Wang Q, Gazumyan A, Azzopardi SA, et al. A Combination of Two Human Monoclonal Antibodies Prevents Zika Virus Escape Mutations in Non-human Primates. *Cell Rep* [Internet]. 2018;25(6):1385-1394.e7. Available from: <https://doi.org/10.1016/j.celrep.2018.10.031>
194. Rompay KKA Van, Keesler RI, Ardeshir A, Watanabe J, Usachenko J, Singapuri A, et al. DNA vaccination before conception protects Zika virus – exposed pregnant macaques against prolonged viremia and improves fetal outcomes. 2019;2736(December):1–12.
195. Terzian ACB, Zini N, Sacchetto L, Rocha RF, Parra MCP, Del Sarto JL, et al. Evidence of natural Zika virus infection in neotropical non-human primates in Brazil. *Sci Rep*. 2018;8(1):1–15.
196. Favoretto S, Araújo D, Oliveira D, Duarte N, Mesquita F, Zanotto P, et al. First detection of Zika virus in neotropical primates in Brazil: a possible new reservoir. *bioRxiv*. 2016;(April).
197. Vanchiere JA, Ruiz JC, Brady AG, Kuehl TJ, Williams LE, Baze WB, et al. Experimental zika virus infection of neotropical primates. *Am J Trop Med Hyg*. 2018;98(1):173–7.

198. Lum FM, Zhang W, Lim KC, Malleret B, Teo TH, Koh JJ, et al. Multimodal assessments of Zika virus immune pathophysiological responses in marmosets. *Sci Rep.* 2018;8(1):1–13.
199. Chiu CY, Sánchez-San Martín C, Bouquet J, Li T, Yagi S, Tamhankar M, et al. Experimental Zika Virus Inoculation in a New World Monkey Model Reproduces Key Features of the Human Infection. *Sci Rep.* 2017;7(1):1–11.
200. Seferovic M, Martín CSS, Tardif SD, Rutherford J, Castro ECC, Li T, et al. Experimental Zika Virus Infection in the Pregnant Common Marmoset Induces Spontaneous Fetal Loss and Neurodevelopmental Abnormalities. *Sci Rep.* 2018;8(1):1–15.
201. Hamel R, Dejarnac O, Wichit S, Ekchariyawat P, Neyret A, Luplertlop N, et al. Biology of Zika Virus Infection in Human Skin Cells. *J Virol.* 2015;89(17).
202. Miner JJ, Diamond MS. Zika Virus Pathogenesis and Tissue Tropism. *Cell Host Microbe* [Internet]. 2017;21(2):134–42. Available from: <http://dx.doi.org/10.1016/j.chom.2017.01.004>
203. Mwaliko C, Nyaruaba R, Zhao L, Atoni E, Karungu S, Mwau M, et al. Zika virus pathogenesis and current therapeutic advances. *Pathog Glob Health* [Internet]. 2021;115(1):21–39. Available from: <https://doi.org/10.1080/20477724.2020.1845005>
204. Tang H, Hammack C, Ogden SC, Wen Z, Qian X, Li Y, et al. Zika virus infects human cortical neural progenitors and attenuates their growth. *Cell Stem Cell* [Internet]. 2016;18(5):587–90. Available from: <http://dx.doi.org/10.1016/j.stem.2016.02.016>
205. Tabata T, Petitt M, Puerta-Guardo H, Michlmayr D, Wang C, Fang-Hoover J, et al. Zika Virus Targets Different Primary Human Placental Cells, Suggesting Two Routes for Vertical Transmission. *Cell Host Microbe* [Internet]. 2016;20(2):155–66. Available from: <http://dx.doi.org/10.1016/j.chom.2016.07.002>
206. Petitt M, Tabata T, Puerta-Guardo H, Harris E, Pereira L. Zika virus infection of first-trimester human placentas: utility of an explant model of replication to evaluate correlates of immune protection ex vivo. *Curr Opin Virol* [Internet]. 2017;27:48–56. Available from: <http://dx.doi.org/10.1016/j.coviro.2017.11.008>
207. Gavegnano C, Bassit LC, Cox BD, Hsiao H-M, Johnson EL, Suthar M, et al. Jak Inhibitors Modulate Production of Replication Competent Zika Virus in Human Hofbauer, Trophoblasts, and Neuroblastoma cells. *Pathog Immun.* 2017;2(2):199.
208. Goo L, DeMaso CR, Pelc RS, Ledgerwood JE, Graham BS, Kuhn RJ, et al. The Zika virus envelope protein glycan loop regulates virion antigenicity. *Virology* [Internet]. 2018;515(August 2017):191–202. Available from: <https://doi.org/10.1016/j.virol.2017.12.032>
209. Kumar A, Jovel J, Lopez-Orozco J, Limonta D, Airo AM, Hou S, et al. Human sertoli cells support high levels of zika virus replication and persistence. *Sci Rep* [Internet]. 2018;8(1):1–11. Available from: <http://dx.doi.org/10.1038/s41598-018-23899-x>
210. Nowakowski TJ, Pollen AA, Di Lullo E, Sandoval-Espinosa C, Bershteyn M, Kriegstein AR. Expression analysis highlights AXL as a candidate zika virus entry receptor in neural stem cells. *Cell Stem Cell* [Internet]. 2016;18(5):591–6. Available from: <http://dx.doi.org/10.1016/j.stem.2016.03.012>
211. Siemann DN, Strange DP, Maharaj PN, Shi P-Y, Verma S. Zika Virus Infects Human Sertoli Cells and Modulates the Integrity of the In Vitro Blood-Testis Barrier Model . *J Virol.* 2017;91(22):1–17.
212. Bhattacharyya S, Zagórska A, Lew ED, Shrestha B, Rothlin C V., Naughton J, et al.

- Enveloped viruses disable innate immune responses in dendritic cells by direct activation of TAM receptors. *Cell Host Microbe*. 2013;14(2):136–47.
213. Miner JJ, Sene A, Richner JM, Smith AM, Santeford A, Ban N, et al. Zika Virus Infection in Mice Causes Panuveitis with Shedding of Virus in Tears. *Cell Rep*. 2016;16(12):3208–18.
  214. The Human Protein Atlas. 2021.
  215. The Human Protein Atlas [Internet]. 2021 [cited 2021 Oct 12]. Available from: <https://www.proteinatlas.org/ENSG00000167601-AXL/celltype/testis>
  216. Meertens L, Labeau A, Dejarnac O, Cipriani S, Sinigaglia L, Bonnet-Madin L, et al. Axl Mediates ZIKA Virus Entry in Human Glial Cells and Modulates Innate Immune Responses. *Cell Rep*. 2017;18(2).
  217. Richard AS, Shim BS, Kwon YC, Zhang R, Otsuka Y, Schmitt K, et al. AXL-dependent infection of human fetal endothelial cells distinguishes Zika virus from other pathogenic flaviviruses. *Proc Natl Acad Sci U S A*. 2017;114(8):2024–9.
  218. Chen J, Yang YF, Yang Y, Zou P, Chen J, He Y, et al. AXL promotes Zika virus infection in astrocytes by antagonizing type I interferon signalling. *Nat Microbiol*. 2018;3(3).
  219. Liu S, Delalio LJ, Isakson BE, Wang TT. AXL-Mediated Productive Infection of Human Endothelial Cells by Zika Virus. *Circ Res*. 2016;119(11):1183–9.
  220. Wells MF, Salick MR, Wiskow O, Ho DJ, Worringer KA, Ihry RJ, et al. Genetic Ablation of AXL Does Not Protect Human Neural Progenitor Cells and Cerebral Organoids from Zika Virus Infection. *Cell Stem Cell*. 2016;
  221. Strange DP, Jiyarom B, Zarandi NP, Xie X, Baker C, Sadri-Ardekani H, et al. Axl Promotes Zika Virus Entry and Modulates the Antiviral. *Am Soc Microbiol*. 2019;10(4):1–16.
  222. Simoni MK, Jurado KA, Abrahams VM, Fikrig E, Guller S. Zika virus infection of Hofbauer cells. *Am J Reprod Immunol*. 2017;77(2).
  223. Chiu CF, Chu LW, Liao IC, Simanjuntak Y, Lin YL, Juan CC, et al. The Mechanism of the Zika Virus Crossing the Placental Barrier and the Blood-Brain Barrier. *Front Microbiol*. 2020;11(February):1–15.
  224. Yan Cheng C, Mruk DD. The blood-testis barrier and its implications for male contraception. *Pharmacol Rev*. 2012;64(1):16–64.
  225. Daneman R, Alexandre Prat. The blood–brain barrier. *Cold Spring Harb Perspect Biol*. 2015;7(1):a020412.
  226. Campbell M, Humphries P. The blood-retina barrier: Tight junctions and barrier modulation. *Adv Exp Med Biol*. 2012;763:70–84.
  227. Ismail AA, Mahboob T, Samudi Raju C, Sekaran SD. Zika virus modulates blood-brain barrier of brain microvascular endothelial cells. *Trop Biomed*. 2019;36(4):888–97.
  228. Leda AR, Bertrand L, Andras IE, El-Hage N, Nair M, Toborek M. Selective Disruption of the Blood–Brain Barrier by Zika Virus. *Front Microbiol*. 2019;10(September):1–14.
  229. Merkle FT, Alvarez-Buylla A. Neural stem cells in mammalian development. *Curr Opin Cell Biol*. 2006;18(6):704–9.
  230. Tang H, Hammack C, Ogden SC, Wen Z, Qian X, Li Y, et al. Zika virus infects human cortical neural progenitors and attenuates their growth. *Cell Stem Cell*. 2016;18(5).
  231. Liang Q, Luo Z, Zeng J, Chen W, Foo SS, Lee SA, et al. Zika Virus NS4A and NS4B Proteins Deregulate Akt-mTOR Signaling in Human Fetal Neural Stem Cells to Inhibit Neurogenesis and Induce Autophagy. *Cell Stem Cell* [Internet]. 2016;19(5):663–71.

- Available from: <http://dx.doi.org/10.1016/j.stem.2016.07.019>
232. Dang J, Tiwari SK, Lichinchi G, Qin Y, Patil VS, Eroshkin AM, et al. Zika Virus Depletes Neural Progenitors in Human Cerebral Organoids through Activation of the Innate Immune Receptor TLR3. *Cell Stem Cell* [Internet]. 2016;19(2):258–65. Available from: <https://www.ncbi.nlm.nih.gov/pmc/articles/PMC5116380/pdf/nihms783149.pdf>
  233. Murphy K, Weaver C. *Janeway's Immunobiology*. 9th ed. New York, NY: Garland Science/Taylor & Francis Group; 2017.
  234. Shah PS, Link N, Jang GM, Sharp PP, Zhu T, Swaney DL, et al. Comparative Flavivirus-Host Protein Interaction Mapping Reveals Mechanisms of Dengue and Zika Virus Pathogenesis. *Cell*. 2018;175(7):1931-1945.e18.
  235. Hu B, Guo H, Zhou P, Shi ZL. Characteristics of SARS-CoV-2 and COVID-19. *Nat Rev Microbiol* [Internet]. 2021;19(3):141–54. Available from: <http://dx.doi.org/10.1038/s41579-020-00459-7>
  236. Deng SQ, Peng HJ. Characteristics of and public health responses to the coronavirus disease 2019 outbreak in China. *J Clin Med*. 2020;9(2).
  237. Chan JFW, Yuan S, Kok KH, To KKW, Chu H, Yang J, et al. A familial cluster of pneumonia associated with the 2019 novel coronavirus indicating person-to-person transmission: a study of a family cluster. *Lancet* [Internet]. 2020;395(10223):514–23. Available from: [http://dx.doi.org/10.1016/S0140-6736\(20\)30154-9](http://dx.doi.org/10.1016/S0140-6736(20)30154-9)
  238. Eurosurveillance Editorial Team. Note from the editors: World Health Organization declares novel coronavirus (2019-nCoV) sixth public health emergency of international concern. *Euro Surveill*. 2020;25(5):2019–20.
  239. Lu R, Zhao X, Li J, Niu P, Yang B, Wu H, et al. Genomic characterisation and epidemiology of 2019 novel coronavirus: implications for virus origins and receptor binding. *Lancet* [Internet]. 2020;395(10224):565–74. Available from: [http://dx.doi.org/10.1016/S0140-6736\(20\)30251-8](http://dx.doi.org/10.1016/S0140-6736(20)30251-8)
  240. Perlman S. Another Decade, Another Coronavirus. *N Engl J Med*. 2020;382(8):760–760.
  241. Gorbalenya AE, Baker SC, Baric RS, de Groot RJ, Drosten C, Gulyaeva AA, et al. The species Severe acute respiratory syndrome-related coronavirus: classifying 2019-nCoV and naming it SARS-CoV-2. *Nat Microbiol*. 2020;5(4):536–44.
  242. World Health Organization (WHO). Situation Report: World Health Organization. Coronavirus Dis 2019 [Internet]. 2020;2019(February):11. Available from: <https://apps.who.int/iris/bitstream/handle/10665/331475/nCoVsitrep11Mar2020-eng.pdf?sequence=1&isAllowed=y%0Ahttps://pandemic.internationalsos.com/2019-ncov/ncov-travel-restrictions-flight-operations-and-screening%0Ahttps://www.who.int/docs/default-source>
  243. Chan JFW, Kok KH, Zhu Z, Chu H, To KKW, Yuan S, et al. Genomic characterization of the 2019 novel human-pathogenic coronavirus isolated from a patient with atypical pneumonia after visiting Wuhan. *Emerg Microbes Infect*. 2020;9(1):221–36.
  244. Andersen KG, Rambaut A, Lipkin WI, Holmes EC, Garry RF. The proximal origin of SARS-CoV-2. *Nat Med*. 2020;26(4):450–2.
  245. Coutard B, Valle C, de Lamballerie X, Canard B, Seidah NG, Decroly E. The spike glycoprotein of the new coronavirus 2019-nCoV contains a furin-like cleavage site absent in CoV of the same clade. *Antiviral Res* [Internet]. 2020;176(February):104742. Available from: <https://doi.org/10.1016/j.antiviral.2020.104742>
  246. Hong Zhou, Xing Chen, Tao HU, Alice C. Hughes, B Y, Shi W. A Novel Bat Coronavirus

- Closely Related to SARSCoV-2 Contains Natural Insertions at the S1/S2 Cleavage Site of the Spike Protein. *Curr Biol* [Internet]. 2020;30(January):2196–293. Available from: <https://www.ncbi.nlm.nih.gov/pmc/articles/PMC7211627/pdf/main.pdf>
247. Renhong Y, Yuanyuan Z, Yanning L, Lu X, Yingying G, Qiang Z. Structural basis for the recognition of SARS-CoV-2 by full-length human ACE2. *Science* (80- ). 2020;367(6485):1444–8.
  248. Trougakos IP, Stamatelopoulos K, Terpos E, Tsitsilonis OE, Aivalioti E, Paraskevis D, et al. Insights to SARS-CoV-2 life cycle, pathophysiology, and rationalized treatments that target COVID-19 clinical complications. *J Biomed Sci* [Internet]. 2021;28(1):1–18. Available from: <https://doi.org/10.1186/s12929-020-00703-5>
  249. Centers for Disease Control and Prevention (CDC). SARS-CoV-2 Variant Classifications and Definitions [Internet]. 2021 [cited 2022 Mar 27]. Available from: [https://www.cdc.gov/coronavirus/2019-ncov/variants/variant-classifications.html?CDC\\_AA\\_refVal=https%3A%2F%2Fwww.cdc.gov%2Fcoronavirus%2F2019-ncov%2Fvariants%2Fvariant-info.html](https://www.cdc.gov/coronavirus/2019-ncov/variants/variant-classifications.html?CDC_AA_refVal=https%3A%2F%2Fwww.cdc.gov%2Fcoronavirus%2F2019-ncov%2Fvariants%2Fvariant-info.html)
  250. Zhou P, Yang X Lou, Wang XG, Hu B, Zhang L, Zhang W, et al. A pneumonia outbreak associated with a new coronavirus of probable bat origin. *Nature* [Internet]. 2020;579(7798):270–3. Available from: <http://dx.doi.org/10.1038/s41586-020-2012-7>
  251. Zhang YZ, Holmes EC. A Genomic Perspective on the Origin and Emergence of SARS-CoV-2. *Cell* [Internet]. 2020;181(2):223–7. Available from: <https://doi.org/10.1016/j.cell.2020.03.035>
  252. Xiao K, Zhai J, Feng Y, Zhou N, Zhang X, Zou JJ, et al. Isolation of SARS-CoV-2-related coronavirus from Malayan pangolins. *Nature*. 2020;583(7815):286–9.
  253. Rahman B, Sadraddin E, Porreca A. The basic reproduction number of SARS-CoV-2 in Wuhan is about to die out, how about the rest of the World? *Rev Med Virol*. 2020;30(4):1–10.
  254. Liu Y, Rocklov J. The reproductive number of the Delta variant of SARS-CoV-2 is far higher compared to the ancestral SARS-CoV-2 virus. *J Travel Med* [Internet]. 2021;28(7):1–3. Available from: <https://doi.org/10.1093/jtm/taab124>
  255. Liu Y, Rocklöv J. The effective reproductive number of the Omicron variant of SARS-CoV-2 is several times relative to Delta. *J Travel Med*. 2022;1–4.
  256. Yu ITS, Li Y, Wong TW, Tam W, Chan AT, Lee JHW, et al. Evidence of Airborne Transmission of the Severe Acute Respiratory Syndrome Virus. *N Engl J Med*. 2004;350(17):1731–9.
  257. Otter JA, Donskey C, Yezli S, Douthwaite S, Goldenberg SD, Weber DJ. Transmission of SARS and MERS coronaviruses and influenza virus in healthcare settings: The possible role of dry surface contamination. *J Hosp Infect* [Internet]. 2016;92(3):235–50. Available from: <http://dx.doi.org/10.1016/j.jhin.2015.08.027>
  258. Doremalen N van, Morris DH, Holbrook MG, Gamble A, Brandi N, Williamson. Aerosol and Surface Stability of SARS-CoV-2 Compared with SARS-CoV. *N Engl J Med*. 2020;0–3.
  259. Sun K, Gu L, Ma L, Duan Y. Atlas of ACE2 gene expression reveals novel insights into transmission of SARS-CoV-2. *Heliyon*. 2021;7(1).
  260. Xiao F, Tang M, Zheng X, Liu Y, Li X, Shan H. Evidence for Gastrointestinal Infection of SARS-CoV-2. *Gastroenterology*. 2020;158(6):1831–3.
  261. Centers for Disease Control and Prevention (CDC). National Wastewater Surveillance

- System (NWSS) [Internet]. Waterborne Disease & Outbreak Surveillance Reporting. 2020 [cited 2022 May 5]. Available from: <https://www.cdc.gov/healthywater/surveillance/wastewater-surveillance/wastewater-surveillance.html>
262. Ong SWX, Tan YK, Chia PY, Lee TH, Ng OT, Wong MSY, et al. Air, Surface Environmental, and Personal Protective Equipment Contamination by Severe Acute Respiratory Syndrome Coronavirus 2 (SARS-CoV-2) from a Symptomatic Patient. *JAMA - J Am Med Assoc.* 2020;323(16):1610–2.
  263. Centers for Disease Control and Prevention (CDC). Interim Clinical Guidance for Management of Patients with Confirmed Coronavirus Disease (COVID-19) [Internet]. COVID-19. 2022. Available from: <https://www.cdc.gov/coronavirus/2019-ncov/hcp/clinical-guidance-management-patients.html>
  264. Arons MM, Hatfield KM, Reddy SC, Kimball A, James A, Jacobs JR, et al. Presymptomatic SARS-CoV-2 Infections and Transmission in a Skilled Nursing Facility. *N Engl J Med.* 2020;382(22):2081–90.
  265. Meng H, Xiong R, He R, Lin W, Hao B, Zhang L, et al. CT imaging and clinical course of asymptomatic cases with COVID-19 pneumonia at admission in Wuhan, China. *J Infect* [Internet]. 2020;81(1):e33–9. Available from: <https://doi.org/10.1016/j.jinf.2020.04.004>
  266. He G, Sun W, Fang P, Huang J, Gamber M, Cai J, et al. The clinical feature of silent infections of novel coronavirus infection (COVID-19) in Wenzhou. *J Med Virol.* 2020;92(10):1761–3.
  267. Centers for Disease Control and Prevention (CDC). Overview of Testing for SARS-CoV-2, the virus that causes COVID-19: [Internet]. COVID-19. 2022 [cited 2022 Feb 12]. Available from: <https://www.cdc.gov/coronavirus/2019-ncov/hcp/testing-overview.html#TestingInfection>
  268. Sit THC, Brackman CJ, Ip SM, Tam KWS, Law PYT, To EMW, et al. Infection of dogs with SARS-CoV-2. *Nature* [Internet]. 2020;586(7831):776–8. Available from: <http://dx.doi.org/10.1038/s41586-020-2334-5>
  269. Newman A, Smith D, Ghai RR, Wallace RM, Torchetti MK, Loiacono C. First Reported Cases of SARS-CoV-2 Infection in Companion Animals. *Morb Mortal Wkly Rep* [Internet]. 2020;69(23):710–3. Available from: <https://www.ncbi.nlm.nih.gov/pmc/articles/PMC7315787/pdf/mm6923e3.pdf>
  270. ProMED. COVID-19 update (166): China (Hong Kong) animal, cat, OIE, resolved [Internet]. 2020. Available from: <https://promedmail.org/promed-post/?id=7314521>
  271. Munnink BBO, Sikkema RS, Nieuwenhuijse DF, Molenaar RJ, Munger E, Molenkamp R, et al. Transmission of SARS-CoV-2 on mink farms between humans and mink and back to humans. *Science* (80- ). 2021;371(6525):172–7.
  272. Molenaar RJ, Vreman S, Hakze-van der Honing RW, Zwart R, de Rond J, Weesendorp E, et al. Clinical and Pathological Findings in SARS-CoV-2 Disease Outbreaks in Farmed Mink (*Neovison vison*). *Vet Pathol.* 2020;57(5):653–7.
  273. McAloose D, Laverack M, Wang L, Killian ML, Caserta LC, Yuan F, et al. From people to panthera: Natural sars-cov-2 infection in tigers and lions at the bronx zoo. *MBio.* 2020;11(5):1–13.
  274. Shi J, Wen Z, Zhong G, Yang H, Wang C, Huang B, et al. Susceptibility of ferrets, cats, dogs, and other domesticated animals to SARS-coronavirus 2. *Science* (80- ). 2020;368(6494):1016–20.

275. Patania OM, Chiba S, Halfmann PJ, Hatta M, Maemura T, Bernard KA, et al. Pulmonary lesions induced by SARS-CoV-2 infection in domestic cats. *Vet Pathol.* 2021;
276. Deng J, Jin Y, Liu Y, Sun J, Hao L, Bai J, et al. Serological survey of SARS-CoV-2 for experimental, domestic, companion and wild animals excludes intermediate hosts of 35 different species of animals. *Transbound Emerg Dis.* 2020;67(4):1745–9.
277. Stout AE, Guo Q, Millet JK, de Matos R, Whittaker GR. Coronaviruses associated with the superfamily musteloidea. *MBio.* 2021;12(1):1–14.
278. Ciurkiewicz M, Armando F, Schreiner T, de Buhr N, Pilchová V, Krupp-Buzimikic V, et al. Ferrets are valuable models for SARS-CoV-2 research. *Vet Pathol.* 2022;
279. Bosco-Lauth AM, Root JJ, Porter SM, Walker AE, Guilbert L, Hawvermale D, et al. Peridomestic mammal susceptibility to severe acute respiratory syndrome Coronavirus 2 infection. *Emerg Infect Dis.* 2021;27(8):2073–80.
280. Ulrich L, Michelitsch A, Halwe N, Wernike K, Hoffmann D, Beer M. Experimental SARS-CoV-2 infection of bank voles. *Emerg Infect Dis.* 2021;27(4):1193–5.
281. Xu L, Yu DD, Ma YH, Yao YL, Luo RH, Feng XL, et al. COVID-19-like symptoms observed in Chinese tree shrews infected with SARS-CoV-2. *Zool Res.* 2020;41(5):517–26.
282. Lu S, Zhao Y, Yu W, Yang Y, Gao J, Wang J, et al. Comparison of nonhuman primates identified the suitable model for COVID-19. *Signal Transduct Target Ther [Internet].* 2020;5(1). Available from: <http://dx.doi.org/10.1038/s41392-020-00269-6>
283. Schlottau K, Rissmann M, Graaf A, Schön J, Sehl J, Wylezich C, et al. SARS-CoV-2 in fruit bats, ferrets, pigs, and chickens: an experimental transmission study. *The Lancet Microbe.* 2020;1(5):e218–25.
284. Freuling CM, Breithaupt A, Müller T, Sehl J, Balkema-Buschmann A, Rissmann M, et al. Susceptibility of Raccoon Dogs for Experimental SARS-CoV-2 Infection. *Emerg Infect Dis.* 2020;26(12):2982–5.
285. Francisco R, Hernandez SM, Mead DG, Adcock KG, Burke SC, Nemeth NM, et al. Experimental Susceptibility of North American Raccoons (*Procyon lotor*) and Striped Skunks (*Mephitis mephitis*) to SARS-CoV-2. *Front Vet Sci.* 2022;8(January).
286. Hale VL, Dennis PM, McBride DS, Nolting JM, Madden C, Huey D, et al. SARS-CoV-2 infection in free-ranging white-tailed deer. *Nature.* 2022;602(7897):481–6.
287. Delahay RJ, de la Fuente J, Smith GC, Sharun K, Snary EL, Flores Girón L, et al. Assessing the risks of SARS-CoV-2 in wildlife. *One Heal Outlook.* 2021;3(1).
288. Chilamakuri R, Agarwal S. Covid-19: Characteristics and therapeutics. *Cells.* 2021;10(2):1–29.
289. Fajgenbaum DC, June CH. Cytokine Storm. *N Engl J Med.* 2020;383(23):2255–73.
290. Lowenstein CJ, Solomon SD. Severe COVID-19 Is a microvascular disease. *Circulation.* 2020;1609–11.
291. Moghimi N, Di Napoli M, Biller J, Siegler JE, Shekhar R, McCullough LD, et al. The Neurological Manifestations of Post-Acute Sequelae of SARS-CoV-2 infection. *Curr Neurol Neurosci Rep.* 2021;21(9).
292. Malkova A, Kudryavtsev I, Starshinova A, Kudlay D, Zinchenko Y, Glushkova A, et al. Post covid-19 syndrome in patients with asymptomatic/mild form. *Pathogens.* 2021;10(11).
293. Wu Z, McGoogan JM. Characteristics of and Important Lessons from the Coronavirus Disease 2019 (COVID-19) Outbreak in China: Summary of a Report of 72314 Cases from

- the Chinese Center for Disease Control and Prevention. *JAMA - J Am Med Assoc*. 2020;323(13):1239–42.
294. Colling ME, Kanthi Y. COVID–19-associated coagulopathy: An exploration of mechanisms. *Vasc Med (United Kingdom)*. 2020;25(5):471–8.
  295. Panigada M, Bottino N, Tagliabue P, Grasselli G, Novembrino C, Chantarangkul V, et al. Hypercoagulability of COVID-19 patients in intensive care unit: A report of thromboelastography findings and other parameters of hemostasis. *J Thromb Haemost*. 2020;18(7):1738–42.
  296. Gu SX, Tyagi T, Jain K, Gu VW, Lee SH, Hwa JM, et al. Thrombocytopeny and endotheliopathy: crucial contributors to COVID-19 thromboinflammation. *Nat Rev Cardiol* [Internet]. 2021;18(3):194–209. Available from: <http://dx.doi.org/10.1038/s41569-020-00469-1>
  297. Levi M, Meijers JC. DIC: Which laboratory tests are most useful. *Blood Rev* [Internet]. 2011;25(1):33–7. Available from: <http://dx.doi.org/10.1016/j.blre.2010.09.002>
  298. Goggs R, Jeffery U, LeVine DN, Li RHL. Neutrophil-Extracellular Traps, Cell-Free DNA, and Immunothrombosis in Companion Animals: A Review. *Vet Pathol*. 2020;57(1):6–23.
  299. Godo S, Shimokawa H. Endothelial Functions. *Arterioscler Thromb Vasc Biol*. 2017;37(9):e108–14.
  300. Calabrese F, Pezzuto F, Fortarezza F, Hofman P, Kern I, Panizo A, et al. Pulmonary pathology and COVID-19: lessons from autopsy. The experience of European Pulmonary Pathologists. *Virchows Arch*. 2020;477(3):359–72.
  301. Pons S, Fodil S, Azoulay E, Zafrani L. The vascular endothelium: The cornerstone of organ dysfunction in severe SARS-CoV-2 infection. *Crit Care*. 2020;24(1):4–11.
  302. Nicosia RF, Ligresti G, Caporarello N, Akilesh S, Ribatti D. COVID-19 Vasculopathy: Mounting Evidence for an Indirect Mechanism of Endothelial Injury. *Am J Pathol* [Internet]. 2021;191(8):1374–84. Available from: <https://doi.org/10.1016/j.ajpath.2021.05.007>
  303. Shi Y, Dong K, Zhang YG, Michel RP, Marcus V, Wang YY, et al. Sinusoid endotheliitis as a histological parameter for diagnosing acute liver allograft rejection. *World J Gastroenterol*. 2017;23(5):792–9.
  304. Varga Z, Flammer AJ, Steiger P, Haberecker M, Andermatt R, Zinkernagel AS, et al. Endothelial cell infection and endotheliitis in COVID-19. *Lancet* [Internet]. 2020;395(10234):1417–8. Available from: [http://dx.doi.org/10.1016/S0140-6736\(20\)30937-5](http://dx.doi.org/10.1016/S0140-6736(20)30937-5)
  305. Akilesh S, Nicosia RF, Alpers CE, Tretiakova M, Hsiang TY, Gale M, et al. Characterizing Viral Infection by Electron Microscopy: Lessons from the Coronavirus Disease 2019 Pandemic. *Am J Pathol* [Internet]. 2021;191(2):222–7. Available from: <https://doi.org/10.1016/j.ajpath.2020.11.003>
  306. Yao H, Song Y, Chen Y, Wu N, Xu J, Sun C, et al. Molecular Architecture of the SARS-CoV-2 Virus. *Cell* [Internet]. 2020;183(3):730-738.e13. Available from: <https://doi.org/10.1016/j.cell.2020.09.018>
  307. Goldsmith CS, Miller SE, Martines RB, Bullock HA, Zaki SR. Electron microscopy of SARS-CoV-2: a challenging task. *Lancet* [Internet]. 2020;395(10238):e99. Available from: [http://dx.doi.org/10.1016/S0140-6736\(20\)31188-0](http://dx.doi.org/10.1016/S0140-6736(20)31188-0)
  308. Centers for Disease Control and Prevention (CDC). COVID-19 [Internet]. 2022 [cited

- 2022 Mar 10]. Available from: <https://www.cdc.gov/coronavirus/2019-ncov/index.html>
309. Centers for Disease Control and Prevention (CDC). COVID-19 Johnson & Johnson's Janssen COVID-19 Vaccine Overview and Safety [Internet]. 2022. Available from: <https://www.cdc.gov/coronavirus/2019-ncov/vaccines/different-vaccines/janssen.html#print>
  310. National Institutes of Health. Treatment Guidelines Panel. Coronavirus Disease 2019 (COVID-19) [Internet]. Vol. 2019, NIH. 2021. Available from: <https://www.covid19treatmentguidelines.nih.gov/> <https://www.covid19treatmentguidelines.nih.gov/>
  311. Chan JFW, Zhang AJ, Yuan S, Poon VKM, Chan CCS, Lee ACY, et al. Simulation of the Clinical and Pathological Manifestations of Coronavirus Disease 2019 (COVID-19) in a Golden Syrian Hamster Model: Implications for Disease Pathogenesis and Transmissibility. *Clin Infect Dis*. 2020;71(9):2428–46.
  312. Winkler ES, Bailey AL, Kafai NM, Nair S, McCune BT, Yu J, et al. SARS-CoV-2 infection of human ACE2-transgenic mice causes severe lung inflammation and impaired function. *Nat Immunol* [Internet]. 2020;21(11):1327–35. Available from: <http://dx.doi.org/10.1038/s41590-020-0778-2>
  313. Bao L, Deng W, Huang B, Gao H, Liu J, Ren L, et al. The pathogenicity of SARS-CoV-2 in hACE2 transgenic mice. *Nature*. 2020;583(7818):830–3.
  314. Sun SH, Chen Q, Gu HJ, Yang G, Wang YX, Huang XY, et al. A Mouse Model of SARS-CoV-2 Infection and Pathogenesis. *Cell Host Microbe* [Internet]. 2020;28(1):124-133.e4. Available from: <https://doi.org/10.1016/j.chom.2020.05.020>
  315. Imai M, Iwatsuki-Horimoto K, Hatta M, Loeber S, Halfmann PJ, Nakajima N, et al. Syrian hamsters as a small animal model for SARS-CoV-2 infection and countermeasure development. *Proc Natl Acad Sci U S A*. 2020;117(28):16587–95.
  316. Carroll T, Fox D, van Doremalen N, Ball E, Morris MK, Sotomayor-Gonzalez A, et al. The B.1.427/1.429 (epsilon) SARS-CoV-2 variants are more virulent than ancestral B.1 (614G) in Syrian hamsters. *PLoS Pathog* [Internet]. 2022;18(2):1–24. Available from: <http://dx.doi.org/10.1371/journal.ppat.1009914>
  317. Roberts A, Vogel L, Guarner J, Hayes N, Murphy B, Zaki S, et al. Severe Acute Respiratory Syndrome Coronavirus Infection of Golden Syrian Hamsters. *J Virol*. 2005;79(1):503–11.
  318. Sia SF, Yan LM, Chin AWH, Fung K, Choy KT, Wong AYL, et al. Pathogenesis and transmission of SARS-CoV-2 in golden hamsters. *Nature* [Internet]. 2020;583(7818):834–8. Available from: <http://dx.doi.org/10.1038/s41586-020-2342-5>
  319. Mulka KR, Beck SE, Solis C V., Johanson AL, Queen SE, McCarron ME, et al. Progression and Resolution of Severe Acute Respiratory Syndrome Coronavirus 2 (SARS-CoV-2) Infection in Golden Syrian Hamsters. *Am J Pathol*. 2022;192(2):195–207.
  320. Richard M, Kok A, de Meulder D, Bestebroer TM, Lamers MM, Okba NMA, et al. SARS-CoV-2 is transmitted via contact and via the air between ferrets. *Nat Commun* [Internet]. 2020;11(1):1–6. Available from: <http://dx.doi.org/10.1038/s41467-020-17367-2>
  321. Kim Y Il, Kim SG, Kim SM, Kim EH, Park SJ, Yu KM, et al. Infection and Rapid Transmission of SARS-CoV-2 in Ferrets. *Cell Host Microbe* [Internet]. 2020;27(5):704-709.e2. Available from: <https://doi.org/10.1016/j.chom.2020.03.023>
  322. Kim Y Il, Yu KM, Koh JY, Kim EH, Kim SM, Kim EJ, et al. Age-dependent pathogenic characteristics of SARS-CoV-2 infection in ferrets. *Nat Commun*. 2022;13(1):1–13.

323. Munster VJ, Feldmann F, Williamson BN, van Doremalen N, Pérez-Pérez L, Schulz J, et al. Respiratory disease in rhesus macaques inoculated with SARS-CoV-2. *Nature* [Internet]. 2020;585(7824):268–72. Available from: <http://dx.doi.org/10.1038/s41586-020-2324-7>
324. Rockx B, Kuiken T, Herfst S, Bestebroer T, Lamers MM, Munnink BBO, et al. Comparative pathogenesis of COVID-19, MERS, and SARS in a nonhuman primate model. *Science* (80- ). 2020;368(6494):1012–5.
325. Chandrashekar A, Liu J, Martino AJ, McMahan K, Mercad NB, Peter L, et al. SARS-CoV-2 infection protects against rechallenge in rhesus macaques. *Science* (80- ). 2020;369(6505):812–7.
326. Jia HP, Look DC, Shi L, Hickey M, Pewe L, Netland J, et al. ACE2 Receptor Expression and Severe Acute Respiratory Syndrome Coronavirus Infection Depend on Differentiation of Human Airway Epithelia. *J Virol*. 2005;79(23):14614–21.
327. Hikmet F, Méar L, Edvinsson Å, Micke P, Uhlén M, Lindskog C. The protein expression profile of ACE2 in human tissues. *Mol Syst Biol*. 2020;16(7):1–16.
328. Kuba K, Imai Y, Penninger JM. Angiotensin-converting enzyme 2 in lung diseases. *Curr Opin Pharmacol*. 2006;6(3):271–6.
329. Imai Y, Kuba K, Ohto-Nakanishi T, Penninger JM. Angiotensin-converting enzyme 2 (ACE2) in disease pathogenesis. *Circ J*. 2010;74(3):405–10.
330. Avolio E, Carrabba M, Milligan R, Williamson MK, Beltrami AP, Gupta K, et al. The SARS-CoV-2 Spike protein disrupts human cardiac pericytes function through CD147 receptor-mediated signalling: A potential non-infective mechanism of COVID-19 microvascular disease. *Clin Sci*. 2021;135(24):2667–89.
331. Koupenova M, Clancy L, Corkrey HA, Freedman JE. Circulating platelets as mediators of immunity, inflammation, and thrombosis. *Circ Res*. 2018;122(2):337–51.
332. Melchinger H, Jain K, Tyagi T, Hwa J. Role of Platelet Mitochondria: Life in a Nucleus-Free Zone. *Front Cardiovasc Med*. 2019;6(October):1–11.
333. Middleton EA, He XY, Denorme F, Campbell RA, Ng D, Salvatore SP, et al. Neutrophil extracellular traps contribute to immunothrombosis in COVID-19 acute respiratory distress syndrome. *Blood*. 2020;136(10):1169–79.
334. Coenen DM, Mastenbroek TG, Cosemans JMEM. Platelet interaction with activated endothelium: Mechanistic insights from microfluidics. *Blood*. 2017;130(26):2819–28.
335. Lui JH, Hansen D V., Kriegstein AR. Development and evolution of the human neocortex. *Cell*. 2011;146(1):18–36.
336. Bolon B. Comparative and Correlative Neuroanatomy for the Toxicologic Pathologist. *Toxicol Pathol*. 2000;28(1):6–27.
337. Ventura C V., Ventura LO, Bravo-Filho V, Martins TT, Berrocal AM, Gois AL, et al. Optical coherence tomography of retinal lesions in infants with congenital zika syndrome. *JAMA Ophthalmol*. 2016;134(12):1420–7.
338. Miranda HA de, Costa MC, Frazão MAM, Simão N, Franchischini S, Moshfeghi DM. Expanded Spectrum of Congenital Ocular Findings in Microcephaly with Presumed Zika Infection. *Ophthalmology* [Internet]. 2016;123(8):1788–94. Available from: <http://dx.doi.org/10.1016/j.ophtha.2016.05.001>
339. De Paula Freitas B, De Oliveira Dias JR, Prazeres J, Sacramento GA, Ko AI, Maia M, et al. Ocular findings in infants with microcephaly associated with presumed zika virus congenital infection in Salvador, Brazil. *JAMA Ophthalmol*. 2016;134(5):529–35.

340. Li H, Saucedo-Cuevas L, Shresta S, Gleeson JG. The Neurobiology of Zika Virus. *Neuron* [Internet]. 2016;92(5):949–58. Available from: <http://dx.doi.org/10.1016/j.neuron.2016.11.031>
341. Yiu G, Thomasy SM, Isabel Casanova M, Rusakevich A, Keesler RI, Watanabe J, et al. Evolution of ocular defects in infant macaques following in utero Zika virus infection. Vol. 5, *JCI Insight*. 2020.
342. De Moraes CG. Anatomy of the visual pathways. *J Glaucoma*. 2013;22(5 SUPPL.1):2–7.
343. Carter AM. Animal Models of Human Placentation - A Review. *Placenta* [Internet]. 2007;28(SUPPL.):S41–7. Available from: <http://dx.doi.org/10.1016/j.placenta.2006.11.002>
344. Yiu G, Thomasy SM, Isabel Casanova M, Rusakevich A, Keesler RI, Watanabe J, et al. Evolution of ocular defects in infant macaques following in utero Zika virus infection. *JCI Insight*. 2020;5(24).
345. Hopper KJ, Capozzi DK, Newsome JT. Effects of maternal and infant characteristics on birth weight and gestation length in a colony of rhesus macaques (*macaca mulatta*). *Comp Med*. 2008;58(6):597–603.
346. National Institutes of Health (NIH). NIH Blueprint NHP Atlas: Postnatal reference series [Internet]. Allen Institute for Brain Science. [cited 2022 Apr 9]. Available from: <https://www.blueprintnhpatlas.org/ish/experiment>
347. Oliveira-Szejnfeld PS De, Levine D, Melo AS de O, Amorim MMR, Batista AGM, Chimelli L, et al. Congenital Brain abnormalities and Zika Virus: What the Radiologist Can Expect to See Prenatally and Postnatally. *Radiology*. 2016;281(1):203–18.
348. Chen W, Foo SS, Hong E, Wu C, Lee WS, Lee SA, et al. Zika virus NS3 protease induces bone morphogenetic protein-dependent brain calcification in human fetuses. *Nat Microbiol* [Internet]. 2021;6(4):455–66. Available from: <http://dx.doi.org/10.1038/s41564-020-00850-3>
349. Garey L, De Courten C. Structural development of the lateral geniculate nucleus and visual cortex in monkey and man. *Behav Brain Res*. 1983;10(1):3–13.
350. Bliss-Moreau E, Moadab G, Santistevan A, Amaral DG. The effects of neonatal amygdala or hippocampus lesions on adult social behavior. *Behav Brain Res*. 2016/12/27. 2017;322(Pt A):123–37.
351. Bauer SA, Baker KC. Persistent effects of peer rearing on abnormal and species-appropriate activities but not social behavior in group-housed rhesus macaques (*Macaca mulatta*). *Comp Med*. 2016;66(2):129–36.
352. Sánchez MM, Hearn EF, Do D, Rilling JK, Herndon JG. Differential rearing affects corpus callosum size and cognitive function of rhesus monkeys. *Brain Res*. 1998;812(1–2):38–49.
353. Saleem KS, Logothetis N. A combined MRI and histology atlas of the rhesus monkey brain in stereotaxic coordinates. Elsevier/AP; 2012. 389 p.
354. Ackermann M, Verleden SE, Kuehnel M, Haverich A, Welte T, Laenger F, et al. Pulmonary Vascular Endothelialitis, Thrombosis, and Angiogenesis in Covid-19. *N Engl J Med*. 2020;383(2):120–8.
355. Becker K, Beythien G, de Buhr N, Stanelle-Bertram S, Tuku B, Kouassi NM, et al. Vasculitis and Neutrophil Extracellular Traps in Lungs of Golden Syrian Hamsters With SARS-CoV-2. *Front Immunol*. 2021;12(April):1–11.
356. Saito A, Irie T, Suzuki R, Maemura T, Nasser H, Uriu K, et al. Enhanced fusogenicity and

- pathogenicity of SARS-CoV-2 Delta P681R mutation. *Nature*. 2021;602(July 2021).
357. Buja LM, Wolf D, Zhao B, Akkanti B, McDonald M, Lelenwa L, et al. The emerging spectrum of cardiopulmonary pathology of the coronavirus disease 2019 (COVID-19): Report of 3 autopsies from Houston, Texas, and review of autopsy findings from other United States cities. *Cardiovasc Pathol* [Internet]. 2020;48:107233. Available from: <https://doi.org/10.1016/j.carpath.2020.107233>
  358. Carsana L, Sonzogni A, Nasr A, Rossi RS, Pellegrinelli A, Zerbi P, et al. Pulmonary post-mortem findings in a series of COVID-19 cases from northern Italy: a two-centre descriptive study. *Lancet Infect Dis* [Internet]. 2020;20(10):1135–40. Available from: [http://dx.doi.org/10.1016/S1473-3099\(20\)30434-5](http://dx.doi.org/10.1016/S1473-3099(20)30434-5)
  359. Tian S, Hu W, Niu L, Liu H, Xu H, Xiao SY. Pulmonary Pathology of Early-Phase 2019 Novel Coronavirus (COVID-19) Pneumonia in Two Patients With Lung Cancer. *J Thorac Oncol* [Internet]. 2020;15(5):700–4. Available from: <https://doi.org/10.1016/j.jtho.2020.02.010>
  360. de Roquetaillade C, Bredin S, Lascarrou JB, Soumagne T, Cojocaru M, Chousterman BG, et al. Timing and causes of death in severe COVID-19 patients. *Crit Care* [Internet]. 2021;25(1):1–8. Available from: <https://doi.org/10.1186/s13054-021-03639-w>
  361. Faes C, Abrams S, Van Beckhoven D, Meyfroidt G, Vlieghe E, Hens N. Time between symptom onset, hospitalisation and recovery or death: Statistical analysis of belgian covid-19 patients. *Int J Environ Res Public Health*. 2020;17(20):1–18.
  362. Ding K, Nataneli N. *Cytomegalovirus Corneal Endotheliitis*. Treasure Island, FL: StatPearls Publishing; 2022.
  363. Monteil V, Kwon H, Prado P, Hagelkrüys A, Wimmer RA, Stahl M, et al. Inhibition of SARS-CoV-2 Infections in Engineered Human Tissues Using Clinical-Grade Soluble Human ACE2. *Cell*. 2020;181(4):905-913.e7.
  364. Paniz-Mondolfi A, Bryce C, Grimes Z, Gordon RE, Reidy J, Lednicky J, et al. Central nervous system involvement by severe acute respiratory syndrome coronavirus-2 (SARS-CoV-2). *J Med Virol*. 2020;92(7):699–702.
  365. Bradley BT, Maioli H, Johnston R, Chaudhry I, Fink SL, Xu H, et al. Histopathology and ultrastructural findings of fatal COVID-19 infections in Washington State: a case series. *Lancet* [Internet]. 2020;396(10247):320–32. Available from: [http://dx.doi.org/10.1016/S0140-6736\(20\)31305-2](http://dx.doi.org/10.1016/S0140-6736(20)31305-2)
  366. Garrido Ruiz MC, Santos-Briz Á, Sánchez A, Alonso-Riaño M, Burgos J, Medina-Miguelañez M, et al. Spectrum of Clinicopathologic Findings in COVID-19-induced Skin Lesions: Demonstration of Direct Viral Infection of the Endothelial Cells. *Am J Surg Pathol*. 2021;45(3):293–303.
  367. Khaddaj-Mallat R, Aldib N, Bernard M, Paquette AS, Ferreira A, Lecordier S, et al. SARS-CoV-2 deregulates the vascular and immune functions of brain pericytes via Spike protein. *Neurobiol Dis* [Internet]. 2021;161:105561. Available from: <https://doi.org/10.1016/j.nbd.2021.105561>
  368. He L, Mäe MA, Muhl L, Sun Y, Pietilä R, Nahar K, et al. Pericyte-specific vascular expression of SARS-CoV-2 receptor ACE2 – implications for microvascular inflammation and hypercoagulopathy in COVID-19. *bioRxiv* [Internet]. 2020;2020.05.11.088500. Available from: <https://www.biorxiv.org/content/10.1101/2020.05.11.088500v2%0Ahttps://www.biorxiv.org/content/10.1101/2020.05.11.088500v2.abstract>

369. Schaefer IM, Padera RF, Solomon IH, Kanjilal S, Hammer MM, Hornick JL, et al. In situ detection of SARS-CoV-2 in lungs and airways of patients with COVID-19. *Mod Pathol* [Internet]. 2020;33(11):2104–14. Available from: <http://dx.doi.org/10.1038/s41379-020-0595-z>
370. Akilesh S, Nast CC, Yamashita M, Henriksen K, Charu V, Troxell ML, et al. Multicenter Clinicopathologic Correlation of Kidney Biopsies Performed in COVID-19 Patients Presenting With Acute Kidney Injury or Proteinuria. *Am J Kidney Dis*. 2021;77(1):82-93.e1.
371. Peleg Y, Kudose S, D'Agati V, Siddall E, Ahmad S, Nickolas T, et al. Acute Kidney Injury Due to Collapsing Glomerulopathy Following COVID-19 Infection. *Kidney Int Reports* [Internet]. 2020;5(6):940–5. Available from: <https://doi.org/10.1016/j.ekir.2020.04.017>
372. Wu H, Larsen CP, Hernandez-Arroyo CF, Mohamed MMB, Caza T, Sharshir M, et al. AKI and collapsing glomerulopathy associated with covid-19 and apoll high-risk genotype. *J Am Soc Nephrol*. 2020;31(8):1688–95.
373. McCracken IR, Saginc G, He L, Huseynov A, Daniels A, Fletcher S, et al. Lack of Evidence of Angiotensin-Converting Enzyme 2 Expression and Replicative Infection by SARS-CoV-2 in Human Endothelial Cells. *Circulation*. 2021;865–8.
374. Brambilla M, Canzano P, Becchetti A, Tremoli E, Camera M. Alterations in platelets during SARS-CoV-2 infection. *Platelets* [Internet]. 2022;33(2):192–9. Available from: <https://doi.org/10.1080/09537104.2021.1962519>
375. Canzano P, Brambilla M, Porro B, Cosentino N, Tortorici E, Vicini S, et al. Platelet and Endothelial Activation as Potential Mechanisms Behind the Thrombotic Complications of COVID-19 Patients. *JACC Basic to Transl Sci*. 2021;6(3):202–18.
376. Zaid Y, Puhm F, Allaey I, Naya A, Oudghiri M, Khalki L, et al. Platelets Can Associate with SARS-CoV-2 RNA and Are Hyperactivated in COVID-19. *Circ Res*. 2020;1404–18.
377. Cappellano G, Raineri D, Rolla R, Giordano M, Puricelli C, Vilaro B, et al. Communication circulating platelet-derived extracellular vesicles are a hallmark of sars-cov-2 infection. *Cells*. 2021;10(1):1–10.
378. Schindelin J, Arganda-Carreras I, Frise E, Kaynig V, Longair M, Pietzsch T, et al. Fiji: An open-source platform for biological-image analysis. *Nat Methods*. 2012;9(7):676–82.